Structure and Dynamics of Block Copolymer Based Soft Materials

A DISSERTATION
SUBMITTED TO THE FACULTY OF THE GRADUATE SCHOOL
OF THE UNIVERSITY OF MINNESOTA
BY

Sangwoo Lee

IN PARTIAL FULFILLMENT OF THE REQUIREMENTS
FOR THE DEGREE OF
DOCTOR OF PHILOSOPHY

Frank S. Bates

February 2011

Acknowledgements

I am greatly indebted to my advisor, Prof. Frank S. Bates for his guidance, support, and patience. I remember numerous things he has taught me during the past years, but if I were asked to say only one moment with him that has greatly influenced me as a scientist, I would like to talk about this episode: Several years ago, I was struggling to come up with an explanation of unexpected research findings. One day after he and I had a meeting to discuss the findings, he suddenly asked me a very simple but pointed question, which was similar to the title of the famous textbook for an introductory undergraduate class of philosophy of science, *What Is This Thing Called Science?*[*] I could not answer the question on the spot, came back to my desk, and fell in a deep thought. This question has struck me like a wake-up call in my mind during my whole graduate program and has driven me to develop better ideas and more rigorous methods, and to pursue highly qualified science in conducting my research. Again, I truly appreciate his thoughtful guidance.

I am also greatly thankful to the faculty members in the polymer group, Prof. Christopher W. Macosoko, Prof. Timothy P. Lodge, Prof. David C. Morse, and Prof.

---

[*] Chalmers, A., *What is this thing called science?* Open Univ. Press, 3rd ed.; New York, NY 1999.

Marc A. Hillmyer. They have taught and guided me in many ways with their high standards in research and passion for education. Because they have offered me this far excellent environment in conducting polymer science, I have never experienced any difficulties in finding resources for my research. I am also thankful to Dr. David Giles, Mr. Chris Frethem, Dr. Ozan Ugurlu, and Dr. Maria Torija for their kind help.

There are many colleagues that I should thank for their warmest help and friendship: Aaron K. Brannan, Joon Chatterjee, Mehul Vora, Adam Meuler, Chris Ellison, Kevin Davis, Jihua Chen, Mark Martello, Luca Martinetti, Minoru Soma, Jin Qin, Michael Bluemle, CEMS Korean people, and other polymer group members.

My deepest gratitude should go to my family. I would like to thank my wife, Soyoen from my heart She has been always supportive and has shown the deepest trust in me . Also, I would like to thank my parents and brother Sangjin, who have given endless encouragements several thousand miles away from Minnesota. Last but not least, I would like to thank my cute and playful daughter, Narah, who has been one of the biggest motivatiors for me to do my best.

To Soyoen, Narah, Mother, Father, and Sangjin

Abstract

Block copolymers are made by joining two or more polymer components into a single molecule. Due to the incompatibility between the interconnected chains, block copolymers form microphase separated domains of long range order at length scales of 5 - 100 nm. These materials have been the subject of intense study for the past four decades and the rich structural and dynamic behavior of block copolymers are still being explored. In this thesis, the structure, dynamics and mechanical properties of block copolymers and block copolymer blends were investigated using small-angle X-ray scattering (SAXS), transmission electron microscopy (TEM), dynamic mechanical spectroscopy (DMS), differential scanning calorimetry (DSC), and tensile testing.

A new equilibrium block copolymer phase, the Frank-Kasper σ-phase was discovered in poly(1,4-isoprene-*b*-DL-lactide) (IL) diblock and poly(styrene-*b*-1,4-isoprene-*b*-styrene-*b*-ethylene oxide) (SISO) tetrablock copolymer melts. The σ-phase has tetragonal symmetry ($P4_2/mnm$) and possesses 30 spheres per unit cell. This gigantic crystal, a dodecagonal quasicrystal approximant, structure has been reported primarily in two heavy metals, numerous metal alloys, and dendrimers. Identification of the σ-phase in block copolymers provides new evidence regarding the complex nature of packing spheres on an ordered lattice.

The dynamics ordered sphere-forming block copolymers was studied using SAXS and rheological techniques. The process of ordering into a body-centered cubic (BCC)

morphology from the disordered state and the order-to-order transition (ODT) from the (metastable) BCC to σ-phase were found to follow nucleation and growth mechanisms.

The IL diblock copolymer phase diagram was investigated as a function of composition and temperature. IL diblock copolymers are strongly segregated due to a relatively large Flory-Huggins interaction parameter χ between polyisoprene and poly(DL-lactide). Fluctuation effects strongly influence the ODT due to the low IL molecular weights and this was evidenced by thermal signatures in DSC thermograms.

The structure and mechanical properties of poly(DL-lactide-*b*-1,4-isoprene-*b*-DL-lactide) (LIL) triblock copolymer thermoplastic elastomer and low molecular weight IL diblock copolymers, and blends of these materials were studied. While the linear response is relatively invariant to the molecular architecture and molecular weight, the extensional properties were dramatically influenced by the triblock content.

Finally, path dependency of microstructures of poly(1,2-butadiene-*b*-ethylene oxide) (PB-PEO) non-ionic block copolymer surfactants in oil and water was examined. Due to an extremely low critical micelle concentration due to the high molecular weight of the PB-PEO block copolymer surfactant, highly path dependent and long-lasting metastable microstructures were generated. This result offers new opportunities for the preparation of target block copolymer microstructures.

Table of Contents

List of Tables x

List of Figures xi

Chapter 1 1

Introduction 1

1.1 Multicomponenet Polymer Systems 1

1.2 Block Copolymer 3

1.3 Surfactants 10

1.4 Block Copolymer Surfactancy 16

1.5. Thesis Outline 22

Chapter 2 23

Block Copolymer Synthesis and Material Characterization 23

2.1 Anionic Polymerization 24

2.2 Nuclear Magnetic Resonance 43

2.3 Size Exclusion Chromatography 49

2.4 Differential Scanning Calorimetry 54

2.5 Dynamic Mechanical Spectroscopy 56

2.6 Small Angle X-Ray Scattering 60

2.7 Cryogenic Scanning Electron Microscopy 75

Chapter 3 81

Frank-Kasper σ-Phase in Block Copolymer Melts 81

3.1 Introduction 81

3.2 Experimental 84

3.3 Result and Analysis 87

3.4 Discussion 95

3.5 Conclusion 106

Chapter 4 108

Rheological Properties of Sphere-Forming Block Copolymer 108

4.1 Introduction 108

4.2 Experimental 109

4.3 Result and Analysis 110

3.4 Discussion 122

Chapter 5 130

Phase Behavior of Poly(1,4-isoprene-*b*-DL-lactide) Diblock Copolymers 130

5.1 Introduction 130

5.2 Experimental 132

5.3 Result and Analysis 135

5.4 Discussion 139

Chapter 6 150

Linear and Non-linear Mechanical Properties of AB and ABA Block Copolymer Blends 150

6.1 Introduction 150

6.2 Experimental 153

6.3 Result and Analysis 156

6.4 Discussion 186

Chapter 7 196

Path-Dependent Microstructures of Block Copolymer Non-ionic Surfactant in Oil and Water 196

7.1 Introduction 196

7.2 Experimental 198

7.3 Result and Analysis 203

7.4 Discussion 233

Bibliography 248

Appendix A 269

Appendix B 273

List of Tables

Table 2.1 44

Table 2.2 67

Table 2.3 78

Table 3.1 85

Table 3.2. 97

Table 3.3 98

Table 5.1 133

Table 5.2 138

Table 5.3 147

Table 6.1 157

Table 6.2 164

Table 7.1 208

List of Figures

Figure 1.1 6

Figure 1.2 6

Figure 1.3 8

Figure 1.4 9

Figure 1.5 13

Figure 1.6 14

Figure 1.7 15

Figure 1.8 18

Figure 1.9 19

Figure 1.10 21

Figure 2.1 27

Figure 2.2 30

Figure 2.3 35

Figure 2.4 39

Figure 2.5 46

Figure 2.6 48

Figure 2.7 53

Figure 2.8 55

Figure 2.9 61

Figure 2.10 63

Figure 2.11 65

Figure 2.12 68

Figure 2.13 68

Figure 2.14 71

Figure 2.15. 76

Figure 2.16 79

Figure 3.1 85

Figure 3.2. 88

Figure 3.3 90

Figure 3.4 93

Figure 3.5 96

Figure 3.6 100

Figure 3.7 105

Figure 4.1 111

Figure 4.2 113

Figure 4.3 115

Figure 4.4. 117

Figure 4.5 118

Figure 4.6 120

Figure 4.7 121

Figure 4.8 125

Figure 4.9 128

Figure 5.1 136

Figure 5.2 140

Figure 5.3 141

Figure 5.4 143

Figure 5.5 146

Figure 6.1 158

Figure 6.2 159

Figure 6.3 161

Figure 6.4 162

Figure 6.5 165

Figure 6.6 166

Figure 6.7 167

Figure 6.8 168

Figure 6.9 169

Figure 6.10 172

Figure 6.11 173

Figure 6.12 174

Figure 6.13 176

Figure 6.14 177

Figure 6.15 178

Figure 6.16 179

Figure 6.17 180

Figure 6.18 181

Figure 6.19 182

Figure 6.20 183

Figure 6.21 184

Figure 6.22 185

Figure 6.23 189

Figure 6.24 191

Figure 7.1. 204

Figure 7.2 205

Figure 7.3 206

Figure 7.4 206

Figure 7.5 209

Figure 7.6 211

Figure 7.7 212

Figure 7.8 214

Figure 7.9 215

Figure 7.10 216

Figure 7.11 218

Figure 7.12 220

Figure 7.13 223

Figure 7.14 224

Figure 7.15. 225

Figure 7.16 226

Figure 7.17 227

Figure 7.18 229

Figure 7.19 231

Figure 7.20 232

Figure 7.21 234

Figure 7.22 236

Figure 7.23 241

Figure A.1 269

Figure A.2 270

Figure A.3 271

Figure A.4 272

Chapter 1
Introduction

1.1 Multicomponenet Polymer Systems

In modern daily life, we rely on a tremendous number of products made with synthetic polymers, e.g., clothing, automobiles, electronics, and even disposable plastic grocery shopping bags, and these products represent one of the most important categories of materials. What makes a polymer so important and special? The basic unit of any polymer is a chemical structure just several nanometers in scale. But this unit is repeated many times leading to a big molecule. The usefulness of polymeric materials come largely from the huge molecular size, which endows extraordinary chemical and mechanical properties compared to the other small molecular compounds. Synthetic polymers are generally prepared by a chemical process called '*polymerization*', which is a

process of repeated addition of small molecules (referred to as monomers) to the ends of a linear polymer chain. By this process, polymers can have very large molecular weight and the total number of repeated monomer additions is denoted as the degree of polymerization *N*.

The large molecular size is also reflected in the thermodynamic behaviors of polymers. Probably, the Gibbs free energy describing a mixture of two polymers is a good example to present the pronounced effect of the high *N*. The free energy of mixing of two polymers ΔG_m can be represented as,[1]

$$\frac{\Delta G_m}{kT} = \frac{\phi_A}{N_A}\ln\phi_A + \frac{\phi_B}{N_B}\ln\phi_B + \phi_A\phi_B\chi \qquad (1.1)$$

where k is the Boltzmann constant, T is temperature, ϕ is the volume fraction, χ is the Flory-Huggins interaction parameter, and each polymer species is denoted by the subscripts (A and B). The last term on the right hand side of in Eqn (1.1) describes the enthalpic contribution from the incompatibility of two polymers and the first two terms reflect the entropic contribution. The significance of molecular size comes in the entropic part. As the denominator N increases, the entropic terms give a negligible contribution to the free energy so mixing of polymers is governed by the enthalpy term χ known as the Flory-Huggins interaction parameter.

Based on regular solution theory, the Flory-Huggins interaction parameter can be estimated by,

$$\chi = \frac{\hat{V}}{RT}\left(\delta_A - \delta_B\right)^2 \tag{1.2}$$

where $\hat{V}$ is the segment (repeat unit) volume, R is the gas constant, and δ is the solubility parameter. In practice, the Flory-Huggins interaction parameter is experimentally measured as a function of temperature,

$$\chi = \frac{\alpha}{T} + \beta \tag{1.3}$$

Thus, as temperature increases, χ decreases and two incompatible polymers become miscible. This inverse dependence of χ on temperature makes a polymer mixture have an upper critical solution temperature (UCST).

1.2 Block Copolymer

Block copolymers are macromolecules made of two or more covalently joined chemically different linear polymer chains. Due to the covalent bonding between the chains, block copolymers cannot form a macrophase separated state, but instead display microphase separation. Leibler described the thermodynamic behaviors of model AB diblock copolymers using the mean field theory, and his approach forms the basis for current theory.[2, 3] He proposed that the thermodynamic behavior of diblock copolymers can be described by two major variables, the compound variable (χN) and the block volume fraction ϕ_A (= 1 - ϕ_B). The variable χN controls the state of order or disorder in

block copolymer melts and the order-disorder transition (ODT) of symmetric diblock copolymers ($\phi_A = 0.5$) is predicted to occur at

$$(\chi N)_{ODT} = 10.5 \tag{1.4}$$

The ODT of diblock copolymers is anticipated to be a first order transition, even for symmetric systems due to fluctuation effects, which has been confirmed theoretically and experimentally.[2, 4-9] In practically encountered block copolymer systems, $(\chi N)_{ODT}$ at $\phi_A = 0.5$ is believed to be higher than 10.5 due to fluctuation effects, which can be shown to derive from finite molecular weights. Fredrickson and Helfand attempted to quantify the effects of fluctuations by a correction to the mean-field theory leading to the following result:

$$(\chi N)_{ODT} = 10.5 + 41N^{-1/3} \tag{1.5}$$

However, this result is expected to be valid only at relatively high N ($\geq 10^4$), values that are much greater than the degree of polymerization of practical block copolymers. Experimental studies have confirmed quantitative inconsistencies with Eqn (1.5).[4, 10] Nevertheless, the importance of fluctuation effects on the ODT of block copolymers is regarded as significant.

The magnitude of (χN) is also manifested in the degree of segregation between chains. When (χN) is of order 10, the domains produced by microphase separated chains are somewhat mixed with the different block chains due to the entropic contribution to the overall free energy relative to the enthalpic effect. Therefore, the density profile of a

block species displays a somewhat sinusoidal form with a periodicity D, which is controlled by the overall polymer radius of gyration R_g. This regime is called as the weakly segregation limit (WSL). For segregated domains with high (χN) (>> 10), referred to as the strongly segregation limit (SSL), the block density profile becomes an alternating box shape (nearly pure domains) due to a predominant enthalpic contribution (large χ). Lastly, the regime between WSL and SSL is referred to as the intermediate segregation limit (ISL).[11]

The other principal parameter, the block volume fraction (ϕ), primarily determines the microphase morphology in an ordered state. Leibler anticipated three major microstructures based on the Landau theory: lamellar (LAM), hexagonally packed cylinders (HEX), and spheres arranged on a body centered cubic (BCC) lattice (Figure 1.1).[2, 12, 13] Later, another cubic phase, the bicontinuous network gyroid (GYR) phase (also referred to as Q^{230}) was confirmed as an equilibrium microphase morphology in diblock copolymers after intensive debate in the block copolymer research community.[14-19] The gyroid phase is located at composition intermediate to those leading to LAM and HEX. Recently, a second non-cubic, network phase with orthorhombic symmetry was discovered in diblock copolymers, denoted O^{70}, following a theoretical prediction.[20-22] Figure 1.2 compares the diblock copolymer phase diagram constructed by the self-consistent field theory and the experimental phase diagram of poly(styrene-*b*-1,4-isoprene).[3, 19]

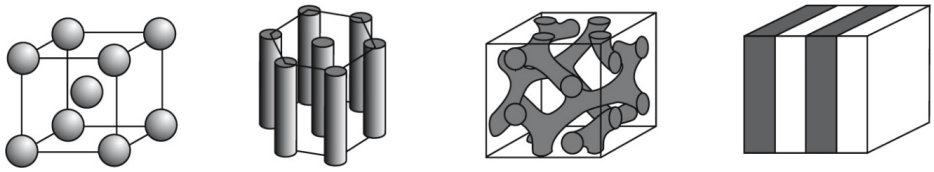

Figure 1.1 Diblock copolymer morphology. From the left to right, body centered cubic (BCC), hexagonally packed cylinders (HEX), gyroid (GYR), and lamellar (LAM). Reproduced from Abetz and Simson.[23]

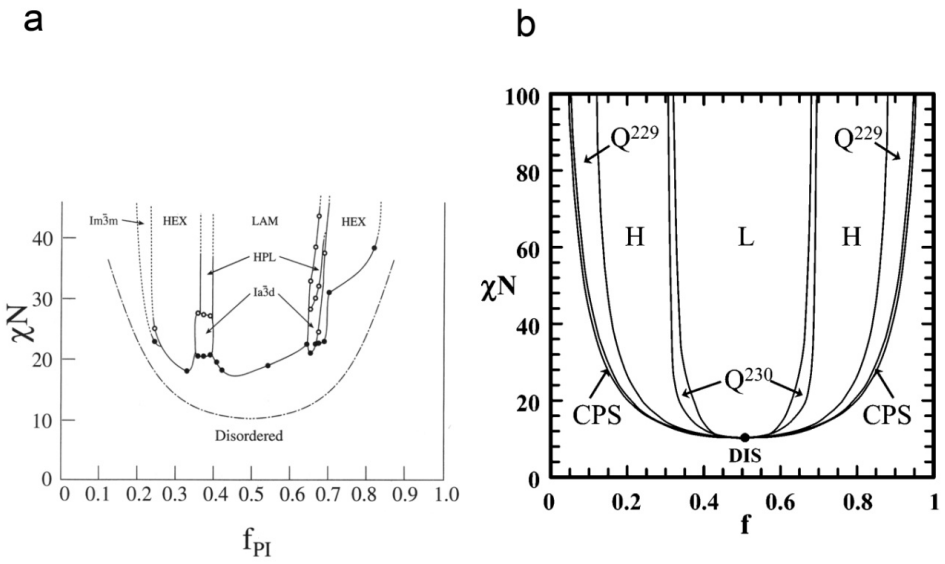

Figure 1.2 Diblock copolymer phase diagrams by block volume composition (f_{PI} and f) and (χN) constructed using (a) poly(styrene-*b*-1,4-isoprene) diblock copolymers and (b) self-consistent field theory (SCFT). Abbreviation L and LAM denote the lamellar morphology, Q^{230} and Ia-3d denote the bicontinuous gyroid phase, H and HEX denote hexagonally packed cylinders, Q229 and Im-3m denote the body centered cubic spheres (BCC), and DIS represents the disordered state. The phase diagrams are reproduced by two reports.[3, 19]

Using the same methods applied to the studies of model AB diblock copolymers, investigations on the thermodynamic behavior of ABA triblock copolymers were conducted by many research groups.[24-26] ABA triblock copolymers are the simplest extension of the AB block copolymer architecture, and for theoretical purposes can be regarded as the coupling of AB and BA diblock copolymers, covalently joined into a single ABA structure. Thus, the thermodynamics of ABA triblock copolymers are very similar to AB diblock copolymers. A detailed theoretical treatment results in the shift of the ODT phase boundary for triblock copolymers, where $(\chi N)_{ODT} = 17.9$ at the symmetric composition ($\phi_A = 0.5$).[24-26] Note that this results includes a doubling of N relative to the diblocks, thus $(\chi_{AB}/\chi_{ABA}) = 1.17$.

In contrast to the thermodynamic similarity between AB and ABA diblock copolymers, the mechanical properties can be significantly different. In the microphase separated states, ABA triblock copolymer chains can have loop and bridge configurations. In the loop configuration, two end A block chains of a ABA triblock copolymer chain are located in the same A domain. The bridge configuration dictates that the two A block chains are located in two separate A domains which makes the middle B chain act as a physical crosslink, significantly altering the mechanical properties of ABA triblock copolymers. These configurations are schematically drawn in Figure 1.3. The fraction of bridging configurations in ABA triblock copolymers was theoretically predicted to vary

from ~ 40 % in LAM to ~ 80 % in the BCC morphology.[24] However, attempts to quantify the bridge fraction experimentally have produced inconsistent results.[27-29]

The thermodynamic and mechanical properties of block copolymers with extended numbers of blocks and more than two block types, e.g., ABC, ABCD, ABAC, and ABCBA, and non-linear molecular architectures, e.g., star block copolymers, have been investigated by many groups.[30-40] Possibly, the most studied multiblock copolymer system is the ABC triblock terpolymers. By only a single extension of the number of block species, ABC triblock terpolymers produce a large number of new morphologies including three domain LAM, hexagonally perforated lamellar (HPL), core-shell morphologies of HEX, BCC, and GYR, alternating gyroid Q^{214}, and the tricontinuous orthorhombic networks O^{70} and O^{52}.[22, 30-39] A representative experimental phase diagram from the poly(1,4-isoprene-*b*-styrene-*b*-ethylene oxide) (ISO) system is presented in Figure 1.4.

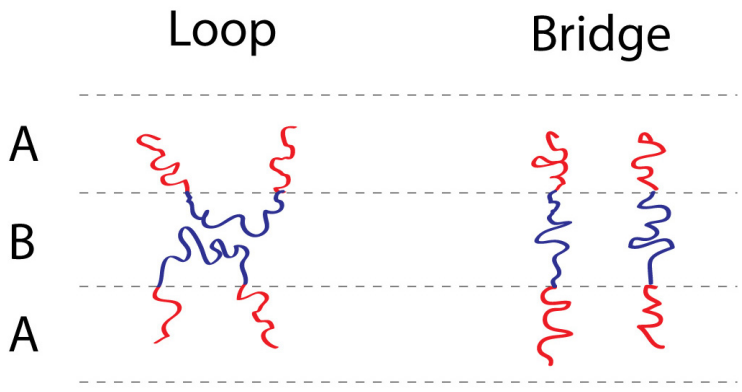

Figure 1.3 Schematic drawing of the loop and bridge chain configurations of microphase separated ABA triblock copolymers.

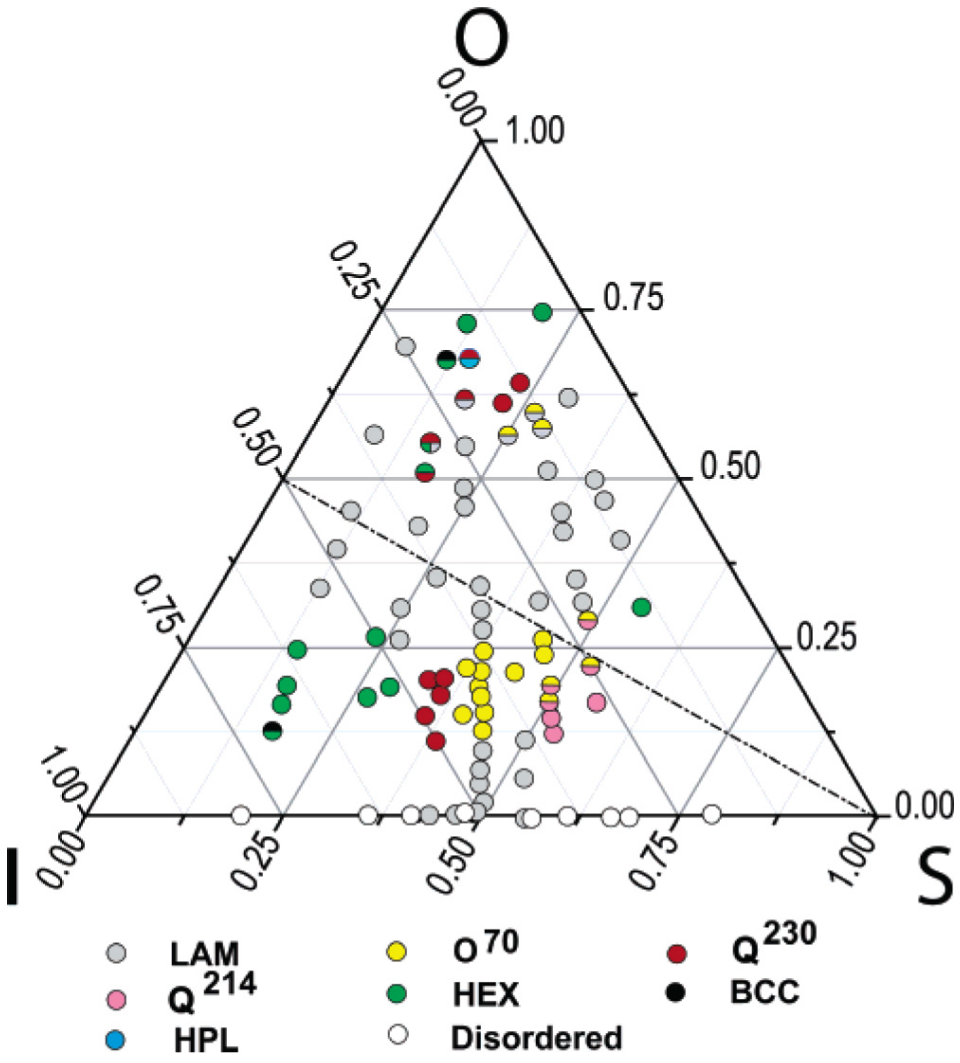

Figure 1.4 Experimental phase diagram of poly(1,4-isoprene-*b*-styrene-*b*-ethylene oxide) (ISO) triblock copolymer. Reproduced from Chatterjee, Jain, and Bates.[35]

1.3 Surfactants

Surfactants (amphiphiles) lower the interfacial tension between two immiscible fluids and promote mixing.[41] This phenomena originates from the structure of surfactant molecules. Similar to the molecular structure of block copolymers, surfactants have two incompatible parts which are selectively miscible with compounds categorized by a specific physical properties, e.g., polarity. Surfactants are generally divided into two groups, ionic, and non-ionic surfactants. Ionic surfactants refer to molecules made of an oil-philic hydrocarbon part and a water-philic ionic functional group, e.g. anion, cation, and zwitterion. Non-ionic surfactants generally contain several ethylene glycol (or ethylene oxide) groups ($-CH_2CH_2O-$) for the water-philic part attached to a hydrocarbon piece with the overall molecule denoted by C_iE_j where "i" is the number of carbon atoms and "j" is the number of ethylene oxide groups. For example, 2-butoxyethanol ($CH_3CH_2CH_2CH_2OCH_2CH_2OH$) is abbreviated as C_4E_1. The oil-philic hydrocarbon chains and water-philic polar groups are generally referred to as tails and heads, respectively. In this work, only non-ionic surfactants are considered.

When a very small amount of surfactant is dissolved in a solvent, only free surfactant chains exist in the solution. As the concentration increases and reaches a certain point, referred to as the critical micellar concentration (CMC), the surfactant molecules begin to form micelles and any additional surfactant is incorporated into micelles.[42] The CMC is significantly dependent on the molecular weight (MW) of the

surfactant and the temperature. For example, the experimentally measured CMC of C_4E_1 (MW = 128 g/mol) in water is 0.98 M, but the CMC of $C_{12}E_6$ (MW = 452.7 g/mol) is 8.7 $\times 10^{-5}$ M at 25 ^{o}C, showing a difference of 5 order of magnitude.[43] The dependence of the CMC on temperature is related to the phase behavior of poly(ethylene glycol) in water.[44] Solutions of poly(ethylene glycol) in water exhibit the lower and upper critical solution temperatures (LCST and USCT), producing phase separation between certain low and high temperatures. Thus, non-ionic surfactants have a temperature window of miscibility in water, and outside this the window, phase separation into the water-rich phase and surfactant-rich mixtures occurs. This temperature dependence of the surfactants and CMC lead to another important definition in the phase behavior of surfactants. On the binary phase diagram (concentration of surfactant versus temperature), there is a point where the CMC and the miscibility boundary of surfactants and solvent cross. This is referred to the Krafft point.[41]

The CMC is not only important to surfactant thermodynamics, but results in pronounced effects in the dynamics because it determines the amount of free surfactant molecules which can migrate between micelles based on mass action.[45, 46] Although there are many other considerations associated with this complex phenomena, it should be noted that a very low CMC can significantly slow the kinetics that control approach to the equilibrium state of a micellar phase.[47, 48]

Surfactants self-assemble into microstructured micelles of spherical, cylinderical, or bilayer geometry, and the resulting geometry is believed to be related to the interplay between the volume of the tail (v_t), tail length (l_t), and surface area of the head (a_h). These molecular characteristics can be parameterized into a criterion in dilute binary solutions for the selection of a micelle geometry, referred to as the packing parameter,

$$P = \frac{v_t}{a_h l_t} \tag{1.6}$$

The micellar structures anticipated by the packing parameter P are summarized in Figure 1.5. The microstructures of micelles are dependent on the composition and temperature, and an idealized binary phase diagram is presented in Figure 1.6.

Surfactants promote the miscibility of two incompatible compounds so the structure of ternary mixtures composed of surfactant, water, and oil are easily conceivable. This topic has been studied extensively through the past half century and is still being expanded.[49-52] The detailed of phase behaviors of ternary mixtures are complex and too vast to be examined in detail here. In this section, only two of the important aspects of this field are discussed, those most related to this thesis work.

A ternary mixture of non-ionic surfactant, water, and oil can form three macrophases, rich in each component (Figure 1.7a). This phenomena is caused by the interplay between the two binary phase gaps of non-ionic surfactant-water and -oil. When a ternary mixture of an isovolume composition of water and oil forms three phases at the temperature $\overline{T} = (T_u + T_l) / 2$ (Figure 1.7a), only a small amount of surfactant is

Lipid	Critical packing parameter	Critical packing shape	Structures formed
Single-chained lipids (surfactants) with large head group areas: SDS in low salt	< 1/3	Cone 	Spherical micelles 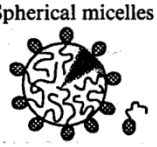
Single-chained lipids with small head group areas: SDS and CTAB in high salt, nonionic lipids	1/3–1/2	Truncated cone 	Cylindrical micelles 
Double-chained lipids with large head group areas, fluid chains: phosphatidyl choline (lecithin), phosphatidyl serine, phosphatidyl glycerol, phosphatidyl inositol, phosphatidic acid, sphingomyelin, DGDG,[a] dihexadecyl phosphate, dialkyl dimethyl ammonium salts	1/2–1	Truncated cone 	Flexible bilayers, vesicles 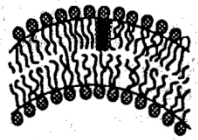
Double-chained lipids with small head group areas, anionic lipids in high salt, saturated frozen chains: phosphatidyl ethanolamine phosphatidyl serine + Ca^{2+}	~1	Cylinder 	Planar bilayers 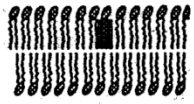
Double-chained lipids with small head group areas, nonionic lipids, poly (cis) unsaturated chains, high T: unsaturated phosphatidyl ethanolamine, cardiolipin + Ca^{2+} phosphatidic acid + Ca^{2+} cholesterol, MGDG[b]	>1	Inverted truncated cone or wedge 	Inverted micelles 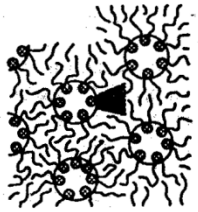

Figure 1.5 Schematic drawing of micellar geometry by the packing parameter. Abbreviation, SDS denotes sodium dodecyl sulfate, CTAB denotes etyltrimethylammoniumbromide, DGDG denotes digalactosyl diglyceride and diglucosyl diglyceride, and MGDG denotes monogalactosyl diglyceride and monoglycosyl diglyceride. Reproduced from Hiemenz and Rajagopalan.[53]

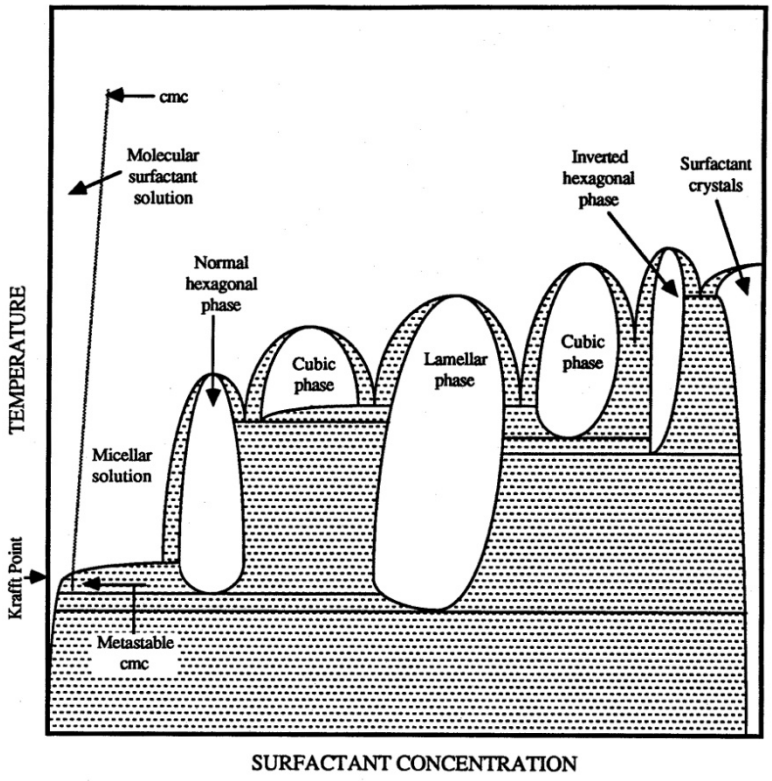

Figure 1.6 Idealized binary phase diagram of surfactant and solvent by composition and temperature. Reproduced from Vinson.[54]

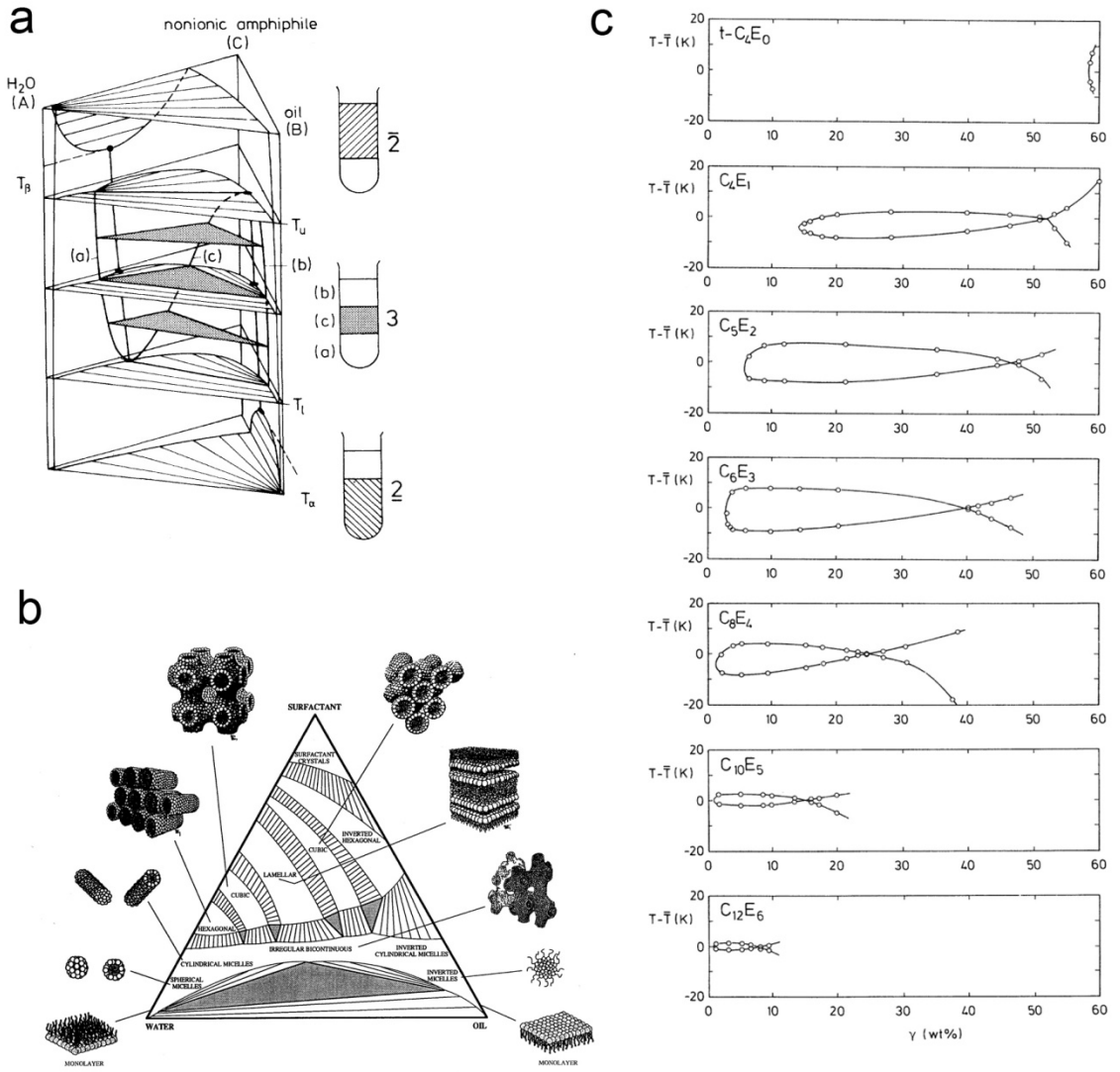

Figure 1.7 Ternary phase diagrams of non-ionic surfactant, water, and oil. Phase prism of (a) an idealized ternary system, (b) water and *n*-octane isovolume phase map of C_iE_j, and (c) Gibbs phase triangle with schematic drawings of micellar microstructures are presented. Phase diagrams are reproduced from two reports.[51, 55]

dissolved in the water and oil phases in the form of spherical and inverted micelles (Figure 1.7b). The majority of the surfactant forms a third surfactant-rich phase between the water and oil phases, with its position driven by the difference in phase densities. The microstructure of this middle surfactant phase is described by a the bicontinuous microemulsion, which occurs due to the extremely low surface tension (Figure 1.7b).[56-58]

The other important observation is the increase of the surfactant efficiency with the molecular weight of the surfactant.[51] The surfactant efficiency is correlated with the minimum amount of surfactant required to emulsify equal volumes of water and oil, and this is very important factor for practical and economical purposes. The experimental phase diagrams in Figure 1.7c clearly shows the proportionality between the molecular weight of the surfactant and the surfactant efficiency (cross points of the phase boundaries).

1.4 Block Copolymer Surfactancy

Block copolymers can be regarded as surfactants with very high molecular weights. The advances of modern synthetic chemistry enable the preparation of block copolymers from various kinds of monomers for target surfactant properties.[59, 60] Compared to traditional low molecular weight surfactants (MW ~ 500 g/mol), the single most important and distinctive characteristic of block copolymer surfactants is the extremely low CMC's due to the high molecular weights and this makes block copolymer

surfactants non-ergodic in many cases.[47, 61-63] Surprisingly, despite significant limitations in the kinetics of block copolymer micellization due to the negligible CMC's, much experimental works on block copolymer surfactants have shown that monodisperse block copolymer micelles can be prepared without difficulty in pseudo- and binary systems.[64-73]

The geometry of block copolymer micelles is primarily controlled by the block compositions. Similar to the packing parameter P for the micellar geometry of the low molecular weight surfactants, Won and co-workers related the micellar geometry of poly(ethylene oxide)-based non-ionic block copolymer surfactants in water to the interfacial area per chain a_0 and the degree of core chain stretching s defined as

$$s = \frac{R_c}{r_0} \tag{1.7}$$

where R_c is the core dimension of the block copolymer micelles and r_0 is the unperturbed end-to-end distance of the core chain. The interfacial area per chain a_0 can be extracted from the number of block copolymer chains based on the experimentally measured micelle dimensions (e.g. core radius). As presented in Figure 1.8, the micelle geometry is clearly related to a_0 and s and these parameters are inversely proportional to the domain geometry.

In the dilute limit (≤ 1 wt. %), the phase behavior of poly(1,2-butadiene-*b*-ethylene oxide) (PB-PEO) non-ionic diblock copolymer surfactant in water was extensively studied and a representative experimental phase portrait is shown in Figure 1.9.[62, 70, 71] Notably, a network morphology was discovered between the cylinder and

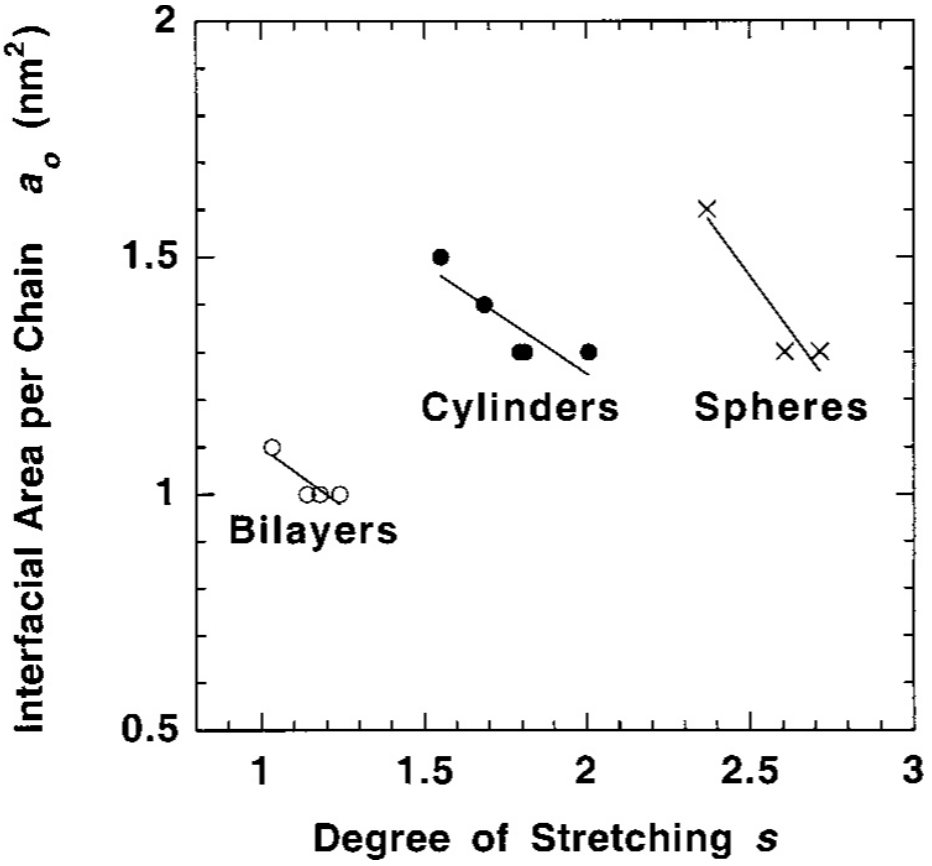

Figure 1.8 Correlation between the interfacial area per chain a_0 and the degree of stretching s as a function the micellar geometry. Reproduced from Won and co-workers.[74]

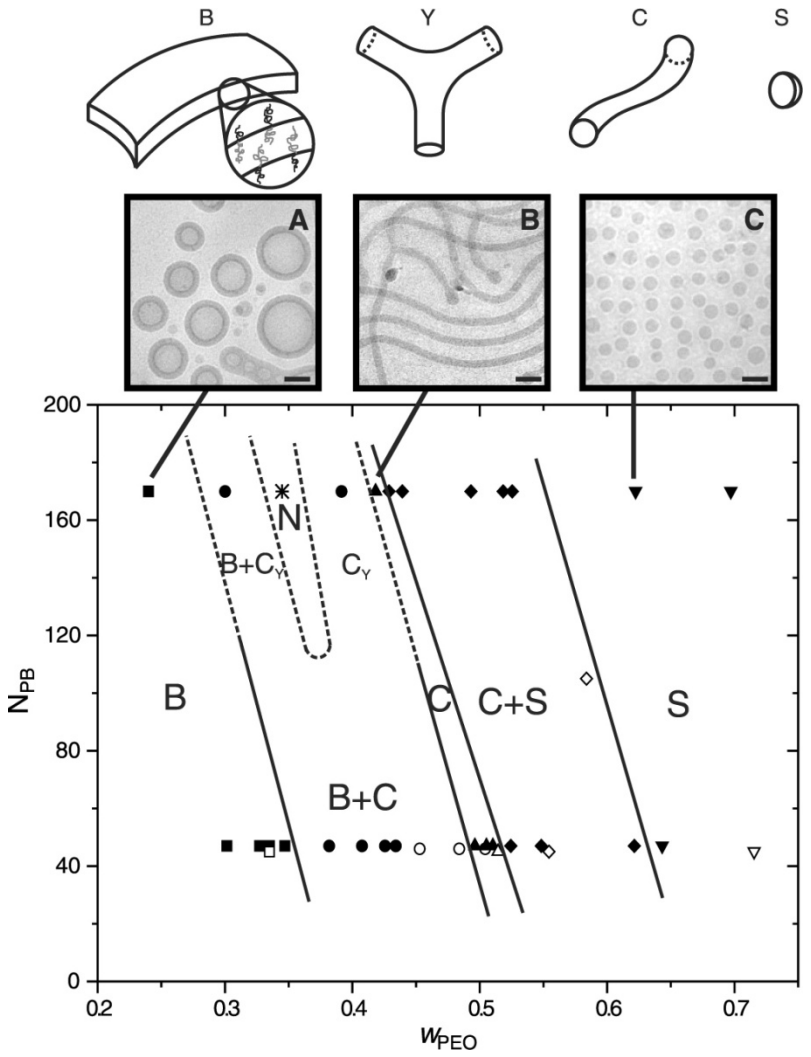

Figure 1.9 Experimental morphology diagram constructed with poly(1,2-butadiene-*b*-ethylene oxide) (PB-PEO) in water (1 wt. %). This diagram is shown with the degree of polymerization of PB block N_{PB} and the weight fraction of PEO w_{PEO}. Abbreviation B, Y, C, and S represent the bilayer, Y-junction, cylinder, and sphere geometries, respectively. Reproduced from Jain and Bates.[71]

bilayer domains, which has morphological similarities to the 3-fold microemulsion network observed from the C_iE_j non-ionic surfactant systems.[75, 76]

The lyotropic phase behavior of PB-PEO block copolymers in water was also investigated and a representative experimental phase diagram is shown in Figure 1.10. PB-PEO diblock copolymers displayed long-range ordered structures above approximately 20 wt. % in water (BCC, FCC, HEX and LAM morphologies) and a randomly-interconnected network morphology was discovered (See the lower panel in Figure 1.10).

Compared to the amount of work on the binary phase behaviors of block copolymer surfactants, the ternary block copolymer solutions (i.e., with water and oil) have barely been studied and only a handful of reports on this subject are available. This is due in part to the fact that the preparation of ternary block copolymer solutions in equilibrium is almost impossible.[77-80] However, Strey and co-workers discovered that block copolymers can be used to boost the surfactant efficiency of non-ionic surfactants.[80-82] In this thesis work, we have attempted to expand the understanding of the phase behavior of block copolymers in ternary systems, with a focus on the path-dependent phase behavior and microstructure morphologies of PB-PEO block copolymer surfactants mixed with water and oil.

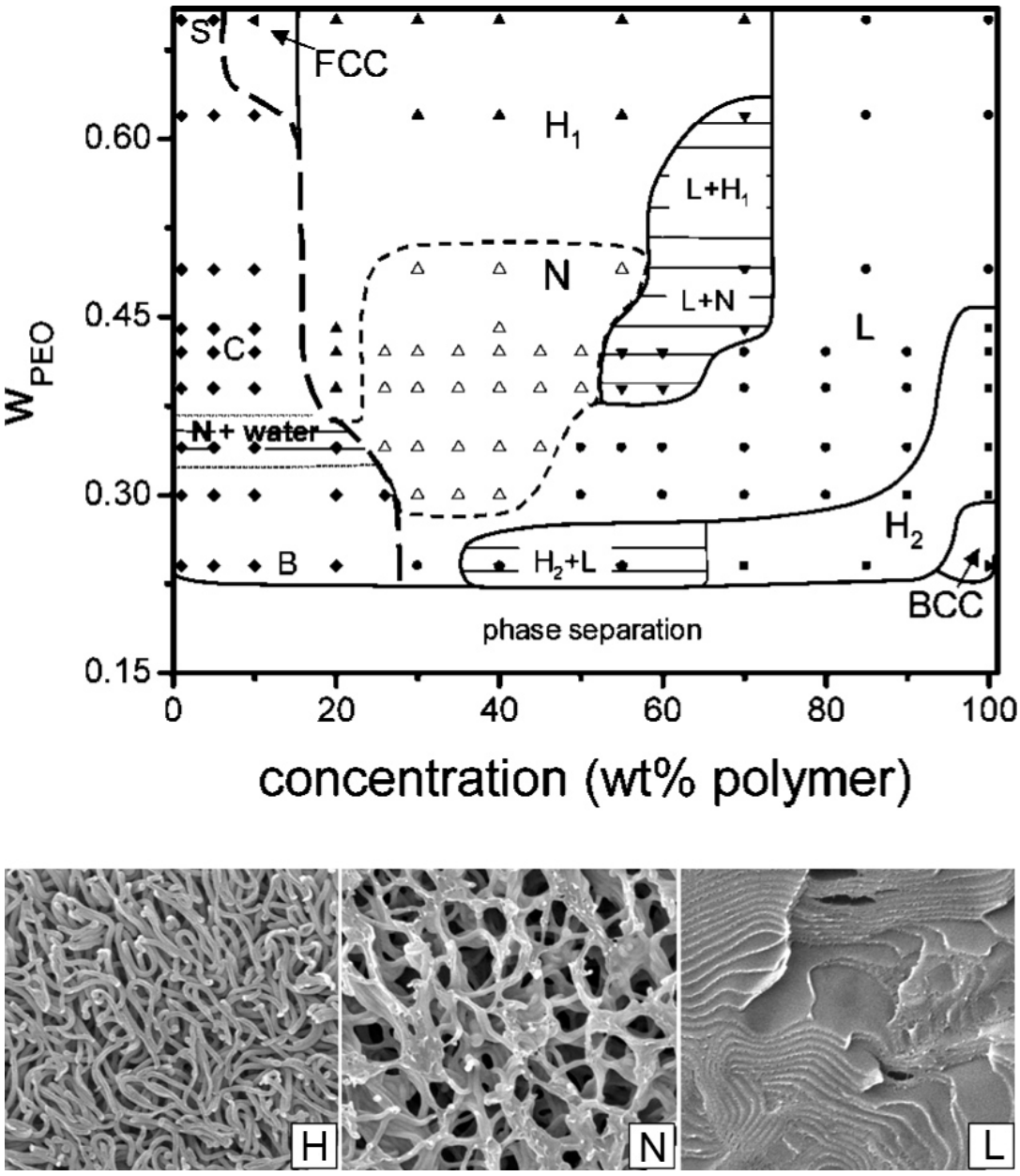

Figure 1.10 Experimental phase diagram of PB-PEO non-ionic block copolymers with N_{PB} = 172 (upper panel) and cryogenic scanning electron micrographs from representative domains (lower panel). Reproduced from Jain and co-workers.[83]

1.5. Thesis Outline

This thesis covers five research topics on block copolymers. Following a summary of the experimental techniques in Chapter 2, experimental evidence of a newly discovered Frank-Kasper σ-phase in poly(1,4-isoprene-*b*-DL-lactide) (IL) and poly(styrene-*b*-1,4-isoprene-*b*-styrene-*b*-ethylene oxide) (SISO) block copolymers and related materials is presented in Chapter 3. The thermodynamic and dynamic behavior of sphere-forming IL block copolymer are further discussed in Chapter 4. An expanded study of the thermodynamics of IL diblock copolymers is presented in Chapter 5. Preliminary results regarding the linear and non-linear mechanical properties of poly(DL-lactide-*b*-1,4-isoprene-*b*-DL-lactide) (LIL) and IL block copolymer blends are summarized in Chapter 6. Finally, comprehensive investigation of the path-dependent phase behavior and microstructures of PB-PEO diblock copolymer surfactant blended with water and oil are presented and discussed in Chapter 7.

Chapter 2
Block Copolymer Synthesis and Material Characterization

The preparation and characterization of well-tailored materials represents the beginning of any successful material research program. Block copolymers used in this research were synthesized by anionic polymerization protocols, and the products were characterized by proton nuclear magnetic resonance (^{1}H NMR) spectroscopy, size exclusion chromatography (SEC) and, differential scanning calorimetry (DSC). Microphase separation-related phenomena and surfactancy were investigated with these block copolymers using dynamic mechanical spectroscopy (DMS), small angle X-ray scattering (SAXS), and cryogenic-scanning electron microscopy (Cryo-SEM). These techniques are briefly reviewed in this chapter.

2.1 Anionic Polymerization

A anionic polymerization is a chain-growth polymerization technique.[59] The reactive centers have excellent stability, and the growing polymerize by the controlled sequential addition of monomers. Based on this stability, anionic polymerization is referred as having a *'living*' character since termination of growing chains and side reactions are virtually negligible in practice.[84] Moreover, the ability to sequentially add batches of monomers is the primary reason that the anionic polymerization technique has been used for the synthesis of well-tailored block copolymers.

A set of macromolecular polymer chains are characterized by two essential quantities: average molecular weight (*M*) and polydispersity index (PDI). The average molecular weight of a polymer is typically described by two different averaging methods, number-averaged M_n and weight-averaged molecular weights M_w defined as follows:

$$M_n = \frac{\sum_i n_i M_i}{\sum_i n_i} \tag{2.1}$$

$$M_w = \frac{\sum_i n_i M_i^2}{\sum_i n_i M_i} \tag{2.2}$$

where n_i is the number of polymer molecules with molecular weight M_i. Dividing M_n and M_w by the monomer molecular weight M_0 yields the number-averaged and weight-averaged degrees of polymerization $N_n = M_n / M_0$ and $N_w = M_w / M_0$, respectively.

In the case of nearly 100 % monomer conversion, which is the typical case in the irreversible anionic polymerization of vinyl monomers, the degree of polymerization is formulated as

$$M_n = \frac{[M]_0}{[I]_0} \tag{2.3}$$

where $[M]_0$ is the initial monomer concentrations, and $[I]_0$ is the initiator concentration.

By the definition, the polydispersity index (PDI) is given by,

$$\text{PDI} = \frac{M_w}{M_n} = \frac{N_w}{N_n} \tag{2.4}$$

When the rate of initiation is rapid relative to the rate of polymerization,

$$\frac{M_w}{M_n} = 1 + \frac{N_n}{(N_n + 1)^2} \cong 1 + \frac{1}{N_n} \tag{2.5}$$

Eqn (2.5) indicates that the PDI approaches unity as the degree of polymerization increases in the ideal case.

In this thesis work, the following block copolymers were synthesized and investigated: poly(1,2-butadiene-*b*-ethylene oxide) (OB or PB-PEO), poly(1,4-isoprene-*b*-DL-lactide) (IL), poly(DL-lactide-*b*-1,4-isoprene-*b*-DL-lactide) (LIL), and poly(styrene-*b*-1,4-isoprene-*b*-styrene-*b*-ethylene oxide) (SISO). The materials and polymerization procedures employed are described below.

Materials The materials for the anionic polymerization of block copolymers used in this research can be grouped into three categories: initiator, monomer, and solvent. The preparation of these ingredients is described below.

Initiator In this research, three kinds of initiators were employed: *sec*-butyllithium (*sec*-BuLi), 3-triisopropylsilyloxypropyl-1-lithium (TIPSOPrLi) , and potassium naphthalenide. *sec*-BuLi was purchased from Aldrich and used after the actual concentration was determined by No D NMR technique (see section 2.2).[85] TIPSOPrLi and potassium naphthalenide were prepared as described below.

- Synthesis of TIPSOPrLi

The TIPSOPrLi protected initiator is necessary to synthesize a polymer with α,ω-dihydroxyl functionality.

All chemicals for the synthesis of TIPSOPrLi were purchased from Aldrich and used as received unless otherwise specified. Synthesis of TIPSOPrLi begins with preparation of the precursor, triisopropylsilyloxypropyl-3-chloride (TIPSOPrCl).[86, 87] A schematic drawing of the TIPSOPrCl synthesis is provided in Figure 2.1a. Equivalent moles of chlorotriisopropylsilane (Gelest) and imidazole were dissolved in anhydrous dimethylformamide (DMF) with ~ 5 mL of DMF per 1 g of imidazole in an Argon-charged dry flask equipped with a rubber septum. For the coupling reaction, a molar excess of 3-chloro-1-propanol was injected into the flask and the solution was stirred overnight at room temperature. This coupling reaction is slightly exothermic so the

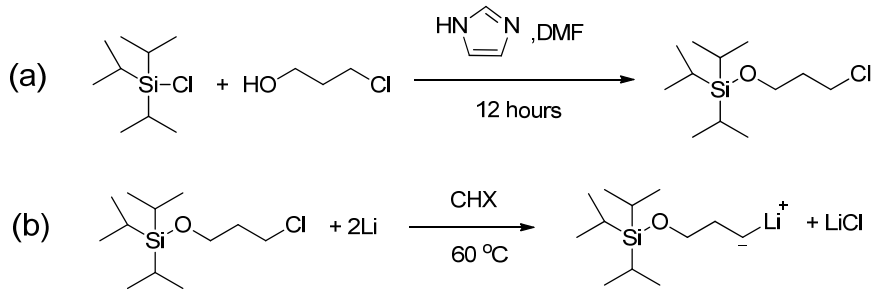

Figure 2.1 Synthesis schemes of triisopropylsilyoxypropyl chloride (a) and 3-triisopropylsilyoxypropyl-1-lithium (b).

solution temperature was monitored until it stabilized. The product solution was diluted with ~ 6 fold volume excess of diethyl ether, washed 3 times with distilled water, and concentrated using a rotary evaporator. The TIPSOPrCl product was purified by fractional distillation from the concentrated solution; the boiling point of TIPSOPrCl, T_{bp}, is approximately 70 ^{o}C at a pressure of ~ 600 mTorr.

The lithiation of TIPSOPrCl is summarized in Figure 2.1b. Lithium wire (10 molar excess lithium to the amount of TIPSOPrCl precursor) was chopped into small pieces in fresh hexane, and transferred into a three-port round bottomed flask reactor equipped with a cold water condenser, an addition funnel, and a rubber septum under dry argon a atmosphere. ***Extreme care must be taken when handling lithium. It reacts violently with protic reagents such as water or alcohols, and generates hydrogen gas. Qualified fire-fighting equipments should be at hand.*** Enough dry cyclohexane (CHX) to immerse the lithium pieces was cannulated into the reactor, and the solution was

vigorously stirred overnight to activate the surfaces of the lithium. Surface activation by mechanical abrasion is a critical step for successful lithiation. The CHX used for the surface activation was removed by cannulation, and fresh CHX was charged to the reactor. The amount of fresh CHX should be large enough to dilute the final concentration of TIPSOPrLi less than ~ 0.6 M. The concentration of TIPSOPrCl in CHX higher than ~ 0.6 M causes the precipitation of TIPSOPrCl initiator during the lithiation process. The reactor was heated to 40 ^{o}C in a silicon oil bath, and TIPSOPrCl was added dropwise through the addition funnel. ***Lithiation is a highly exothermic reaction. The reactor temperature should be watched carefully during the addition of TIPSOPrCl. Also, the initiation of the lithiation reaction cannot be controlled so each addition of TIPSOPrCl should be done only after the abrupt rise in temperature has subsided and the temperature has retained to 40 ^{o}C.*** After the required amount of TIPSOPrCl was added to the reactor, the reactor temperature was increased to 60 ^{o}C, and the solution was vigorously stirred until full conversion of TIPSOPrCl is confirmed by the No-D NMR technique.[87] Although the time for complete reaction may vary, approximately 48 hours is generally required. The crude solution was filtered through a pack of dry celite under positive argon pressure and the collected yellowish initiator solution was stored in a freezer in a dry box at -20 ^{o}C.

- Synthesis of potassium naphthalenide

Potassium naphthalenide is an electron transfer agent that can be used to convert hydroxyl groups into oxyanions containing potassium counter ions, These reactive site

can serve as initiators for the polymerization of ethylene oxide (oxirane) into poly(ethylene oxide) (PEO).[88] Other electron transfer agents such as potassium hydride or diphenylmethylpotassium can be used for the polymerization of ethylene oxide as well, but potassium naphthalenide was chosen as the electron transfer agent in this study because of its facile preparation and convenience in titration work through visual observation of color change.[89, 90]

The preparation of potassium naphthalenide is illustrated in Figure 2.2. Potassium chunks and naphthalene were purchased from Aldrich and used as received. Dry tetrahydrofuran (THF) was collected from a solvent purification column. The desired amount of solid potassium (typically 0.5 g per 200 mL of THF) was washed in fresh hexane. ***Potassium is extremely reactive to water and protic reagents such as alcohols and acids. Extreme care must be taken when handling potassium.*** The washed potassium chunks and 10% molar excess of naphthalene were transferred into a vacuum flask with a glass stir bar under a dry argon atmosphere. Dry THF was charged into the flask by cannulation. The potassium naphthalenide solution is ready for use after 24 hours of stirring at room temperature. A prepared solution of potassium naphthalenide should be used within 2 weeks.

Monomer In anionic polymerizations, purity of monomer is one of the critical requirements for the successful production of well-tailored polymers. In this section, purification methods for the monomers used in this research are described.

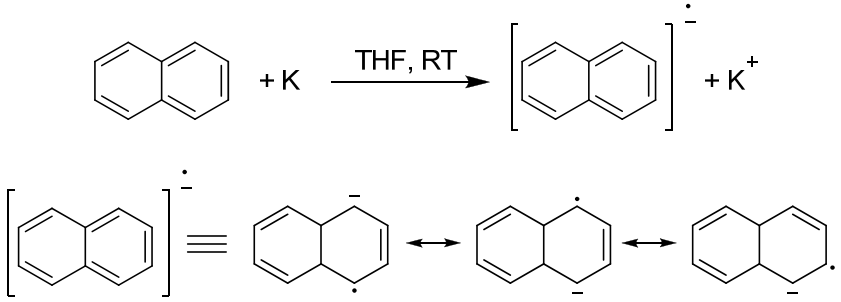

Figure 2.2 Synthesis scheme for potassium naphthalenide

- Purification of isoprene and 1,3-butadiene

All chemicals were handled and transferred under vacuum or inert atmosphere unless otherwise specified. Two round-bottom purification flasks equipped with Teflon *pressure-relief stopcocks* and Teflon-coated stir bars were used as purification reactors. 2.5 M *n*-butyllithium in hexane (*n*-BuLi, Aldrich) was transferred into the purification flasks at a ratio of ~ 2 ml per 5 g of monomer, and dried under dynamic vacuum. The solvent drying process of this purification agent is not critical in the purification of monomers or polymerizations, but required for precise assessment of amount of the purified monomer. Isoprene monomer purchased from Acros (T_{bp} = 34 ^{o}C) or 1,3-butadiene monomer from Aldrich (T_{bp} = -4.5 ^{o}C) was collected in a round-bottomed flask equipped with a Teflon stopcock and a stir bar. The isoprene can be collected by pouring directly into the flask in a hood. The 1,3-butadiene can be collected by the low-pressure vacuum transfer technique from a metal cylinder container. ***The collected 1,3-butadiene should not be heated above 0 ^{o}C. This is very important to prevent any possible***

explosion due to high vapor pressure of 1,3-butadiene or more serious violent exothermic reaction with the purifying agent while being cleaned. The collected monomers were repeatedly degassed by a freeze-pump-thaw process until the pressure gauge of the purification vacuum line showed no sign of residual gas in the monomer flask after the monomers were frozen. The isoprene and 1,3-butadiene were thawed at 25 ^{o}C and 0 ^{o}C, respectively, transferred by low-pressure vacuum distillation to the first purification flask containing dried *n*-BuLi, stirred vigorously at 0 ^{o}C for 1 hour, transferred into the second purification flask, and stirred again for another 1 hour. This double purification process ensures that the product is free of impurities. The presence of residual *n*-BuLi in the residual of the first purification flask (evident during neutralization) provides confirmation of a successful destructive purification. Purified monomers were collected into dry monomer burettes, and the burettes with monomer were assembled on a reactor or stored in an isopropanol-dry ice bath.

- Purification of ethylene oxide (Oxirane)

The purification procedure for ethylene oxide (Aldrich, T_{bp} = 10.7 ^{o}C) is very similar to the procedure for 1,3-butadiene except for two differences: the purification agent and the purification time. Due to the high reactivity of ethylene oxide, which derives from the strained ring structure, a mild purification reagent, butylmagnesium chloride (BuMgCl, Aldrich, 2M in tetrahydrofuran) was used. Ethylene oxide monomer was collected by the low-pressure vacuum transfer technique from a metal cylinder

container, twice purified with BuMgCl for 30 minutes, and collected into a dry monomer burette. One notable point during this procedure is that the ethylene oxide mixture with BuMgCl can become very viscous during the vacuum distillation and result in abrupt and violent boiling from a quiescent state. This undesirable flashing boiling can contaminate the vacuum and inert gas line, but can be avoided by closing the purification flask valve to stop the vacuum distillation when the quiescent state is observed. After a couple of minutes, the vacuum distillation of ethylene oxide can be continued by opening the purification flask valve. ***All safety warnings for 1,3-butadiene purification apply to the ethylene oxide purification procedure. Moreover, ethylene oxide is highly toxic so more care should be taken when this compound.***

- Purification of styrene

The procedure to purify styrene (Sigma) is similar to the isoprene purification procedure except for two differences: di-*n*-Butylmagnesium (BuMg, Aldrich, 1 M in heptane) was used as a purification agent and distillation of styrene were carried out at 40 ^{o}C. These differences are due to the relatively high boiling temperature (T_{bp} = 145 ^{o}C at 760 Torr). Styrene monomer was purified by two destructive distillations with BuMg at 40 ^{o}C (1 hour each) with final collection in a dry monomer burette. The monomer was stored in a dark place until the polymerization.

- Purification of DL-lactide

DL-lactide (Purac) was purified by re-crystallization in toluene (TLN, T_{bp} = 110 ^{o}C, Sigma). Raw DL-lactide monomer was dispersed in toluene (~ 100 g / 1 L of toluene) at room temperature, and the solution was heated up to 95 ^{o}C in a silicon-oil bath with vigorous stirring for 2 hours. After dissolution, if residual solid DL-lactide was observed, more toluene was added to the solution for full dissolution. After a clear solution was obtained, the saturated DL-lactide solution was allowed to cool down overnight to room temperature under a quiescent conditions resulting in recrystallization of the DL-lactide. The recrystallized DL-lactide was filtered through a glass filter, washed with fresh toluene, dried under dynamic vacuum overnight, and stored in a dry box. ***The hot toluene gives off toluene vapor which easily catches fire. Before purification of DL-lactide, any flammable material in the working hood should be removed and qualified fire-fighting materials should be at hand.***

Solvent Solvents for anionic polymerization are selected in order to meet the specific conditions for the synthesis of target block copolymer materials. First, a solvent should be able to dissolve the growing anionic polymer chains. Second, the solvent should be inert to the growing chains. Third, a practical propagation rate should be attainable. Last, in cases of polydiene polymerizations, the microstructures of polydienes are controlled by solvent polarity. More details can be found in the reference.[84]

In this study, cyclohexane (CHX , T_{bp} = 80.7 ^{o}C, Sigma), TLN (T_{bp} = 110 ^{o}C, Sigma) and tetrahydrofuran (THF, T_{bp} = 65-67 ^{o}C, Sigma) were used as solvents. Solvent purifications were accomplished by feeding the solvents through columns packed with activated alumina.[91] The CHX and TLN were deoxygenated by sparging with Argon for 1 hour, followed by passing the Argon sparged solvents through the copper-alumina redox catalyst (CU-0226S, Engelhard) under positive Argon pressure (15 pisg). Further purification was carried out by subsequent treatment with activated alumina (LaRoche, A15 grade). THF was purified by successive exposure to two activated alumina columns; the ether group of THF is reactive towards the copper-alumina redox catalyst. If greater purity is required, the THF can be exposed to *sec*-BuLi followed by distillation.

Polymerization The protocols used to synthesize block copolymers in this research can be divided into three categories: synthesis of α-hydroxyl or α,ω-dihydroxyl functionalized polymers, poly(ethylene oxide) block synthesis, and poly(DL-lactide) block synthesis. Those polymerizations are described below and more detailed synthesis schemes can be found in references[40, 60, 92].

Synthesis of α-hydroxyl or α,ω-dihydroxyl functionalized polymers

- Synthesis of ω -hydroxyl 1,2-polybutadiene (PB-OH)

The polymerization of PB-OH is shown in Figure 2.3a. A reactor was assembled with THF solvent flasks containing dry THF, stoppers, a thermocouple housing, and a manifold with double stacked Teflon-lined septa held in place by Teflon ferrules and

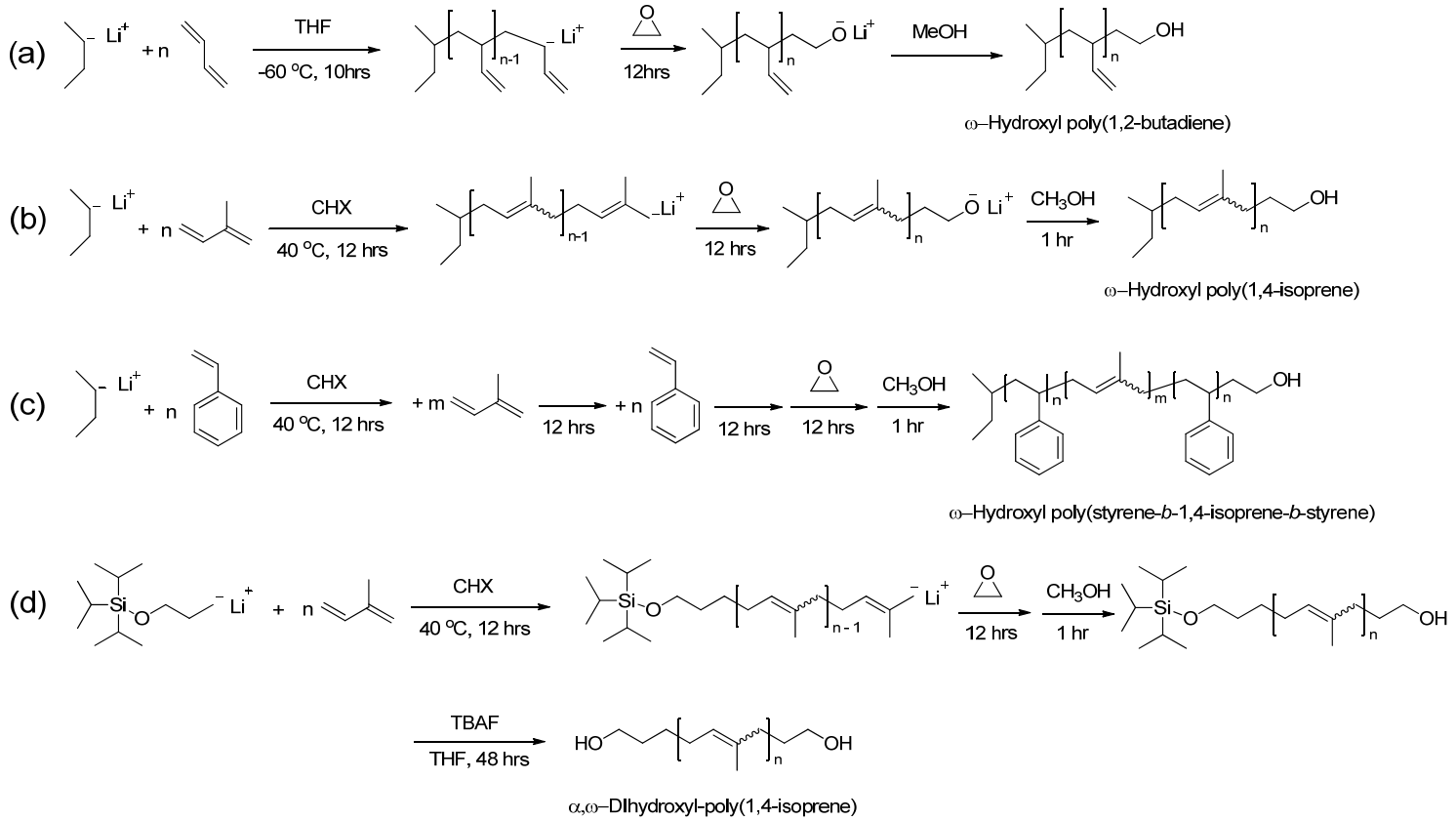

Figure 2.3 Synthesis schemes for polymerization of hydroxyl end-functionalized polymers. (a) PB-OH, (b) PI-OH, (c) SIS-OH, (d) HO-I-OH

nylon bushings. Purified 1,3-butadiene and ethylene oxide burettes, maintained at less than -60 ^{o}C using an isopropanol-dry ice bath, were connected to the reactor using flexible stainless steel tubes. The assembled reactor was deoxygenated and dried by cyclic purging with argon and vacuum (≈ 20 mTorr) five times. The glass reactor was gently heated using a torch during these purges. After charging argon to the reactor (~ 3 psig), THF was introduced, and cooled with an isopropanol-dry ice bath until the temperature of the THF in the reactor reached to -60 ^{o}C. The reactor pressure was monitored carefully during the cooling procedure and a slight overpressure was maintained.

A calculated amount of *sec*-BuLi was injected into the reactor using a glass gas-tight syringe through the double-stacked Teflon-lined septa and the solution was vigorously stirred for about one hour. Then the 1,3-butadiene was added into the reactor and the solution was stirred at -60 ^{o}C, resulting in the complete polymerization of the monomer after 8 hours. Approximately 10 times molar excess of ethylene oxide to the amount of initiator was added to the reactor, the solution was stirred for one hour at -60 ^{o}C, and then slowly warmed up to room temperature (≈ 50 ^{o}C/hour) while regulating the reactor pressure in the range of 3 – 6 psig. Subsequently the polymer solution was stirred overnight at room temperature and the reaction was terminated by injecting large excess of Argon-purged (deoxygenated) methanol. After stirring the solution for one hour with methanol, excess ethylene oxide was vented for three hours with vigorously stirring. The

polymer solution was precipitated in 10 fold volume excess of methanol, and the PB-OH product was recovered, dried under dynamic vacuum, and stored in a freezer at -20 ^{o}C.

- Synthesis of ω-hydroxyl 1,4-polyisoprene (PI-OH)

The procedure for synthesizing PI-OH (Figure 2.3b) is very similar to that for PB-OH except for a few differences: monomer species, polymerization solvent, and polymerization temperature. The polymerization of PI-OH was carried out with isoprene monomer in CHX at 40 ^{o}C (water bath) for 12 hours, followed by the addition of approximately 10 time molar excess of ethylene oxide to the amount of initiator, reacted for 12 hours at 40 ^{o}C, and terminated with large excess of deoxygenated methanol. The product was precipitated in 10 fold volume excess of methanol. The rest procedures are same to the polymerization of PB-OH.

- Synthesis of ω-hydroxyl poly(styrene-*b*-1,4-isoprene-*b*-styrene) (SIS-OH)

The synthesis of SIS-OH (Figure 2.3c) was carried out at the same conditions used for PI-OH except for the sequential addition of styrene and isoprene monomers all at 40 ^{o}C. After polymerization of the first polystyrene block, isoprene followed by styrene monomer were sequentially polymerized each for 12 hours. The rest end-capping with ethylene oxide and work-up procedures were the same as for PI-OH

- Synthesis of α,ω-dihydroxyl 1,4-polyisoprene (HO-PI-OH)

The preparation of HO-PI-OH (Figure 2.3d) resembles the synthesis of PI-OH with two differences: initiation with TIPSOPrLi followed by deprotection of the TIPSO-

PI-OH product. TIPSO-PI-OH was synthesized at 40 ^{o}C in CHX using the TIPSOPrLi initiator instead of *sec*-BuLi, that was used in the synthesis of PI-OH. After termination with large excess of deoxygenated methanol, the TIPSO-PI-OH solution in CHX was diluted with equivalent volume of THF (not necessarily dry) to the CHX, and 10 molar excess of tetra-*n*-butylammonium fluoride solution in water (TBAF, Aldrich) to the mole number of TIPSO-PI-OH was added, and the TIPSO-PI-OH solution stirred for 48 hours for the deprotection of TIPS group. The deprotected HO-PI-OH was purified by repeated precipitation in methanol, recovered, dried under vacuum, and stored in a freezer at -20 ^{o}C.

Synthesis of OB, SISO, IL, and LIL block copolymers

After the synthesis of hydroxyl functionalized polymer precursors, additional blocks were polymerized from the hydroxyl groups.

- Synthesis of OB diblock copolymers

The OB diblock copolymer was prepared by polymerization of PEO block at the hydroxyl functional group of the PB-OH precursor polymer. The synthesis scheme is shown in Figure 2.4a. A specified amount of PB-OH (the amount of PB-OH precursor varies by the target amount of OB diblock copolymer product) was dissolved in benzene and poured into an assembled reactor through a reactor opening. A glass stir bar was used instead of a Teflon bar for stirring because the latter reacts with potassium naphthalenide. After all reactor openings were capped, the PB-OH-benzene solution in the reactor was

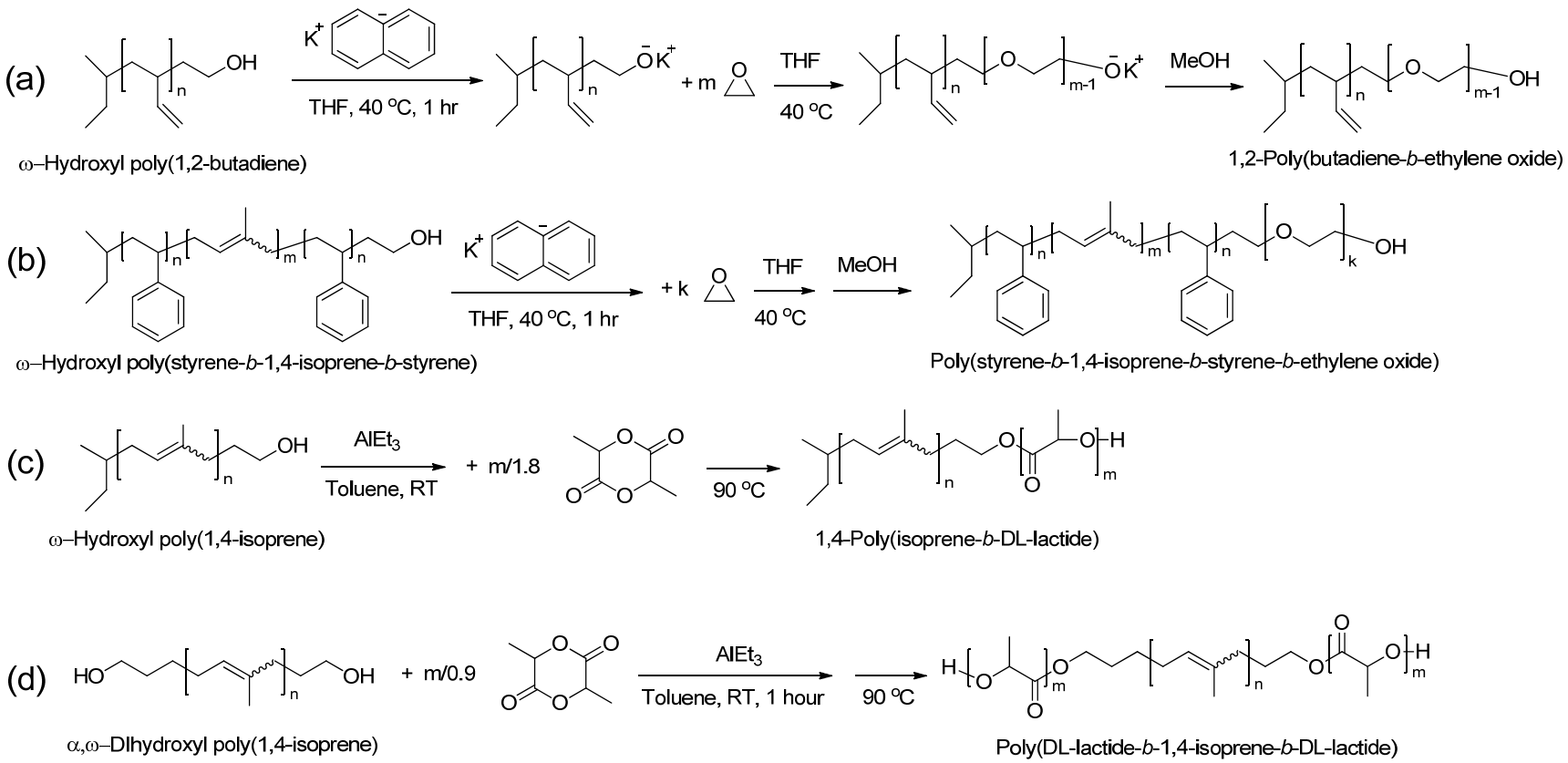

Figure 2.4 Synthesis schemes of (a) OB, (b) SISO, (c) IL, and (d) LIL block copolymers

frozen by immersing the reactor in liquid nitrogen and dried overnight under dynamic vacuum to remove residual water. Dry argon was charged and removed with a vacuum, and this process was repeated five times to eliminate oxygen from the reactor followed by the addition of dry THF. The solution was stirred until all the PB-OH was fully dissolved in the THF. The reactor temperature was set to 40 or 45 ^{o}C and the potassium naphthalenide solution was transferred into the reactor by cannulation to convert the dried PB-OH into PB-O^{-}K^{+} macroinitiator. The PB-OH activation process can be monitored by observing color change of the solution from clear to light green. A green color indicates the presence of potassium naphthalenide hence full initiation. The titrated solution should be stirred vigorously for at least one hour prior the addition of ethylene oxide to ensure full conversion of PB-OH into PB-O^{-}K^{+} macroinitiator. If the solution loses the light green color, more potassium naphthalenide should be added. After confirming the full activation of PB-OH, the required amount of ethylene oxide was added into the reactor and the solution was stirred for 48 hours. ***The ethylene oxide addition should be carried out with extreme care due to large temperature difference between the boiling point of ethylene oxide (10.7 ^{o}C) and the polymerization temperature (40 or 45 ^{o}C). If vaporized, the reactor pressure may rise abruptly and the reactor could explode.*** The polymerization was terminated by injecting large excess of deoxygenated methanol into the reactor, and after 1 hour stirring with the methanol, residual ethylene oxide was vented for three hours. The PB-PEO solution was concentrated to approximately 10 – 20

wt. % using a rotary evaporator, precipitated in 10-fold volume excess of isopropanol, recovered, and dried. The dried PB-PEO was dissolved in dichloromethane, washed 3 times with distilled water, concentrated using a rotary evaporator, freeze-dried in benzene, and stored in a freezer at -20 ^{o}C. A synthesized PB-PEO can have a light yellow color by residual reagents. This color can be removed by repeated precipitation of the PB-PEO in isopropanol.

- Synthesis of SISO tetrablock terpolymer

The synthesis of SISO tetrablock terpolymer (Figure 2.4b) is similar to the synthesis of OB diblock copolymer except the PEO block was synthesized at the terminal hydroxyl group of a of SIS-OH triblock copolymer. The other procedures are the same.

- Synthesis of IL diblock copolymer

IL diblock copolymers were prepared by polymerizing DL-lactide from the hydroxyl group of PI-OH precursor (Figure 2.4c). PI-OH was added to a round-bottom flask with a Teflon stir bar, dissolved in TLN, then dried overnight under dynamic vacuum to remove water. The dried PI-OH was re-dissolved in dry TLN in a dry box, triethylaluminum ($AlEt_3$) catalyst was added, and the solution was stirred for 15 minutes. Subsequent to the PI-OH activation, the required amount of DL-lactide was added to the reactor. The reactor was tightly sealed and heated to 90 ^{o}C in an oil bath with stirring. The required amount of dry TLN and polymerization time varied depending on the polymerization conditions such as molecular weight of PI-OH and the amount of DL-

lactide monomer added.[93] In this work, the concentration of PI-OH and DL-lactide in TLN were adjusted to be approximately 0.02 M and less than 1.5 M, respectively, and the polymerization time was varied depending on the polymerization conditions . After the desired conversion was achieved, the polymerization solution was quenched with the large excess of a mixture of water and THF at room temperature. The polymerized IL diblock copolymer was precipitation in methanol, recovered, dried under dynamic vacuum, and stored in a freezer at -20 ^{o}C.

- Synthesis of LIL triblock copolymer

The procedure for synthesizing LIL triblock copolymer (Figure 2.4d) is the same as that used for IL diblock copolymers except for two differences: the precursor polymer and the sequence of chemical addition. HO-I-OH polymer was dissolved in TLN, dried to remove water, and redissolved in dry TLN. DL-lactide was added and the solution was stirred to disperse the monomer homogeneously prior to addition of $AlEt_3$. Because the HO-I-OH polymerization solution becomes a temporal gel state with addition of $AlEt_3$, this pre-dispersion of DL-lactide reduces the concentration gradient of DL-lactide monomer by the gravity during polymerization which can cause increase of the PDI. After the pre-dispersion, $AlEt_3$ was added to the solution and the polymerization carried out at 90 ^{o}C. Termination and recovery were the same as with the IL synthesis.

2.2 Nuclear Magnetic Resonance

Nuclear magnetic resonance (NMR) is an analytical spectroscopy technique used to elucidate the structures of chemical species.[94] In the case of the polymeric materials, it provides the most direct means of determining the microstructure of repeating units, the composition of block copolymers, and in some cases (e.g. relatively low molecular weight) the number-averaged molecular weight (M_n).

In Fourier Transform NMR, structural information of a chemical species is acquired from the *free induction decay* (FID) *signal* emitted from the nuclei excited by the pulses of radio frequency radiation under an external magnetic field. The FID signal is collected as time-domain data and it is converted into a frequency domain for interpretation. On a frequency spectrum, a chemical species associated with a specific chemical environment shows a corresponding peak response, and the position of the peak location is identified by a *chemical shift* δ. Also, the peak area from baseline is proportional to the number nuclei associated with that response. These features make NMR a very powerful qualitative and quantitative technique. However, only nuclei that contain a non-zero atomic spin such as ^{1}H, ^{13}C, ^{19}F, and ^{31}P are susceptible to NMR analysis. Table 2.1 shows ^{1}H NMR chemical shifts for the protons contained in the repeat units of the polymers used in this study.

Based on the integrated peak areas of protons associated with the end-groups of a polymer chain, the number averaged molecular weight M_n of a polymer can be calculated.

Table 2.1 ^{1}H NMR chemical shifts of polymers used in this study. The chemical shifts are shown in ppm downfield from tetramethylsilane (TMS).

Chemical Structure	Chemical Shift (H: peak type*, ppm)	Chemical Structure	Chemical Shift (H: peak type*, ppm)
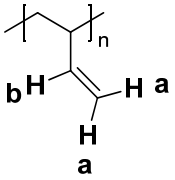 Poly(1,2-butadiene)	**a**: m, 4.8 – 5.0 **b**: m, 5.4	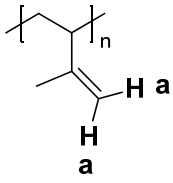 Poly(3,4-isoprene)	**a**: m, 4.7
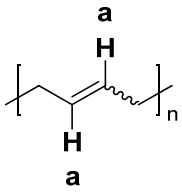 Poly(1,4-butadiene)	**a**: m, 5.4	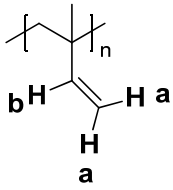 Poly(1,2-isoprene)	**a**: m, 4.7 – 4.9 **b**: m, 5.0 – 5.3
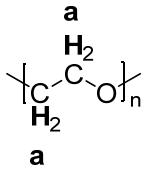 Poly(ethylene oxide)	**a**: m, 3.5 – 3.8	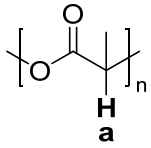 Poly(DL-lactide)	**a**: m, 5.2 – 5.4
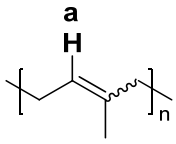 Poly(1,4-isoprene)	**a**: m, 5.0 – 5.3	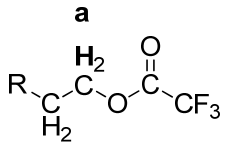 Methyelene trifluoromethylether	**a**: m, 4.4
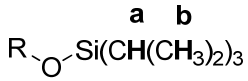 Triisopropylsilyloxy ether	**a**: sep, 1.35 **b**: d, 1.1	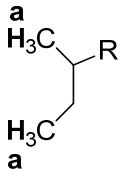 *sec*-Butyl	**a**: m, 0.9

* d: doublet m: multiplet, sep: septet

For a polymer polymerized by a characteristic initiator species, the ratio between integrated areas of distinctive polymer chain groups and the initiator gives the averaged number of repeating units that were polymerized by one initiator molecule. This information can be converted to M_n by multiplying the resulting number average degree of polymerization by the monomer unit mass M_0.

In the practice, the end-group analysis of hydroxyl terminated polymers like PB-OH, PI-OH, or HO-PI-OH can be difficult due to interference of the signals from –OH terminal groups from other alcohol impurities. To help the identification of polymer –OH terminal groups, trifluoroacetic anhydride (TFA) can be used to modify the hydroxyl groups as shown:

$$-C\mathbf{H}_2-O\mathbf{H}+F_3CCOOCOCF_3 \rightarrow -C\mathbf{H}_2-O-COCF_3+F_3CCO-O\mathbf{H} \qquad (2.6)$$

This modification moves the chemical shift of the hydroxyl methylene groups from ~ 3.6 ppm to ~ 4.4 ppm and allows for a more precise calculation of M_n as follows:

$$M_n = \frac{\text{Area}(\delta_{\text{repeat unit}})/\text{N}_{\text{H, repeat unit}}}{\text{Area}(\delta_{\text{initiator}})/\text{N}_{\text{H, initiator}}} M_0 \qquad (2.7)$$

where N_H is the number of protons associated with each signal.

Following Eqn (2.7), the molecular analysis of 1,2-poly(butadiene-*b*-ethylene oxide) is shown below as an example. In Figure 2.5, a NMR spectrum of PB-OH with TFA is shown and the number averaged molecular weight $M_{n\,\text{PB}}$ is calculated as follows:

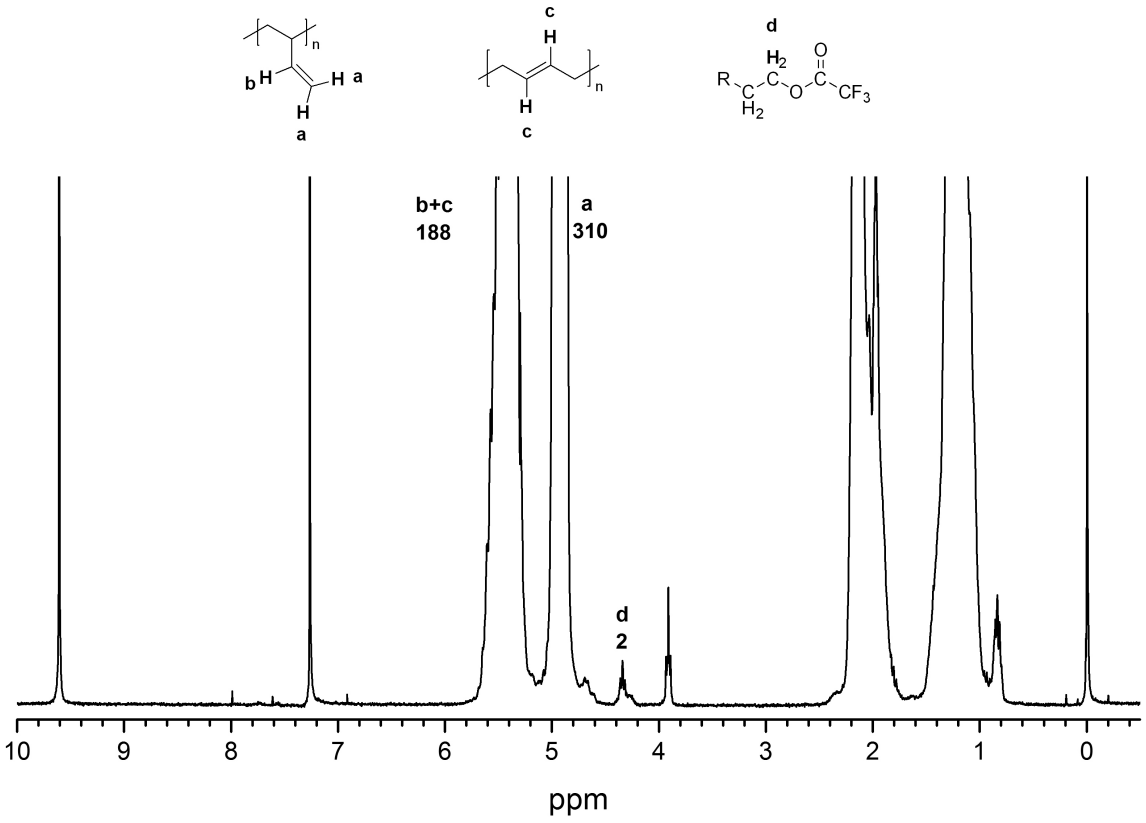

Figure 2.5 ^{1}H NMR spectrum of ω-hydroxyl poly(1,2-butadiene) with trifluoroacetic anhydride in $CDCl_3$. The chemical shifts of associated protons and integrated areas are denoted above peaks. Protons associated with trifluoroacetic acid show up at 9.6 ppm.

$$M_{n,\,\mathrm{PB}} = \frac{\dfrac{\mathrm{A(b+c)\text{-}A(a)/N_{H,a}}}{\mathrm{N_{H,c}}} + \dfrac{\mathrm{A(a)}}{\mathrm{N_{H,a}}}}{\dfrac{A(d)}{N_{H,d}}} M_{0,B} = \frac{\dfrac{188\text{-}310/2}{2} + \dfrac{310}{2}}{\dfrac{2}{2}} 54.09\,\mathrm{g/mol} = 9{,}276\,\mathrm{g/mol} \quad (2.8)$$

where $M_{0,B}$ is the monomer molecular weight of 1,3-butadiene. The fraction of 1,2-polybutadiene $f_{1,2}$ in PB block can be calculated as well:

$$f_{1,2} = \frac{\mathrm{A(a)/N_{H,a}}}{\mathrm{A(a)/N_{H,a}} + \dfrac{\mathrm{A(b+c)\text{-}A(a)/N_{H,a}}}{\mathrm{N_{H,c}}}} = 0.903 \quad (2.9)$$

After a diblock copolymer is synthesized, it is possible to calculate the M_n of each block by a single NMR experiment using the end-group analysis. However, M_n of the additional blocks is generally determined based on the first block M_n because the end-group analysis gives a more reliable result with lower total M_n due to the signal-to-noise ratio. In practice, a M_n by the end-group analysis technique becomes rather inaccurate for the high molecular weight polymers over M_n = ~ 50 kg/mol. In this case, size exclusion chromatography (SEC) was preferred for the molecular weight characterization. SEC technique will be discussed in the following section.

Figure 2.6 shows the ^{1}H NMR spectrum of an OB diblock copolymer. Based on the calculated $M_{n,\,PB}$ using ^{1}H NMR spectrum of PB-OH shown in Figure 2.5, the number-averaged PEO block molecular weight ($M_{n,PEO}$) can be calculated by following equation:

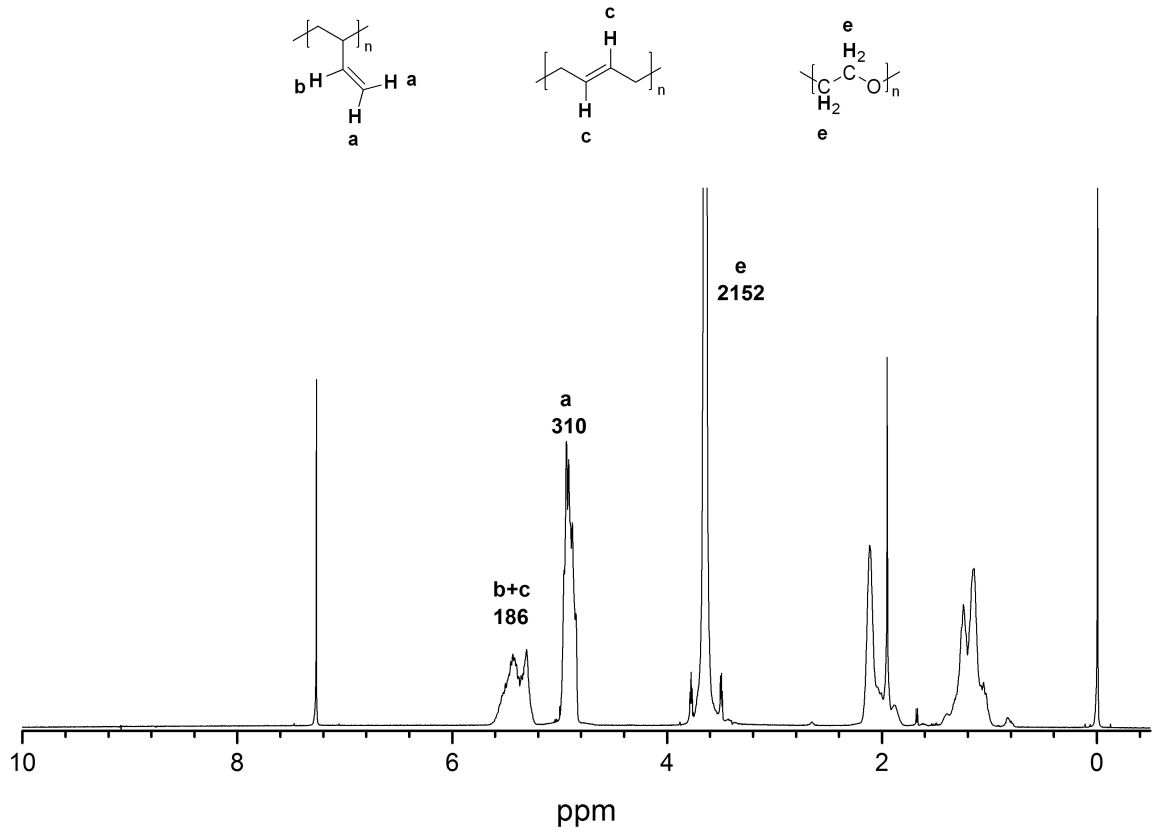

Figure 2.6 ^{1}H NMR spectrum of poly(1,2-butadiene-*b*-ethylene oxide) in $CDCl_3$. The associated chemical shifts with each protons and integrated areas are denoted above corresponding peak.

$$M_{n,\mathrm{PEO}} = \frac{\mathrm{M_{n,PB}} \dfrac{\mathrm{A(e)}}{\mathrm{N_{H,e}}} M_{0,EO}}{\dfrac{\mathrm{A(a)/N_{H,a}}}{f_{1,2}} M_{0,B}} = 23{,}756 \text{ g/mol} \tag{2.10}$$

where $M_{0,EO}$ is the monomer molecular weight of ethylene oxide. From the calculated $M_{n,\mathrm{PB}}$ and $M_{n,\mathrm{PEO}}$, the total OB diblock copolymer molecular weight is $M_{n,\mathrm{OB}} = M_{n,\mathrm{PB}} + M_{n,\mathrm{PEO}} = 33.0$ kg/mol, and the weight fraction of PEO w_{PEO} is

$$w_{\mathrm{PEO}} = \frac{\mathrm{M_{n,PEO}}}{\mathrm{M_{n,PB}} + \mathrm{M_{n,PEO}}} = 0.72 \tag{2.11}$$

2.3 Size Exclusion Chromatography

Size exclusion chromatography is accepted as a standard analytical method in modern polymer science. It measures the number- and weight-averaged molecular weights ($\mathrm{M_n}$ and $\mathrm{M_w}$, respectively). The SEC is frequently referred to as a gel permeation chromatography (GPC) to emphasize the packed material in columns though it is not an appropriate terminology in broader sense.

The separation mechanism of SEC is based on the different traveling distances of polymer chains in a column due to the difference in hydrodynamic volumes V_h.[1] A SEC column is packed with micro-porous material, referred to a stationary phase. Solutes, i.e. polymer chains, pass through the column aided by a flowing solvent, referred to as an eluent. While a polymer chain is passing through a column packed with a micro-porous material, the polymer chain can access pores that have similar or larger pore sizes than

the hydrodynamic volume of the polymer chain. Thus, a polymer chain with a larger hydrodynamic volume has less chance of accessing to the pores than that of a small polymer chain, and spends less time in passing through the column than the small polymer chain does. This difference in the accessibility to the internal pore spaces of the packed material makes the polymer chains travel different lengths in a given time. Therefore, a larger polymer chain comes out first, and a smaller polymer chain comes out later.

The hydrodynamic volume can be directly related to the polymer molecular weight assuming that the hydrodynamic volume of a polymer chain is proportional to the cubic of the radius of gyration (R_g^3). In turn, the radius of gyration of a polymer chain is proportional to molecular weight of a polymer chain, $R_g \sim \mathrm{M}^{\nu}$. Thus, a SEC instrument separates polymer chains by their molecular weights based on different elution volumes or time in the case of a constant flow rate.

The elution volume or elution time is associated with a particular molecular weight and the correlation between elution volumes and molecular weights is determined by calibration procedures. Two calibration methods are commonly employed in SEC experiments: (1) using a series of polymer standards with known molecular weights and (2) universal calibration by using intrinsic viscosities of two different polymer species. In the calibration using polymer standards, elution volumes of a series of polymer standards are measured, and the measured elution volumes are correlated with corresponding

molecular weights using a known or polynomial function. This method is very convenient and a relatively accurate calibration method provided the calibrants are the same type of polymer as the one being measured. However, inaccuracies in the nominal molecular weights of the standards (5 - 10 %) is inevitable and more importantly polymer standards of same polymer species may not be available. In this case, the universal calibration method can be employed to assess the molecular weights of the polymer analyte. Nevertheless, the polydispersity index, M_w/M_n, can be estimated by SEC, even under circumstances where the calibration standards are chemically different.

Another consideration in a SEC experiment is the choice of a detection method for the eluted solutes. Refractive index, ultraviolet-visible spectrum, and light scattering detectors are commonly used for this purpose. In this study, the refractive index, n_R, of eluting solutions was measured to determine the concentration of solute, and the refractive index can be expressed as follows:

$$n_R(c) = n_{\mathrm{R,S}} + \left(\frac{\partial n_R}{\partial c}\right)c + \cdots \tag{2.12}$$

where $n_{\mathrm{R,S}}$ is the refractive index of the solvent and c is the polymer concentration. Therefore, the polymer concentration is directly proportional to n_R-$n_{R,S}$, where the $\partial n_R / \partial c$ is the proportionality constant.

The number-averaged and weight-averaged molecular weights (M_n and M_w) are calculated as follows:

$$M_n = \frac{\sum_i n_i M_i}{\sum_i n_i} = \frac{\sum_i (c_i / M_i) M_i}{\sum_i (c_i / M_i)} = \frac{\sum_i c_i}{\sum_i (c_i / M_i)} \tag{2.13}$$

and

$$M_w = \frac{\sum_i w_i M_i}{\sum_i w_i} = \frac{\sum_i c_i M_i}{\sum_i c_i} \tag{2.14}$$

where n_i and w_i, are the mole number and weight of solute, respectively and c_i is the concentration at certain elution volume or time i. Note that the constant $\partial n_R / \partial c$ cancels in Eqns (2.13) and (2.14). Thus, substituting c_i in Eqns (2.13) and (2.14) with the n_R-$n_{R,S}$ presents direct means of M_n and M_w calculations from the refractive index chromatogram data.

Figure 2.7 shows representative SEC chromatogram of a PB-OH and the OB diblock copolymer using chloroform as the solvent; these are the polymers shown in Figure 2.5 and Figure 2.6. Although SEC is a standard method to determine the molecular weight of a homopolymer, it cannot be used directly to determine the molecular weight of a block copolymer because it is not feasible to formulate a calibration curve for block copolymers due to the hydrodynamic volume heterogeneity between blocks. However, SEC is still an essential technique for the characterization of polydispersity and verification of the integrity of block copolymers, e.g. identification of homopolymer impurities.

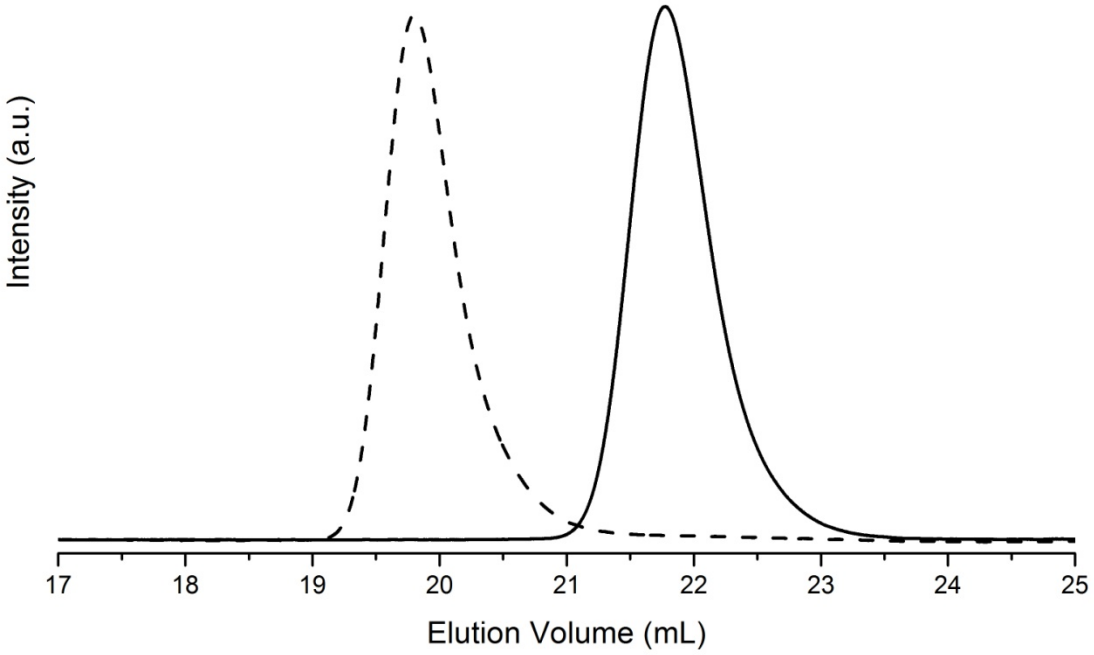

Figure 2.7 SEC chromatograms of ω-hydroxyl poly(1,2-butadiene) (PB-OH, solid line) and poly(1,2-butadiene-*b*-ethylene oxide) (PB-PEO, dashed line) obtained with a refractive index detector using chloroform as the mobile phase. The PDI of PB-OH and OB is 1.06 and 1.05, respectively based on polystyrene standards. The OB ($M_{n,\mathrm{OB}}$ = 33 kg/mol) peak emerges at a lower elution volume the peak position of PB-OH ($M_{n,\mathrm{PB\text{-}OH}}$ = 9.2 kg/mol) due to a higher molecular weight.

2.4 Differential Scanning Calorimetry

Differential scanning calorimetry (DSC) is a technique used for characterizing the thermal properties of materials.[95] DSC measures the difference of heat flow required to increase or decrease the temperature of an analyte relative to a reference (typically an empty sample container).

In polymer science, the most important thermal properties are the glass transition temperature (T_g) and the melting temperature (T_m). These characteristic temperatures are the key parameters that determine the mechanical properties of a polymeric material. In the amorphous glassy state, the movement of polymer segments is virtually halted and the material assumes solid-like properties. The transition from a glassy to rubbery (liquid) state resembles a second-order transition,[1] and in a DSC analysis, heat flow occurs over a 20 to 30 K temperature window. The experimental example of a DSC thermogram is shown in Figure 2.8 with the PB-PEO diblock copolymer (same polymer characterized in Figure 2.5, 2.6, and 2.7) and the glass transition temperatures of PB and PEO blocks ($T_{g,PB}$ and $T_{g,PEO}$, respectively) are denoted.

Upon melting on a heating cycle, a solid semi-crystalline polymer becomes a (rubbery) liquid. This first order phase transition is evidenced in a DSC experiment as an endotherm, where the melting temperature T_m, is usually associated with the peak temperature. During a cooling cycle, a crystallization from a liquid to a solid semi-crystalline, which is a reverse transition of the metling, is also evidenced by another first

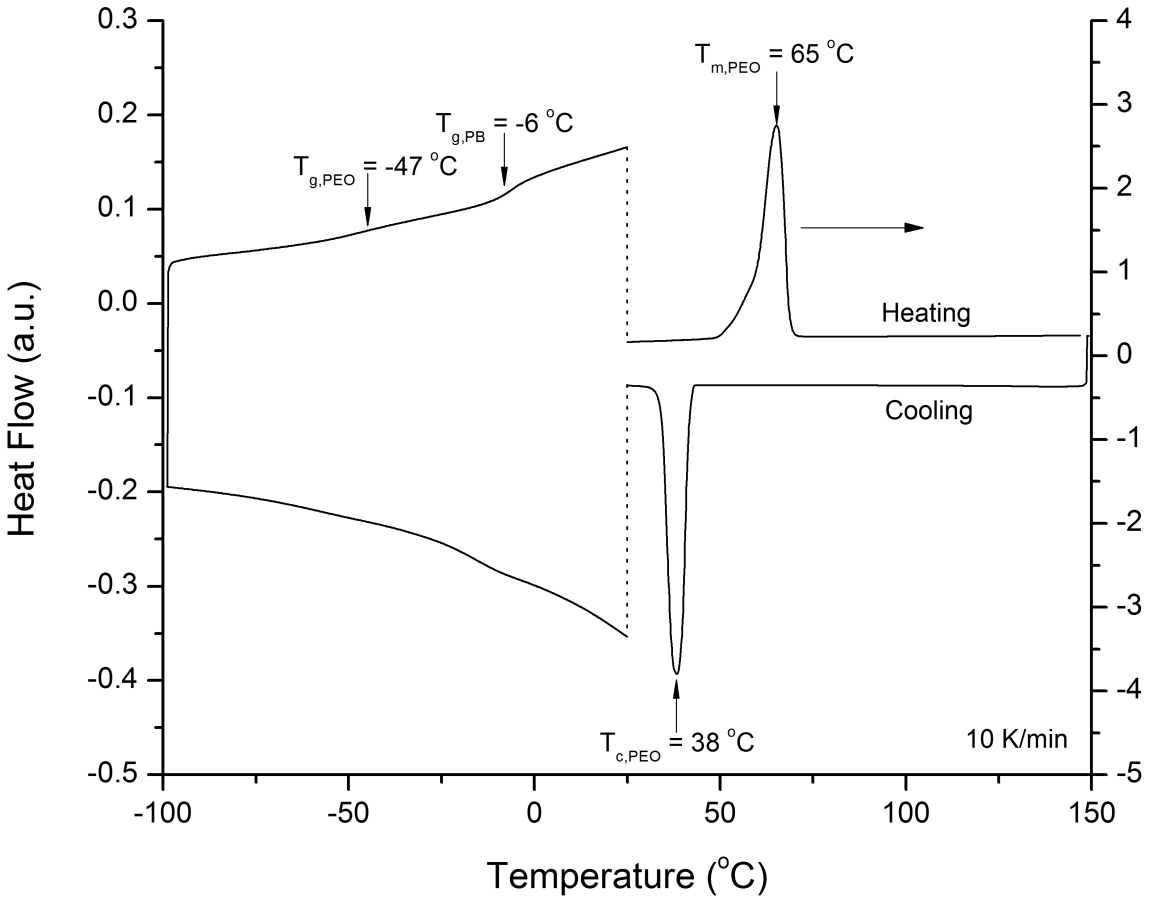

Figure 2.8 DSC thermogram of poly(1,2-butadiene-*b*-ethylene oxide) (PB-PEO) diblock copolymer (M_n = 33 kg/mol, w_{PEO} = 0.72). The sample was cooled down and heated at a rate of 10 K/min. The glass transition temperatures of PEO ($T_{g,\,PEO}$ = -47 °C) and PB ($T_{g,\,PB}$ = -6 °C) were determined by the mid-points of the glass transitions on the heating cycle. The melting and crystallization temperatures of PEO block ($T_{m,\,PEO}$ = 65 °C and $T_{c,\,PEO}$ = 38 °C, respectively) were identified with the peak temperatures on heating and cooling cycles respectively. The degree of crystallinity of PEO block $w_{c,PEO}$ = 74 %.

order transition peak with the crystallization temperature T_c. The melting and crystallization peaks of PEO block of the PB-PEO diblock copolymer are shown in Figure 2.8 as an example.

The amount of polymer crystals is generally dependent on the thermal history of a sample, and the quantity of a polymer crystal is characterized by the degree of crystallinity or crystallization w_c which is defined as follows:

$$w_c = \frac{\Delta H_f^{'}}{\Delta H_f} \tag{2.15}$$

where $\Delta H_f^{'}$ is the heat of fusion of a semi-crystalline sample and ΔH_f is the heat of fusion of the fully crystalline polymer.[96] In Figure 2.8, the degree of crystallinity of PEO block is calculated with the area of the melting peak on the heating cycle: $w_{c,PEO}$ = 74 %.

2.5 Dynamic Mechanical Spectroscopy

Polymer melts have unique mechanical properties compared to those of simple liquids and solids, referred to the *viscoelasticity*. The viscoelasticity of a polymer is generally characterized by dynamic mechanical spectroscopy (DMS), which measures the dynamic shear elasticity and viscosity of a material at certain applied mechanical frequencies.

DMS measures the stress σ and phase angle δ that are resulted from an applied strain γ or *vice versa*. In elastic solids, the and strain are related by as follows:[1]

$$\sigma = \hat{G}\gamma \tag{2.16}$$

where $\hat{G}$ is defined as the modulus, which acts as a spring constant that manifests the amount of stored mechanical energy by the strain. In viscous liquids, the stress is linearly related to the strain rate $\dot{\gamma}$:

$$\sigma = \hat{\eta}\dot{\gamma} \tag{2.17}$$

where $\hat{\eta}$ is the viscosity which is related to the amount of dissipated energy by the strain rate. The maximum strain that the Eqn (2.16) holds is referred to the linear limit.

When applying an oscillating sinusoidal strain $\gamma^* = \gamma_0 e^{it\omega}$ to a polymer melt, the resulted time-varying viscoelastic responses of the sinusoidally strained polymer melt can be resolved into two components: the elastic part which is in phase with the applied sinusoidal strain and the viscous part that is 90^o out phase to the applied sinusoidal strain. These elastic and viscous responses of polymer melts are denoted by the complex dynamic shear modulus G^* which can be resolved into the storage modulus G' and loss modulus G'':

$$G^*(\omega) = \frac{\sigma^*}{\gamma^*} = G' + iG'' \tag{2.18}$$

$$G' = \frac{\sigma_0}{\gamma_0}\cos\delta \tag{2.19}$$

$$G'' = \frac{\sigma_0}{\gamma_0} \sin \delta \tag{2.20}$$

where $\sigma^* = \sigma_0 e^{i(t\omega+\delta)}$ is the complex stress. The ratio between G' and G'' is referred to the *loss tangent* $\tan\delta$ which represents how a material behaves like a solid or liquid:

$$\tan \delta = \frac{G''}{G'} \tag{2.21}$$

When the $\tan\delta$ of a polymer melt becomes smaller, it dictates that the polymer melt behaves like a solid and a larger $\tan\delta$ indicates a liquid-like behavior.

In molecular level, the elastic response of polymer melts are believed to be related to the equilibrium state of polymer chain conformations: when a polymer melt is stressed, the equilibrium chain conformations are disturbed, but upon the removal of the stress, the polymer chains come back to the equilibrium chain conformations. This recovery process of deformed polymer chain conformations represents the elastic response of polymer melts. The other case, the viscous response is believed to come from the friction between polymer chain segments under dynamic chain movements.[1]

In DMS experiments, a frequency which is applied to a polymer melt at a certain temperature is directly related to the viscoelastic responses of parts of the polymer chains in corresponding length scales. In other words, polymer segments in Angstrom length scales are responsible for the viscoelastic responses at relatively high frequency domain, and nanoscale structures are attributed to the viscoelastic responses at low frequency domain.[1] These frequency responses are also known as a function of temperature, and the

time-temperature superposition (TTS) principle is generally practiced though the theoretical background for block copolymers is not clearly established.[1, 97]

In terms of the structural length scales, block copolymers have wide-range of structural components ranging from Angstrom (chain segment) to nm sizes (crystal structures of segregated domains). Thus, DMS has been used as a major technique to investigate the thermodynamic behaviors of block copolymers.[6, 98, 99] For example, the isochronal dynamic temperature sweep have been employed to investigate T_{OOT}'s and T_{ODT}'s of block copolymers because the change of microstructure from an ordered state to another ordered state or disordered state is directly reflected to the change of the moduli G' and G".

Another major practice of DMS to probe the microstructures of block copolymers is the dynamic shear frequency sweep experiments to construct a master frequency curve using the TTS. The G'(ω) and G"(ω) responses of diblock copolymers are known to show fingerprint responses depending on a morphology over at least two orders of frequency magnitudes.[100-105] Although the construction of a master curve cannot be solely used to determine a specific morphology of block copolymer without aid of other characterization techniques such as small angle X-ray scattering and transmission electron microscopy, DMS still offers valuable information on the thermodynamic behaviors of block copolymers.

2.6 Small Angle X-Ray Scattering

In block copolymer research, small angle X-ray scattering (SAXS) has been used as a primary technique to study microphase separation. The advantages of the SAXS technique include the ability to characterize nanoscale morphologies (5 - 100 nm) as a function of a temperature. This section reviews the basic principles of X-ray scattering and mathematical formulations used in this study

X-rays are a form of electromagnetic radiation covering the range of the wavelengths from 0.1 to 100 Å. The scattering of X-rays derives from the interactions between the incident X-rays and the electrons in a material. The process of X-ray scattering generates two different kinds of scattered waves: elastic (coherent) and inelastic (incoherent). In SAXS, the inelastic scattering is generally not considered because the maximum wavelength shift in inelastic scattering is negligible at small angles.[106]

The amplitude of a travelling wave A at a given time t and at position x can be represented in the form of complex notation as follows:

$$A = \hat{A}e^{i2\pi(\nu t - x/\lambda)} \tag{2.22}$$

where $\hat{A}$ is the absolute value of A, and ν and λ are the frequency and wavelength of the wave, respectively. As described in Figure 2.9, when a collimated X-ray beam intersects two bodies, P and O, the combined wave amplitude at the detector is the sum of the scattered waves from the point P and O (A_P and A_O) that have the path difference of

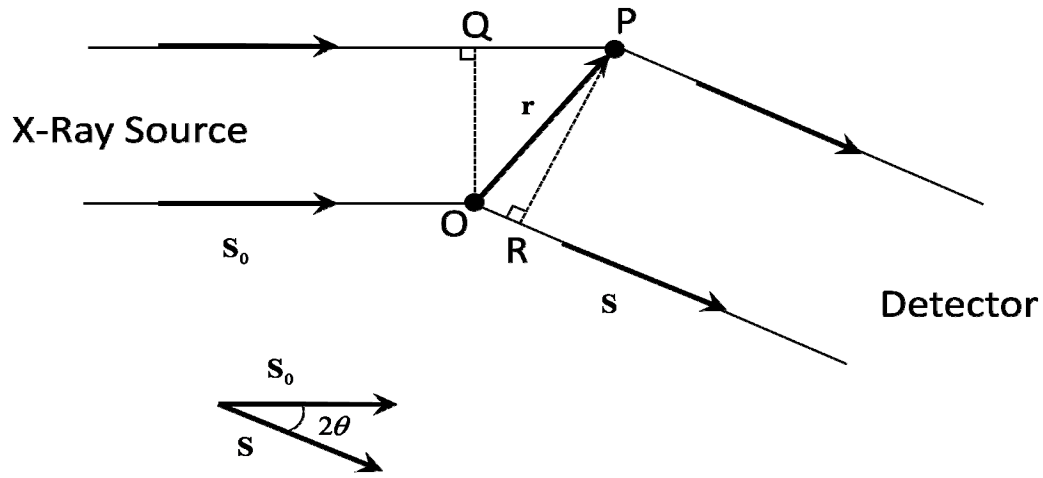

Figure 2.9 Path difference of the scattered waves by two bodies.

$\overline{\mathrm{QP}} - \overline{\mathrm{OR}}$. In other words, the phase difference $\Delta\phi$ between the two waves is

$$\Delta\phi = \frac{2\pi(\overline{\mathrm{QP}} - \overline{\mathrm{OR}})}{\lambda} = \frac{2\pi(\mathbf{S}_0 \cdot \mathbf{r} - \mathbf{S} \cdot \mathbf{r})}{\lambda} = -\mathbf{q} \cdot \mathbf{r} \tag{2.23}$$

where $\mathbf{q}$ is defined as

$$\mathbf{q} = 2\pi \frac{\mathbf{S} - \mathbf{S}_0}{\lambda} \tag{2.24}$$

The vector $\mathbf{q}$ is referred to the scattering vector or momentum transfer vector. An equivalent representation of $\mathbf{q}$ is using the scattering angle 2θ between $\mathbf{S}$ and $\mathbf{S}_0$

$$|\mathbf{q}| = \frac{4\pi \sin\theta}{\lambda} \tag{2.25}$$

In terms of combined amplitude of scattered waves, the amplitude of the combined waves at the detector is

$$A(x,t) = A_P(x,t) + A_O(x,t) = A_0 b e^{i2\pi(\nu t - x/\lambda)}(1 + e^{-i\mathbf{q}\cdot\mathbf{r}}) \tag{2.26}$$

where A_0 is the amplitude of the incident wave and b is the scattering length that accounts for the efficiency of scattering by the bodies. In X-ray scattering, b is proportional to the electron density of the bodies.

At the detector, the scattered X-rays are measured in terms of intensity, which is a measure of the flux of photons over a interval of time (Intensity $I \sim A \cdot A^*$), hence the instantaneous time t and position x are not factors. Also, for the multiple bodies in a given volume V, Eqn (2.26) can be generalized to the following expression:[106]

$$A(\mathbf{q}) = \int_V \rho(\mathbf{r}) e^{-i\mathbf{q}\cdot\mathbf{r}} d\mathbf{r} \tag{2.27}$$

where $\rho(\mathbf{r})$ is the scattering length density distribution over radial distance **r**.

In X-ray scatting experiments, the scattering phenomena in a multi-particle system can be grouped into two kinds: inter-particle and intra-particle interferences. A representative phenomenon of the former is Bragg diffraction and of the latter is single particle form factor. The intensities of inter- and intra-particle interferences are referred to the structure factor $S(\mathbf{q})$ and form factor $P(\mathbf{q})$, respectively (Figure 2.10):

$$I(\mathbf{q}) \sim S(\mathbf{q}) \cdot P(\mathbf{q}) \tag{2.28}$$

The diffraction and form factor formulations related to this thesis research are discussed below.

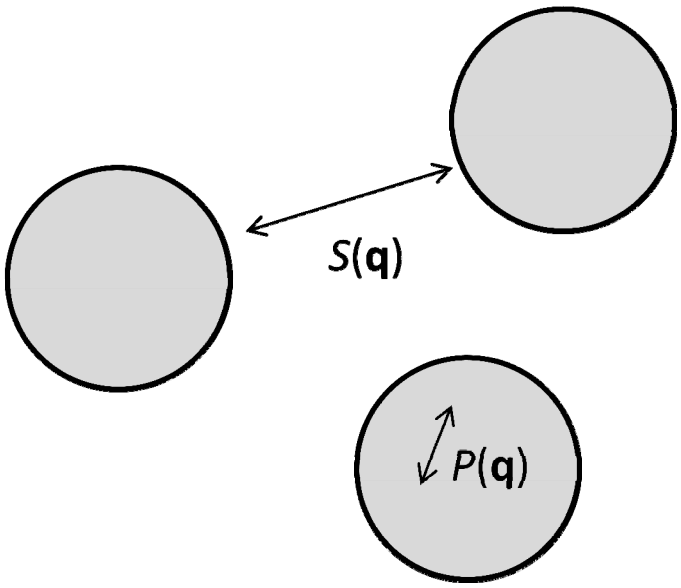

Figure 2.10 Schematic representation of the structure factor S(q) and the form factor P(q) in a multi-particle system.

Diffraction In scattering experiments on condensed matter, scattered waves produced by many objects with spatial regularity yield characteristic interference patterns; the interference relationship is referred to as *Bragg's law*. In Figure 2.9, we considered a system consisting of two bodies to introduce the general expression for the amplitude of scattered waves, Eqn (2.27). If we expand the two particle system to a multi-particle system with the same spatial regularity, diffracted waves display a constructive addition at the detector when the path differences of the waves are the integers of the wavelength, i.e. the diffracted waves are in phase. From Eqn (2.23), the condition for constructive addition is formulated as

$$\mathbf{q} \cdot \mathbf{r} = 2\pi n \tag{2.29}$$

where n is an integer, which is the general statement of Bragg's law. Another formulation of Eqn (2.29) is

$$\frac{q}{2\pi} = \frac{1}{d_{hkl}} \tag{2.30}$$

where $q = |\mathbf{q}|$, and d_{hkl} is the interplanar spacing between parallel crystallographic planes with Miller indices *h*, *k*, and *l*. For a given lattice with vectors $a = |\mathbf{a}|$, $b = |\mathbf{b}|$, and $c = |\mathbf{c}|$ with angles α, β, and γ between the unit cell vectors of $\mathbf{b}$ and $\mathbf{c}$, $\mathbf{c}$ and $\mathbf{a}$, and $\mathbf{a}$ and $\mathbf{b}$ as shown in Figure 2.11, the inverse of the interplanar spacing $1/d_{hkl}$ is the absolute value of the reciprocal lattice vector $\mathbf{r}^*_{hkl}$ which is defined as

$$\mathbf{r}^*_{hkl} = h\mathbf{a}^* + k\mathbf{b}^* + l\mathbf{c}^* \tag{2.31}$$

where $\mathbf{a}^*, \mathbf{b}^*$, and $\mathbf{c}^*$ are the basis vectors of the reciprocal lattice:

$$\mathbf{a}^* = \frac{\mathbf{b} \times \mathbf{c}}{V_u}, \quad \mathbf{b}^* = \frac{\mathbf{c} \times \mathbf{a}}{V_u}, \quad \mathbf{c}^* = \frac{\mathbf{a} \times \mathbf{b}}{V_u} \tag{2.32}$$

where V_u is the unit cell volume given by

$$V_u = \mathbf{a} \cdot (\mathbf{b} \times \mathbf{c}) = \mathbf{b} \cdot (\mathbf{c} \times \mathbf{a}) = \mathbf{c} \cdot (\mathbf{a} \times \mathbf{b}) \tag{2.33}$$

Thus, the inverse of interplanar spacing $1/d_{hkl}$ can be expressed by following general relation in terms of the unit cell vectors:

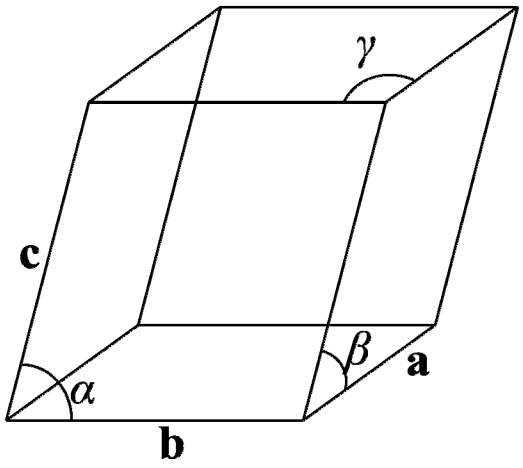

Figure 2.11 Generalized unit cell representation. A crystal structure of a material is described by stacked unit cells in three dimensions. The unit cell vectors are represented by a, b, and c. The angles between the unit cell vectors are denoted by α, β, and γ.

$$\frac{1}{d_{hkl}^2} = (h\mathbf{a}^* + k\mathbf{b}^* + l\mathbf{c}^*) \cdot (h\mathbf{a}^* + k\mathbf{b}^* + l\mathbf{c}^*) \tag{2.34}$$

For a given lattice system, the lattice vectors have specific conditions. In a cubic system, the lattice vectors are $a = |\mathbf{a}| = |\mathbf{b}| = |\mathbf{c}|$ and angles between the unit cell vectors are $\alpha = \beta = \gamma = 90^o$. By these conditions, Eqn (2.34) become

$$\frac{1}{d_{CUB}} = \sqrt{\frac{h^2 + k^2 + l^2}{a^2}} \tag{2.35}$$

For hexagonally packed cylinders, the inter planar spacing becomes by the unit cell conditions $a = |\mathbf{a}| = |\mathbf{b}|$, $c = \infty$ and $\alpha = \beta = 90^{o}$, $\gamma = 60^{o}$:

$$\frac{1}{d_{HEX}} = \sqrt{\frac{h^2 + k^2 + hk}{a^2}} \tag{2.36}$$

A tetragonal lattice system has the unit cell conditions of $a = |\mathbf{a}| = |\mathbf{b}|$, $c = |\mathbf{c}|$ and $\alpha = \beta = \gamma = 90^{o}$, and the inter planar spacing of a tetragonal system becomes:

$$\frac{1}{d_{TET}} = \sqrt{\frac{h^2 + k^2}{a^2} + \frac{l^2}{c^2}} \tag{2.37}$$

Finally, for one dimensional lamellar array, the unit cell conditions are $a = |\mathbf{a}|$, $b = c = \infty$ and $\alpha = \beta = \gamma = 90^{o}$ and the inter planar spacing is

$$\frac{1}{d_{LAM}} = \sqrt{\frac{h^2}{a^2}} \tag{2.38}$$

Eqns (2.35) to (2.38) formulate the inter planar spacings of typical block copolymer crystal systems. In a crystal symmetry or space group, the atoms or scattering particles are arranged by specific spatial configurations which follow allowed crystal symmetry operation elements. These allowed symmetry elements determine the ways of constructive and destructive conditions of scattering waves from crystal planes and the constructive reflection conditions are manifested by the allowed Miller indices (*hkl*). The allowed Miller indices of space groups can be found in the *International Tables of*

Crystallography, [107] and Table 2.2 shows the allowed reflection (peak) ratios of typical block copolymer crystals.

Figure 2.12 illustrates the general arrangement of a small angle X-ray scattering experiment. Monochromatic X-rays radiate from a source (typically from CuKα or synchrotron radiation) are collimated before impinging on the sample, and the scattered X-rays are recorded on an area detector. The recording time varies depending on the power of the X-ray source and the sample characteristics. Figure 2.13 displays the 2D and azimuthally integrated 1D scattering patterns.

Form Factor Scattering from an isolated object with a specific geometry in a homogeneous medium (i.e. uniform scattering length density) is governed by the geometry of the particle, which is referred to as the form factor. The mathematical formulation of the scattering response of an isolated object begins with the amplitude Eqn (2.27), usually expressed as the average density distribution A_ρ:

Table 2.2 Allowed reflections for the typical block copolymer morphologies

Morphology	Allowed Reflection Ratios
Lamellae	1, 2, 3, 4, 5, 6…
Hexagonally packed cylinders	1, √3, √4, √7, √9, √12…
Gyroid	√6, √8, √14, √16, √20…
Face-centered cubic with spheres	√3, √4, √8, √11, √12…
Body-centered cubic with spheres	1, √2, √3, √4, √5, √6, √7…

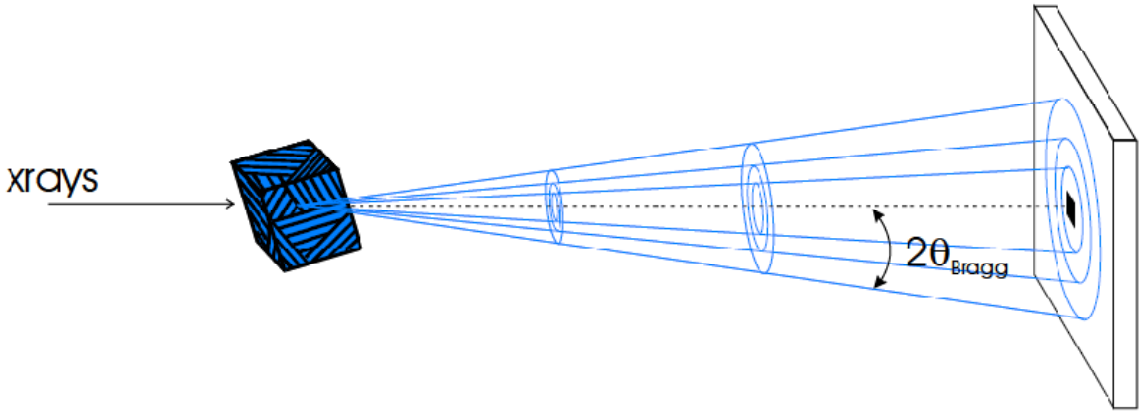

Figure 2.12 Schematic drawing of a small angle X-ray scattering experiment from a polycrystalline sample. The isotropic nature of the sample generates continuous diffraction rings on the detector. Drawing is from Bailey.[108]

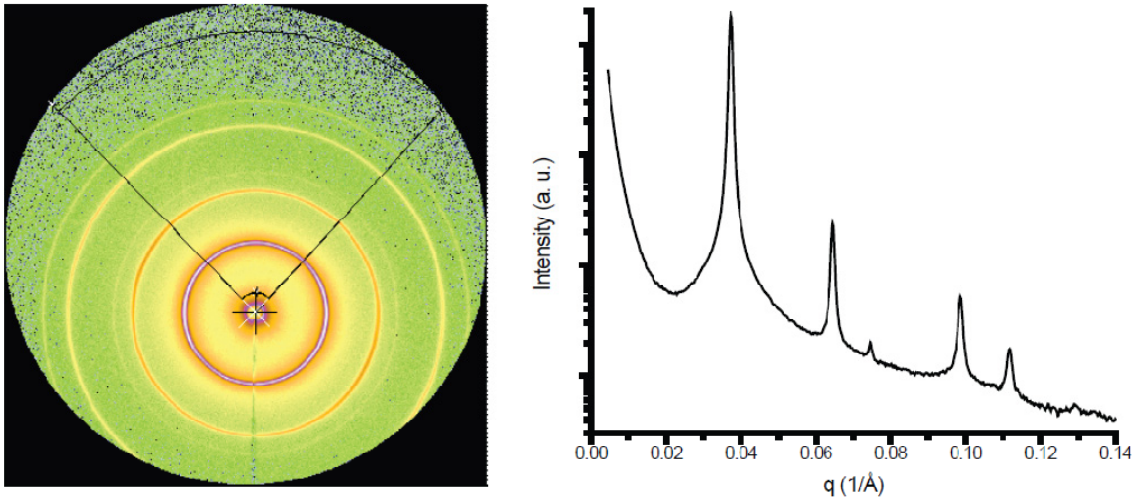

Figure 2.13 Azimuthal integration of 2 dimensional SAXS from a point collimated source. The cross on the left 2D SAXS picture indicates the beam center, and the area enclosed by black lines was integrated to acquire one-dimensional plot (right)

$$A_\rho(\mathbf{q}) = \frac{\int_V \rho(\mathbf{r}) e^{-i\mathbf{q}\cdot\mathbf{r}} d\mathbf{r}}{\int_V \rho(\mathbf{r}) d\mathbf{r}} \tag{2.39}$$

For a polymeric micelle, two scattering length densities can be recognized along with a solvent medium background: core and corona. For a non-interacting polymeric micelle system, the general intensity profile is given by pairing possible inter-particle correlations between the core and corona:[109]

$$\begin{aligned} I(q) = {} & N\left(\rho_{core} - \rho_{solvent}\right)^2 \left(N_{core} A_{core}(q)\right)^2 + N\left(\rho_{corona} - \rho_{solvent}\right)^2 \left(N_{corona} A_{corona}(q)\right)^2 \\ & + 2N\left(\rho_{core} - \rho_{solvent}\right)\left(\rho_{corona} - \rho_{solvent}\right) N_{core} N_{corona} A_{core}(q) A_{corona}(q) \end{aligned} \tag{2.40}$$

where N is the micelle number density; ρ_{core}, ρ_{corona}, and $\rho_{solvent}$ are the scattering length density of the core, corona, and solvent, respectively; N_{core} and N_{corona} are the number of core and corona chains of a micelle; and $A_{core}(q)$ and $A_{corona}(q)$ are the averaged scattering amplitude for the core and corona.

In a micelle geometry, the averaged scattering amplitude $A_\rho(\mathbf{q})$ of Eqn (2.39) can be expressed as a more analytical form for the core and corona of the micelle, and putting the exact forms of analytical averaged scattering amplitude in Eqn (2.40) gives the system specific intensity profile.

The micelle geometry specific expression of $A_\rho(\mathbf{q})$ is discussed below and an illustration of the micelle geometries investigated in this research is shown in Figure 2.14.

Spherical Micelle The geometry of a spherical micelle is shown in Figure 2.14a. The scattering length density of a spherical micelle with the core radius R_{core} can be formulated as:

$$\rho(r) = \begin{cases} \rho_0 \text{ for } r \le R_{core} \\ 0 \quad \text{for } r > R_{core} \end{cases} \tag{2.41}$$

and by integrating Eqn.(2.39) in the spherical coordination, the core scattering amplitude of spherical micelle $A_{core,sph}(q)$ becomes

$$A_{core,sph}(q) = \frac{(\sin qR_{core} - qR_{core}\cos qR_{core})}{(qR_{core})^3} \tag{2.42}$$

For the corona domain, by the spherical symmetry and radial distribution function of corona brushes $n(r)$, Eqn (2.39) becomes

$$A_{corona,sph}(q) = \frac{\int_{R_{core}}^{R_{mic}} n(r)\frac{\sin qr}{qr} r^2 \mathrm{d}r}{\int_{R_{core}}^{R_{mic}} n(r) r^2 \mathrm{d}r} \tag{2.43}$$

where R_{mic} is the radius of micelle. The R_{mic} does not represent an actual micelle size, but a hypothetical boundary in the form factor calculation. Won *et al*. proposed the Fermi-Dirac distribution to describe the radial distribution function of corona brushes $n(r)$:[109]

$$n(l) \approx \frac{1}{\exp\left(\frac{l - l_0}{s}\right) + 1} \tag{2.44}$$

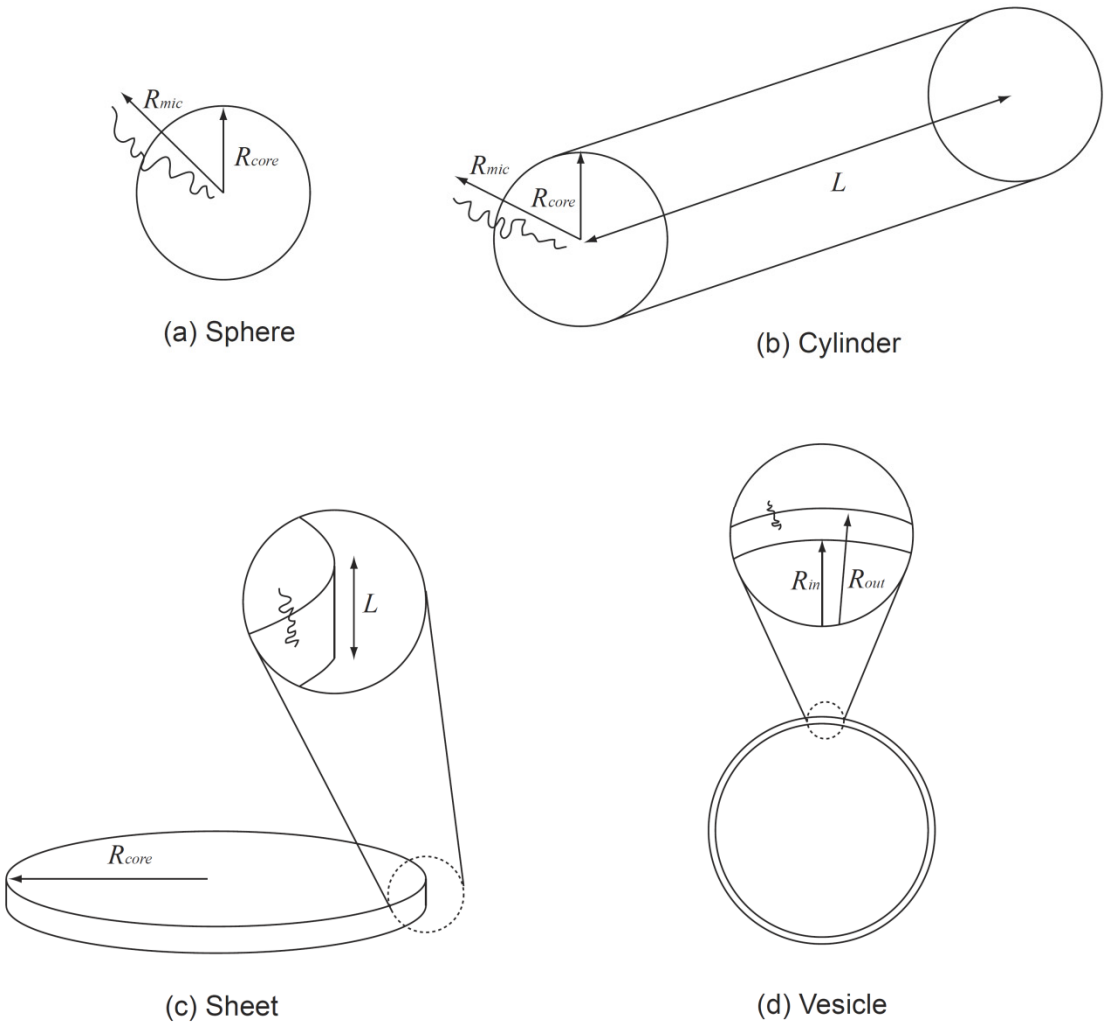

Figure 2.14 Geometrical illustration of micelle cores.

where l_0 and s are adjustable parameters for an experimentally acquired intensity profile with a spherical micelle sample.

Cylindrical Micelle The derivation of the form factor amplitude of a cylindrical micelle follows the similar procedure employed in the derivation of the spherical micelle form factor, but it requires more mathematical work. The geometrical representation of a cylindrical micelle is shown in Figure 2.14b. Won *et al*. proposed a simplified form factor amplitude for a cylindrical micelle to reduce the extent of calculation.[109] In the case of $L \gg R_{core}$ and $qR_{core} \ll 1$, the proposed form factor amplitudes of core $A_{core,cyl}(q)$ and corona $A_{corona,cyl}(q)$ with the cylinder length L are

$$A_{core,cyl}(q) = \frac{2J_1(qR_{core})}{qR_{core}} \left(A_{axial}(q)\right)^{1/2} \tag{2.45}$$

$$A_{corona,cyl}(q) = \frac{\int_{R_{core}}^{R_{mic}} n(r) J_0(qr) r \mathrm{d}r}{\int_{R_{core}}^{R_{mic}} n(r) r \mathrm{d}r} \left(A_{axial}(q)\right)^{1/2} \tag{2.46}$$

where J_0 and J_1 are the zeroth and first order Bessel functions. $A_{axial}(q)$ represents the amplitude from the axial part of a cylindrical micelle, and it is given by

$$A_{axial}(q) \approx \frac{\pi}{qL} \tag{2.47}$$

A detailed discussion on the cylinder form factor formulation can be found elsewhere.[109, 110]

Infinite Sheet The form factor formulation of an infinite sheet with finite thickness can be derived from a cylinder model with infinite radius *R* and finite cylinder length *L* (Figure 2.14c). Burge and Draper proposed the squared form factor amplitude of the infinite sheet based on the work by Fournet.[111, 112]

$$A^2_{\substack{core,sheet \\ R\to\infty}}(q) = \frac{1}{\pi R^2}\frac{2\pi}{q^2}\frac{\sin^2\left(\frac{qL}{2}\right)}{\left(\frac{qL}{2}\right)^2} \tag{2.48}$$

In this thesis work, the form factor amplitude from the corona in infinite sheets was not considered because the samples which have infinite sheet micelles have the matched scattering length densities between the corona and the solvent.

Bilayer Vesicle In this work, the vesicle form factor proposed by Bang *et al.* was employed. They formulated the core form factor of a vesicular structure using the hollow sphere model (Figure 2.14d).[113]

$$A_{core,vesicle}(q) = \left[V_{out}\Phi\left(qR_{out}\right) - V_{in}\Phi\left(qR_{in}\right)\right]\exp\left(-q^2\sigma^2/2\right) \tag{2.49}$$

where $V_{out} = 4\pi R^3_{out}/3$ and $V_{in} = 4\pi R^3_{in}/3$, and $\Phi(x) = 3\left[\sin x - x\cos x\right]/x^3$ which is the hard sphere form factor. The exponential term at the right end of Eqn (2.49) represents the soft interface between vesicle core and corona domains. In terms of the center radius of a vesicle core R and the half thickness of the core L_c, the outer radius R_{out} and the inner radius R_{in} can be expressed as $R + L_c$ and $R - L_c$, respectively. These R, L_c, R_{out}, and R_{in} representations can be used interchangeably.

Micelle Polydispersity The core sizes of polymeric micelles are not uniform and core radius polydispersity gives a significant smearing effect to the idealized form factor models. In this study, the polydispersity effect of core radii was formulated using the zeroth-order-log-normal (ZOLD) probability distribution.[109]

$$P_{R_{core}}(R_{core}) = \frac{1}{(2\pi)^2 \sigma_0 \bar{R}_{core} \exp(\sigma_0^2/2)} \exp\left(-\frac{(\ln R_{core} - \ln \bar{R}_{core})^2}{2\sigma_0^2} \right) \tag{2.50}$$

where $\bar{R}_{core}$ is the mean modal core radius and σ_0 is the width of the distribution. The polydispersity effect can be incorporated with the scattering intensity profile by the following formulation:

$$\langle I(q) \rangle = \int_0^\infty I(q, R_{core}) P_{R_{core}}(R_{core}) \mathrm{d}R_{core} \tag{2.51}$$

and the standard deviation of core radius distribution σ is

$$\sigma = \bar{R}_{core} \sqrt{\exp(4\sigma_0^2) - \exp(3\sigma_0^2)} \tag{2.52}$$

Form Factor Fitting The form factor fitting is a numerical process to find physically meaningful parameters from experimental data by employing an appropriate form factor model. Form factor fitting can be carried out in two ways: manual adjustment of parameters and machine fitting using a program. In the case of a system of many form factor fitting variables, the manual fitting is very complex and nearly impossible to find the best fitting parameters. However, it is generally preferred practice since the machine fitting works by only numerical approach not by physical feasibility. Computer fitting

can lead to erroneous solutions. In this work, the most crucial parameters (core radius) were adjusted manually, and the other parameters were determined by machine fitting with marginal changes of the initial parameters. Although the machine fitting process can alter the manually adjusted initial parameters including the core radius, only reasonable final results were accepted. All fitting work employed in this work was carried out with the commercially available IGOR Pro software version 6.1 software marketed by WaveMetrics.

To compare the results of the form factor formulations, representative plots of spheres, cylinders, infinite sheets, and vesicles are shown in Figure 2.15. These plots were prepared with a common core radius or thickness R_{core} or L = 300 Å and width of distribution σ_0 = 15. The overall features of the form factors are similar to each other, but the frequencies of maxima and minima of sinusoidal features over the scattering vector are different. Ideally, a form factor fitting is conducted after the geometry of the micelles in a sample is confirmed by electron microscopy or using another technique.

2.7 Cryogenic Scanning Electron Microscopy

Cryogenic scanning electron microscopy (Cryo-SEM) is a powerful technique for the visualization of three-dimensional real space structures in a volatile solvent(s).[114, 115]

Compared to the other major cryogenic electron microscopy technique, cryogenic transmission electron microscopy (Cryo-TEM), Cryo-SEM has several distinctive

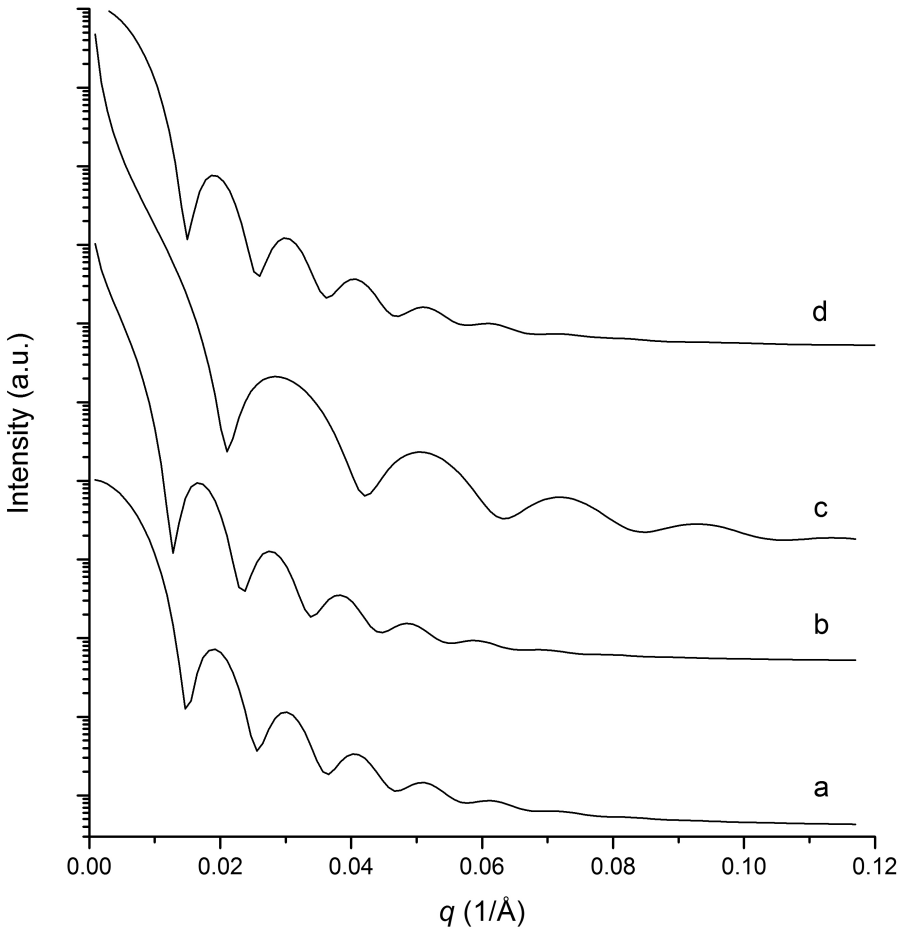

Figure 2.15 Representative form factor plots of (a) sphere, (b) cylinder, (c) infinite sheet, and (d) vesicle. All plots were drawn with the core radius or thickness R_{core} or L = 300 Å and the width of distribution σ_0 = 15.

advantages and a few short-comings.[74] Notable characteristic differences between these two cryogenic microscopy techniques are described in Table 2.3.

As with cryo-TEM,[55] cryo-SEM requires a dedicated sample preparation procedure for a successful characterization. A schematic description of the sample preparation procedure is depicted in Figure 2.16: a solution or gel sample is transferred into two small brass or aluminum metal hats (Ted Pella) with a depth of ~ 200 μm, then the two metal hats are sandwiched at room temperature (Figure 2.16a) and frozen using a stream of liquid nitrogen (~ 2100 bar) in less than ~ 10 ms (Balzers HPM 010 High Pressure Freezer, Figure 2.16b). This high pressure rapid freezing process is required to prevent the crystallization of water, which can possibly alter or destroy the micelle structures. The frozen sample is quickly transferred in liquid nitrogen from the high pressure freezer, and fractured along with the side of the sandwiched hats in liquid nitrogen using a knife (Figure 2.16c). One of the fractured sample hats is mounted on the pre-cooled cryo-SEM sample stage (Gatan 626). The sample is then etched under vacuum at a selected temperature where the temperature controls the etching rate of the solvent(s) (Figure 2.16d). Finally, the etched specimen is coated with a platinum film (10 nm) in a Bal-Tec MED 010 freeze drying/sputter coating device (Figure 2.16e), and imaged and recorded using a field emission gun scanning electron microscopy S-900 (FEGSEM) manufactured by Hitachi. The acceleration voltage is 3 keV which produces mostly back-scattered electrons (BSE) (Figure 2.16f).

Table 2.3 Comparison of cryo-TEM and cryo-SEM techniques.

Description	Cryo-TEM	Cryo-SEM
Origin of signal	Electron density difference	Spatial scattering difference of incident electrons
Characteristics of micrographs	2D projections of real space objects	Topology of specimen surface
Applicable solute size	Few Angstroms to few micrometers	Few nanometers to few millimeters
Strength	Information on internal structures and relatively accurate dimensional information	Information on topological 3D structures
Weakness	Substrate should be discrete and small enough to be embedded in supporting lacy carbon TEM grid	Lack of information of internal structures

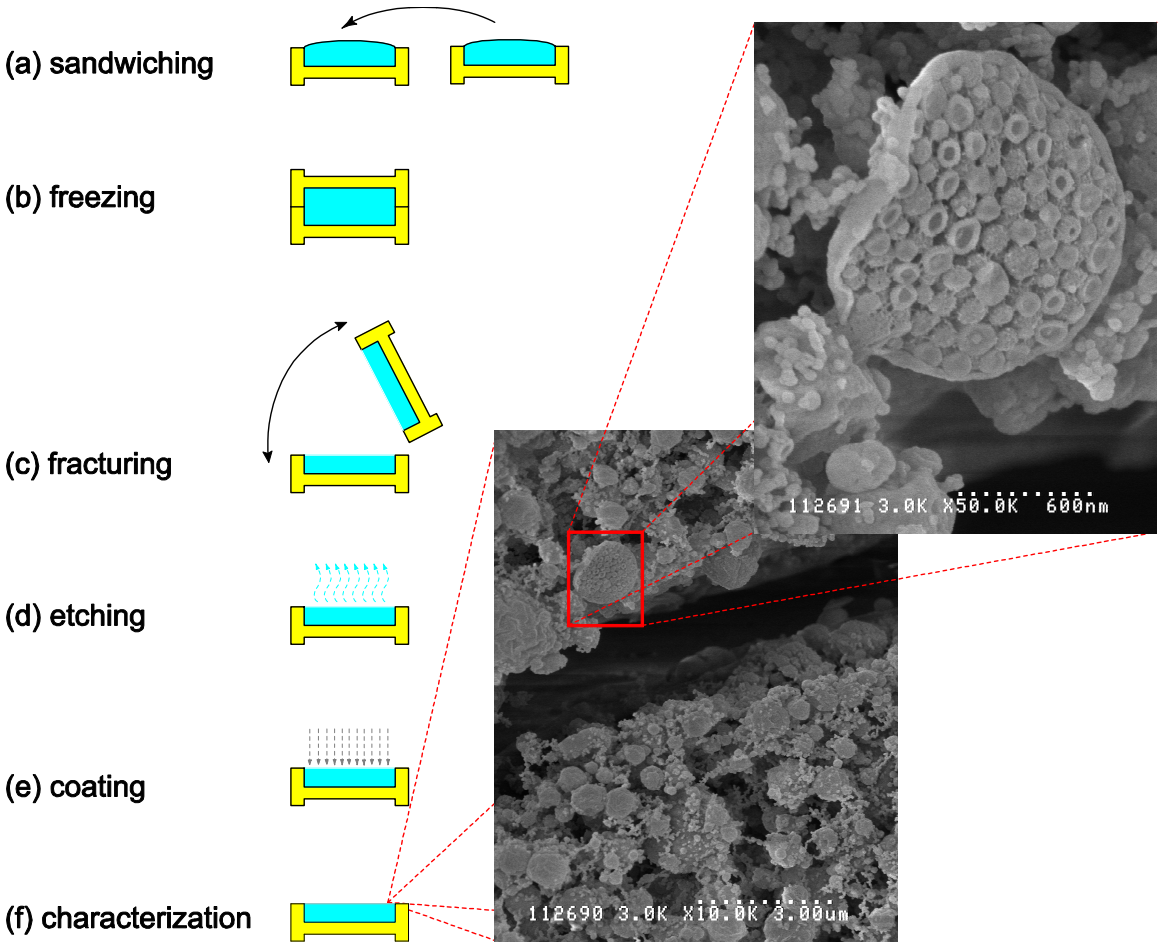

Figure 2.16 Schematic drawing of cryo-SEM sample preparation.

The etching rates of water and 1,5-cyclooctadiene (COD, a solvent used in this study) were selectively controlled by the etching temperature and time. The etching rate of a frozen solvent increases linearly with the difference between the saturated vapor pressure of frozen solvent P_s and the condenser pressure P_c (or chamber pressure) and is inversely proportional to the etching temperature T. The sublimation rate of vitrified water r can be modified as[115]

$$r = \kappa(P_s - P_c)\left(\frac{M_{H_2O}}{2\pi RT}\right)^{1/2} \tag{2.53}$$

where κ is the coefficient of evaporation, M_{H_2O} is the molecular weight of water, and R is the gas constant. The saturate vapor pressure of ice, P_s, given by Davis is[116]

$$\log_{10}\frac{P_s}{130} = -\frac{2400}{T} + 8.2\log_{10}T - 0.017T + 1.2\times10^{-5}T^2 - 6.8 \tag{2.54}$$

Taking $\kappa = 1$ and $P_c = 2\times10^{-9}$ bars (typical chamber pressure of MED 010), the sublimation rates of ice at -110, -100, and -90 ^{o}C are approximately 10, 100, and 1000 nm/min respectively (for these values, the error is less than 60%).[115] Due to a lack of available thermodynamic data, the etching rate of COD was estimated based on the cryo-SEM observations of binary polymer-COD samples at different temperatures. An etching rate of 20-40 nm/min was estimated at -102 ^{o}C, which is approximately 30% of the etching rate of water at this temperature.

Chapter 3
Frank-Kasper σ-Phase in Block Copolymer Melts*

3.1 Introduction

A block copolymer is a macromolecule made of two or more different polymer blocks connected end-to-end.[117] The chemical dissimilarity of the repeating units of the blocks leads to a thermodynamic penalty upon mixing, and this incompatibility, quantified by the Flory-Huggins interaction parameter χ, drives microphase separation, resulting in nanometer scale periodic structures comprised of microphase separated domains.

Leibler showed that the phase behavior of AB diblock copolymers can be discussed using two terms:[2] the block volume fraction f and the compound variable χN,

---

* Part of this work was published in 'Sangwoo Lee, Michael J. Bluemle, Frank S. Bates, *Science*, 2010, 330, 349'

where N is the degree of polymerization. Using a free energy expression based on the Landau theory, he suggested three diblock copolymer periodic morphologies as a function of f and χN: lamellar (LAM), hexagonally-packed cylinders (HEX), and spheres arrayed on a body-centered cubic (BCC) lattice.[118, 119]

Several years after the Leibler's seminal work, the first bicontinuous network phase was reported and identified as the ordered bicontinuous double diamond (OBDD) phase.[14, 15] However, the OBDD network phase was reevaluated by several other groups, and reassigned as the gyroid (GYR) network phase (space group No. 230), which is now accepted as the correct assignment.[16-18] Recently, a second non-cubic, orthorhombic network phase was discovered in diblock copolymers, denoted O^{70}, following a theoretical prediction that followed identification of this structure in several ABC and diblock copolymers.[20-22, 34, 120]

New phases of block copolymers have been explored by expanding the parameter space. Extending the number of chemically different blocks is the most accessible approach, e.g., connecting a new block to an AB diblock copolymer to construct an ABC triblock terpolymer. Many new morphologies have been reported for ABC triblock terpolymers including from the poly(1,4-isoprene-*b*-styrene-*b*-ethylene oxide) ISO triblock terpolymer system: three domain LAM, core-shell morphologies of HEX, BCC, and GYR, alternating gyroid Q^{214}, and tricontinuous orthorhombic network O^{70} and O^{52}.[22, 30-39]

Aside from controlling the number of components, modifications of block sequences and architectures also have been shown to be effective design parameters to control phase behavior of block copolymers. For example, as a modification of the ISO triblock terpolymer, placing the I block between equally sized S blocks results in a poly(styrene-*b*-1,4-isoprene-*b*-styrene-*b*-ethylene oxide) SISO tetrablock terpolymer, which show drastically different phases compared to ISO triblock terpolymers at the same compositions.[40] In addition to such linear modifications, still more diverse mesoscale periodic structures have been documented by judicious alteration of molecular structure and chemical composition, i.e. starblock, polydispersity, block chirality, and blending.[39, 93, 121-129]

While working on small angle X-ray scattering (SAXS) experiments with a poly(1,4-isoprene-*b*-DL-lactide) (IL) diblock copolymer, a scattering pattern containing a large number of Bragg peaks was observed, one never reported in block copolymer systems to the best of my knowledge. Serendipitously, this pattern was discovered to be almost identical to a SAXS pattern obtained with a SISO tetrablock terpolymer, synthesized by my colleague, Dr. Michael J. Bluemle. This finding motivated us to investigate the crystal structure of these polymers and we concluded that the new scattering pattern represents a Frank-Kasper σ-phase ($P4_2/mnm$), known to be a dodecagonal quasicrystal approximant. This chapter describes the experiments and analysis that resulted in this conclusion.

3.2 Experimental

Materials The block copolymers used in this study were polymerized by anionic polymerization techniques and the detailed procedures are described elsewhere.[40, 130] The molecular weights of poly(1,4-isoprene-*b*-DL-lactide) (IL-15) diblock and poly(styrene-*b*-1,4-isoprene-*b*-styrene-*b*-ethylene oxide) (SISO-3) tetrablock copolymers were characterized by ^{1}H nuclear magnetic resonance (NMR) spectroscopy (Varian 300 or 500 MHz). Size exclusion chromatography (SEC) with chloroform as the mobile phase was employed to characterize the molecular weights and polydispersities of these components. Glass transition (T_g) and melting (T_m) temperatures were determined using a TA instrument Q1000 differential scanning calorimetry (DSC). The molecular structures and characterization data of IL-15 and SISO-3 are shown in Figure 3.1 and Table 3.1, respectively. The DSC thermograms of IL-15 and SISO-3 are presented in Figure A.1 in Appendix A.

X-ray scattering Small angle X-ray scattering (SAXS) experiments were performed at the DND-CAT (beamline 5IDD) at the Advanced Photon Source (APS) located at the Argonne National Laboratory (Argonne, IL). Two dimensional SAXS patterns were collected using a Mar CCD area detector, a sample to detector distances of 4.042 and 6.640 m, and a wavelength of $\lambda = 0.729$ Å. Samples were held in quartz capillary tubes for room temperature experiments or aluminum DSC pans (TA instruments) with Kapton windows for the high temperature measurements. Two

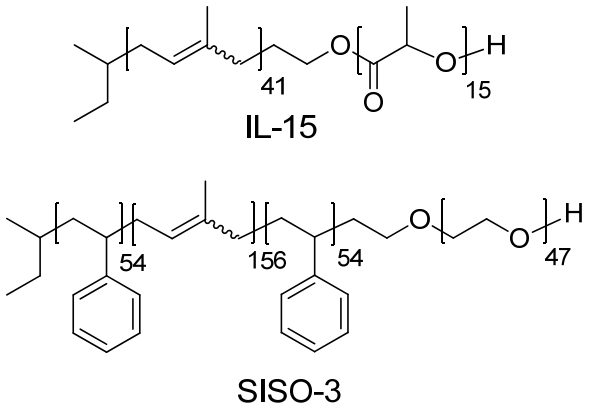

Figure 3.1 Molecular structures of IL-15 and SISO-3. Numbers below brackets represent degree of polymerization.

Table 3.1 Molecular characterization data of IL-15 and SISO-3

Polymer	M.W. (kg/mol)	f_I[a]	f_L[a]	f_S[a]	f_O[a]	$T_{g,I}$[b] (^oC)	$T_{g,L}$[b] (^oC)	$T_{g,S}$[b] (^oC)	$T_{m,O}$[c] (^oC)	T_{ODT}[d] (^oC)	PDI[e]
IL-15	3.89	0.78	0.22			-66	-5			50±1	1.12
SISO-3	23	0.46		0.46	0.08	-58		< 100	38	224±3	1.04

[a]volume fraction. Subscripts I, L, S, and O represent 1,4-polyisoprene, poly(DL-lactide), polystyrene, poly(ethylene oxide) blocks, respectively. These volume fractions can have a error of ±0.01. [b]glass transition temperature. [c]melting temperature. DSC thermograms are shown in Figure A.1 in Appendix [d]order-to-disorder transition temperature. The T_{ODT}'s of IL-15 and SISO-3 were measured by DMS and SAXS. [e] polydispersity.

dimensional data were azimuthally averaged to the one-dimensional form of intensity (arbitrary unit) versus the magnitude of scattering wavevector [$q = 4\pi\lambda^{-1} \sin(\theta/2)$ where θ is the scattering angle].

Microphase Symmetry Analysis and Rietveld Powder Pattern Simulation

Microphase symmetry analysis and Rietveld power pattern simulation of IL-15 SAXS data were conducted using the JADE X-ray diffraction analysis software (version 9) marketed by Material Data Inc. The JADE software is specialized for atomic scattering patterns so the powder SAXS pattern of IL-15 was modified for the software analysis: the background pattern of IL-15 powder SAXS pattern was subtracted by an intensity profile modeled after the correlation hole scattering pattern of IL-15, obtained after quenched to 25 ^{o}C from a disordered state at elevated temperature. Then, the background corrected IL-15 SAXS pattern was deconvoluted with a calculated spherical form factor with the radius R = 42 Å ($\Delta R/R$ = 2.1 %) for specimen IL-15 (see Figure A.2 in Appendix A). Because the JADE software only takes the scattering data of scattering angle θ versus intensity in a wide angle X-ray scattering domain (atomic scale), the q axis of IL-15 powder SAXS pattern was multiplied by 90 to reduce the domain spacing into an Å range and the q axis was converted into the θ axis using $\theta = 2*\sin^{-1}(q\lambda/4\pi)$. After these modifications, selected peak positions were employed to estimate possible microphase symmetries. Argon was employed as a hypothetical spherical scattering particle for the JADE software analysis.

The Rietveld technique was implemented using the JADE software and simulated Rietveld patterns from the modified IL-15 SAXS pattern were reconstructed by reversing the modifications described above. The scattering length density of scattering sites were adjusted using a set of atomic species based on relative Wigner-Seitz cell volumes (scattering power is proportional to the volume of Wigner-Seitz cell. See below).

TEM Projected images of the SISO-3 microstructures were obtained using transmission electron microscopy (TEM). Thin slices of SISO-3 (~ 70 nm) were prepared using a Reichert UltraCut S Ultramicrotome (Leica) at -80 ^{o}C and stained by the vapor from a 4 % aqueous OsO_4 solution for 10 minutes at room temperature. Micrographs of SISO-3 were acquired at room temperature using a FEI Tecnai G^2 F30 field emission gun TEM operating at 300 kV and equipped with a Gatan 4k × 4k pixels Ultrascan CCD camera.

3.3 Result and Analysis

In this section, SAXS data obtained from IL-15 and SISO-3 and TEM micrograph of SISO-3 are presented.

Figure 3.2 presents the time-resolved scattering patterns of IL-15 at 40 ^{o}C after quenched from 70 ^{o}C at a rate of ~ 100 ^{o}C/min. Right after quenching, IL-15 displayed a correlation hole scattering pattern (Figure 3.2b), but a small hint of an additional peak at q^* = 0.0648 Å^{-1} evolved at the top of the correlation hole-peak within 2 minutes (Figure

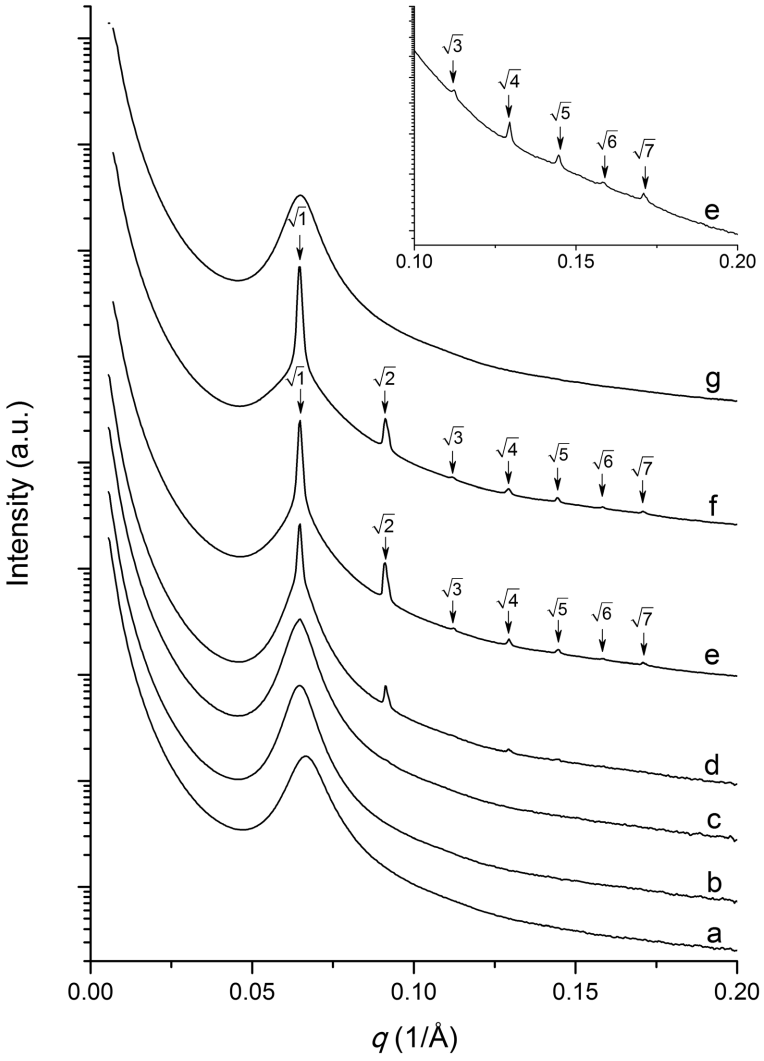

Figure 3.2 Synchrotron powder SAXS patterns from IL-15 quenched to 40 ^{o}C from 70 ^{o}C. SAXS patterns were obtained sequentially from bottom to top at (a) 70 ^{o}C, annealed for 1.5 minute, (b) 40 ^{o}C, 0.5 minute, (c) 40 ^{o}C, 2 minutes, (d) 40 ^{o}C, 15 minutes, (e) 40 ^{o}C, 30 minutes including the inset, (f) 40 ^{o}C, 60 minutes, and (g) 52 ^{o}C, 6 minutes. After 30 minutes annealing, IL-15 displayed the reflection peaks, consistent with BCC phase, q/q^* = √1: √2: √3: √4: √5: √6: √7, where q^* = 0.0648 Å^{-1}.

3.2c). Subsequently, this peak and 6 additional peaks became apparent within 30 minutes (Figure 3.2d to e) and stabilized thereafter (Figure 3.2f).

The relative positions of these 7 peaks (q/q^* = √1: √2: √3: √4: √5: √6: √7 where q^* = 0.0648 Å^{-1}) are consistent with BCC symmetry, having unit cell size a = 137 Å. The BCC morphology is assumed to have pure PLA spherical domains with radius 41 Å [= $(3f_L a^3/8\pi)^{1/3}$], incorporating approximately 193 block copolymers per sphere based on the bulk densities of poly(1,4-isoprene) (PI) and poly(DL-lactide) homopolymers (ρ_{PI} = 0.9 g/cm^3 and ρ_{PLA} = 1.248 g/cm^3) at 25 ^{o}C.[131, 132] The IL-15 specimen with BCC symmetry at 40 ^{o}C was heated to 52 ^{o}C, resulting in the loss of the Bragg reflections, consistent with a state of disorder (Figure 3.2g). Based on isochronal dynamic mechanical spectroscopy measurements (see Figure 4.2 in chapter 4), T_{ODT} = 50 ± 1 ^{o}C for this specimen.

Compared to the BCC SAXS pattern obtained at 40 ^{o}C, a remarkably different result was recorded when IL-15 was quenched to room temperature. IL-15 was disordered at 120 ^{o}C, quenched to room temperature, and aged. Right after the quench (3 minutes), IL-15 displayed a typical correlation hole scattering pattern (Figure 3.3a),but after 2.4 hours, 4 diffraction peaks, consistent with BCC symmetry (q/q^* = √1: √2: √3: √4 where q^* = 0.0633 Å^{-1}) had emerged. Along with these cubic reflections, evidence of 4 other small peaks around the primary peak at q^* were noticeable (marked with short vertical lines above Figure 3.3b). These peaks became more intense during aging and surprisingly, a large number of additional peaks (≥ 48 peaks) developed during 26 days

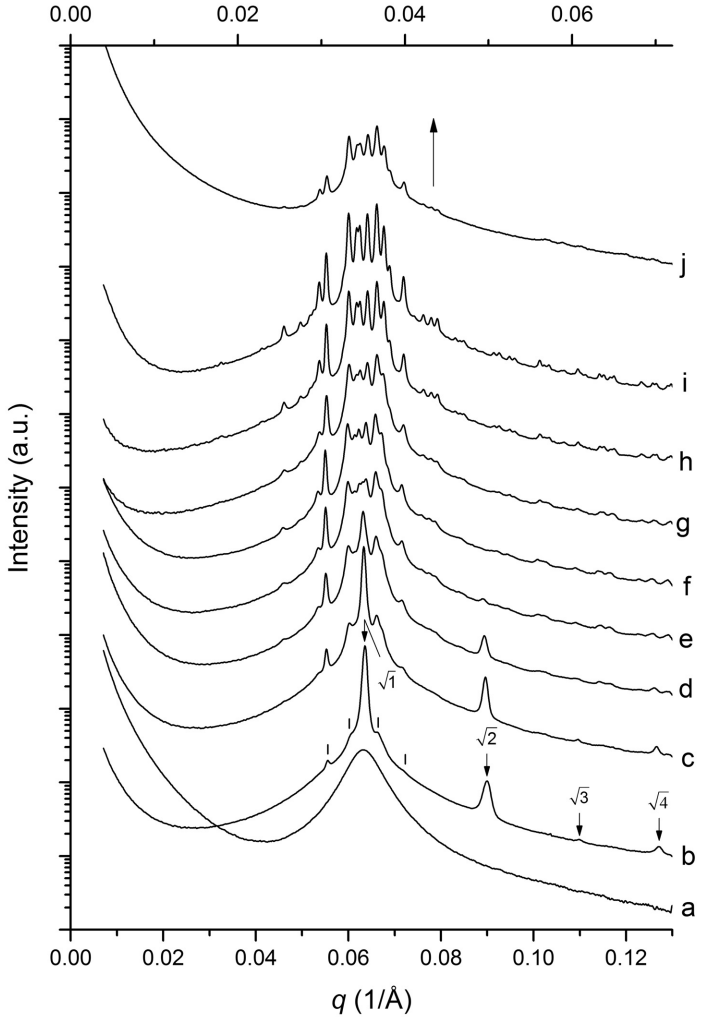

Figure 3.3 Synchrotron powder SAXS patterns from IL-15 at room temperature and SISO-3 at 140 ^{o}C. The IL-15 SAXS patterns were obtained after quenched from 120 ^{o}C to room temperature, and aged for (a) 3 minutes, (b) 2.4 hours, (c) 4.7 hours, (d) 9 hours, (e) 14 hours, (f) 38 hours, (g) 5 days, (h) 12 days, and (i) 26 days. The SISO-3 pattern was obtained with the specimen annealed at 140 ^{o}C for 1 day (j).

of aging (Figure 3.3c to i). Growth of this large set of peaks was accompanied by the loss of the initial BCC reflections, which became extinct after almost 38 hours of aging (Figure 3.3f).

By a remarkable coincidence, we found that the unusual SAXS pattern displayed by IL-15 after 26 days of aging contained the same relative peak positions as those of a SAXS pattern obtained from SISO-3, following annealing at 140 ^{o}C for 1 day (Figure 3.3j). Although the scattering pattern from SISO-3 contains fewer high q domain reflections than that from IL-15, based on the relative peak positions and intensities at low q, we concluded these samples have the same microphase symmetry.

The SAXS pattern obtained from IL-15 after aging for 26 days at 25 ^{o}C (Figure 3.3i) was analyzed using the JADE software. Background scattering pattern was removed using a pattern modeled after the correlation hole scatting data (Figure 3.3), the scale of q axis was adjusted to be appropriate for the JADE software analysis, and spherical form factor was decoupled from the experimental SAXS pattern of IL-15 (see experimental section for details). Utilizing the peak positions of the corrected SAXS pattern, the JADE software calculations suggested several tetragonal symmetry with a very large unit cell dimensions: a = 431 Å, c = 228 Å. Based on the block copolymer composition (f_L = 0.22), the estimated density of PLA and PI, and assuming a spherical morphology with a sphere volume identical to that determined from the BCC result (i.e., after 3 hours at room temperature), the tetragonal unit cell contains 30 spheres. The unit cell dimensions of

SISO-3 were calculated by comparison of the relative diffraction peak position ratios between IL-15 and SISO-3: a = 777 Å and c = 411 Å.

For definitive assignment of a morphology (e.g., spheres) to these compounds, TEM microscopy work was conducted. Although IL-15 provided a well-resolved SAXS pattern, unfortunately it did not yield useful TEM micrographs due to the low molecular weight and reduced glass transitions temperatures of the PI and PLA blocks. Thus, mechanically robust SISO-3 was characterized.

Figure 3.4 presents representative TEM micrographs obtained from SISO-3, annealed in vacuum for 10 hours at 140 ^{o}C and then quenched in liquid nitrogen. In certain region of the microtomed slices (≈ 70 nm thick), regular arrays (up to 1 μm × 500 nm in area) of bright spots surrounded by black and gray-regions could be observed. This pattern shown in Figure 3.4 are clearly periodic, with translational order, and a two-dimensional unit cell illustrated by the parallelogram in Figure 3.4b. Careful examination of the higher magnification image reveals that the gray regions contain white spots that are also distributed in a regular manner throughout the specimen (marked by arrows in Figure 3.4b). These images can be interpreted as containing vertical stacks of spheres (brightest white spots containing PS and PEO) surrounded by dark annuli of PI (stained with osmium tetraoxide), with the remaining gray areas made up of PS and PEO spheres embedded in stained PI. Projection through the ≈ 70 nm thick specimen leads to

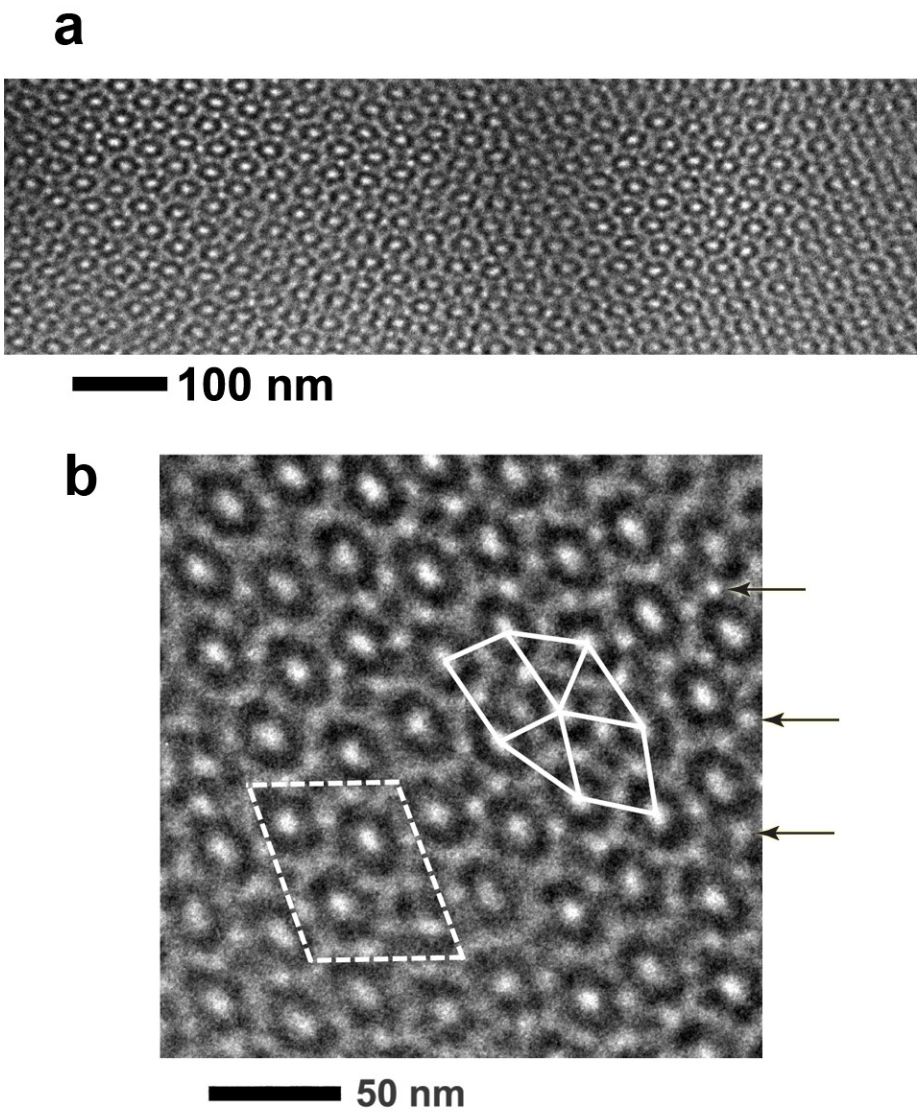

Figure 3.4 Representative SISO-3 TEM micrographs. (a) relatively large crystal grain of SISO-3. (b) Enlarged SISO-3 micrograph with a unit cell (dashed white line) and two dimensional $3^2 \cdot 4 \cdot 3 \cdot 4$ Archimedean tiling (solid white line) representations. SISO-3 was annealed at 140 ^{o}C for 10 hours, quenched in liquid nitrogen, and characterized.

these three levels of contrasts. Note that each sphere is roughly 14 nm in diameter as that the thick section spans several domain dimensions.

Based on the SAXS result, a tetragonal unit cell is anticipated for this specimen. The parallelogram stacked in Figure 3.4b is associated with the square $a \times a$ face of this unit cell, where the distortion is attributed to projection through a tilted crystal structure. Yet, closer examination of the TEM micrographs (Figure 3.4b) reveals the periodic placement of $3^2 \cdot 4 \cdot 3 \cdot 4$ Archimedean tiles (a sequence of 2 triangles, a square, a triangle, and a square), a very provocative piece of evidence indicating the unusual SAXS patterns of IL-15 and SISO-3 derive from a Frank-Kasper σ-phase.[133]

The Frank-Kasper σ-phase will be discussed in more detail in the following section (e.g., see Figure 3.6a for an illustration of the unit cell). For the purposes of the immediate analysis, we note that this crystal structure has a gigantic tetragonal unit cell with 30 spheres and 3 possible space group symmetries based on the reflection conditions: $P\bar{4}n2$, $P4_2nm$ $P4_2/mnm$.[107, 134] Following a general practice, the highest symmetry $P4_2/mnm$ was assigned to the symmetry of IL-15 at room temperature, and real space electron density maps were constructed using the Rietveld powder diffraction pattern simulation for $0.017 \leq q \leq 0.081$ Å^{-1} (see chapter 3.2 experimental section for details). The Rietveld powder pattern calculated with a single type of sphere (Argon) and using the 17 most intense experimental peaks showed excellent agreement with the experimental data except several peak intensities for $q \leq 0.04$ Å^{-1} with approximately 13 %

error (R) in intensity as shown in Figure 3.5c. From the result of this preliminary Rietveld analysis, the volume of a Wigner-Seitz cell was found different to each other and this difference was corrected by introducing 5 different atomic species to the Wyckoff positions to match scattering powers in further JADE analysis (see Table 3.2 for the atomic species and relative scattering power). The matched atomic species improved the degree of agreement of simulated pattern with the experimental data (approximately R = 10 % error in intensity), especially for the peak intensities for $q \leq 0.04$ Å^{-1} as shown in Figure 3.5b. Optimized Wyckoff positions, cell volumes and the experimental and calculated peak positions by the Rietveld pattern simulation are also listed in Table 3.2 and 3.3.

3.4 Discussion

The phase behavior of model diblock copolymer IL-15 and tetrablock terpolymer SISO-3 were investigated by SAXS and TEM studies. These samples showed identical SAXS patterns with a large number of Bragg peaks, suggesting a new block copolymer morphology. Computer analysis of this pattern revealed a tetragonal symmetry with a large unit cell size, containing approximately 30 spherical domains. TEM micrographs of SISO-3 revealed $3^2 \cdot 4 \cdot 3 \cdot 4$ Archimedean tiles, a characteristic tessellation feature of a Frank-Kasper σ-phase. With the $P4_2/mnm$ space group, the SAXS pattern of IL-15 was simulated using the Rietveld powder pattern refinement method and the calculated SAXS

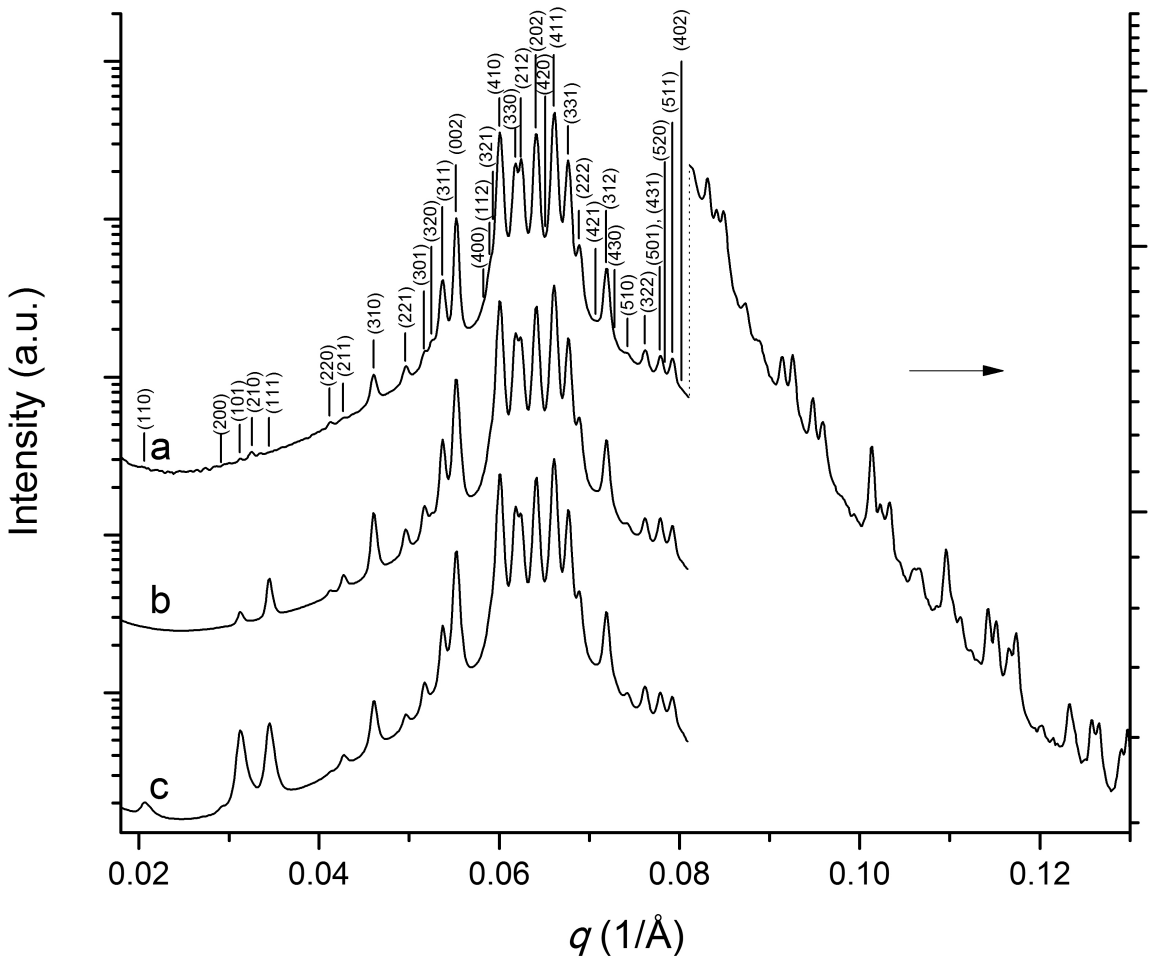

Figure 3.5 Rietveld analysis of the IL-15 power SAXS pattern (a) IL-15 synchrotron powder SAXS pattern after 26 days at 25 ^{o}C. The SAXS pattern in high q domain is enlarged for detailed representation (right). Allowed (hkl) reflections of $P4_2/mnm$ symmetry are noted. (b) Simulated Rietveld powder scattering pattern of IL-15 using different types of scatters to match scattering powers (R = 10.2 %). See text. (c) Simulated Rietveld powder pattern using a single type of scatter (R = 12.6 %).

Table 3.2 Wyckoff positions derived from the Rietveld analysis. Wyckoff positions are listed after multiplicity of scattering sites. On the right columns, the atomic species used for the Rietveld analysis and relative scattering powers are listed.

Wyckoff Position[a]	X	Y	Z	Relative Wigner-Seitz Cell Volume (%)	Atomic Species[b]	Relative Scattering Power[c] (%)
2b	0	0	0.5	91.0	Dysprosium	91.9
4f	0.104	0.104	0	106.5	Iridium	107.2
8j	0.319	0.319	0.745	100.9	Tantalum	101.7
8i	0.571	0.243	0	94.0	Erbium	94.7
8i'	0.371	0.031	0	104.2	Rhenium	104.5

[a]Number indicates multiplicity. [b]Atomic species used for the Rietveld analysis. [c]relative scattering power was calculated from the electron numbers of atomic species.

Table 3.3 Experimentally observed (q_{obs}) and calculated (q_{calc}, Rietveld refinement) peak positions based on the IL-15 SAXS pattern (26 days aged at room temperature) in $q <$ 0.08 Å^{-1}. The Miller indices (*hkl*) for $P4_2/mnm$ are identified.

q_{obs} (1/Å)	q_{calc} (1/Å)	(*h*	*k*	*l*)	q_{obs} (1/Å)	q_{calc} (1/Å)	(*h*	*K*	*l*)
-	0.0206	1	1	0	0.0618	0.0618	3	3	0
-	0.0291	2	0	0	0.0624	0.0624	2	0	2
0.0312	0.0312	1	0	1	0.0641	0.0641	2	1	2
0.0325	0.0326	2	1	0	-	0.0651	4	2	0
-	0.0344	1	1	1	0.0661	0.0661	4	1	1
0.0412	0.0412	2	2	0	0.0677	0.0677	3	3	1
0.0427	0.0427	2	1	1	0.0689	0.0689	2	2	2
0.0461	0.0461	3	1	0	-	0.0707	4	2	1
0.0496	0.0496	2	2	1	0.0719	0.0719	3	1	2
0.0518	0.0517	3	0	1	-	0.0728	4	3	0
0.0526	0.0525	3	2	0	0.0742	0.0743	5	1	0
0.0537	0.0537	3	1	1	0.0762	0.0762	3	2	2
0.0552	0.0552	0	0	2	0.0779	0.0779	5	0	1
-	0.0583	4	0	0	0.0779	0.0779	4	3	1
0.0591	0.0589	1	1	2	-	0.0784	5	2	0
-	0.0593	3	2	1	0.0792	0.0792	5	1	1
0.0601	0.0601	4	1	0	-	0.0803	4	0	2

pattern was in excellent agreement with the experimental data, corroborating that the SAXS patterns were produced by the Frank-Kasper σ-phase.

The σ-phase is constructed from huge tetragonal unit cells each containing 30 spheres. Figure 3.6a illustrates this unit cell showing the major part of this complex crystal structure formed by stacks of hexagonally coordinated antiprismic spheres along the c axis (solid blue line in Figure 3.6a). The c axis projection is presented in Figure 3.6b with the $3^2 \cdot 4 \cdot 3 \cdot 4$ tiling (right upper black solid lines) and tetragonal unit cell face (left bottom), consistent with the SISO-3 TEM micrograph (Figure 3.4b).

All condensed matter is formed from arrangements of atoms, molecules or mesoscale objects, and the specific organization of these elements dictate the physical properties of the resulting material. Simple hard spheres can be packed into face-centered cubic (FCC) or hexagonally packed (HCP) arrangements recognized as the most densely packed arrays.[135-138] These close packed crystal structures, along with body centered cubic (BCC) packing, account for almost all the crystalline states of the metallic elements. However, if multiple sphere sizes are allowed in a system, the packing problem becomes more complex, which is relevant to many practical systems such as metallic alloys. About 50 years ago, Frank and Kasper attempted to elucidate a wide range of other possible atomic packing symmetries for single (elemental) and multiple (alloys) sphere sizes. They considered various ways of assembling tetrahedrally close-packed (TCP) elements

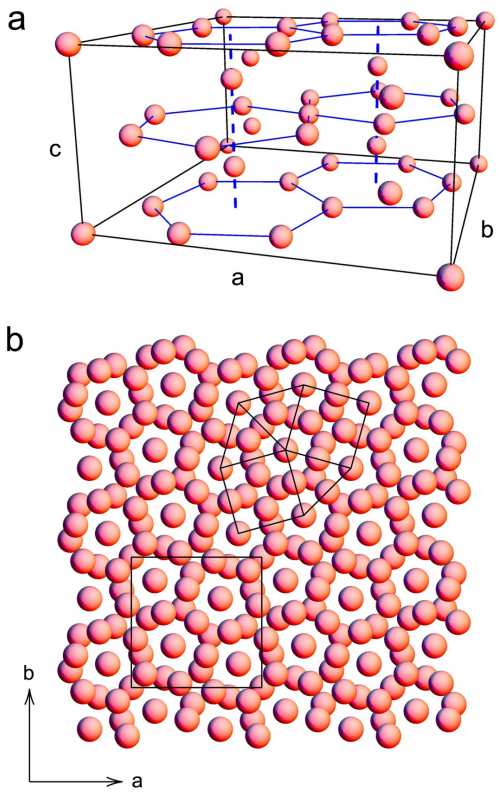

Figure 3.6 (a) Unit cell representation of the $P4_2/mnm$ symmetry based on the Rietveld refinement of the IL-15 SAXS powder pattern. Two sets of hexagonally coordinated antiprismic spheres (solid blue lines) in two parallel planes share a center sphere and the center spheres form the columnar sphere arrays along c axis (dashed blue lines). In a unit cell, two columnar sphere arrays exist as fused hexagonal antiprismic spheres. (b) Projection of the $P4_2/mnm$ symmetry along c axis. The 5-fold coordination of the dodecagonal element, $3^2 \cdot 4 \cdot 3 \cdot 4$ tiling (solid black line, top right) and the tetragonal face of unit cell (solid black line, bottom left) are sketched on this illustration as shown in Figure 3.4

together, resulting in a fascinating arrays of complex crystal structures, including the σ-phase.[133, 139]

Even before an accurate crystal structure of the σ-phase was identified, this morphology was well known in certain metal alloys, and was especially notorious in the stainless steel industry because it occurs along the bcc ferrite grain boundaries and embrittles certain steel alloys.[140-146] Surprisingly, the σ-phase also was found in two pure metallic elements, *β*-uranium and *β*-tantalum, rare examples of monoatomic σ-phase.[147, 148]

In soft material, Ungar *et al.* first reported the σ-phase in an undiluted wedge-shaped dendritic compound.[149-151] While it was observed along with other phases, including $Pm\bar{3}n$ (A15), BCC, and dodecagonal quasicrystal.[152] Interestingly, the σ-phase is known as a dodecagonal quasicrystal approximant and the close relationship between these periodic and aperiodic structures has been pointed out.[153] In simulation trials on a quenched monoatomic liquid system, Dzugutov first attempted to show stability of a dodecagonal quasicrystal in the mid 1990's, but later Roth argued that the σ-phase is the thermodynamic equilibrium state, not the dodecagonal quasicrystal.[154-156] Recently, Keys and Glotzer claimed that the dodecagonal quasicrystal phase emerges as a metastable phase during the formation of the equilibrium σ-phase.[157] They claimed that the dodecahedron quasicrystal emerges first in a supercooled monoatomic liquid system, rather than the real equilibrium σ-phase, because the high energy penalty caused by

supercooling (quenching) can be relaxed easily through the rapid formation of a dodecagonal quasicrystal, consisting of σ-phase motifs ($3^2 \cdot 4 \cdot 3 \cdot 4$ Archimedean tiles), and the metastable quasicrystal slowly transforms to the σ-phase.[157]

Remarkably, this theoretical interpretation is qualitatively consistent with the dendritic soft dodecagonal quasicrystal reported by Zeng *et al*.[152] On heating, the dendrons showed dodecagonal quasicrystal first, then transformed to the σ-phase in a very narrow temperature window (1 ^{o}C) and finally became the liquid (disordered) state. However, on cooling only a dodecagonal quasicrystal phase emerged.

In Leibler's seminal work published about 30 years ago,[2] he predicted that spherical domains formed by asymmetric diblock copolymer melts would order with BCC symmetry near the order-to-disorder transition (ODT) in weakly segregated regime.[158] This result which is now generally accepted is derived from the free energy space analysis based on the Landau theory, first proposed by Alexander and McTague.[13] Both groups also considered the possibility of dodecagonal order (which corresponds to icosahedral symmetry in reciprocal space) based on the Landau theory, but because the five-fold symmetry of dodecagonal order cannot form periodic structure with translational symmetry, they dismissed this option.

Discovery of quasicrystals just 4 years after Leibler's publication expanded the insight on the organization of materials,[159] and numerous aperiodic structures with heptagonal, octagonal, decagonal, dodecagonal and icosahedral order have been

documented in intermetallic systems as well as rare examples in soft materials.[150-153, 160-164] Compared to these intermetallic aperiodic structures, the dodecagonal quasicrystal is the only quasicrystal class found in soft material systems: undiluted dendrons and a blend of homo polystyrene and polyisoprene, polystyrene, and poly(2-vinylpyridine) star-shaped terpolymer.[150-152, 163, 164]

The ordered symmetry state of block copolymer microphases are a result of a delicate tradeoff between the enthalpic (*H*) and entropic (*S*) contributions that determine the system free energy at a given temperature and pressure.[17] Ordered microphases of block copolymers display the characteristic interfacial area Σ and interfacial tension $\gamma \sim \chi^{1/2}$ that governs the enthalpic contribution $H \sim \Sigma\gamma$. The other factor, the entropic contribution *S* is determined by the distribution of chain configurations of block copolymer chains that are tethered to the interface.

Based on the BCC and σ-phase cell sizes for IL-15 determined by SAXS at room temperature (Figure 3.3b and 3.5b), the average interfacial areas per unit volume of these morphologies were calculated (for σ-phase, the Wigner-Seitz cell volumes were also counted in this calculation. See Table 3.2) and the overall interfacial area of σ-phase is slightly smaller: $\langle\Sigma_\sigma\rangle / \Sigma_{BCC} = 0.99$, suggesting σ-phase has energetic benefit by lowering enthalpic contribution (smaller interfacial area) than that of BCC.

All the phases reported in diblock copolymers prior to this work (LAM, HEX, GYR, and BCC) contain only a single uniform domain or unit domain interface

configuration. In contrast, the σ-phase has 5 different domain types associated with ten 12-fold, sixteen 14-fold, and four 15-fold coordinated sites. Based on the Wyckoff positions obtained from the Rietveld simulation, the σ-phase unit cell can be divided into five distinct types of Wigner-Seitz polyhedra with volumes ranging from 91 % to 106 % of the average cell volume (Figure 3.7, see Mathematica code in Appendix B for the visualization and volume calculation of Wigner-Seitz cells). These five subdomains represent a compromise between the purely dodecahedron and truncated octahedron (BCC) arrangements anticipated by the Landau theory and possibly relieve some of the chain packing frustration (in nearly monodisperse block copolymer chains) created by those ordered state, i.e. broader distribution of chain packing length scales (this conjecture may not be valid for monodisperse chains).

Although IL-15 and SISO-3 have relatively narrow molecular weights and composition distributions, one might argue that polydispersity can alter the chain packing frustration and facilitate the formation of the σ-phase rather than BCC.[39] However, for the dendritic σ-phase, which incorporates relatively fewer dendrons per site (11.6), polydispersity is not likely a constituting factor, and by analogy is probably not a factor in block copolymer melts. However, we cannot rule out the possibility that the polymer chains are distributed asymmetrically among the different sites within the σ-phase unit cell by the effect of polydispersity. Obviously, the origin of σ-phase must be further elucidated with quantitative theory.

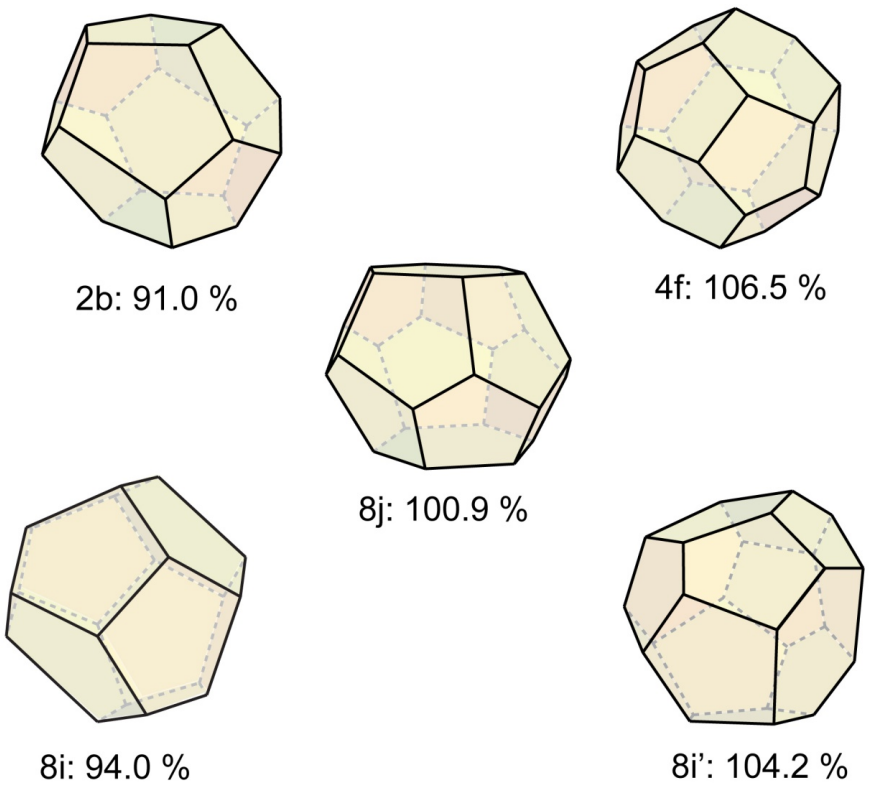

Figure 3.7 Wigner-Seitz cell representation derived based on the calculated Wyckoff positions using the Rietveld analysis of the IL-15 SAXS powder pattern. Site multiplicity, Wyckoff position, and relative unit volume to average cell volume are identified below each polygon illustration.

As Keys and Glotzer pointed out, dodecagonal quasicrystals emerge as a metastable state, slowly evolving to the equilibrium state σ-phase, and this anticipation is qualitatively consistent with the dendritic quasicrystal.[152, 157] In contrast, the time-resolved SAXS patterns of IL-15 obtained after rapidly cooling to 25 ^{o}C from the disordered state reveal that BCC phase occurs as a metastable state not the dodecagonal quasicrystal (Figure 3.3b). Possibly, this observation suggests that the occurrence of a metastable dodecagonal quasicrystal is dependent on the depth of quench or block copolymer melts might follow a qualitatively different energy potential governing microphase separated domains relative to the Dzugutov potential.[154, 165] Also, the slow (> 24 hour) transformation of the material from a state disorder to the σ-phase may involve both BCC and quasicrystalline transient states.

3.5 Conclusion

In the past four decades, the key parameters of block copolymer thermodynamics and kinetic aspects have been elucidated by numerous theoretical and experimental studies.[2, 19, 98, 117, 166, 167] The discovery of the σ-phase in single component block copolymer melts not only promotes our understanding on universality of how materials organize, but also offers new opportunities to practical applications. The number of spheres in a σ-phase unit cell is 15 times larger than the number of spheres in a unit cell of BCC. Thus, a judiciously designed block copolymer with appropriate block components and molecular weight will form a block copolymer σ-phase with gigantic

unit cell size, e.g. block copolymer with 100 kg/mol molecular weight will form a σ-phase with approximately 0.4 μm unit cell size, potentially suitable for photonic crystal applications (assuming the domain size of block copolymer crystal is proportional to the two-thirds power of block copolymer molecular weights).[168, 169]

Sol Gruner suspected that the phenomenological structural similarity may exist between different material classes.[170] The discovery of the σ-phase in block copolymer melts might suggest the possibility of Frank-Kasper TCP phases and quasicrystals in the other systems with different structural units. The chain packing frustration argument on block copolymers is possibly applicable to inorganic colloidal particles with tethered polymer brushes and surfactant.[171, 172]

I thank to Dr. Michael J. Bluemle for helpful discussion, fruitful collaboration, and material synthesis and also thank to Dr. Maria Torija for her help on JADE software analysis.

Chapter 4
Rheological Properties of Sphere-Forming Block Copolymer*

4.1 Introduction

The viscoelastic properties of block copolymer melts directly reflect the underlying microphase separated morphologies, and this has been the topic of a large number of investigations in the past 3 decades.[6, 11, 98, 100, 103, 104, 173] The rheological finger prints of block copolymer melts as a function of applied mechanical frequency ω, include the following characteristic behaviors of the dynamic shear storage modulus G' as a function of morphology: G' ~ $\omega^{1/2}$ for 1 dimensional lamella (LAM), G' ~ $\omega^{1/3}$ for 2 dimensional hexagonal cylinders (HEX), G' ~ ω^{0} for 3 dimensional gyroid (GYR) and body centered cubic phases (BCC), and G' ~ ω^{2} for the disordered state.

---

* Part of this work was published in 'Sangwoo Lee, Michael J. Bluemle, Frank S. Bates, *Science*, 2010, 330, 349'

These responses have been harnessed to aid in establishing the thermodynamic properties of block copolymers, i.e. the order-to-order transition temperatures (T_{OOT}) and the order-to-disorder transition temperatures (T_{ODT}).[3, 174] These two types of thermodynamic transitions have been characterized predominantly using isochronal G' temperature sweep experiments with slow temperature changes (~ 0.1 ^{o}C/min). Other experimental results obtained using small angle X-ray scattering (SAXS), transmission electron microscopy (TEM), and birefringence techniques have been used to identify the symmetry and microdomain morphology of block copolymer phases and additional thermodynamic characteristics.[34, 175-178]

In this chapter, rheological data obtained with sample, IL-15 which display the BCC and newly discovered σ-phase as reported in chapter 3, are presented. Various viscoelastic properties of the BCC and σ-phases formed in IL-15 are described.

4.2 Experimental

Material and Morphology Characterization Diblock copolymer IL-15, described in Chapter 3 was used in all the measurements described in this chapter. Characterization methods and other details about this material can be found in the experimental section of Chapter 3 and in Table 3.1

DMS Dynamic mechanical spectroscopy (DMS) measurements were performed in the shearing mode using a Rheometrics ARES dynamic mechanical spectrometer. Samples were loaded on 25 mm diameter parallel plates and temperature was controlled

by purging nitrogen gas to prevent oxidative degradation of the IL-15 specimen. Data were collected using three procedures: heating or cooling at a constant frequency, isothermal frequency sweeps (0.01 or $0.1 \leq \omega \leq 100$ rad/sec), and isothermal and isochronal measurements as a function of time. In all cases, a strain amplitude test within the linear viscoelastic regime (typical strain amplitudes were $\gamma \leq 10$ %) was applied.

4.3 Result and Analysis

In this section, rheological data along with additional SAXS results obtained from IL-15 in the ordered BCC and σ-phase states are presented. Based on the results shown in the SAXS and TEM data reported in Chapter 3, the existence of two distinct ordered states in specimen IL-15 between 0 ^{o}C and 50 ^{o}C were confirmed: a σ-phase at lower temperatures and BCC at higher temperatures. The rate of isothermal ordering was probed using the following procedures: a rapid (≈ 100 ^{o}C/min) jump from 120 ^{o}C to either 40 ^{o}C or 25 ^{o}C followed by monitoring G' (0.1 rad/s) as a function of time at constant temperature using a strain amplitude of 0.1 %.

Growth of G' (0.1 rad/s) following the temperature quench is nearly identical at both temperatures up to about 30 minutes (see Figure 4.1) after which a time independent value G' (0.1 rad/s) $\cong 10^5$ Pa is obtained at 40 ^{o}C. At 25 ^{o}C, G' (0.1 rad/s) slowly increases for up to a day after the initial 30 minutes rise, achieving a value of G' (0.1 rad/s) $\cong 10^5$ Pa after 22

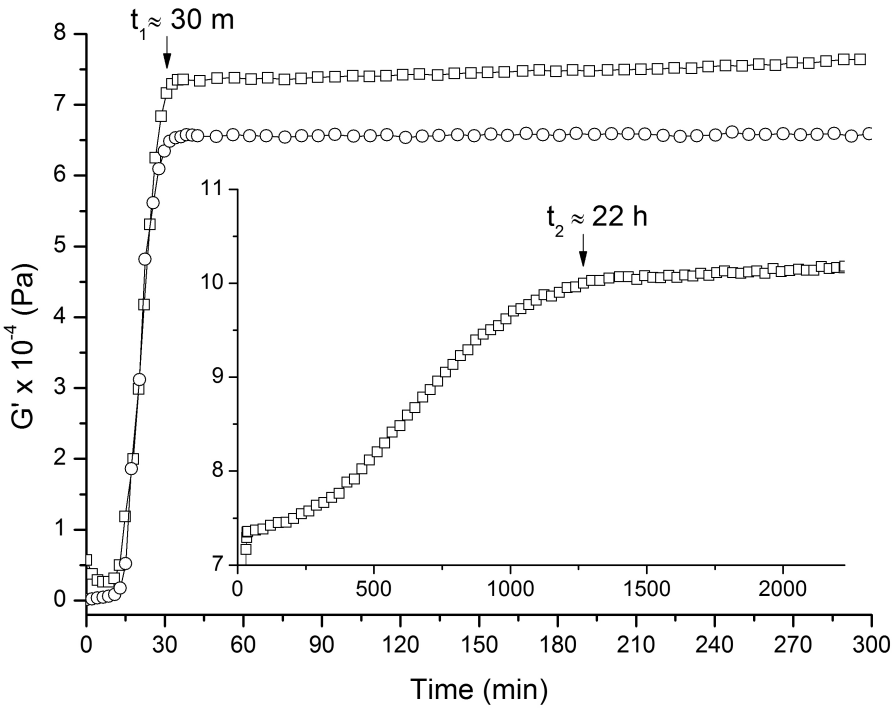

Figure 4.1 Linear (0.1 %) isothermal and isochronal (0.1 rad/s) dynamic shear storage modulus (G') measurements conducted with IL-15 after being quenched from 120 ^{o}C to 25 ^{o}C (□) or 40 ^{o}C (○).

hours. These isothermal experiments reinforce the conclusion that IL-15 contains two different ordered phases governed by very different nucleation and growth rates.

Figure 4.2 shows isochronal (ω = 0.1 or 0.5 rad/s) storage modulus (G') data acquired from IL-15 while cooling and heating at three different rates. Cooling experiments were initiated in the disordered state (> 50 ^{o}C) (or in certain cases in an ordered state at 35 ^{o}C) and ended at 0 ^{o}C (or in certain cases 15 ^{o}C). Cooling experiments were followed in all cases by heating experiments. As the material is cooled from T > T_{ODT}, G' (0.1 rad/s) increases by nearly five orders of magnitude reaching G' $\approx 5\times10^{4}$ Pa at 40 ^{o}C; additional cooling down to 0 ^{o}C elevates G' to 10^{5} Pa. The plateau in G' between 40 and 0 ^{o}C is associated with a state of order. Upon heating (0.1 ^{o}C/min), G' (0.1 rad/s) tracks the cooling result up to about 40 ^{o}C, then plummets between about 47 and 50 ^{o}C. This drop in G' is associated with the ODT, which is identified as $T_{ODT} = 50 \pm 1$ ^{o}C.

Increasing the cooling and heating rate significantly alters the G'(T) pattern documented at dT/dt = 0.1 ^{o}C/min. Upon cooling at 1 ^{o}C/min, G' (0.1 rad/s) rises in two distinct steps, first between 50 and 45 ^{o}C and then between 35 and 20 ^{o}C, again attaining a value G' (0.1 rad/s) $\cong 10^{5}$ Pa at 0 ^{o}C. During the subsequent 1 ^{o}C/min heating cycle, an order of magnitude drop in G' (0.1 rad/s) is recorded between about 15 and 27 ^{o}C; above this point the elastic modulus tracks the 0.1 ^{o}C/min result with disordering again signaled

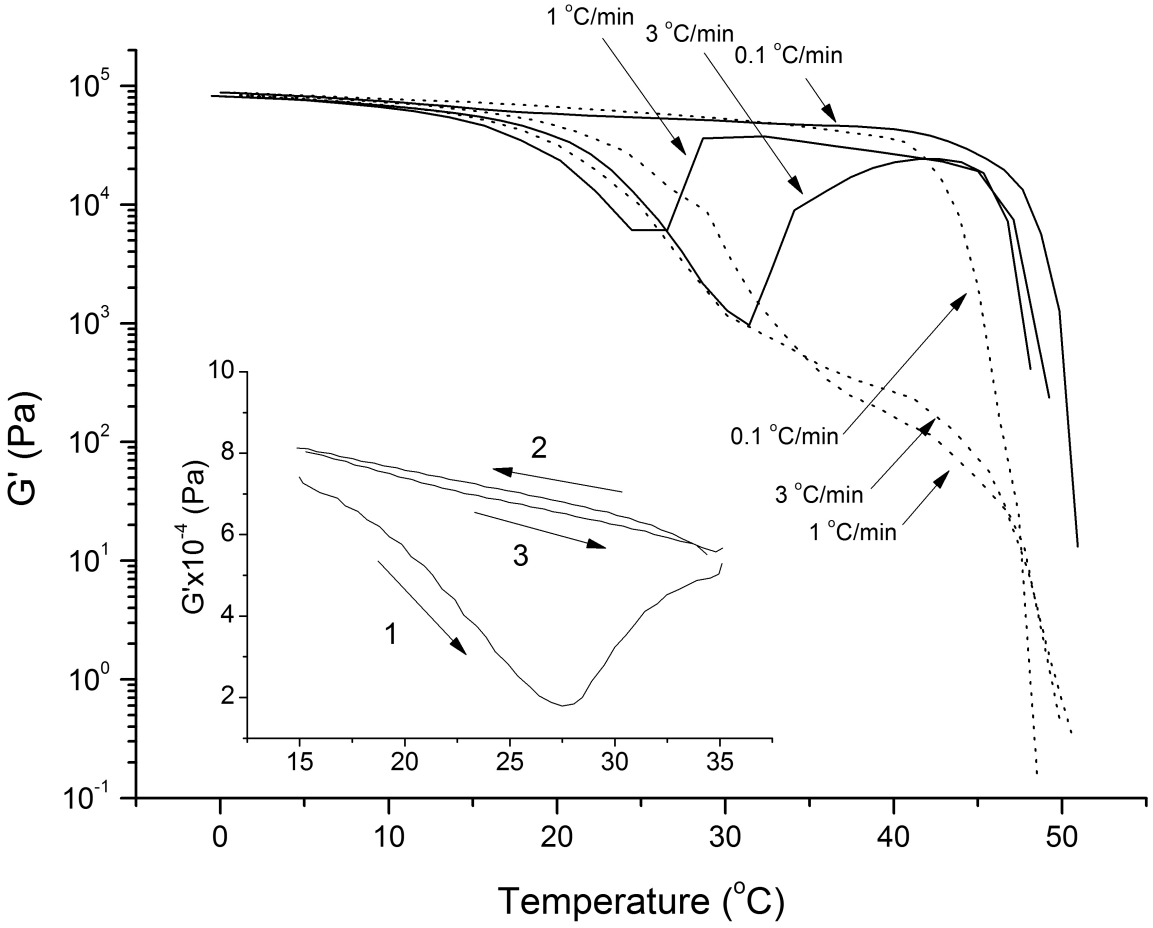

Figure 4.2 Isochronal temperature sweep dynamic shear storage moduli (G') of IL-15 at 5 % strain. Specimen was cooled down (dotted line) and then heated (solid line) at 0.1 °C/min and 0.1 rad/s; 1 °C/min and 0.1 rad/s; and 3 °C/min and 0.5 rad/s. Inset shows repeated isochronal (0.5 rad/s) temperature sweep G' measured at 1 °C/min and 3 % strain. The order of temperature sweep measurements are denoted by numbers. The precipitous G' drop vanished on the second heating cycle (3).

by an abrupt drop in elasticity above about 47 ^{o}C. Clearly, faster cooling leads to two states as evidenced by G'(T).

Yet, faster cooling and heating dT/dt = 3 ^{o}C, results in similar responses although the transition upon heating is displaced to slightly higher temperatures (20 to 35 ^{o}C); a higher frequency was employed for these experiments (ω = 0.5 rad/s) since the data acquisition time at the lower frequency was not compatible with the rate of temperature change.

In order to further access the two-state G'(T) pattern, a specimen was cooled from disorder to 15 ^{o}C at 1 ^{o}C/min, then heated to 35 ^{o}C, cooled to 15 ^{o}C, and reheated again to 35 ^{o}C, while recording G' (0.5 rad/s) with a modesty smaller 3 % strain amplitude (see inset to Figure 4.2). Remarkably, the drop and rise in G'(T) recorded during the first heat cycle is absent during the second heating cycle (after cooling to 15 ^{o}C from 35 ^{o}C). These results will be considered further in the discussion section.

Time-resolved isothermal frequency sweep experiments also were conducted at 40 ^{o}C and 25 ^{o}C. G' and G" were measured from high (100 rad/s) to low (0.1 or 0.01 rad/s) frequencies; these measurements took approximately 10 minutes for 100 - 0.1 rad/s and 80 minutes for 100 - 0.01 rad/s. Immediately following a quench to 40 ^{o}C, G' and G" showed terminal behavior (G' ~ ω^2 and G" ~ ω) between 10 to 1 rad/s as shown in Figure 4.3; this range corresponds to the first 2 minutes of measurement following the quench.

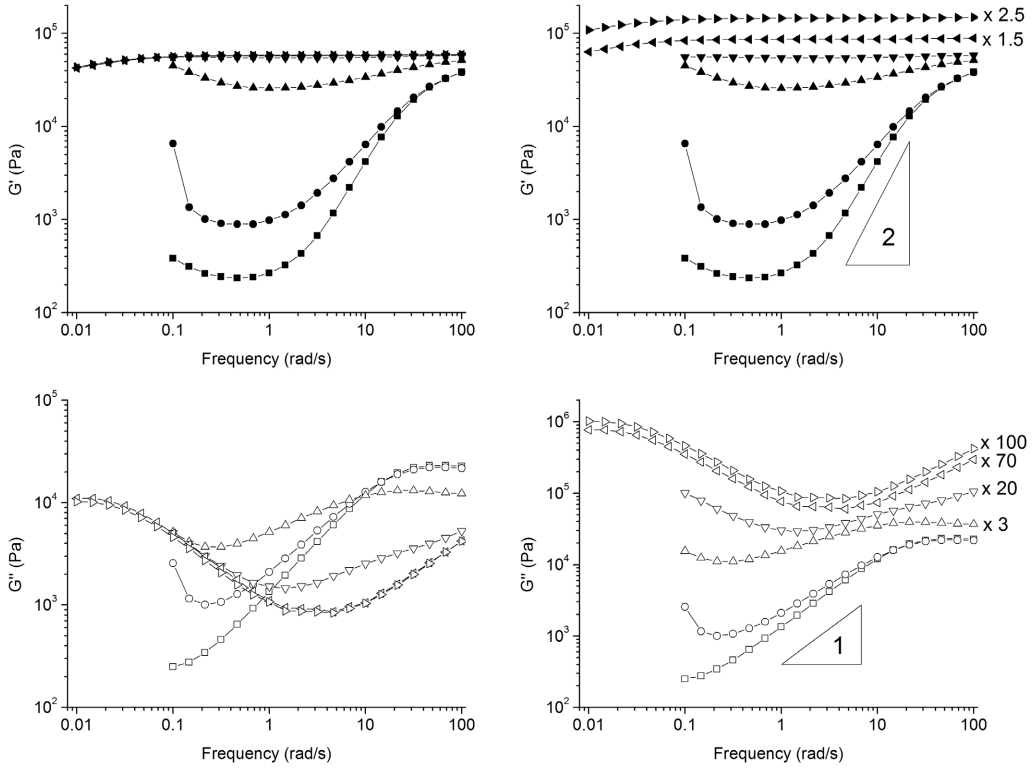

Figure 4.3 Time-resolved linear (0.5 %) and isothermal (40 ^{o}C) frequency sweep data of IL-15 (left panel). Shifted G' and G" data are shown in the right panel for clear representation. After quench to 40 ^{o}C, the dynamic frequency sweep data were obtained during the annealing period. The G' and G" are denoted by ■, □: right after quench; ●, ○: after 8 minutes; ▲,△: after 19 minutes; ▼,▽: after 28 minutes; ◄,◁: after 37 minutes; and ►,▷: after 5.3 hours, respectively. The indistinguishable dynamic shear moduli after 37 minutes and 5.3 hours annealing indicate that an ordered phase settled in 30 minutes, which is consistent with the constant G' at 40 ^{o}C after 30 minutes in Figure 4.1.

Both moduli increase at lower frequencies ($\omega < 1$ rad/s) during this initial sweep which was interpreted as ordering. During the following 30 minutes (t_1), G' increases and flattens with frequency and G" takes on a distinctive sinusoidal shape which stabilizes after 37 minutes. These final elastic and loss curves are typical of a triply periodic morphology.[104]

After quenching to 25 ^{o}C, IL-15 displayed a similar evolution although the overall patterns are shifted to higher frequencies, thus exposing less of the terminal response at the earliest times. However, in contrast to the moduli at 40 ^{o}C (Figure 4.1), at 25 ^{o}C the G' and G" were still changing up to 54 hours, and only appeared to stabilize thereafter.

In order to find the order-to-order transition temperature (T_{OOT}), a linear (0.5 %) isochronal (0.2 rad/s) temperature scan was conducted (Figure 4.5). First, IL-15 was quenched to 40 ^{o}C from the disordered state (120 ^{o}C), annealed for 2 hours, cooled down to 0 ^{o}C, and heated to 55 ^{o}C at a rate of 0.2 ^{o}C/min. On the cooling cycle, G' and G" showed a small, but noticeable change at 27 ^{o}C, indicating at transition from BCC to the σ-phase. However, during heating cycle, IL-15 did not show any sign of T_{OOT} until it disordered at 50 ^{o}C.

To study the phase transition from BCC to the σ-phase of IL-15, the BCC phase was evolved at 40 ^{o}C by annealing for 2 hours after being quenched from 120 ^{o}C, followed by aging at room temperature for 13 hours. This sample showed a mixed SAXS

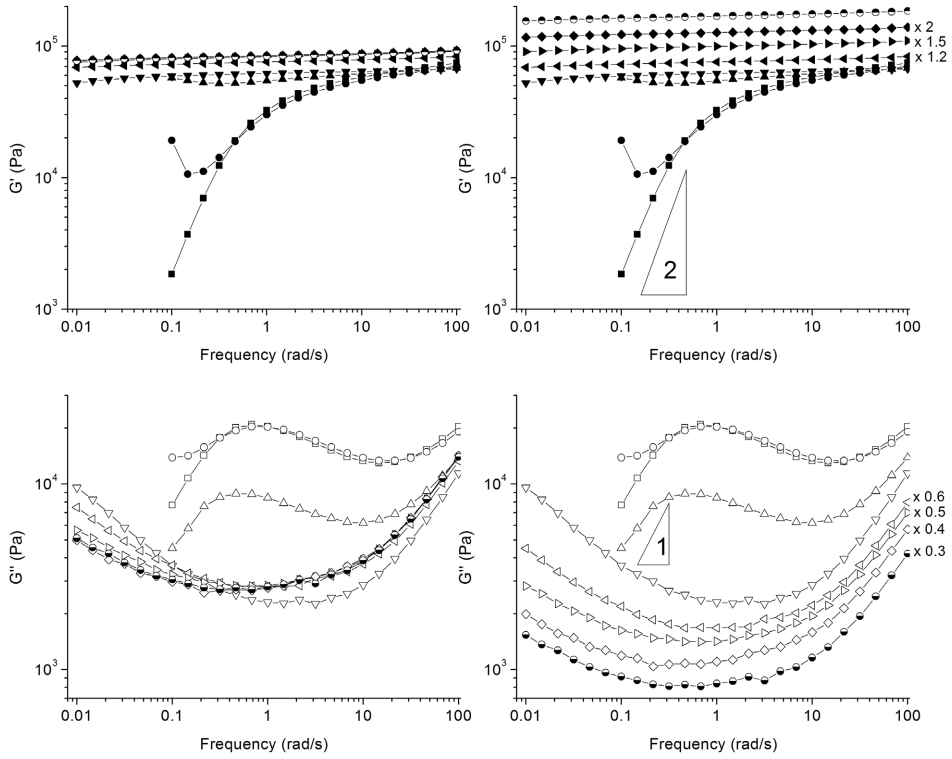

Figure 4.4 Time-resolved linear (0.5 %) and isothermal (25 ^{o}C) frequency sweep data of IL-15 (left panel). Shifted G' and G" data are shown in the right panel for clear representation. After IL-15 was quenched to 25 ^{o}C from 120 ^{o}C, frequency sweep data were obtained during aging. The G' and G" are denoted by ■, □: right after quench; ●, ○: after 10 minutes; ▲,△: after 20 minutes; ▼,▽: after 30 minutes; ◄,◁: after 12 hours; ►,▷: after 22 hours; ◆,◇: after 54 hours; and ◓,◒: after 68 hours, respectively. The G' and G'' spectra showed apparent shape changes for the first 30 minutes (t_1), and the change continued during next 22 hours annealing (t_2). After t_2, the spectra kept changing (see low frequency domains), but appeared equilibrated after 54 hours (◆,◇).

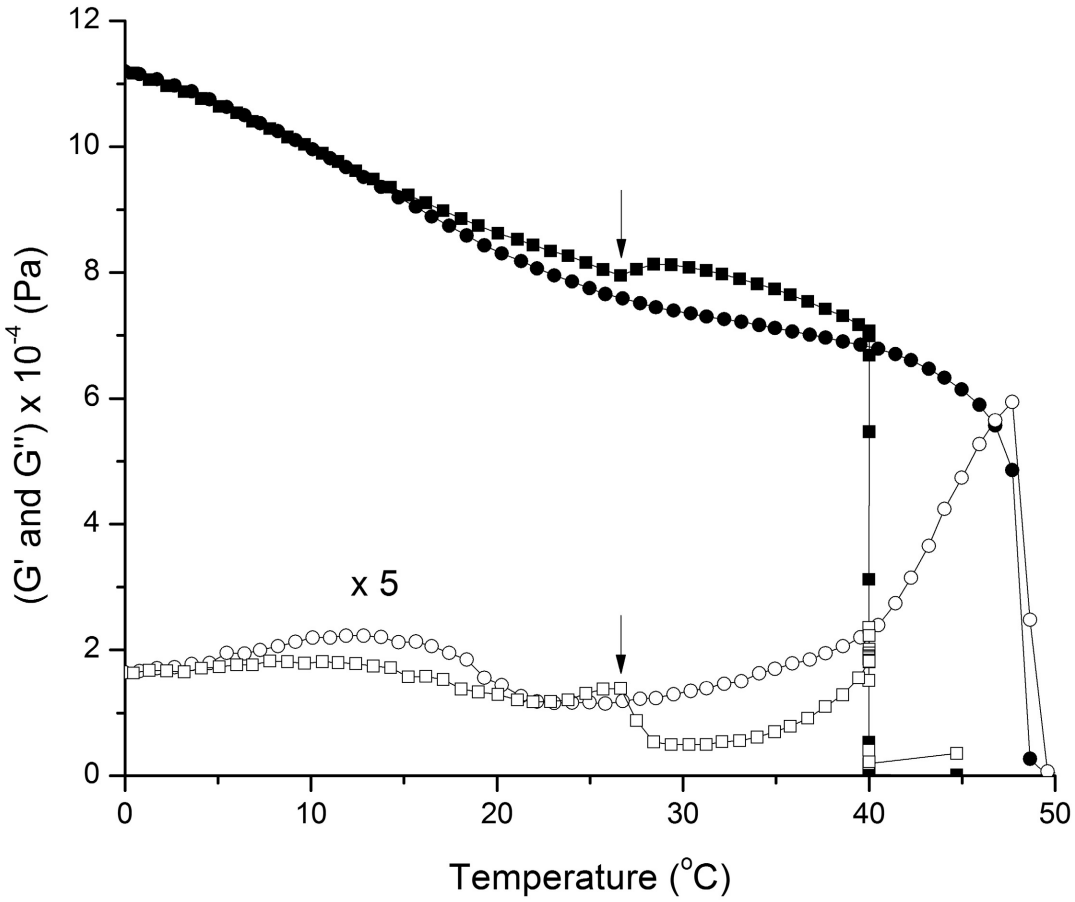

Figure 4.5 Linear (0.5 %) and isochronal (0.2 rad/s) dynamic temperature sweep data measured with IL-15 after quenched to 40 ^{o}C from 120 ^{o}C. The IL-15 specimen was annealed for 2 hours at 40 ^{o}C to evolve BCC phase, cooled to 0 ^{o}C (G': ■, G": □), and heated to 55 ^{o}C (G': ●, G":○) at 0.2 ^{o}C/min. Small decrease of G' and rise of G" at 27 ^{o}C on cooling cycle (marked by arrows) suggests the order-order transition temperature (T_{OOT}) from BCC phase to σ-phase. On heating cycle, the dynamic shear moduli did not show any signature of phase transition, consistent with the SAXS data shown in Figure 4.6. (see text)

pattern with BCC and σ-phase reflections (Figure 4.6a), which is similar to the SAXS pattern in Figure 3.3c.

The reverse phase transition, σ-phase to BCC, also was attempted. IL-15 was annealed for 24 hours at room temperature after being quenched from 120 ^{o}C and the characteristic σ-phase SAXS pattern was observed (Figure 4.6b). This sample was heated to 40 ^{o}C and annealed for 26 minutes without any noticeable change, followed by 3 minutes at 48 ^{o}C (Figure 4.6d), again without change. However, after 1 minute at 60 ^{o}C the Bragg scattering disappeared completely, leaving only a broad (correlation hole) peak, consistent with a state of disorder.

Because the σ-phase was shown to be stable at 40 ^{o}C at least for 26 minutes, it was possible to collect dynamic frequency shear moduli data for this structure at this temperature. Figure 4.7 shows the dynamic shear moduli of BCC phase at 40 ^{o}C after being annealed for 5.3 hours at 40 ^{o}C and for the σ-phase obtained right after being heated to 40 ^{o}C following 69 hours of annealing at 25 ^{o}C (both specimens were quenched from 120 ^{o}C before annealing). Although the G' and G'' of the σ-phase are larger than those for BCC, indicating a higher complex modulus $G_m = [(G')^2 + (G'')^2]^{1/2}$, no qualitative differences in G' and G'' between BCC and σ-phase were found. However, G''(ω) for the σ-phase is significantly larger at all frequencies. This trend is consistent with the interpretation of the transition at 27 ^{o}C in G'' during cooling in Figure 4.5.

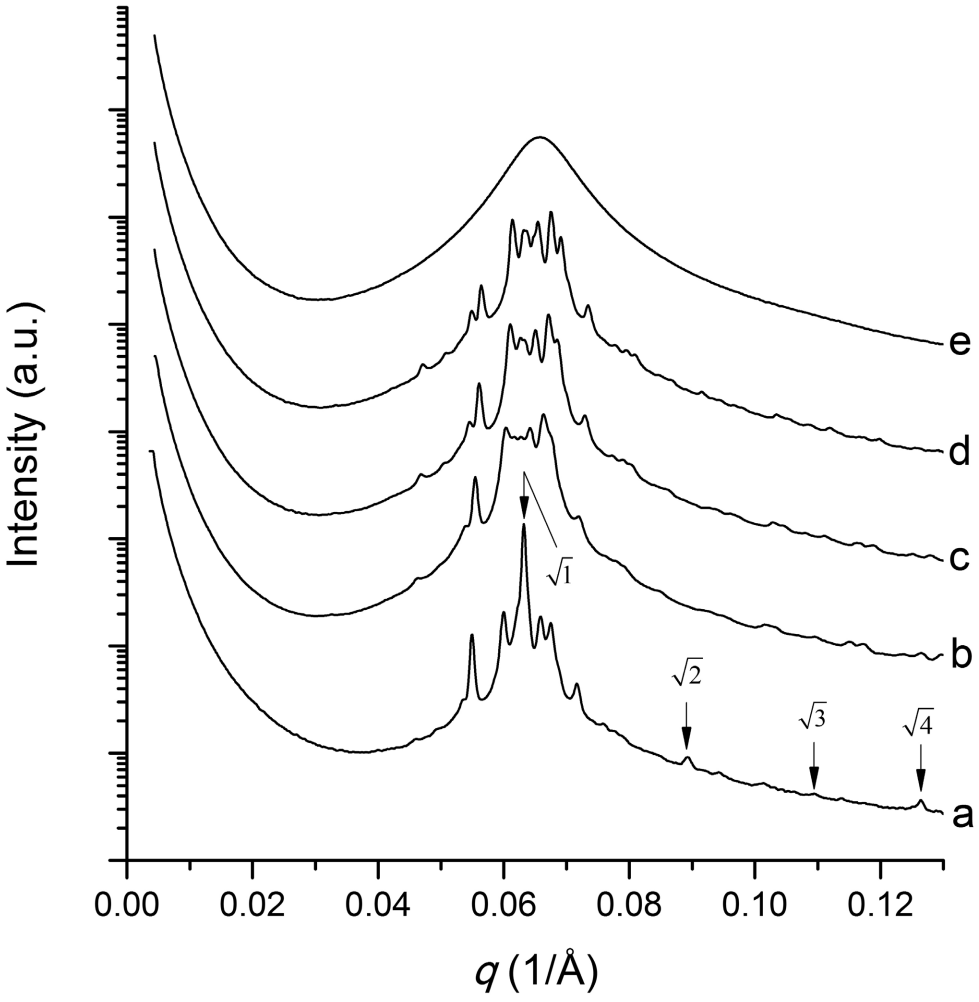

Figure 4.6 Synchrotron IL-15 SAXS powder patterns to study order-to-order phase transition. (a) IL-15 SAXS obtained at 25 ^{o}C after BCC phase evolved. The specimen was annealed at 40 ^{o}C for 2 hours after quenching from 120 ^{o}C, cooled to room temperature, and aged for 13 hours. To investigate σ-phase to BCC phase transition, IL-15 was annealed for 24 hours at room temperature after being quenched from 120 ^{o}C (b), heated to 40 ^{o}C for 26 minutes (c), heated further to 48 ^{o}C for 3 minutes (d), and finally to 60 ^{o}C for 1 minute (f).

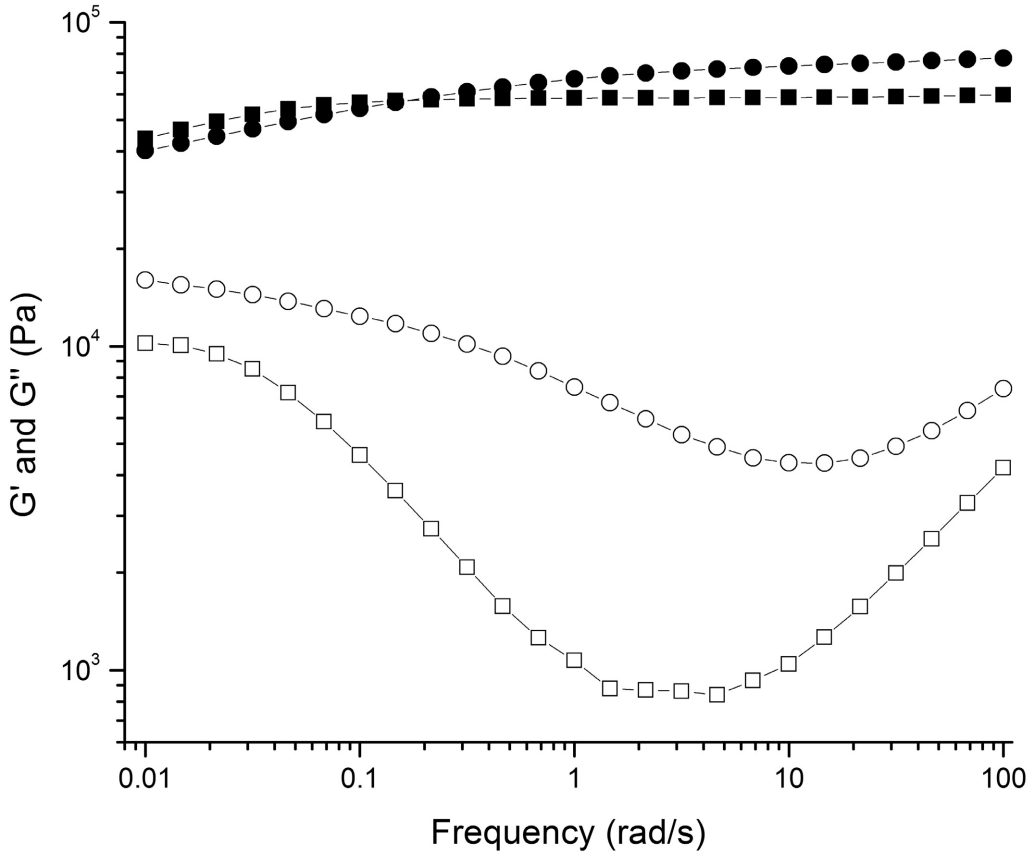

Figure 4.7 Isothermal (40 ^{o}C) frequency sweep spectra of IL-15 with BCC and σ-phase. The dynamic shear moduli of the BCC phase was obtained at 40 ^{o}C after 5.3 hours at 40 ^{o}C (G': ■, G'': □). To measure the dynamic moduli data of σ-phase at 40 ^{o}C (G': ●, G'': ○), IL-15 specimen aged at 25 ^{o}C for 69 hours was heated to 40 ^{o}C and immediately frequency sweep experiment was conducted.

3.4 Discussion

The rheological properties of model diblock copolymer IL-15 which form BCC and σ-phases was studied by DMS. Isochronal and isothermal dynamic shear and time-resolved frequency sweep measurements conducted at 40 ^{o}C indicate that quenched IL-15 orders on a BCC lattice from the disordered state in 30 minutes (t_1), consistent with the time-resolved SAXS (Figure 3.2) and frequency sweep (Figure 4.3) experiments.

At 25 ^{o}C, isochronal and isothermal time sweep experiments revealed that following a quench from disorder IL-15 passes through 3 distinct mechanical states. These states are also evident in the time resolved SAXS (Figure 3.3) and frequency sweep experiments (Figure 4.4), and can be interpreted as growth of a metastable BCC phase from the disordered state with subsequent transition, nucleation and growth of the σ-phase.

Fredrickson and Binder argued that ordering of symmetric block copolymers in the weakly segregated regime follows a homogeneous nucleation and growth mechanism.[167] However, this conjecture was not supported by experimental results obtained with nearly symmetric poly(ethylene-*alt*-propylene-*b*-ethyl-*alt*-ethylene) diblock copolymer as reported by Rosedale and Bates.[98] Later, Groot and co-workers studied the ordering process of diblock copolymers using a simulation method based on a coarse-grain model known as "dissipative particle dynamics."[179, 180] They concluded the ordering process of the lamellar phase occurs via spinodal decomposition whereas

hexagonally packed cylinders (and possibly other non-lamellar structures) follows a nucleation and growth mechanism. Their anticipation is consistent with other experimental studies at least for the ordering kinetics of asymmetric block copolymers, and nucleation and growth is widely accepted as the mechanism that controls ordering kinetics of microphase separated block copolymer morphologies.[181-187]

Rosedale and Bates suggested that the fraction of ordered polymer present $X(t)$ during the isothermal ordering process at time t can be correlated with G'(t):[98]

$$X(t) = \frac{G'(t) - G'_0}{G'_\infty - G'_0} \tag{4.1}$$

where G'_0 and G'_∞ are the initial and leveled off (asymptotic $t \to \infty$) dynamic storage moduli, respectively. Using the Avrami equation, G'(t) can be formulated as a function of time in terms of $X(t)$:

$$X(t) = 1 - \exp(-kt^n) \tag{4.2}$$

where k is a crystallization constant, and n is the Avrami exponent, related to the dimensionality of crystal growth, nucleation mode in crystal growth process, and other crystallization characteristics. Eqn (4.2) also can be rearranged for linear representation of n and logarithm t:

$$\ln\left(-\ln\left(1 - X(t)\right)\right) = n \ln t + \ln k \tag{4.3}$$

Using Eqn (4.3), the G' time sweep data of quenched IL-15 shown in Figure 4.1 was fitted to extract the Avrami exponent n. However, as Liu and co-workers pointed out, the

actual fractional crystallization at $t_0 = 0$ of a quenched block copolymer melt cannot be extracted from G'_0.[187] Therefore, the t_0 was considered to be an adjustable parameter and included in the fitting procedure. The initial BCC phase growing at 25 ^oC and 40 ^oC resulted in the Avrami exponent $n = 3.2 \pm 0.1$ and for the growth of the σ-phase at 25 ^oC from the metastable BCC phase, $n = 2.5 \pm 0.2$ was obtained (Figure 4.8). These excellent fitting results of the Avrami equation also indirectly support that the kinetic process governing the disorder-to-order and (metastable) order-to-order transitions of sphere forming block copolymer follows nucleation and growth mechanism. The exponent results indicate the ordered phases grow with the spherical geometry, and the nucleation modes are the simultaneous mode for ordering of the (metastable) BCC phase and the sporadic mode for the metastable BCC to the σ-phase.

The nucleation and growth kinetics of IL-15 ordered phases was also evidenced in the time-resolved SAXS patterns. Following a temperature to 40 ^oC (Figure 3.2), a principal reflection appeared at $q^* = 0.0648$ $Å^{-1}$ and intensified during the first 30 minutes of annealing (t_1). This peak emerged as a sharp reflection, clearly distinct from the correlation-hole scattering pattern, consistent with nucleation and growth of BCC crystals. The time scale for the growth and saturation of the BCC Bragg scattering is consistent with the isochronal isothermal frequency sweep data at 40 ^oC (Figure 4.1). The time-resolved SAXS patterns obtained during growth of the σ-phase at 25 ^oC (Figure 3.3) also suggest that the transition from the metastable BCC phase to σ-phase occurs via

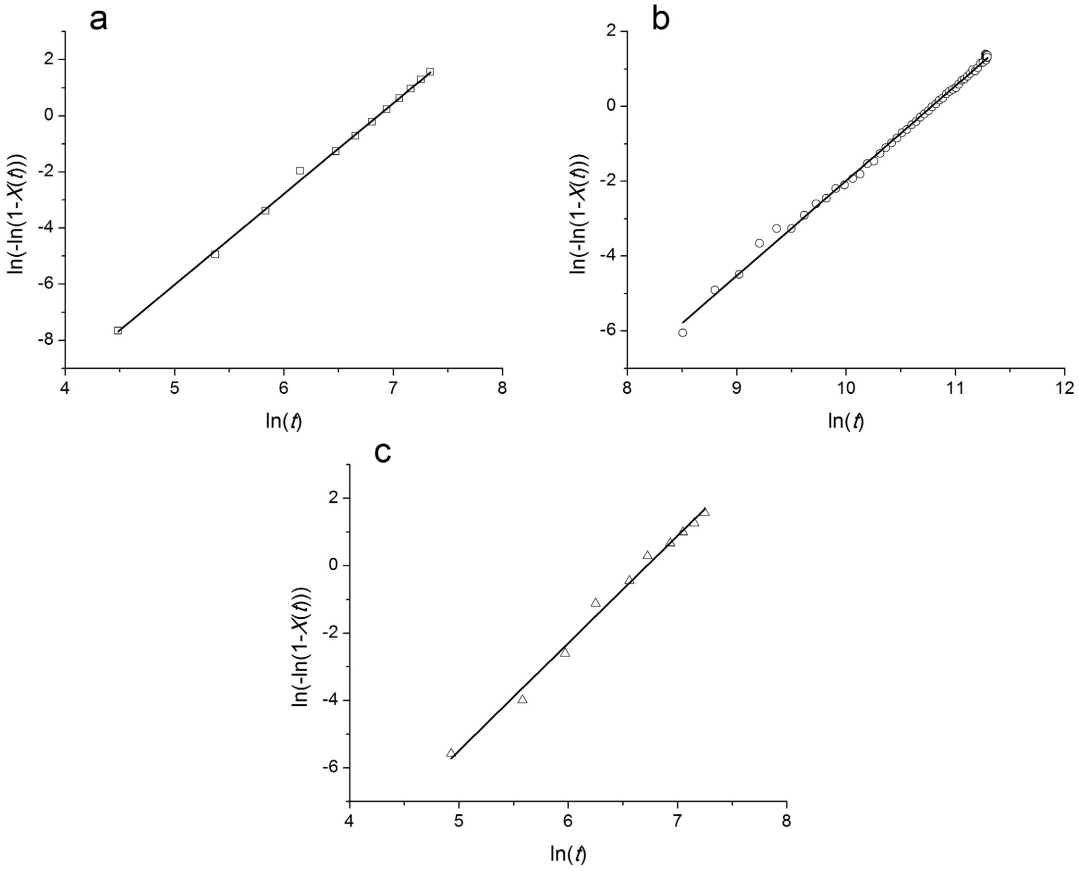

Figure 4.8 Avrami fits (solid line, —) with the isothermal isochronal dynamic shear G' time sweep data of IL-15 shown in Figure 4.1. (a) BCC phase growth during initial 30 minutes (t_1) after quenched to 25 ^{o}C. The Avrami exponent $n = 3.2 \pm 0.1$ was resulted. (b) σ-phase growth during following 22hours after t_1 at 25 ^{o}C. $n = 2.5 \pm 0.2$. (c) BCC phase growth after being quenched during initial 30 minutes (t_1) from 120 ^{o}C to 40 ^{o}C. $n = 3.2 \pm 0.2$.

nucleation and growth. Growth and intensification of sharp σ-phase reflections is accompanied by the attenuation of the BCC peaks with the overall process taking about 22 hours (Figure 4.1).

These time scales of nucleation and growth of ordered phases also agree with the time-resolved frequency sweep measurements (Figure 4.3 and 4.4). Right after IL-15 was quenched, G' and G" at 25 ^{o}C and 40 ^{o}C showed terminal behavior, consistent with a state of disorder.[187] With time, G' increased and became independent of frequency, indicating that IL-15 had solidified. This change first becomes evident in the low frequency data because the time scale of the high frequency measurement (taken first) is relatively short ($\sim 2\pi/\omega$) while the low frequency moduli take too longer to acquire.

Regarding the drop in G' observed with IL-15 near 25 ^{o}C (Figure 4.2), Yamaguchi *et al*. reported a similar G' response with sphere forming poly(styrene-*b*-1,4-isoprene) diblock copolymer near T_{ODT}.[188, 189] They claimed that this feature results from a slow ordering process due to the proximity of T_{ODT} to the glass transition temperature of the polystyrene blocks. However, this claim is questionable in the sense of overall complexity of the ordering kinetics of block copolymer. Theoretical and experimental evidence show that the speed of ordering from the disordered state follows a concave dependence on depth of quenching temperature, $\Delta T = T_{ODT} - T$. For shallow quenching, nucleation controls the rate of ordering while diffusion limitations dominate in deep quenching.[167, 187] These concepts are applicable to many types of phase separation

involving order (crystallization) including microstructure formation in metal alloys.[190] As Groot and co-workers argued, a quenched block copolymer solution forms a metastable microphase separated state, the one most immediately available to relax the large free energy penalty of the mixed but incompatible blocks.[179, 180] In the case of an asymmetric block copolymer, there is a considerable body of evidence that the metastable microphase separated state is an array of disordered microphase separated spheres, referred to as liquid-like packed (LLP) spheres.[189, 191-195] The viscoelastic fingerprint of LLP spheres as a function of frequency resembles the viscoelastic behavior of concentrated colloidal systems.[196, 197] Thus, when IL-15 was cooled down at a fast rate (1 ^{o}C and 3 ^{o}C), it is a reasonable conjecture that the specimen had insufficient time to transform into the BCC state. Instead, the spherical domains settled into the (metastable) LLP state, which requires no nucleation or growth events. Once cooled down to $T_g \cong 5$ ^{o}C, ordering will likely be exceedingly slow. On the following heating cycle, G' initially traces the cooling behavior up to about 26 ^{o}C (at 1 ^{o}C/min) when G' increases rapidly (ca 2 min.) up to a value associated with order. The temperature where this transition occurs is coincident with T_{ODT} for the BCC to σ-phase transition identified in Figure 4.5. Thus, we believe the G'(T) features recorded in Figure 4.2 obtained while cooling and heating at 1 and 3 ^{o}C/min originate from the combined effects of finite and temperature dependent ordering kinetics, correlated with competing states of order and metastable LLP on an order-order

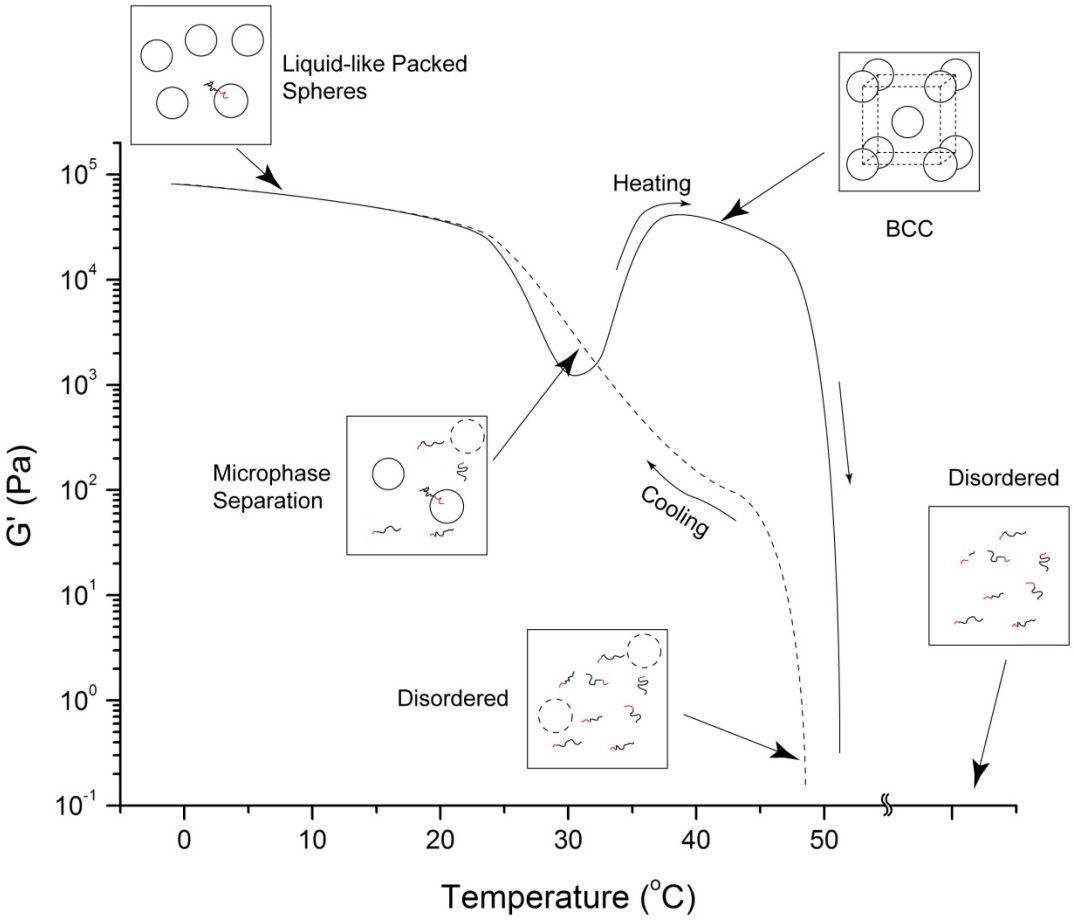

Figure 4.9 Schematic drawing of time-temperature dependent G' response with illustrations of possible microphase separation kinetics on rapid cooling (dashed line) followed by heating (solid line). See text for details.

transition. This time-temperature dependent G' response with the microphase separation kinetics is schematically described in Figure 4.9.

As presented in Figure 4.4 (annealed for 68 hours), G'(ω) and G"(ω) for the σ-phase resemble the viscoelastic patterns of the BCC (and gyroid) cubic phases; as noted earlier there are quantitative differences in G"(ω) between the σ and BCC phases. As Kossuth and co-workers illustrated,[104] the flat G' response is consistent with the linear elastic behavior of triply periodic crystals. This mechanical response is in contrast with the behavior of lamellar and hexagonal (cylinder) forming block copolymer which resemble liquid crystals, displaying elastic or viscous properties depending on direction of deformation.

Chapter 5
Phase Behavior of Poly(1,4-isoprene-*b*-DL-lactide) Diblock Copolymers

5.1 Introduction

Leibler predicted that AB diblock copolymer phase behavior depends on two parameters: the volume fraction *f* of block A and the combined parameter χN, which is the product of the Flory-Huggins interaction parameter χ and the degree of polymerization *N*.[2, 3, 93, 117, 125, 198] The block volume fraction *f*, which is determined by the degree of polymerization of each block (and to a lesser extent the repeat unit densities), primarily controls the geometry of the microphase separated structures, while χN dictates the strength of segregation between the blocks. For systems governed by van der Waals interactions, χ is proportional to the inverse of temperature: $\chi = \alpha / T + \beta$ where α and β are empirically determined constants and *T* is the temperature. Thus, heating a block copolymer melt reduces χN. Leibler showed that the transition from a state of disorder to

order occurs at $(\chi N)_{ODT} = 10.5$ for symmetric ($f = 1/2$) block copolymers. The magnitude of χ is determined by the chemical structure of the repeat units, which can be approximated by the associated solubility parameters δ_i: $\chi = V/RT(\delta_A - \delta_B)^2$ where V is the repeat unit molar volume and R is the gas constant.

In the past decade, polylactide (PLA), a biorenewable plastic, has been investigated as a potential substitute for petroleum based polymers. PLA is biodegradable, biocompatible, and has a practical glass transition and melt temperatures suitable for everyday commodities. Cyclic lactide monomers with two enantiomeric forms exist; L and D, which controls whether the polymer product is glassy (racemic mixture, Tg ≅ 60 ^{o}C) or semicrystalline (all L and D, T_m ≅ 180 ^{o}C). Moreover, crystal properties of PLA can be adjusted by mixing stereoisomers and this offers further adjustability to produce PLA products with targeted mechanical properties.[199-201]

Recently, there have been several reports on PLA-containing hybrid materials prepared with traditional petroleum based polymers such as polyisoprene (PI), poly(ethylene-alt-propylene) (PEP), 1,4-polybutadiene (PB).[99, 130, 202, 203] One of the most notable features of these materials is the high incompatibility between PLA (δ_{PLA} = 19.7 $J^{1/2}/cm^{3/2}$) and the aliphatic hydrocarbon based block components (δ_{PI} = 16.6, δ_{PEP} = 16.0, and δ_{PB} = 17.0 $J^{1/2}/cm^{3/2}$) reflecting large values of χ.[96, 99] This indicates that an ordered morphology can be prepared with low molecular weight block copolymer though a large χ parameter should be considered to obtain the disordered state: the order-disordered transition temperatures for moderate molecular weights are inaccessible in the practical

polymer processing temperature window (less than ~ 250 ^{o}C), i.e. $\chi N >> 10$ in that window.

In this chapter, we present experimental results obtained with PI-PLA diblock copolymers containing glass forming (racemic L and D) PLA blocks. These materials were prepared by combination of anionic and ring opening polymerization techniques. Small angle X-ray scattering (SAXS) and dynamic mechanical spectroscopy (DMS) measurements have been used to estimate $\chi(T)$ and the phase behavior for this system has been characterized near the order to disorder transition phase boundary.

5.2 Experimental

Materials and Material Characterizations a detailed synthesis scheme for the preparation of IL diblock copolymers is described in Chapter 2.[130] The molecular weights and compositions of the IL diblock copolymers were determined by ^{1}H nuclear magnetic resonance (NMR) experiments (Varian VI-500). The molecular weights of PI-OH precursors were calculated using the end-group analysis technique and the IL block compositions and molecular weights were calculated from the ratio of the integrated area of PI and PLA polymer block proton intensities. A more detailed discussion of this NMR characterization method is presented by Schmidt and Hillmyer.[130] Polydispersities of the IL diblock copolymers were measured by size exclusion chromatography (SEC) using chloroform as the mobile phase; the instrument was calibrated with polystyrene standards. Molecular characterization results are listed in Table 4.1

Table 5.1 Molecular characterization data for IL diblock copolymers.

Polymer	$M_{n,\mathrm{I}}$[a] (g/mol)	$M_{n,\mathrm{L}}$[a] (g/mol)	M_n[a] (g/mol)	f_{L}[b]	PDI	N[c]	$T_{g,\,PLA}$ (°C)
I-1	1,130	-		-	1.06	19	-
I-2	1,350	-		-	1.06	23	-
I-3	1,720	-		-	1.07	29	-
I-4	2,810	-		-	1.06	47	-
IL-1	1,130	1,620	2,750	0.51	1.12	39	20
IL-2	1,350	2,200	3,550	0.54	1.09	49	22
IL-3	1,720	2,810	4,530	0.54	1.09	63	29
IL-5	1,130	4,260	5,390	0.73	1.08	71	29
IL-6	1,130	3,140	4,270	0.67	1.08	57	28
IL-7	1,350	2,340	3,690	0.56	1.11	51	21
IL-8	1,350	3,030	4,380	0.62	1.13	59	35
IL-9	1,130	4,930	6,060	0.76	1.08	79	35
IL-10	1,720	2,360	4,080	0.50	1.11	57	24
IL-11	1,720	1,620	3,340	0.40	1.10	48	11
IL-12	2,810	1,190	4,000	0.23	1.11	62	5
IL-13	2,810	1,320	4,130	0.25	1.13	63	11
IL-14	2,810	1,770	4,580	0.31	1.15	69	15
IL-15	2,810	1,080	3,890	0.22	1.12	60	5
IL-16	2,810	2,220	5,030	0.36	1.04	74	32

[a]number averag molecular weight. [b]calculated volume fraction of PLA using bulk densities of PI (0.9 g/cm^3) and PLA (1.25 g/cm^3) at 25 °C with experimental error ± 0.01.[96, 131] [c]number averag degree of polymerization with the reference volume of $V_{\mathrm{ref}} = (V_{\mathrm{PI}}V_{\mathrm{PLA}})^{1/2} \approx 110$ Å^3 where V_{PI} and V_{PLA} are PI and PLA unit segment volumes at room temperature, respectively.

DSC A TA instrument Q1000 differential scanning calorimer (DSC) was used to measure the glass transition temperatures (T_g) of the PI and PLA blocks. Samples (~ 10 mg) were placed in aluminum hermetic pans, heated to 200 ^oC, cooled to -100 ^oC, and heated to 200 ^oC again at a rate of 10 ^oC/min. The T_g values were determined using the final heating results.

Several of the symmetric and nearly symmetric IL diblock copolymer produced DSC traces that showed distinct order to disorder and disorder to order phase transition peaks, and the on-set temperatures of these peaks were taken as T_{ODT}. This finding is considered in more detail in the results section (section 5.3).

SAXS the phase behavior of the IL diblock copolymers were characterized by small angle X-ray scattering experiments (SAXS) conducted at DND-CAT (beamline 5I-D) at the Advanced Photon Source (APS) located at the Argonne National Laboratory (Argonne, IL). The sample to detector distances employed for the experiments were 4.03 or 5.5 m and the X-ray wavelength was 0.729 Å. Scattering data was collected with a Mar area CCD detector, and azimuthally integrated to the one-dimensional form of intensity versus scattering momentum transfer vector, $q = 4\pi\lambda^{-1}\sin(\theta/2)$, where θ is the scattering angle . The sample temperature was controlled using a DSC chamber cooled with liquid nitrogen and maintained under a helium atmosphere; temperature changes were implemented at a rate of approximately 100 ^oC/min. The samples were held at target temperatures for 2 minutes before data collection unless otherwise specified.

DMS The order-disorder transition temperatures (T_{ODT}) and order-order transition temperature (T_{OOT}) of each IL diblock copolymer was measured using dynamic mechanical spectroscopy (DMS) experiments,[6] conducted with a Rheometrics ARES mechanical spectrometer. The IL diblock copolymers were loaded between 25 mm diameter parallel plates and cooled and heated at a temperature rate of 0.1 ^{o}C/min while conducting isochronal (0.1 rad/s) dynamic shear temperature sweep measurements. The T_{ODT}'s were obtained from the final heating step.

5.3 Result and Analysis

In this section, experimentally measured characterization data for the equilibrium phase behavior of IL diblock copolymers is presented and evaluated.

Order-disorder transition temperatures were determined for the symmetric or nearly symmetric IL diblock copolymers (IL-1, 2, 3, 7, and 10) by DMS during slow heating (0.1 ^{o}C/min) as shown in Figure 5.1a to e. The DSC thermograms obtained from these polymers, also shown in Figure 5.1, display first-order transition peaks (endotherms) at temperatures a few degree higher than the transition temperatures determined by DMS. These peaks displayed sizeable high-temperature tails that extended up to 30 – 50 ^{o}C above the onset of the endotherms during heating and made the peaks appear asymmetric in temperature.

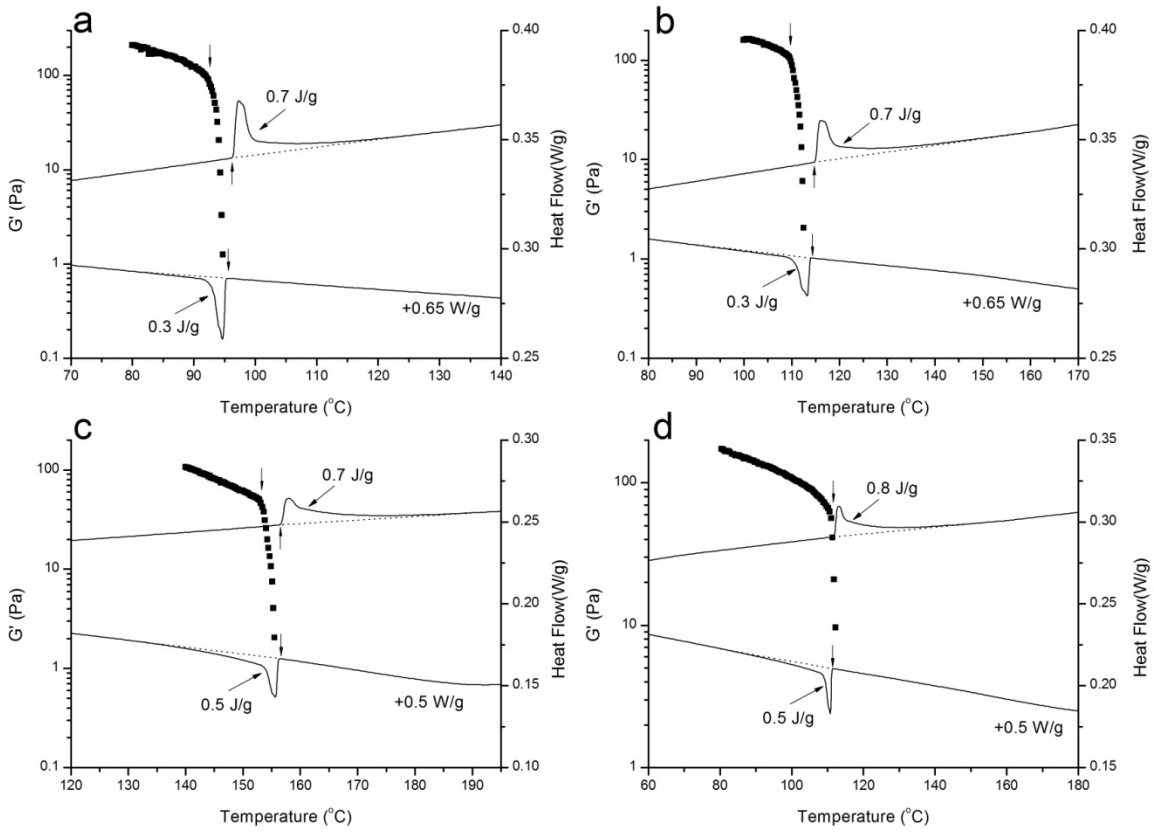

Figure 5.1 Isochronal (0.1 rad/s) dynamic shear storage modulus (G') and DSC thermograms obtained from (a) IL-1, (b) IL-2, (c) IL-3, (d) IL-7, (e) IL-10, and (f) IL-5 while heating at 0.1 (DMS) and 10 ^{o}C/min (DSC). Panels e to f are shown in the next page for clear representation. The temperature that showed a precipitous G' drop was regarded as the T_{ODT}. The slight temperature difference (< 4 ^{o}C) between the onset of the drop in G' and the start of the endotherm is attributed to the rate of nucleation of the first order phase transition.

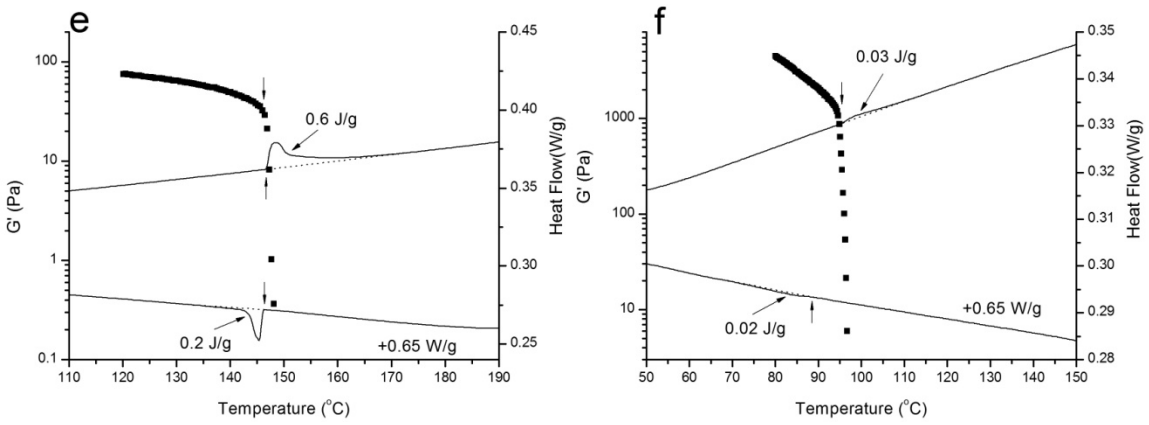

(Continued from the previous page)

These endotherms are also interpreted as evidence of the ODT although DSC-based onset temperatures are slightly (ca. 1 - 4 ^{o}C) higher than those determined by DMS. A more detailed examination of this thermal response with sample IL-2 reveals that the end points of these high-T tails are rate-independent and even reproducible on cooling curves at approximately ~ 10 ^{o}C lower temperatures. However, IL-5 (HEX morphology, see below) showed very small endothermic responses on heating and cooling DSC curves (Figure 5.1f). We return to these observations in the discussion section, and note here that the DMS results are accepted as the equilibrium values due to the much slower heating rate employed during the measurements (the slow heating rate employed in the DMS measurement could not be applicable to the DSC measurement due to a very low signal at this rate, i.e. DSC measures the rate of heat flow during change of temperature). Both values are listed in Table 5.2.

Table 5.2 Phase behavior of IL diblock copolymers.

Polymer	Phase and Phase Transition Temperature (^oC)[b]	q^* (1/Å) (Sample Temperature (^oC), Phase)[c]
IL-1[a]	LAM – 93(96) – DIS	0.0736 (50, LAM)
IL-2[a]	LAM – 110(114) – DIS	0.0699 (50, LAM)
IL-3[a]	LAM – 153(157) – DIS	0.0604 (50, LAM)
IL-5	HEX – 95(95) – DIS	0.0676 (90, HEX)
IL-6	LAM – 77 – DIS	0.0658 (50, LAM)
IL-7[a]	LAM – 111(112) – DIS	0.0685 (50, LAM)
IL-8	LAM – 110 – DIS	0.0615 (50, LAM)
IL-9	HEX – 97 – DIS	0.0590 (25, HEX)
IL-10[a]	LAM – 146(147) – DIS	0.0628 (50, LAM)
IL-11	LAM – 98 – DIS	0.0697 (50, LAM)
IL-12	HEX – 65 – DIS	0.0674 (50, HEX)
IL-13	HEX –105 – DIS	0.0605 (25, HEX)
IL-14	HEX – 130 – DIS	0.0595 (57, HEX)
IL-15	σ-Phase – 27 – BCC – 50 – DIS	0.0648 (40, BCC)
IL-16	HEX – 200 < DIS	0.0392 (200, HEX)

[a]polymers used for the χ_{IL} extraction. [b]$T_{ODT,DMS}$ and T_{OOT} were measured by DMS and $T_{ODT,DSC}$'s are marked in the parenthesis. [c]principal peak positions (q^*) on the SAXS patterns. The specimen temperatures and observed phases are marked in the parenthesis.

We have estimated $\chi_{IL}(T)$ with symmetric and nearly symmetric IL samples based on the mean-field theoretical result, $(\chi N)_{ODT} = 10.5$ and assuming $\chi_{IL} = \alpha / T + \beta$ at approximately constant composition $f_I \approx 0.5$. The results are plotted in Figure 5.2, where we define N based on a segment reference volume of 110 Å^3, the geometric average for PI and PLA. Within experimental uncertainty, these data are consistent with a linear form, yielding:

$$\chi_{IL}^{110} = \frac{(230 \pm 60)}{T} - (0.38 \pm 0.14) \quad (4.1)$$

The IL diblock copolymer ordered phases are identified by synchrotron SAXS experiments and representative SAXS patterns are presented in Figure 5.3. Four distinctive scattering patterns were identified, leading to for definitive phase assignments: σ (IL-15), BCC (IL-15), HEX (IL-5, 9, 12, 13, 14, and 16), and LAM (IL-1, 2, 3, 6, 7, 8, 10, and 11).

5.4 Discussion

PI and PLA are governed by a relatively large interaction parameter, significantly greater than that for most hydrocarbon based block copolymers.[204, 205] For example, with the common segment volume (110 Å^3) used in this work, polystyrene (PS) and PI are characterized at 140 °C by $\chi_{SI}(140\ ^oC) = 0.07$, compared to $\chi_{IL}(140\ ^oC) = 0.18$, i.e. approximately 2.5 times larger.[3] A bigger χ parameter dictates a smaller molecular weight at constant T_{ODT}, which leads to a stronger (less mean-field like) order-disorder transition.

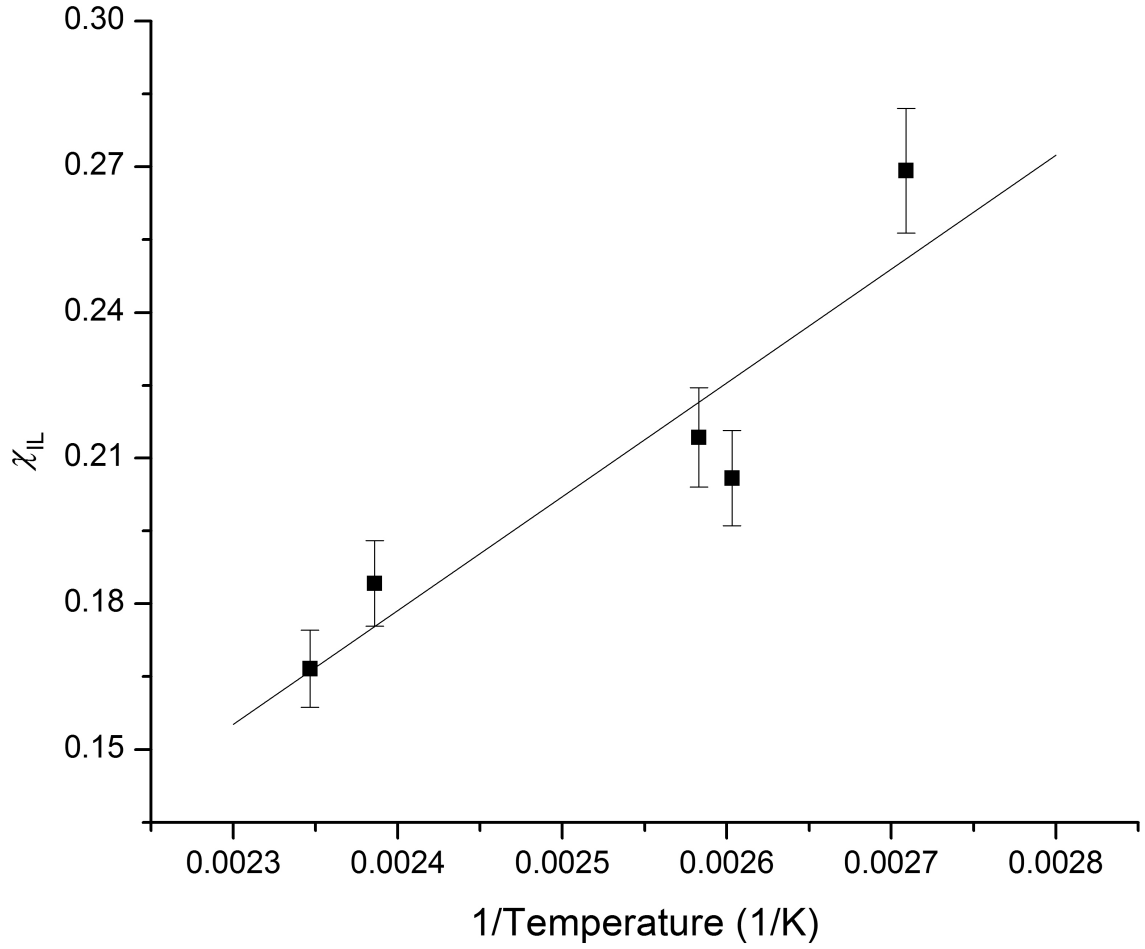

Figure 5.2 IL diblock copolymer interaction parameter χ_{IL} as a function of temperature *T*. The values of χ_{IL} were calculated based on the mean field order-disorder criterion, $(\chi N)_{ODT} = 10.5$. The T_{ODT}'s of IL-1, 2, 3, 7, and 10 were determined using DMS.

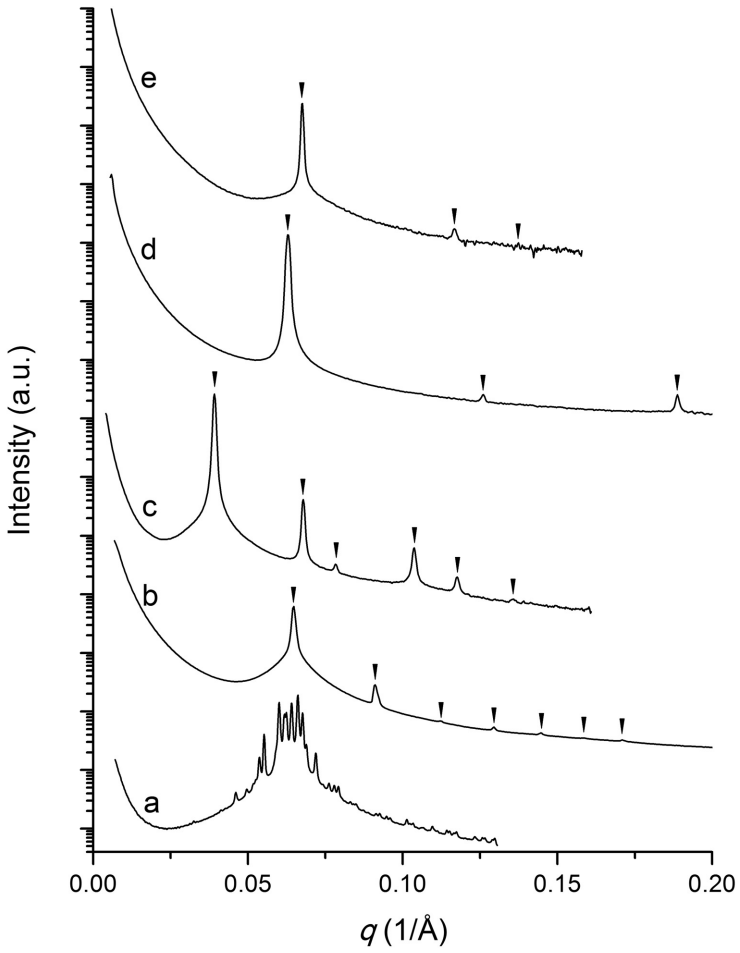

Figure 5.3 Synchrotron SAXS patterns obtained from the IL diblock copolymers. (a) σ-phase identified with IL-15 (f_L = 0.22) at room temperature after 26 days aging. (see chapter 3) (b) BCC phase identified with IL-15 (f_L = 0.22) after 30 minutes annealing at 40 ^oC. The relative peak positions of BCC phase, q/q^* = √1, √2, √3, √4, √5, √6, √7 are marked by inverse triangles where $q^*$is the primary peak. (c) HEX phase identified with IL-16 (f_L = 0.36) at 200 ^oC with q/q^* = √1, √3, √4, √7, √9, √12. (d) LAM phase identified with IL-10 (f_L = 0.50) at 50 ^oC with q/q^* = √1, √4, √9 (e) HEX phase identified with IL-5 (f_L = 0.73) at 90 ^oC with q/q^* = √1, √3, √4.

A striking consequence of this effect is the observation of the ODT by DSC (Figure 5.1). Thermal signatures of the ODT with enthalpy (heat) of transitions ΔH_{ODT} around 0.1 – 3 J/g have been reported in a number of publications.[7-9, 206-208] The ΔH_{ODT} of IL samples are also comparable to the range of the previous reports (because ΔH_{ODT} is dependent on a sample history, direct comparison between ΔH_{ODT} is not reasonable), but the IL samples showed more distinctive features than the thermal responses at the ODT with moderate molecular weight block copolymers.

For a block copolymer with a finite molecular weight, the order-disorder transition is known to be weakly first order, which produces an order-disorder transition driven by fluctuation effects in the vicinity of T_{ODT}.[2, 4-6] Closer examination of the endothermic DSC peaks in Figure 5.1 reveals thermal features persistent up to 30 to 50 ^{o}C above the T_{ODT} disordering temperature and the terminal point of this thermal features is nearly independent on the heating and cooling rates (Figure 5.4). We associate these smoothly decaying endotherms with composition fluctuations. Consistent with theory, the magnitude of this effect is greatest for the lowest molecular weight specimens. Thus, the long thermal tails observed for $T > T_{ODT}$ reflect a significant degree of block segregation which only reaches a state of homogeneous mixing well above T_{ODT}. To the best of our knowledge this represents the first direct thermal documentation of fluctuations in block copolymer melts.

The apparent overall enthalpy of transition (ΔH_{ODT}) obtained from IL-2 varied depending on the heating rate of the DSC measurements (1 J/g at 20 ^{o}C/min, 0.7 J/g at 10

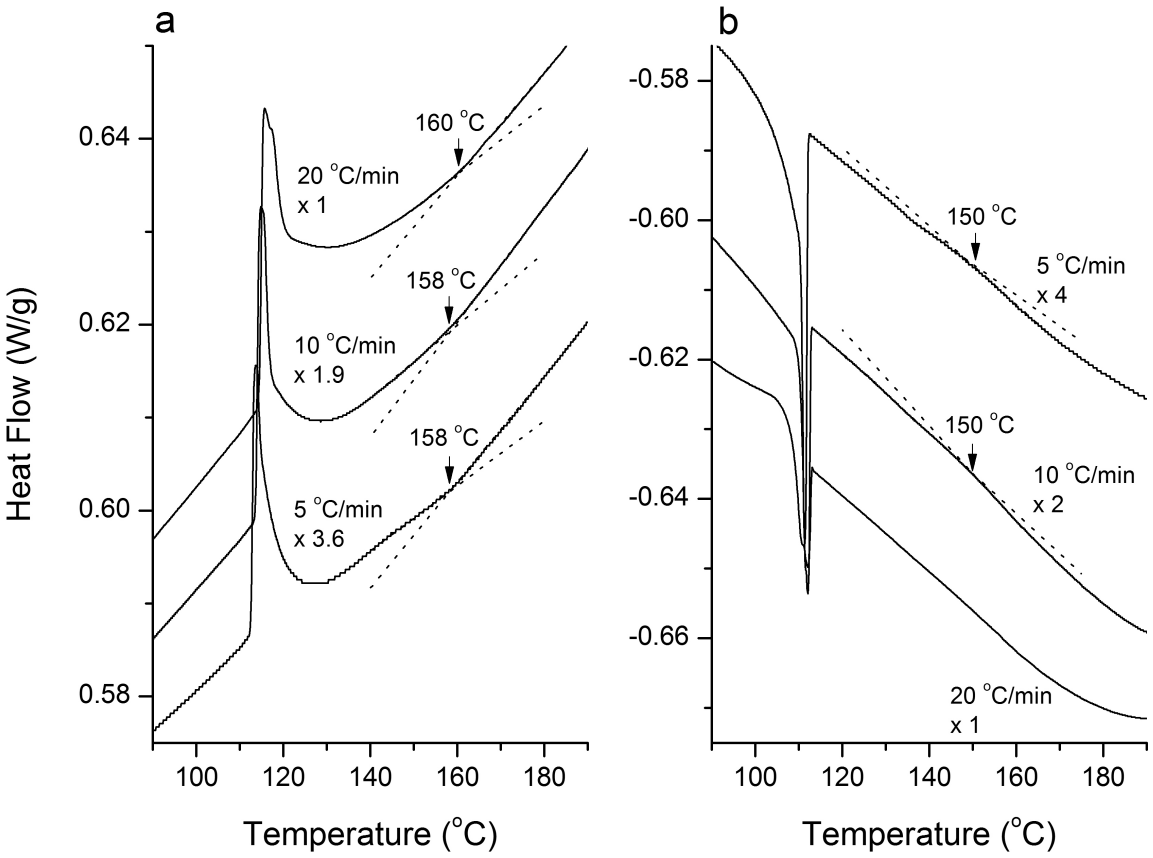

Figure 5.4 IL-2 DSC thermograms on (a) heating and (b) cooling cycles at different rates. Closer examination on heating and cooling curves reveals distinctive temperature points that show inflections of heating capacity C_p over temperature (see cross points of extrapolated dash lines). The apparent overall enthalpy of transition (ΔH_{ODT}) varied depending on the heating rate: 1 J/g at 20 °C/min, 0.7 J/g at 10 °C/min, and 0.4 J/g at 5 °C/min.

^{o}C/min, and 0.4 J/g at 5 ^{o}C/min. See Figure 5.4). The ΔH_{ODT} is proportional to the heating rate and appears to be related to a enthalpy overshoot (superheating).

In determining $\chi_{IL}(T)$, the order to disorder transition phase boundary of the symmetric and nearly symmetric IL diblock copolymers was assumed to conform with mean field theory, i.e. the order to disorder transition was assumed to occur at $(\chi N)_{ODT} = 10.5$.[2, 19] Clearly, this is not strictly valid as evidenced by the non-ideal fluctuation effects evident in the DSC data. Fluctuations suppress T_{ODT}, hence the absolute $(\chi N)_{ODT}$ values for the IL diblock copolymers must be somewhat higher than those determined based on mean-field theory. Because amplitude of fluctuation is inversely proportional to temperature and composition fluctuations in the disordered state represent a degree of microphase separation prior to ordering, the ordering transition produces relatively strongly segregated microphase structures.[2, 5, 6]

In the strongly segregated regime, the density profile of microphase separated block copolymer approaches a box function, compared to the sinusoidal form in the weakly segregated regime, i.e. the segregated domains becomes purer and the domain interfaces thinner.[17] The domain sizes of the IL diblock copolymers are around 5 nm, which is considerably smaller than the typical domain sizes for hydrocarbon block copolymers, $d > 20$ nm.[3, 204] Thus, strongly incompatible block components such as PI and PLA are useful for the fabrication of self-assembled morphologies and structures with small nanometer scale dimensions.

The IL diblock phase diagram constructed using Eqn (4.1) is presented in Figure 5.5. Compared to the ideal theoretical phase diagram (assuming a conformationally symmetric system with perfect monodispersity of chain length), the order-order phase boundaries are shifted toward higher PLA compositions.[2, 19] For a minority of PLA, the HEX-LAM phase boundary is located at $f_{L,(HEX\text{-}LAM)} = 0.38 \pm 0.02$ while at higher PLA content, $f_{L,(HEX\text{-}LAM)} = 0.70 \pm 0.02$; in the strong segregation limit for AB diblock copolymer, theory anticipates $f_A \cong 0.32$ and 0.68, respectively.[19, 209]

Asymmetrically placed phase boundaries can be attributed to differences in block polydispersities and conformational asymmetry.[93, 124, 125, 198] Although the polydispersities of the PLA blocks are only slightly higher than those of the PI counterparts (this is evidenced by somewhat larger IL diblock copolymer polydispersities compared to the PI values. see tabel 5.1), we do not believe the modest shifts in the IL phase diagram can be attributed to these minor differences. Most likely, the locations of the phase boundaries reflect conformational asymmetry between PI and PLA: the ratio of statistical segment lengths b at a common reference volume at 140 ^{o}C is $a_{PLA}/a_{PI} = 1.5$.[210, 211]

Several experimental studies of diblock copolymer phase behavior have correlated a shift of the phase boundaries toward higher fractions of the blocks with the larger statistical segment length. Table 5.3 summarizes the composition windows where LAM phases have been reported in the literature, which are consistent with the current finding and supported by self-consistent mean-field theory (SCFT).[198]

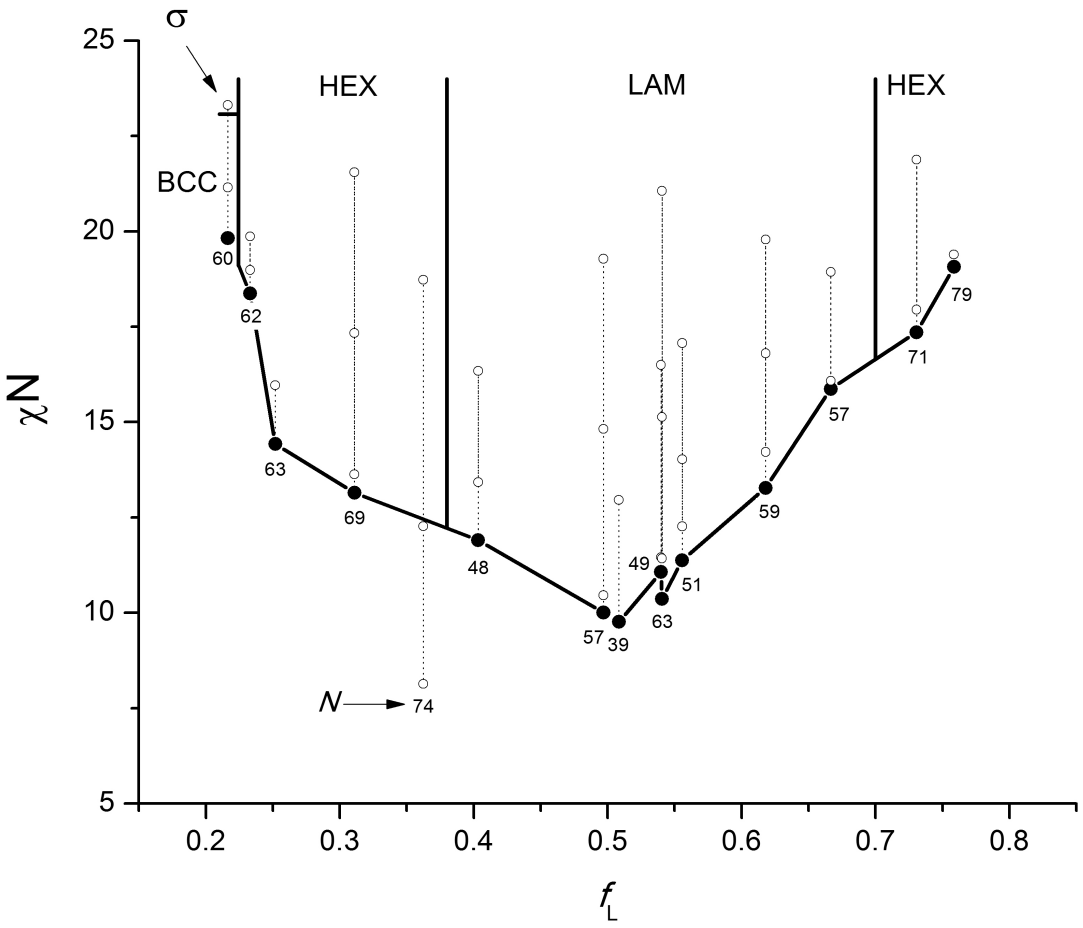

Figure 5.5 Experimental phase diagram constructed with IL diblock copolymers. The phase space points examined by SAXS are marked by white dots (○) and ODT [$(\chi N)_{ODT}$] identified by rheology is marked by black dots (●). Below or near the $(\chi N)_{ODT}$ points, degrees of polymerization N is identified. Data points obtained from each sample are connected with dashed lines (···) and the interpolated phase boundaries are marked by solid lines (–).

Table 5.3 Lamellar phase windows summarized from selected diblock copolymers with different conformational asymmetry.

Block 1	Block 2	a_1/a_2[a]	Lamellar Window (f_1)	χN[b]	Reference
polystyrene	poly(2-vinylpyridine)	1.0	0.40 – 0.63	20	[176]
polystyrene	1,4-polyisoprene	1.1	0.40 – 0.65	30	[3]
poly(ethylene oxide)	poly(oxybutylene)	1.3	0.46 – 0.74	30	[212]
poly(ethylene oxide)	1,4-polyisoprene	1.3	0.36 – 0.85	75	[213]
poly(DL-lactide)	poly(ethylene-*alt*-propylene)	1.4	0.32 – 0.78	30	[99]
poly(DL-lactide)	polystyrene	1.4	0.44 – N/A[c]	-	[202]
poly(DL-lactide)	1,4-polyisoprene	1.5	0.38 – 0.70	15	This Work

[a] statistical segment lengths at 140 ^{o}C were used for the a_1/a_2 calculation.[211]

[b] Nominal χN where LAM phase window is estimated on the reported phase diagram.

[c] Experimental data is not available.

The experimental IL phase diagram (Figure 5.5) exhibits several unusual features. IL-16 ($f_L = 0.36$ and $N = 74$) produced clean evidence of an ordered HEX phase well below the order-disorder phase boundary interpolated from neighboring samples (IL-14 and IL-11) and did not show any signature of an order-disorder transition by DMS up to 250 ^oC (while heating at 3 ^oC/min). IL-16 has a PLA block just 5 lactide repeat units longer on average than IL-14 ($f_L = 0.31$, $N = 69$). These compounds were polymerized using the same PI precursor (I-4), yet resulted in drastically different $(\chi N)_{ODT}$ values. Surprisingly IL-11 ($f_L = 0.40$, $N = 48$) showed $(\chi N)_{ODT} = 11.9$, seemingly consistent with the overall trend in the order to disorder phase boundary extended by the complete set of IL diblock copolymers. We do not understand the true origins of this anomaly.

However, it may be another consequence of fluctuation effects, which introduce an additional N dependence to $(\chi N)_{ODT}$. One of the central concepts that distinguish the thermodynamic (and dynamic) properties of long chain molecules, i.e. homopolymers and block copolymers, from small molecules including liquid crystals is Gaussian chain statistics.[1, 11, 214, 215] As $N \rightarrow \infty$, the assumptions associated with Gaussian coil behavior become exact while in the opposite limit $N \rightarrow 1$, these approximations must fail. Fluctuation theory which represents a modest correction to mean-field theory, retains the Gaussian coil approximations. The IL system reported here may require drastic theoretical revisions including relaxing the Gaussian approximation, i.e. modeling the relatively short polymer blocks as semiflexiable worm-like chains.

Finally, this notion of strongly segregated and non-Gaussian chain conformations near the ODT may contribute to the absence of the gyroid phase (of course this must be confirmed with additional experiments) and the presence of the σ-phase in Figure 5.5

Chapter 6
Linear and Non-linear Mechanical Properties of AB and ABA Block Copolymer Blends

6.1 Introduction

Due to the thermodynamic incompatibility of chemically different polymer chains, block copolymers segregate into nearly pure domains and form well-ordered structures with nanometer length scales.[2, 19, 117] Such microphase separation phenomena, combined with judicious choice of components and molecular design, e.g. glassy-rubbery-glass ABA triblock copolymers, can lead to outstanding mechanical properties for many practical applications, e.g. pressure-sensitive adhesives, thermoplastic elastomers, and additives to modify mechanical properties of various products.[216]

Linear AB diblock copolymers have been studied extensively in efforts to understand the thermodynamic and kinetic properties of these materials. However, the application of these model compounds for mechanical purposes is rather limited due to the weak mechanical properties.[3, 179] Several strategies to improve the mechanical properties of block copolymers have been employed. Linear ABA linear triblock copolymers are amongst the simplest and most extensively studied block structures due to the enhanced mechanical properties achievable with glassy (A) and rubbery (B) components. Microphase separation of the end 'A' blocks constrains the middle 'B' block chains leading to bridging configurations that greatly enhance the mechanical properties relative to the AB diblock counterpart.[24, 27, 174, 217, 218] Numerous variations of this simple ABA model system have been proposed and studied including increasing the number of alternating blocks referred to as linear $(AB)_n$ or $(ABA)_n$ type block copolymers,[219-221] changing the molecular architectures (e.g. star block copolymers),[222, 223] expanding the number of block components (e.g. ABC, ABCD, etc.),[224, 225] and substituting a rubbery or glass component with a semi-crystalline block.[226-230]

Another approach to enhance the mechanical properties involves expanding the number of components such as blending a block copolymer with (1) domain-selective components (solvents or homopolymers)[129, 231-237] or (2) other block copolymers.[103, 127, 238-248] In the latter systems, Hashimoto and co-workers attempted to generalize the phase behavior of block copolymer blends using poly(styrene-*b*-1,4-isoprene) (PS-PI) diblock

copolymers by varying certain thermodynamic parameters, including the block weight fractions, molecular weight difference, and blend composition.[238-240, 244-246] They proposed a key factor to predict miscibility between diblock copolymers of different molecular weights, which is defined as $R = M_{n,1}/M_{n,2}$, where M_n is the number averaged molecular weight; the subscripts denote polymer species, and species 1 has the larger molecular weight. Although this R factor criterion for diblock copolymer miscibility ignores other molecular characteristics (e.g. block compositions), these authors concluded that diblock copolymer with $R \geq 7$ are generally immiscible.

In Chapter 5, the thermodynamic behavior of poly(1,4-isoprene-*b*-DL-lactide) (PI-PLA) is investigated, and one of the most important observations was the high incompatibility between the PI and PLA blocks, denoted by a large χ value, approximately 2.5 times larger than that for PS-PI block copolymers. This high χ drives microphase separation of PI-PLA diblock copolymers at relatively low molecular weights. When blended with moderate molecular weight PLA-PI-PLA triblock copolymer, a host of interesting and potentially useful mechanical properties were obtained. The linear viscoelastic properties of these blends were relatively insensitive to the blend composition, but the non-linear properties were greatly improved by PLA-PI-PLA triblock copolymer as well as the failure characteristics. This result suggests that blending strategy for thermoplastic elastomers with diblock copolymers can offer great opportunities to improve mechanical properties for highly stretchable materials.

This chapter describes the structure and mechanical properties of blend samples prepared from a moderate molecular weight poly(DL-lactide-*b*-1,4-isoprene-*b*-DL-lactide) (LIL) triblock copolymer and low molecular weight PI-PLA diblock copolymer. The principle objective of this work is to establish whether the commonly studied linear viscoelastic properties of elastomeric block copolymers can be decoupled from the poorly understood extensional behavior through this blending approach. Mixtures were characterized using small angle X-ray scattering (SAXS), transmission electron microscopy (TEM), dynamic mechanical spectroscopy (DMS), and extensional viscosity fixture (EVF) techniques. Preliminary data on the microphase and macrophase separation and linear and non-linear viscoelastic properties of these blends are presented and discussed.

6.2 Experimental

Materials The block copolymers used in this study were prepared by anionic polymerization techniques and the detailed procedures are described elsewhere.[87, 92, 130] The microstructures of the poly(1,4-isoprene-*b*-DL-lactide) (IL) diblock and poly(DL-lactide-*b*-1,4-isoprene-*b*-DL-lactide) (LIL) triblock copolymers were characterized by ^{1}H nuclear magnetic resonance (NMR) spectroscopy (Varian 500 MHz). This technique was utilized to determine the IL molecular weights. Size exclusion chromatography (SEC) with chloroform as the mobile phase was employed to characterize the molecular weights

and polydispersities of these components. Glass transition temperatures (T_g) were determined using a TA instrument Q1000 differential scanning calorimetry (DSC).

Blending Procedures IL and LIL block copolymers were blended by a solvent-casting procedure using chloroform. Weighted amounts of block copolymers were placed in glass jars and dissolved in chloroform (~ 20 weight/volume %), then covered with slightly vented aluminum foil, and the solutions were dried in a hood over a period of 1 week at room temperature. Dried blends were annealed at ~ 100 ^{o}C under vacuum overnight and then slowly cooled to room temperature.

X-ray scattering Small angle X-ray scattering (SAXS) experiments were performed at the DND-CAT (beamline 5IDD) at the Advanced Photon Source (APS) located at the Argonne National Laboratory (Argonne, IL). Two dimensional SAXS patterns were collected using a Mar CCD area detector, a sample to detector distance of 6.64 m, and a wavelength of $\lambda = 0.729$ Å. Samples were attached on the Kapton window for collection of SAXS data at room temperature, and high temperature SAXS data was acquired using a Linkam DSC stage with samples contained in aluminum hermetic DSC pans (TA instruments). Two dimensional data were azimuthally averaged to the one-dimensional form of intensity (arbitrary unit) versus the magnitude of scattering wavevector $q = 4\pi\lambda^{-1} \sin(\theta/2)$ where θ is the scattering angle.

TEM Projected images of selected pure component and blends were obtained using transmission electron microscopy (TEM). Thin slices of the blend (~ 70 nm) were

prepared using a Reichert UltraCut S Ultramicrotome (Leica) at -80 ^{o}C and stained by the vapor from a 4 % aqueous OsO_4 solution for 10 minutes at room temperature. Micrographs were acquired at room temperature using a FEI Tecnai G^2 F30 field emission gun TEM operating at 300 kV equipped with Gatan 4k × 4k pixels Ultrascan CCD camera.

DMS Linear dynamic mechanical spectroscopy (DMS) measurements were performed in the shearing mode using a Rheometrics ARES dynamic mechanical spectrometer. The solvent-cast samples were hot-pressed at ~ 130 ^{o}C for 10 minutes before loading on 8 or 25 mm diameter parallel plates. Elastic (G') and viscous (G") moduli were measured at 37 ^{o}C and temperature was controlled by purging with nitrogen gas. In all cases, the strain amplitude applied was within the linear viscoelastic regime (typical strain amplitudes were $\gamma \leq 3$ %).

EVF Non-linear mechanical properties were measured using a TA instrument ARES-G2 rheometer equipped with an extensional viscosity fixture (EVF) tool. The samples were hot-pressed at ~ 130 ^{o}C into a rectangular geometry (approximately 21 mm × 5 mm × 1 mm), and the EVF measurements were conducted at 37 ^{o}C after 3 minutes soaking period. A true strain (Hencky strain) of 1 s^{-1} rate was applied for all the measurements. Each blend sample was measured 3 - 8 times to establish reproducibility. EVF data was acquired by Luca Martinetti.

6.3 Result and Analysis

In this section, the thermal properties, phase behavior, and mechanical response of various LIL/IL binary and ternary blends are presented and analyzed. The two diblock and one triblock copolymers used as blend components are listed in Table 6.1. Weight fractions of PLA (w_{PLA}) were calculated based on the densities of PI and PLA homopolymers (ρ_{PI} = 0.9 g/cm^3 and ρ_{PLA} = 1.248 g/cm^3) at 25 ^oC.[131, 132] The order-to-disorder transition temperature (T_{ODT}) of IL-20 was measured using a isochronal (0.1 rad/s) temperature sweep test with a slow heating rate (0.3 ^oC/min) and T_{ODT} = 108 ± 5 ^oC for IL-20 as shown in Figure 6.1. Measurement of T_{ODT} for IL-21 was attempted using SAXS experiments, but T_{ODT} for this specimen was found to be over 200 ^oC as evidenced by the sharp diffraction peaks (q/q^* = √1:√3:√4:√7:√9 where q^* = 0.040 Å^{-1}) at 200 ^oC (see Figure 6.2d). This SAXS pattern is consistent with a hexagonally packed cylinder morphology (HEX) and IL-21 at 80 ^oC also showed the same scattering pattern (Figure 6.2e, q^* = 0.037 Å^{-1}). T_{ODT} was not determined for LIL-4 due to the high molecular weight of this material (M_n = 95.1 kg/mol), which leads to T_{ODT} >> 200 ^oC.

The SAXS pattern of IL-20 at 85 ^oC (Figure 6.2a) contains a diffraction pattern with peaks at q/q^* = √1:√2:√3:(√4):√5 where q^* = 0.048 Å^{-1} consistent with body-centered cubic (BCC) symmetry and a unit cell parameter a = 18.5 nm. Solvent casting this block copolymer changes the morphology, resulting in a SAXS pattern with two

Table 6.1 Molecular characterization data for IL and LIL block copolymers.

Polymer	M_n[a] (kg/mol)	$M_{n,\ PLA}$[b] (kg/mol)	Polydispersity Index (PDI)	w_{PLA}[c]	$T_{g,\ PLA}$ (^oC)	T_{ODT} (^oC)[d]
LIL-4	95.1	33.2	1.08	0.35	55	Not determined
IL-20	5.5	1.2	1.08	0.22	11	108 ± 5
IL-21	7.4	3.1	1.16	0.41	39	> 200

[a]Number averaged molecular weight. [b]Number averaged PLA block molecular weight. [c]Weight fraction of PLA block. [d]Determination of T_{ODT} of LIL-4 was not attempted because T_{ODT} of LIL-4 is believed not accessible in a practical temperature range (≤ 200 ^oC) due to the high M_n of LIL-4. See Chapter 5 for details. T_{ODT}'s of IL-20 and IL-21 were determined by DMS and SAXS experiments, respectively.

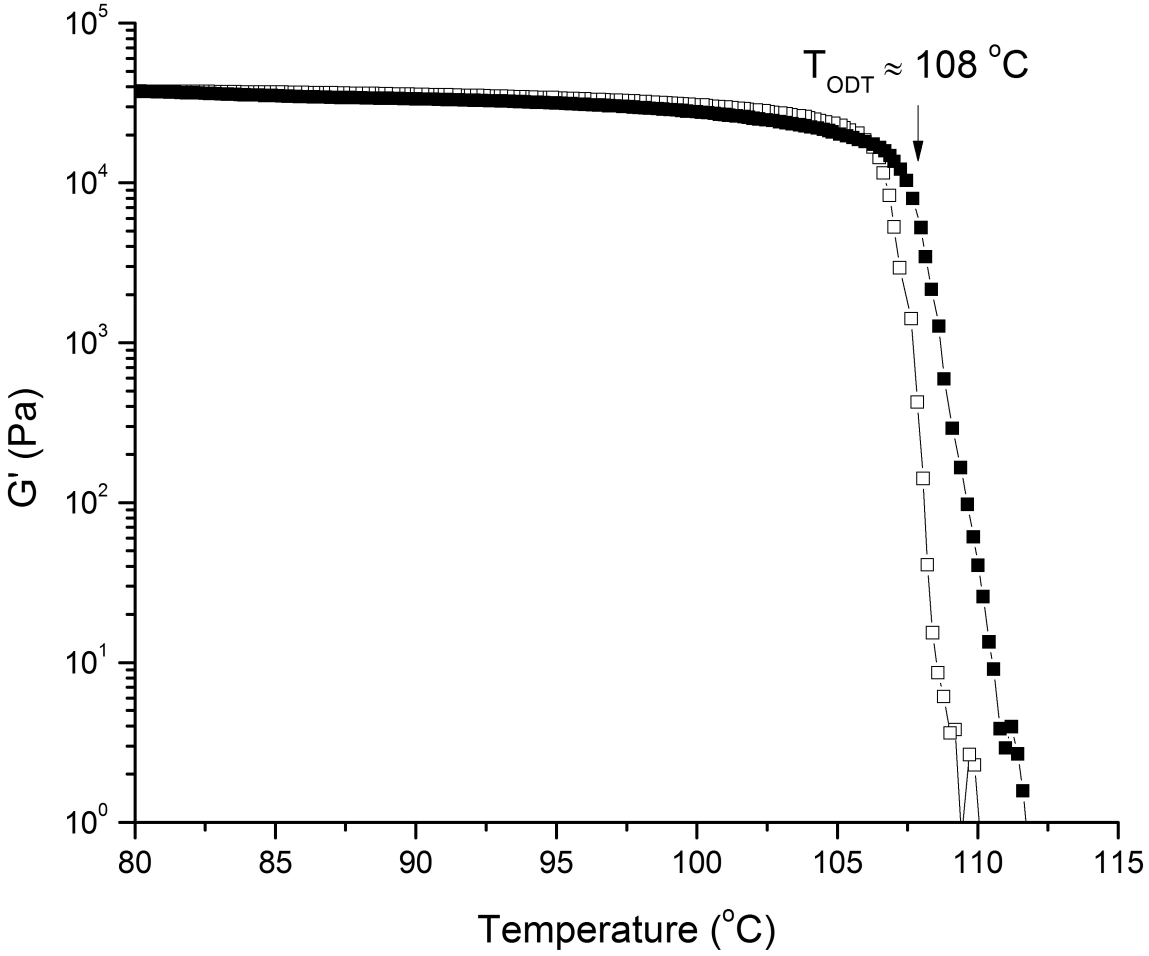

Figure 6.1 Isochronal (0.1 rad/s) temperature G' sweep of IL-20. Specimen was cooled (□) from an elevated temperature (> 110 ^{o}C) to 80 ^{o}C and heated (■) until IL-20 showed the precipitous drop of G' at a rate of 0.3 ^{o}C/min. A small strain amplitude (1 %), in the linear viscoelastic regime, was applied.

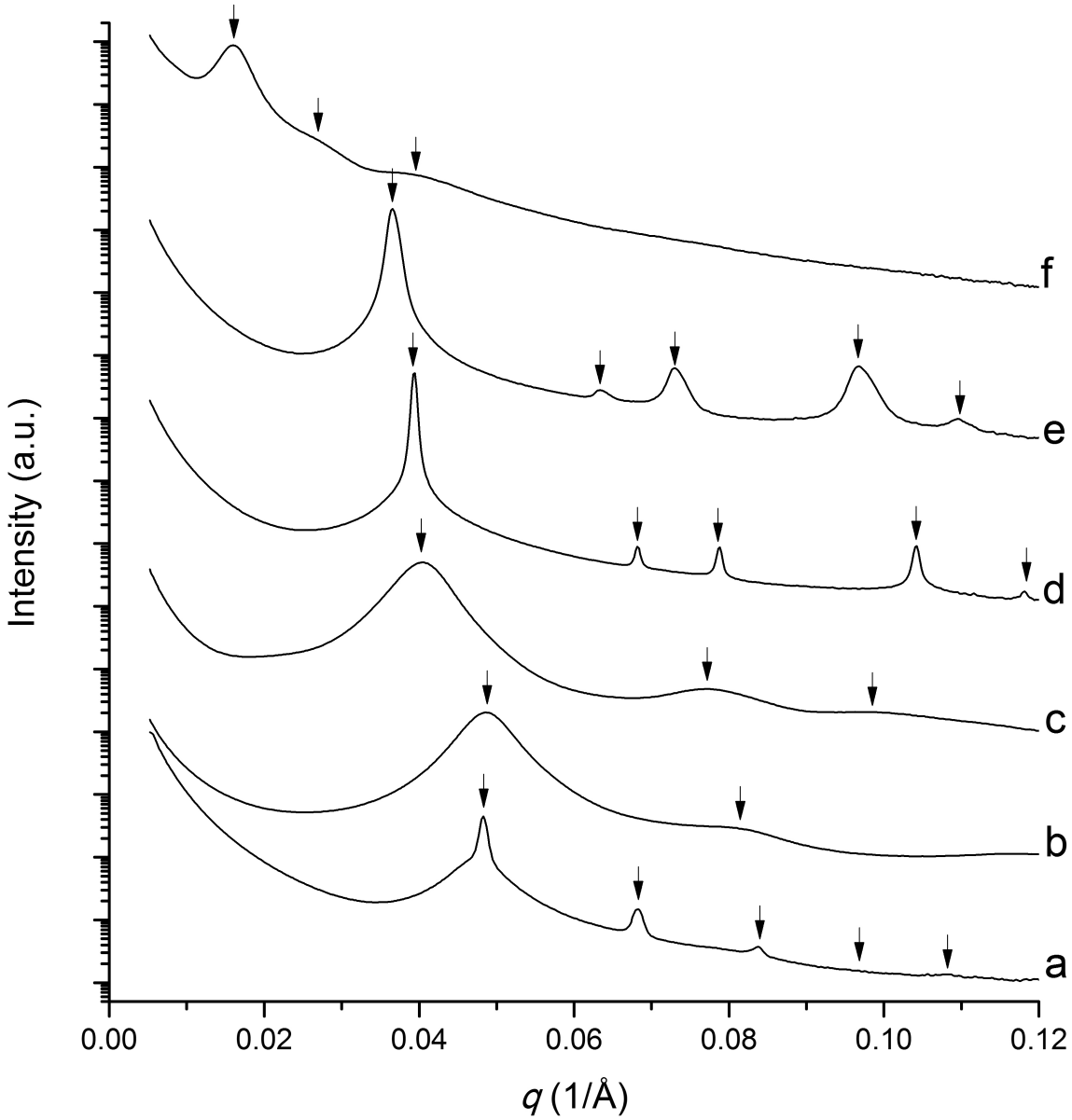

Figure 6.2 Synchrotron SAXS patterns of (a) IL-20 at 85 ^{o}C, (b) solvent-casted IL-20, (c) solvent-casted IL-20/21 50 wt. % blends, referred to as B3-0 below, (d) IL-21 at 200 ^{o}C, (e) IL-21 at 80 ^{o}C, and (f) solvent-casted LIL-4.

broad peaks (marked by down arrows in Figure 6.2b), suggesting a lack of long range order. These broad peak characteristics also were evident in the SAXS patterns obtained from solvent casted IL-20/IL-21 (50 wt. % blend referred to as B3-0, see below) and LIL-4 (Figure 6.2c and f).

Real space morphology information of LIL-4 was obtained using TEM and representative micrographs are presented in Figure 7.3. These micrographs clearly shows the microphase separation into PI and PLA domains. However, the PLA domains are irregular (white regions in Figure 6.3) and any long range ordered structure is not observed, which is consistent with the SAXS pattern obtained from LIL-4 shown in Figure 6.2f.

The linear viscoelastic (G' and G") frequency sweep data obtained from IL-20, IL-21, and LIL-4 at 37 ^{o}C are shown in Figure 6.4. The G' and G" values of IL-21 and LIL-4 are very close in the measured frequency domain despite the large molecular weight difference between these compounds.

Using IL-20, IL-21, and LIL-4, over 30 block copolymer blends were prepared as listed in Table 6.2. The blends were prepared to investigate the effect on G'(ω) and G" (ω) and the non-linear (extensional) mechanical properties while varying two phase-space variables: the relative weight ratios of IL-20 to IL-21 and the weight fraction of LIL-4.

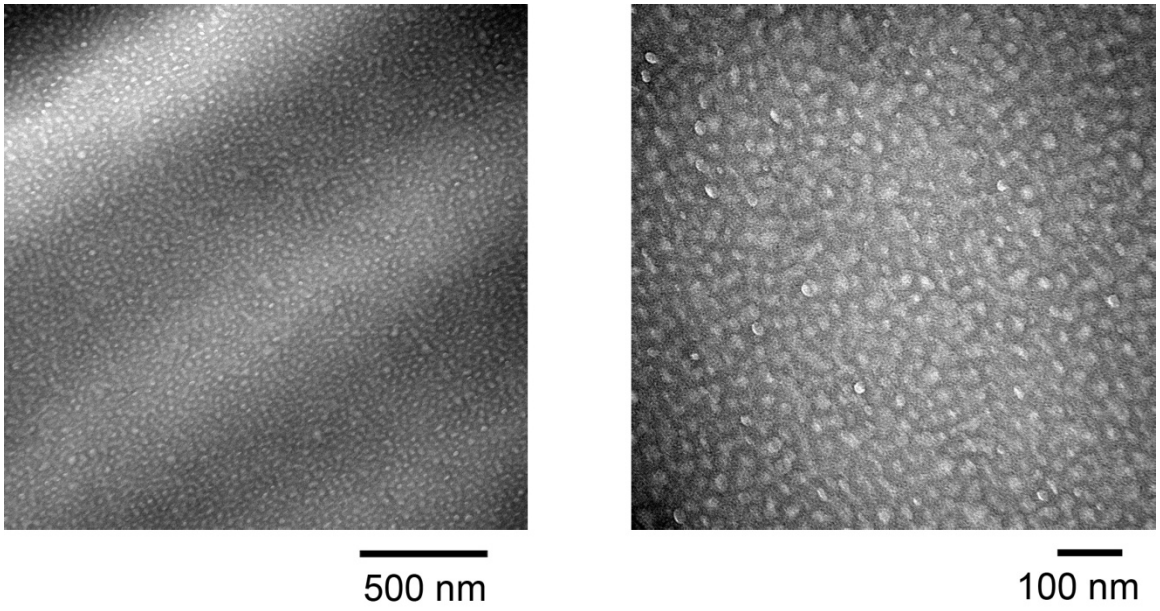

Figure 6.3 Representative TEM micrographs obtained from LIL-4. Microphase separation of PI (dark regions, stained by the OsO_4 vapor) and PLA (white regions) domains is identified (right panel), but the shape of these PLA domains is irregular without long range order.

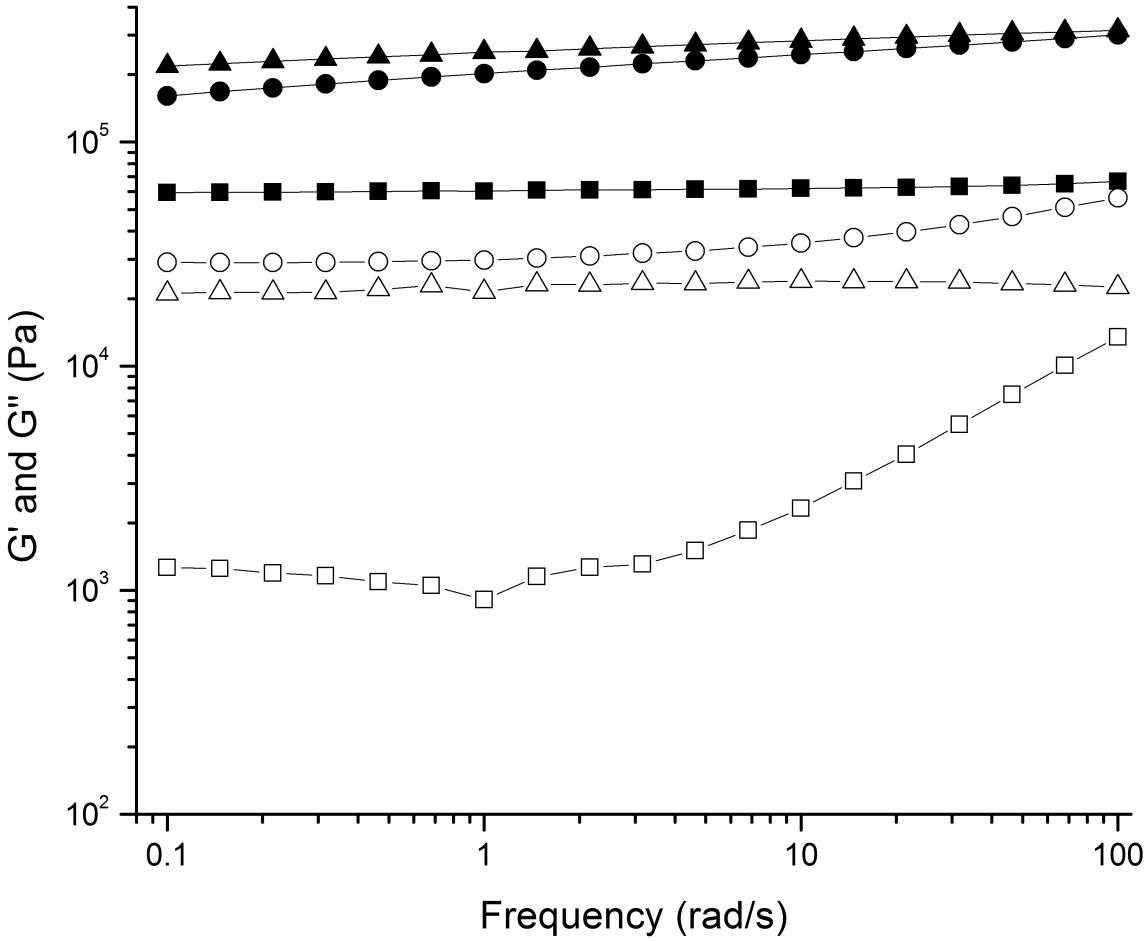

Figure 6.4 Linear (1 %) viscoelastic G' and G" frequency sweep data obtained from (a) IL-20 (G': ■, G": □), (b) IL-21 (G': ●, G": ○) , and (c) LIL-4, (G': ▲, G": △) at 37 ^{o}C.

The glass transition temperature of the PLA blocks, $T_{g,PLA}$, of these blends was found to be dependent on the composition (Table 6.2) as summarized in Figure 6.4. At low weight fraction of LIL-4 (< 20 wt. %), the blend composition of IL-20 and 21 was the primary factor (higher content IL-21 has higher $T_{g,PLA}$), but T_g asymptotically approached $T_{g,PLA}$ of LIL-4 (55 ^oC) for blend compositions containing over approximately 50 wt. % of LIL-4.

The phase behavior of the blends was studied by SAXS experiments. Selected results drawn from blend samples in three representative blend sets (B1, B3, and B5) are shown in Figure 6.6 to 6.8. The scattering pattern obtained from IL-20 (Figure 6.6) showed a broad primary peak at $q^* = 0.0487$ Å^{-1} with a second broad response with much lower intensity at $q = 0.081$ Å^{-1} (1.2 %). This characteristic scattering fingerprint persisted with the B1 series of blends up to 20 wt. % of LIL-4 (B1-5 to 20). As indicated by stars (*) in Figure 6.6, one or two broad peaks emerge at lower q (< 0.017 Å^{-1}) upon addition of LIL- 4 to IL-20, indicating microstructures with large domain spacings ($D = 2\pi/q$) relative to the microstructure size of IL-20. Another noticeable change induced by adding LIL-4 to IL-20 is that the position of the primary peak (down arrows in Figure 6.6) shifts to lower q, signaling that the domain spacing of the blends is proportional to the amount of LIL-4. This effect is summarized in Figure 6.9. In contrast to the results obtained from the other B1 samples, B1-5 showed relatively small but sharp diffraction

Table 6.2 List of LIL-4/IL-20/IL-21 block copolymer blends.

Blend Name[a]	Weight Fraction (%)			IL-20:IL-21 Weight Ratio (%)	w_{PLA}	$T_{g,\,PLA}$[b] (°C)
	LIL-4	IL-20	IL-21			
B1-1	1	99	0	100:0	0.22	5
B1-5	5	95	0	100:0	0.23	9
B1-10	10	90	0	100:0	0.23	9
B1-15	15	85	0	100:0	0.24	13
B1-20	20	80	0	100:0	0.25	14
B1-40	40	60	0	100:0	0.27	21
B1-60	60	40	0	100:0	0.30	53
B1-80	80	20	0	100:0	0.32	53
B2-0	0	75	25	75:25	0.27	17
B2-10	10	67.5	22.5	75:25	0.28	13
B3-0	0	50	50	50:50	0.32	22
B3-1	1	49.5	49.5	50:50	0.32	21
B3-5	5	47.5	47.5	50:50	0.32	23
B3-10	10	45	45	50:50	0.32	24
B3-15	15	42.5	42.5	50:50	0.32	24
B3-20	20	40	40	50:50	0.32	33
B3-40	40	30	30	50:50	0.33	44
B3-60	60	20	20	50:50	0.34	52
B3-80	80	10	10	50:50	0.34	54
B4-0	0	25	75	25:75	0.36	25
B4-10	10	22.5	67.5	25:75	0.36	24
B5-1	1	0	99	0:100	0.41	39
B5-5	5	0	95	0:100	0.41	42
B5-10	10	0	90	0:100	0.40	43
B5-15	15	0	85	0:100	0.40	44
B5-20	20	0	80	0:100	0.40	39
B5-40	40	0	60	0:100	0.39	46
B5-60	60	0	40	0:100	0.37	52
B5-80	80	0	20	0:100	0.36	53

[a]Blend names are composed of the prefix 'B' followed by a set number of IL-20 and IL-21 composition (1 to 5) and LIL-4 weight fraction in percentile. [b]$T_{g,PLA}$ was determined based on the assumption of a single phase (no macrophase separation).

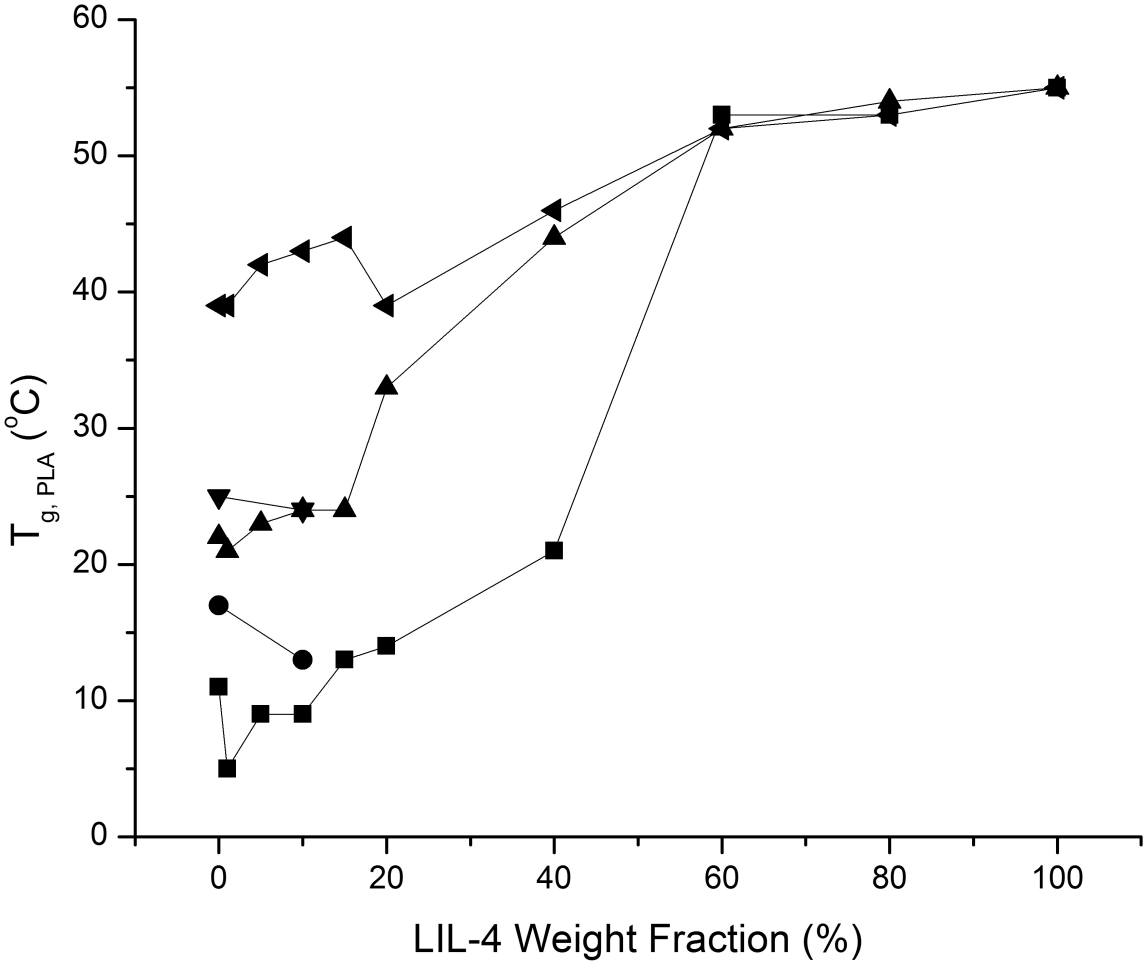

Figure 6.5 PLA block glass transition temperatures $T_{g,PLA}$ of IL/LIL blends versus LIL-4 wt. fraction. $T_{g,PLA}$ is dependent on IL-20/IL-21 wt. fraction at low LIL-4 composition, but increases asymptotically to $T_{g,PLA}$ of LIL-4 at a high content of LIL-4. Blend series are denoted by following symbols: ■(B1), ●(B2), ▲(B3), ▼(B4), and ◄(B5).

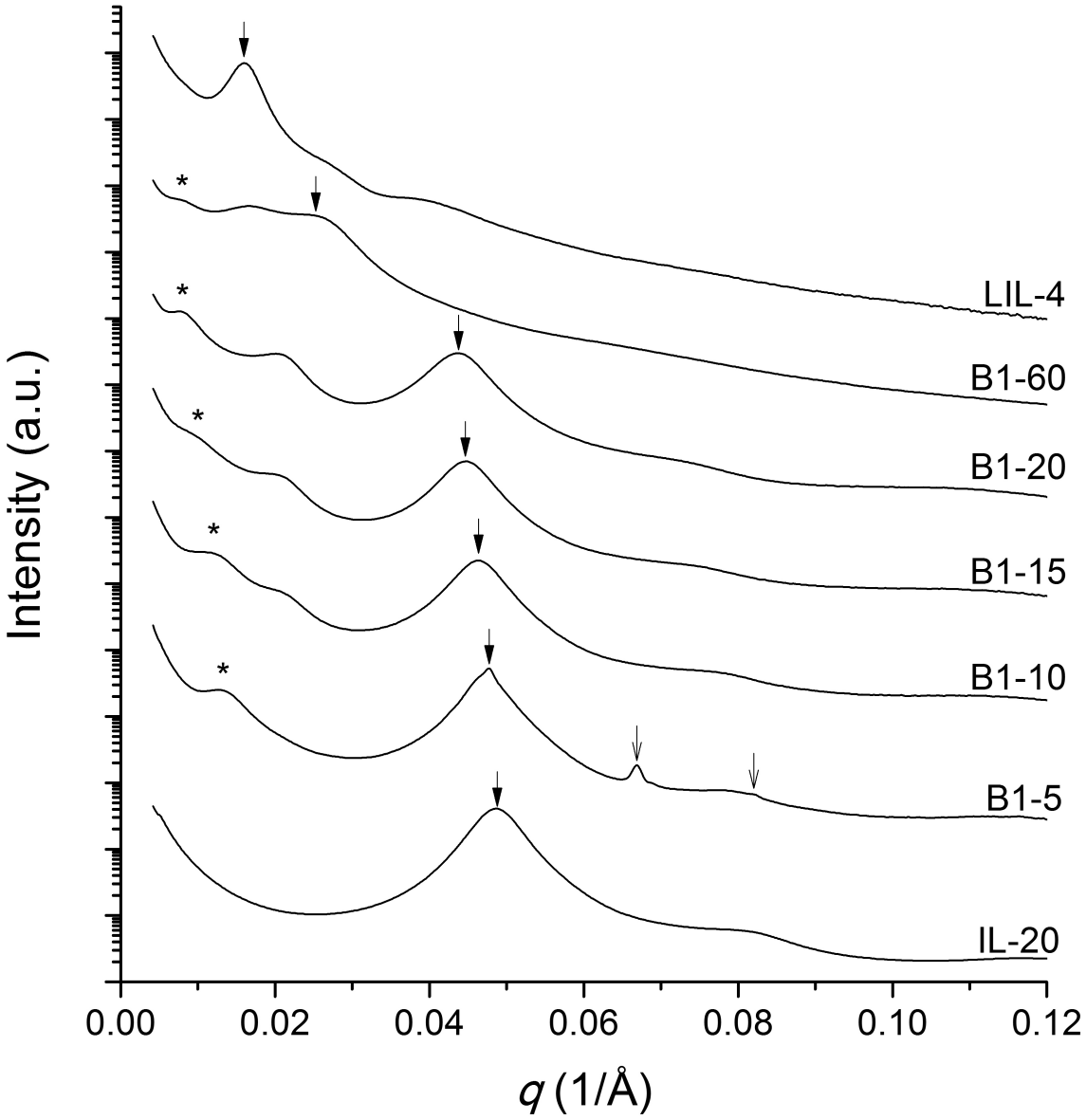

Figure 6.6 Synchrotron SAXS patterns of B1 series. All scattering patterns were obtained at room temperature. Primary peaks are denoted by down solid arrows and higher order peaks are denoted by down line arrows. Broad peaks emerging by addition of LIL-4 are indicated by stars (*).

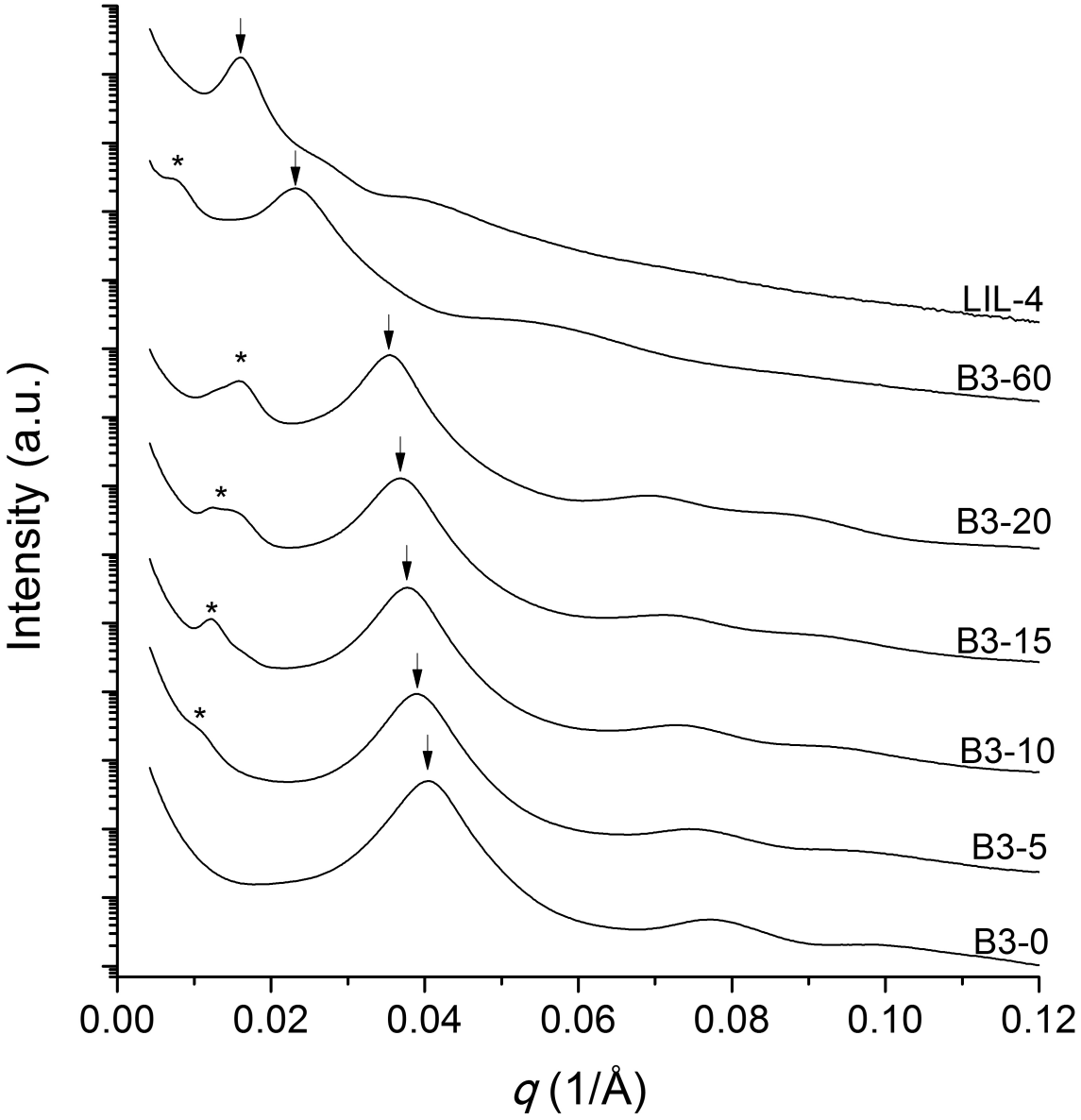

Figure 6.7 Synchrotron SAXS patterns of B3 series. All scattering patterns were obtained at room temperature. Primary peaks are denoted by down solid arrows. Broad peaks emerging by addition of LIL-4 are indicated by stars (*).

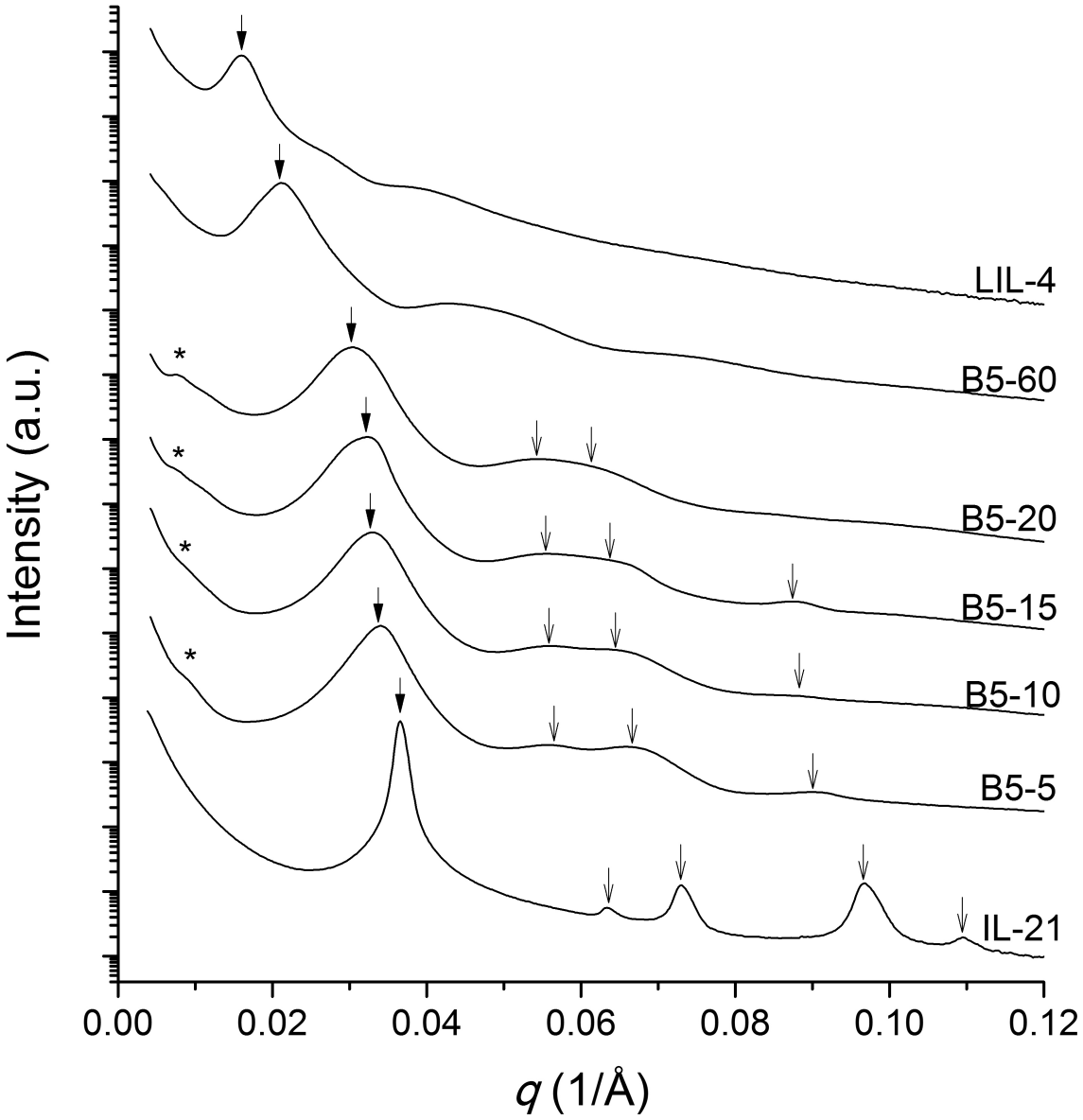

Figure 6.8 Synchrotron SAXS patterns of B5 series. All scattering patterns were obtained at room temperature except the pattern of IL-21 (80 ^{o}C). Primary peaks are denoted by down solid arrows and higher order peaks are denoted by down line arrows. Broad peaks emerging by addition of LIL-4 are indicated by stars (*).

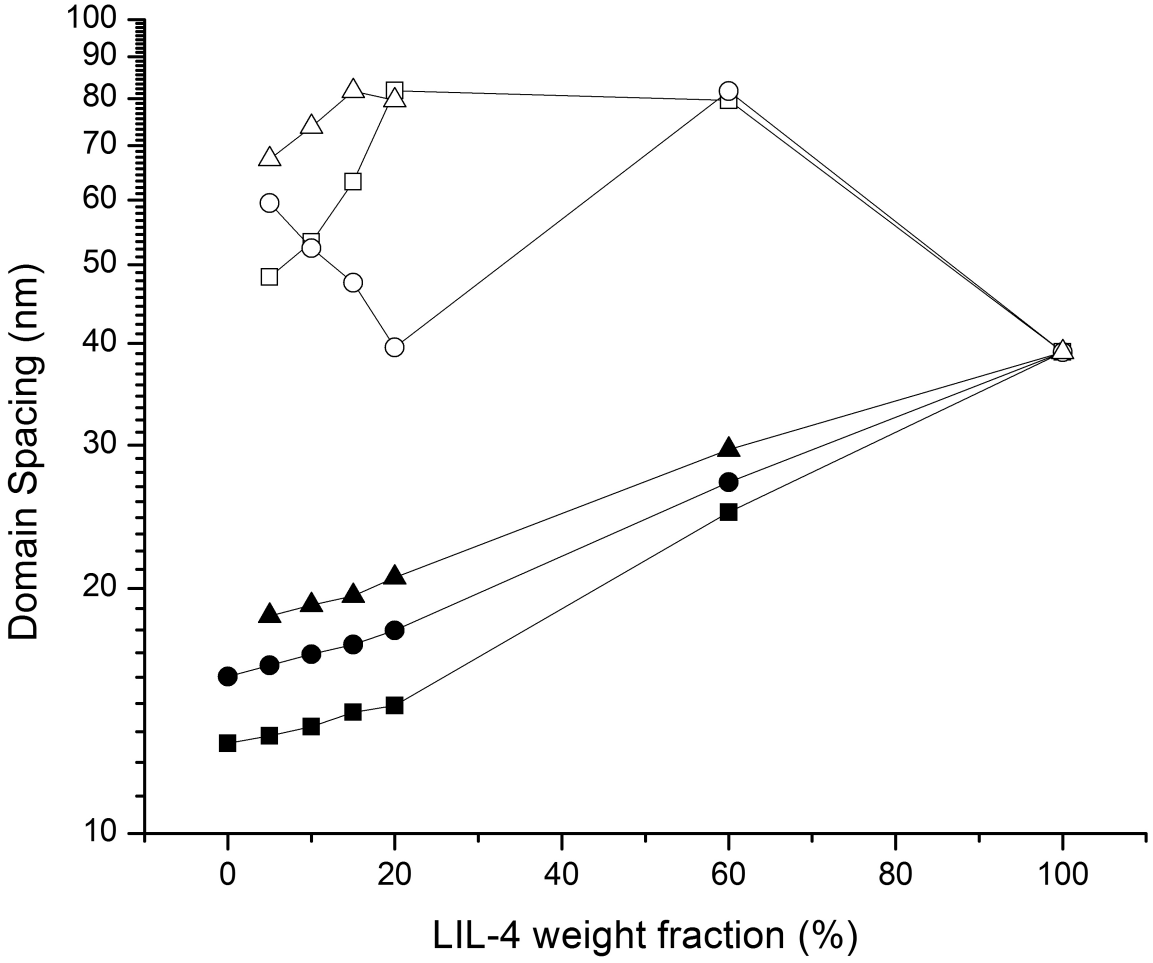

Figure 6.9 Characteristic domain spacings ($D = 2\pi/q^*$) of B1(■, □), B3(●, ○), and B5(▲,△) series at room temperature. Solid and white symbols represent the domain spacings denoted by solid down arrows and stars in Figures 6.5 to 6.7, respectively.

peaks with the relative ratios $q/q^* = \sqrt{1}:\sqrt{2}:\sqrt{3}$ where $q^* = 0.047$ Å^{-1}, consistent with a body-centered cubic (BCC) morphology with a unit cell parameter $a = 18.9$ nm.

The broad peaks found in the B1 blends also appeared in the B3 and B5 series with other accompanying features (Figure 6.7 and 6.8). In these materials, the primary peak also shifts to lower q by addition of LIL-4, and peaks near $q = 0.01$ Å^{-1} (marked by *) were also observed. A summary of the characteristic domain spacings associated with these features is shown in Figure 6.8.

Real space morphology information from selected blend samples, B5-60, B5-20, and B3-50 were obtained using TEM performed on microtomed thin films following staining with osmium tetraoxide. At first glance, most of the read from B5-60 recorded appears homogeneous (left panel in Figure 6.10), but high magnification micrographs (right panel in Figure 6.10) reveals microphase separation between the PI and PLA blocks with a rough domain spacing of 25 nm. During the TEM characterization of B5-60, small speckle-like regions with a relatively large domain spacing (~ 40 nm, marked by arrows in Figure 6.10) were occasionally observed (these regions occupied at less than 1 % of the recorded area).

The TEM micrographs obtained from B5-20 are very interesting (Figure 6.11). Roughly the half area of the recorded micrographs shows a HEX morphology as seen by the hexagonal and axial views of hexagonally arrayed cylinders in Figure 6.11 and 6.11b, respectively. Tut the rest of the imaged areas contain an irregularly microphase separated

domain structure (Figure 6.11c). Although the geometrical features of these morphologies are different, the characteristic domain spacings of the HEX and irregular regions are quite close (approximately 20 nm). Along with these regions, distinctive circular regions (Figure 6.11d) with a significantly different characteristic domain spacing (approximately 40 - 80 nm) and even an onion-like structure at the center of the circular domain were occasionally observed although these larger features are present in less than 5 % of the recorded area. Surprisingly, the SAXS pattern obtained from B5-60 (Figure 6.8) does not show higher-order diffraction peaks expected from regular HEX morphology found in the TEM images.

The last blend sample characterized using TEM, B3-60, also showed two distinctive regions with large (denoted "a" in Figure 6.12) and small domain (denoted "b") spacings similar to the B5 blend specimens. These regions are microphase separated and the region "a" covered approximately 5 - 10 % of the recorded micrographs.

The distinctive domain spacings of two characteristic regions observed from B5-20 and B3-60 are qualitatively consistent with the domain spacings from the SAXS patterns. For example, the domain spacing in region "a" is roughly 80 nm while region "b" shows a domain spacing of ~ 30 nm, while correspond closely to the domain spacings obtained by SAXS, i.e., $D = 2\pi/q(= 0.0075\ \text{Å}^{-1}) = 85$ nm for the peak marked by a star and $D = 2\pi/q(= 0.023\ \text{Å}^{-1}) = 27$ nm for the peak marked by a down arrow as shown for B3-60 in Figure 6.7.

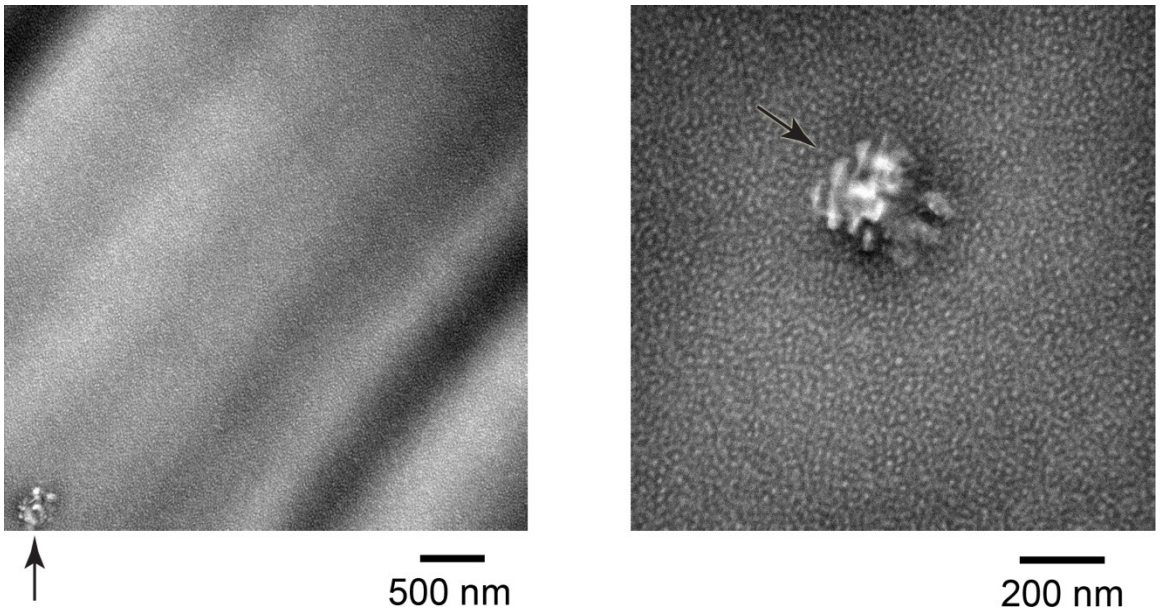

Figure 6.10 Representative TEM micrographs obtained from B5-60. Small speckle-like regions are marked by arrows.

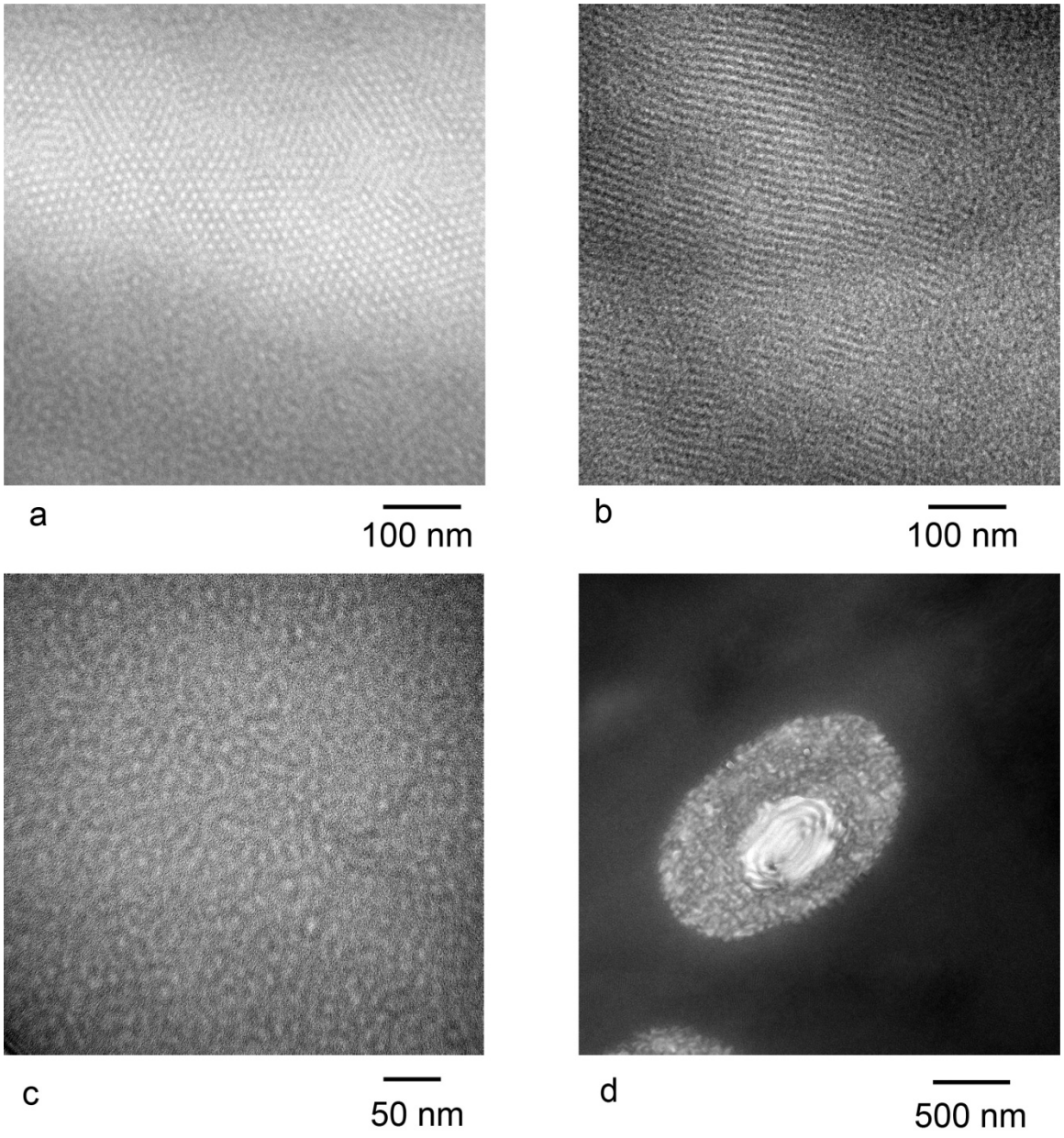

Figure 6.11 Representative TEM micrographs obtained from B5-20.

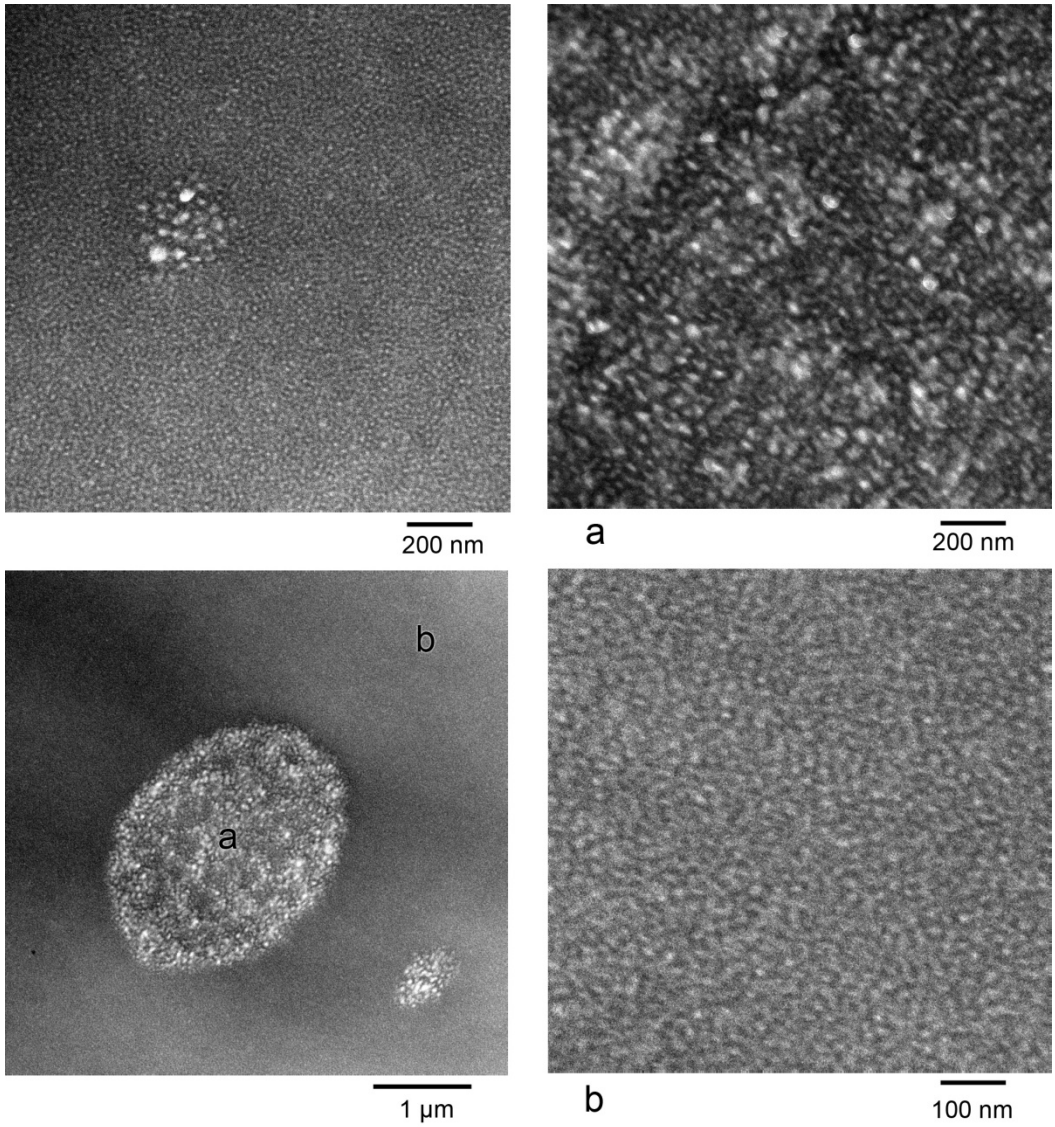

Figure 6.12 Representative TEM micrographs obtained from B3-60. Bright PLA domains are clearly distinctive to dark PI matrix (stained by the OsO_4 vapor). Two distinctive domains with different domain spacings were observed (denoted "a" and "b" in the left bottom panel.) Magnified micrographs of these regions are shown in the panel a and b on the right.

Linear viscoelastic (G' and G") properties of selected blends were measured by employing isothermal (37 ^{o}C) frequency sweep (100 - 0.1 rad/s) experiments with small strain amplitudes (< 3 %) as presented in Figure 6.13 to 6.16. The elastic moduli (G') of these blends is relatively insensitive to small amount of LIL-4 (< 20 wt. %) and is mainly determined by the diblock copolymer compositions as shown in Figure 6.16 (higher IL-21 fraction results in higher G'). The dependence of G' and G" at 1rad/s on the amount of LIL-4 is summarized in Figure 6.17 and shows on inverse parabolic behavior.

Non-linear extensional stresses σ_E of selected blends were measured by applying a true (Hencky) strain at a rate of 1 rad/s at 37 ^{o}C as presented in Figures 6.18 to 6.21 (IL-20 and B3-0 were too soft for the EVF measurement). The consequences on the extensional stress behavior upon varying the diblock compositions and LIL-4 weight fraction is complex, but notable features can be identified. For example, in the B1 blends with up to 20 wt. % of LIL-4 (B1-20), the level of σ_E at small ε (≤ 0.05) varied dramatically with the weight fraction of LIL-4. For $\varepsilon > 0.05$, σ_E is relatively invariant and linear with strain for B1-1, 5, and 10 up to the limit $\varepsilon \approx 0.15$ (marked by the down arrow in Figure 6.15a). Above this value, σ_E becomes highly non-linear and depends significantly on the LIL-4 content. The failure stress ($\sigma_{E,F}$) for B1-1, 5, 10, and 20 increases in proportion to the amount of LIL-4, but the failure strain (ε_F) peaks $\varepsilon_F \cong 4.2$ with blend B1-5, which contains just 5 % LIL-4 triblock copolymer (Figure 6.18 and 6.22). Compared to these blends, B1-60 displays a σ_E curve vertically shifted by

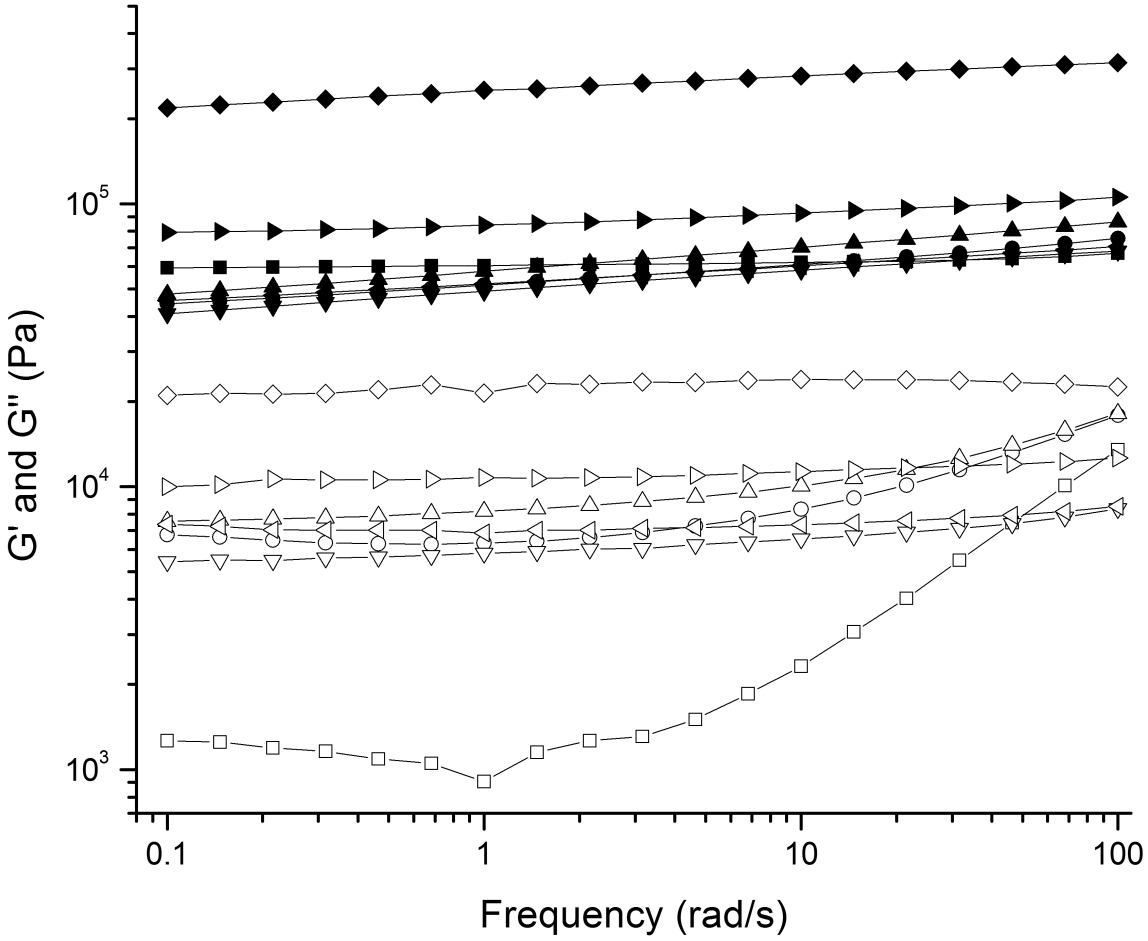

Figure 6.13 Dynamic shear linear elastic (G', solid symbols) and viscous (G', white symbols) moduli of B1 series at 37 ^{o}C. Samples are denoted by (■, □) for IL-20, (●, ○) for B1-5, (▲,△) for B1-10, (▼,▽) for B1-15, (◄,◁) for B1-20, (►,▷) for B1-60, and (◆,◇) for LIL-4.

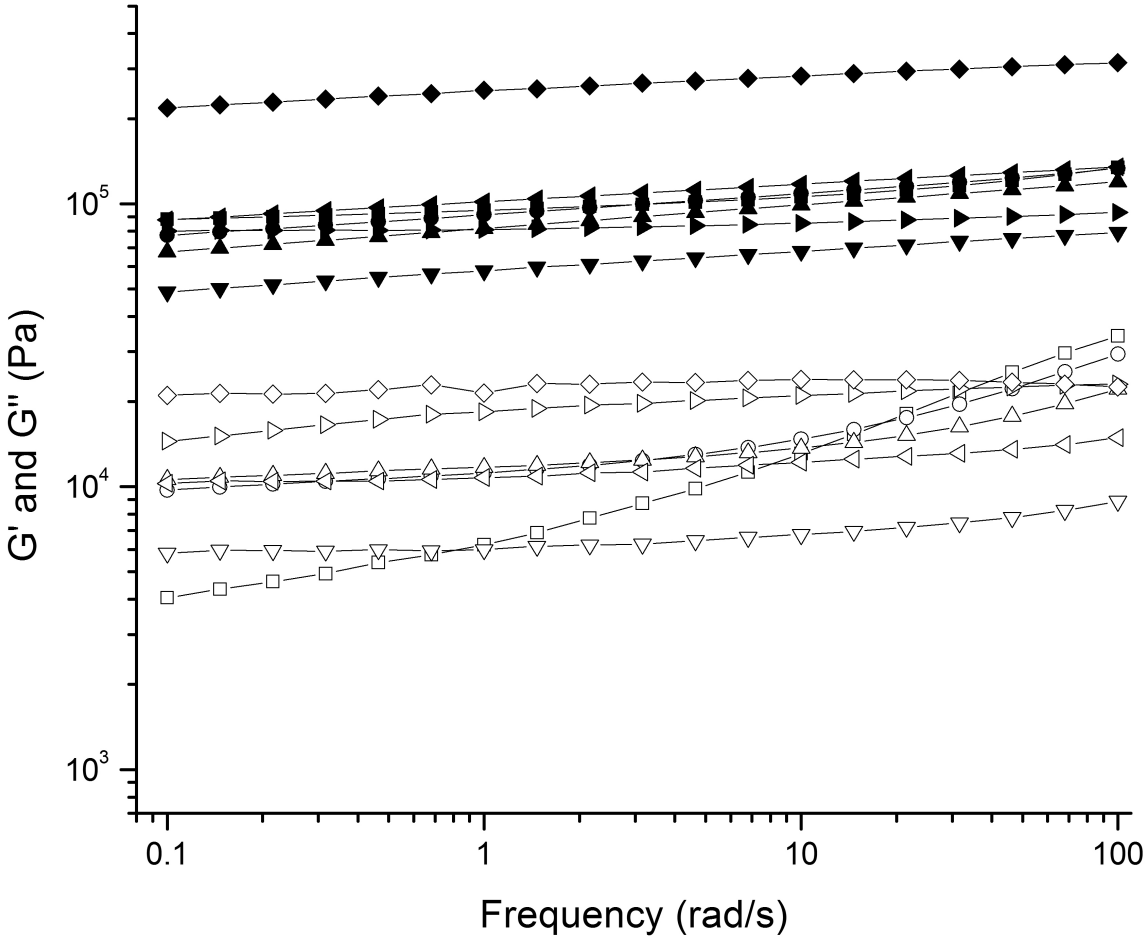

Figure 6.14 Dynamic shear linear elastic (G', solid symbols) and viscous (G', white symbols) moduli of B3 series at 37 ^{o}C. Samples are denoted by (■, □) for B3-0, (●, ○) for B3-5, (▲,△) for B3-10, (▼,▽) for B3-15, (◀,◁) for B3-20, (►,▷) for B3-60, and (◆,◇) for LIL-4.

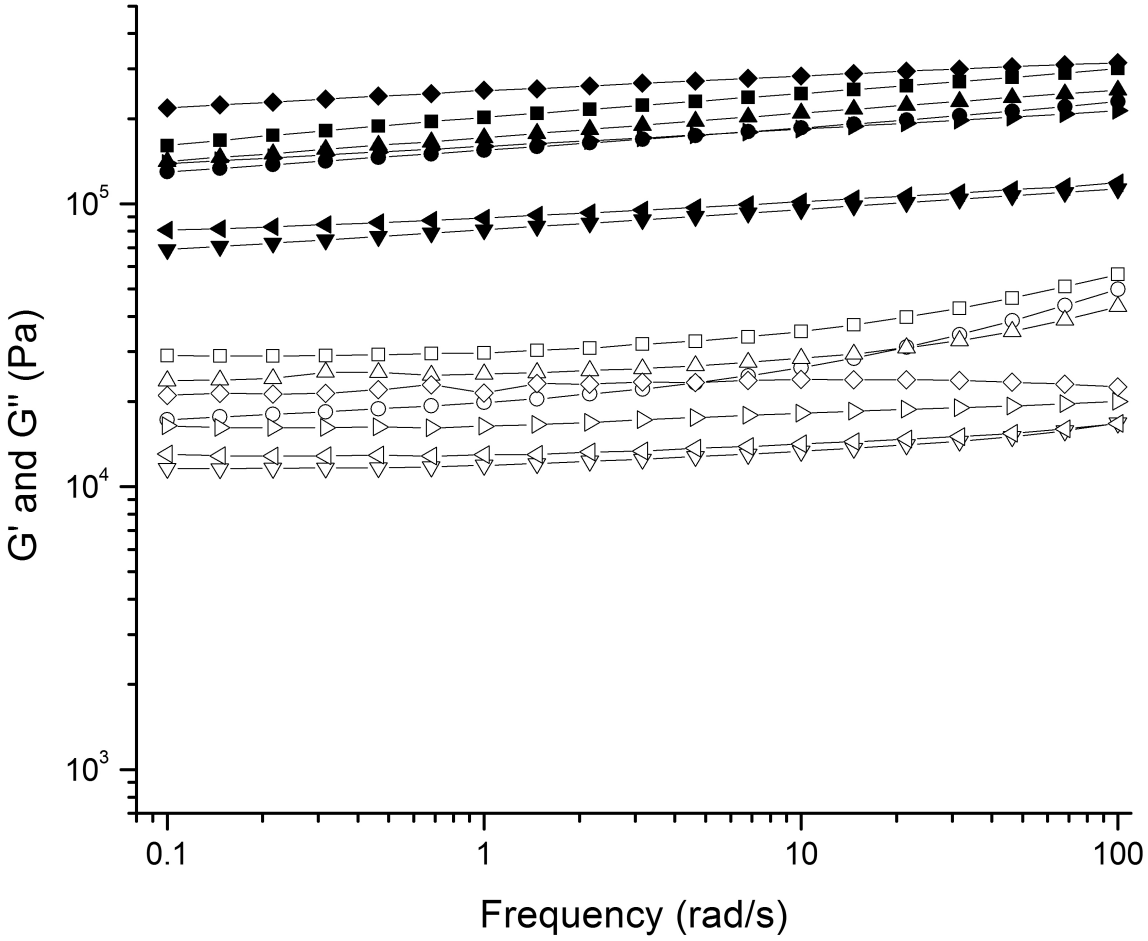

Figure 6.15 Dynamic shear linear elastic (G', solid symbols) and viscous (G', white symbols) moduli of B5 series at 37 ^{o}C. Samples are denoted by (■, □) for IL-21, (●, ○) for B5-5, (▲,△) for B5-10, (▼,▽) for B5-15, (◄,◁) for B5-20, (►,▷) for B5-60, and (◆,◇) for LIL-4.

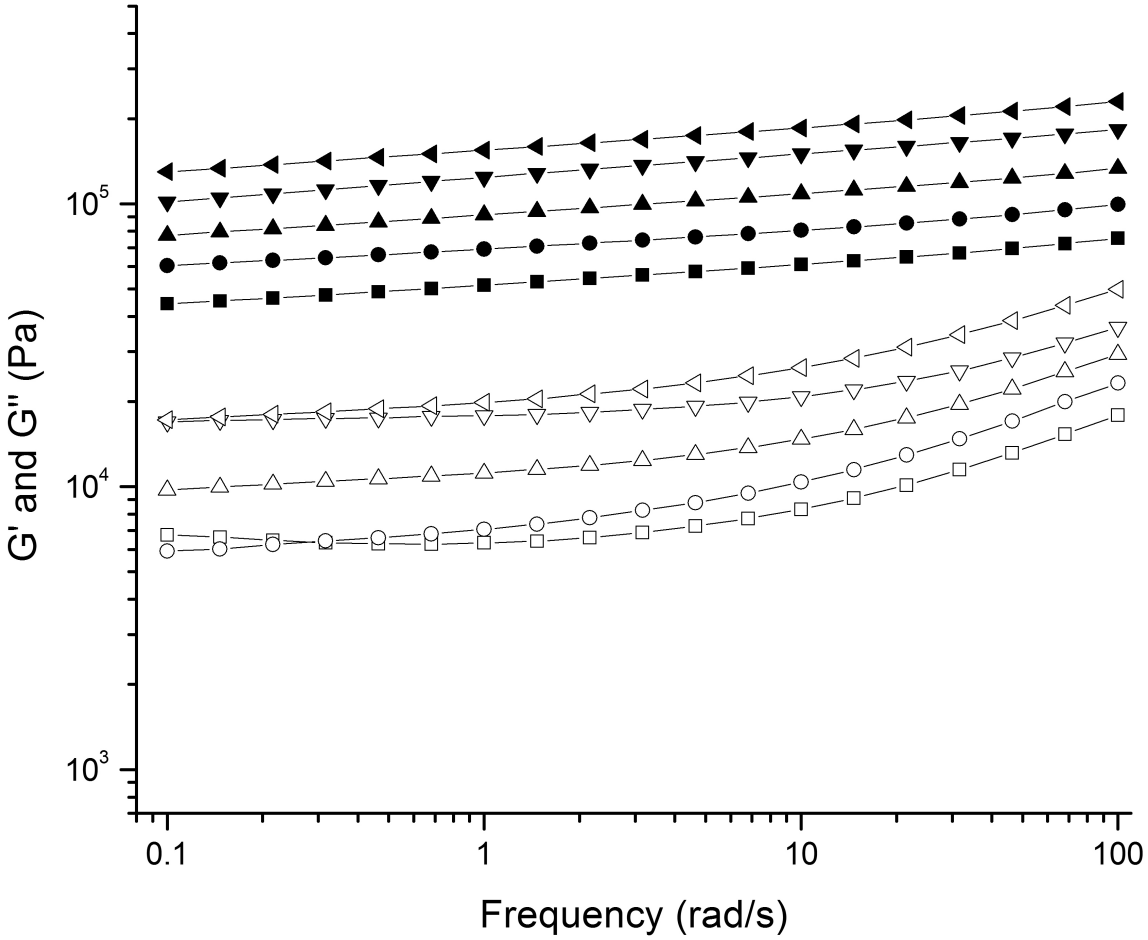

Figure 6.16 Elastic (G', solid symbols) and viscous (G', white symbols) moduli obtained from B1-10 (■, □), B2-10 (●, ○), B3-10 (▲,△), B4-10 (◀,◁), and B5-10 (►,▻) blends to present the effect of diblock copolymer compositions on linear viscoelastic properties.

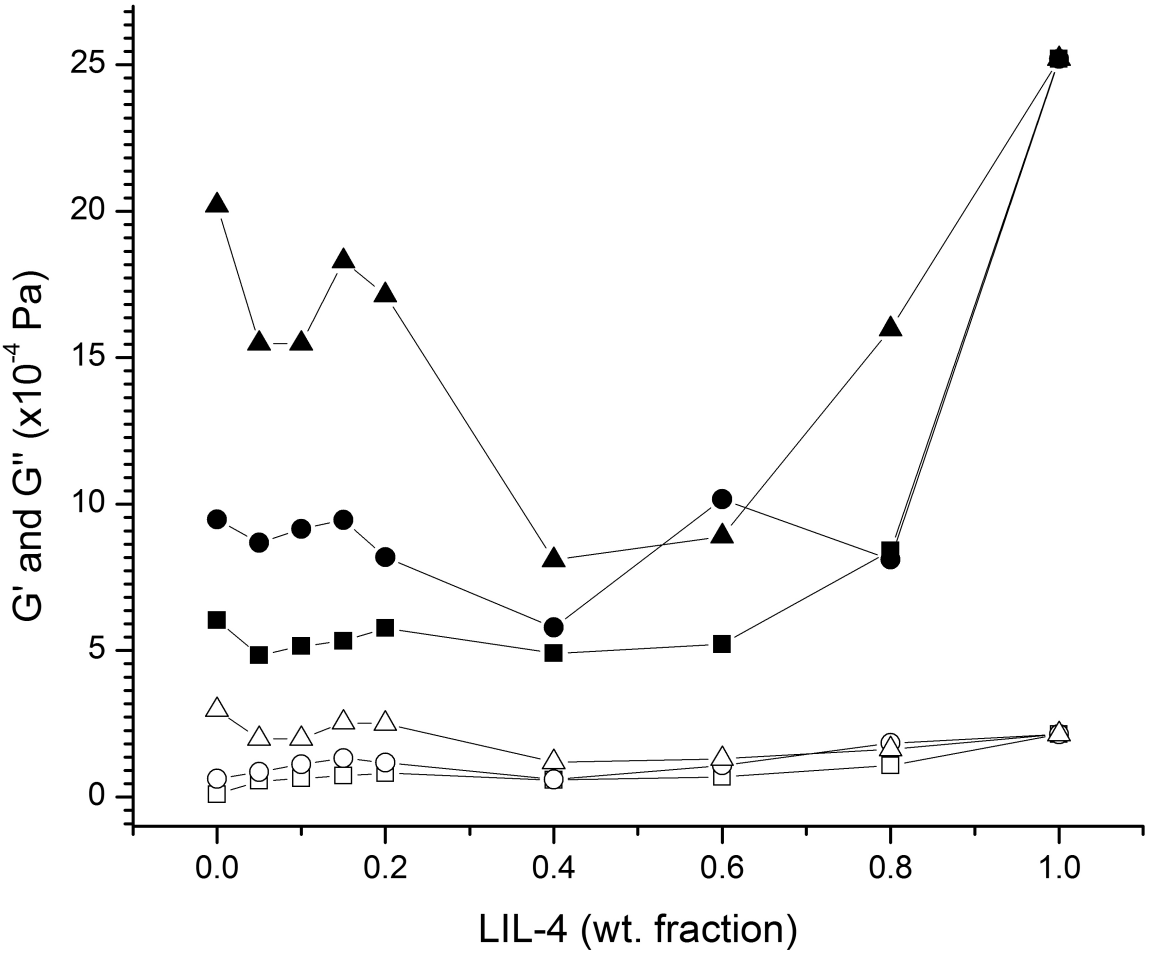

Figure 6.17 Summary of dynamic elastic (G', solid symbols) and viscous (G", white symbols) moduli at 1rad/s and 37 ^{o}C for blend series B1(■, □), B3(●, ○), and B5(▲,△) versus LIL-4 wt. fraction.

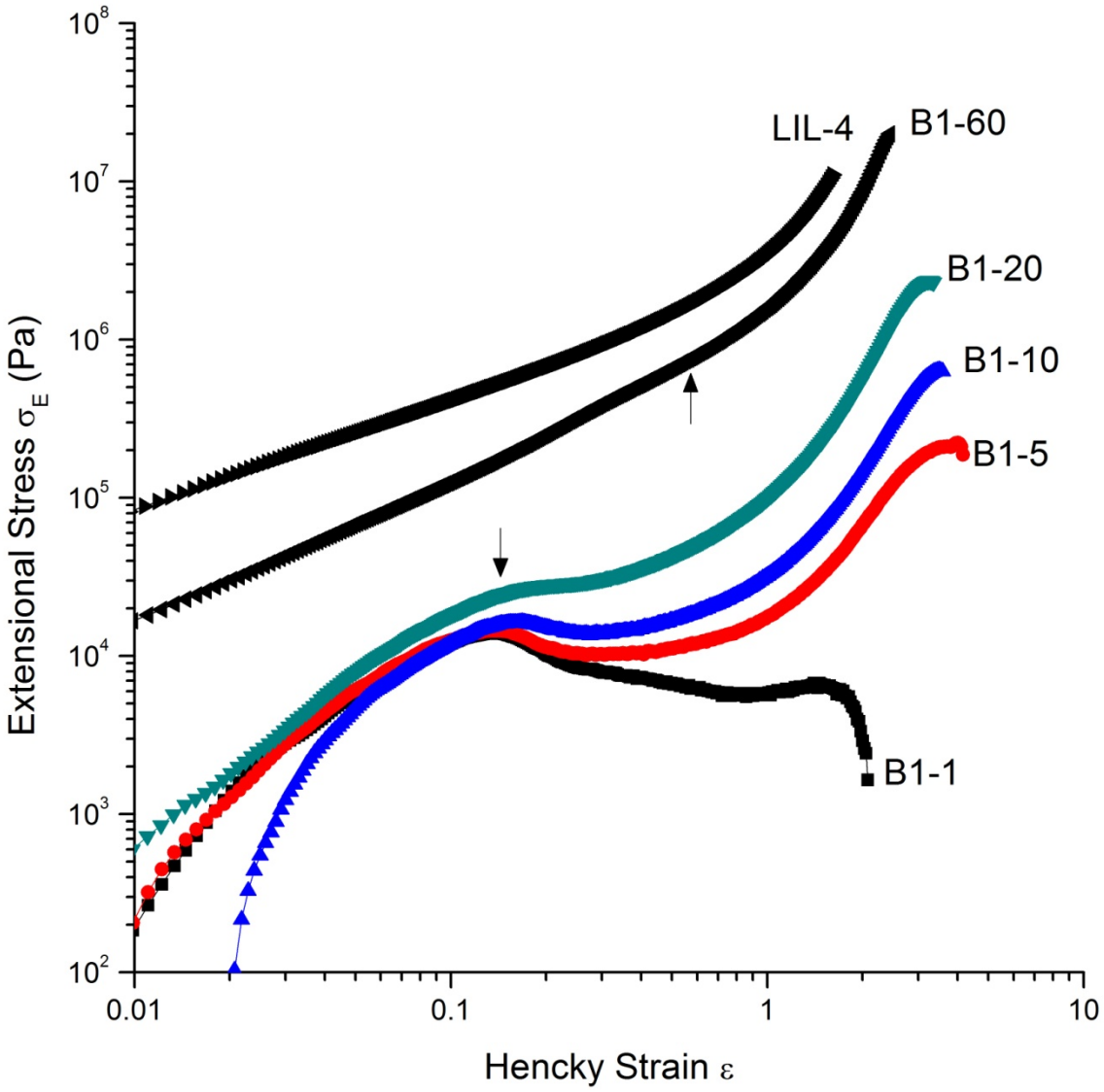

Figure 6.18 Extensional stress σ_E of selected blends from B1series by applying true (Hencky) strain ε of 1 s^{-1} rate at 37 ^oC. Sample names are denoted near failure points and colors are used for clear representation.

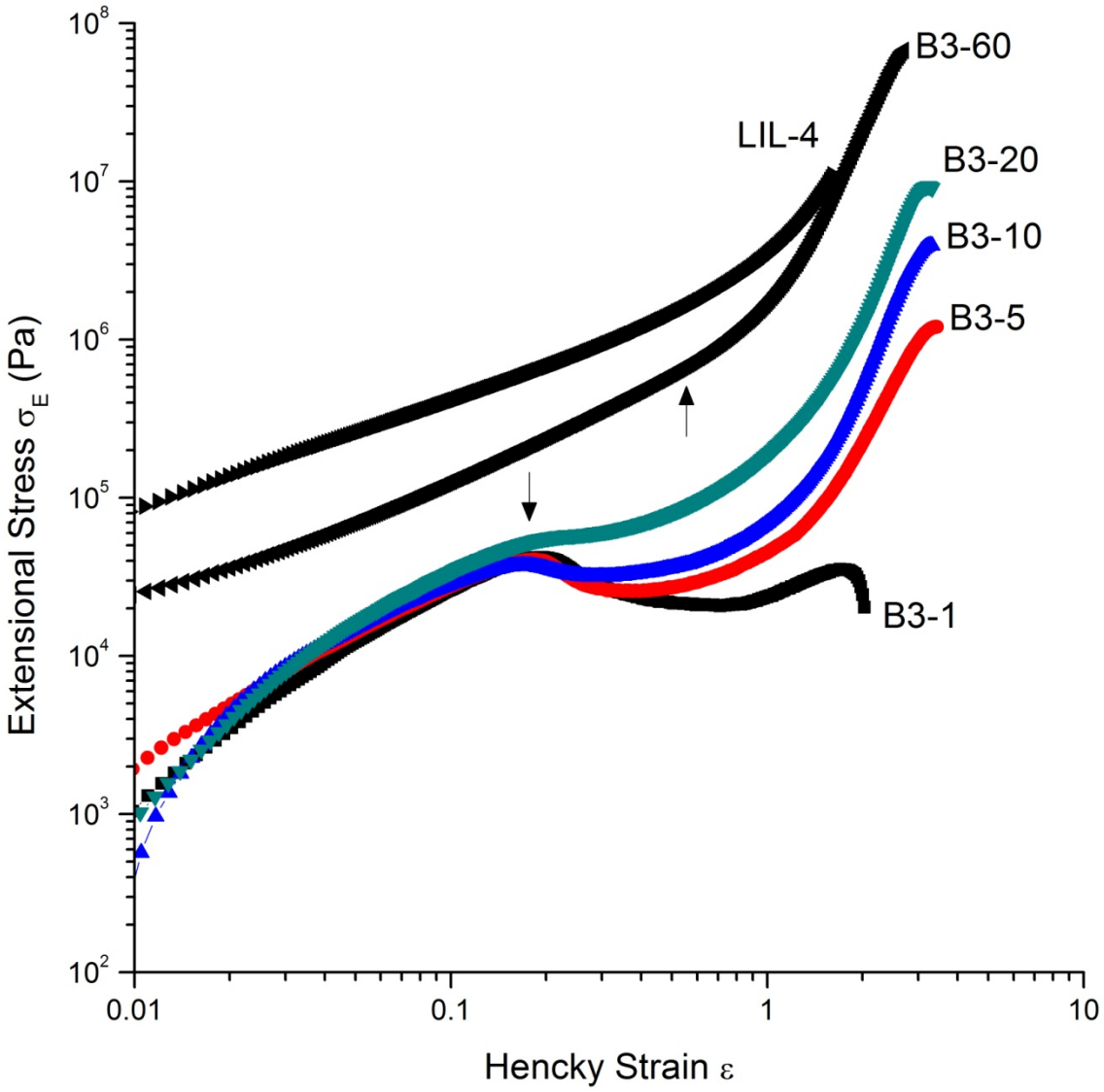

Figure 6.19 Extensional stress σ_E of selected blends from B3 series by applying true (Hencky) strain ε of 1 s^{-1} rate at 37 ^oC. Sample names are denoted near failure points and colors are used for clear representation.

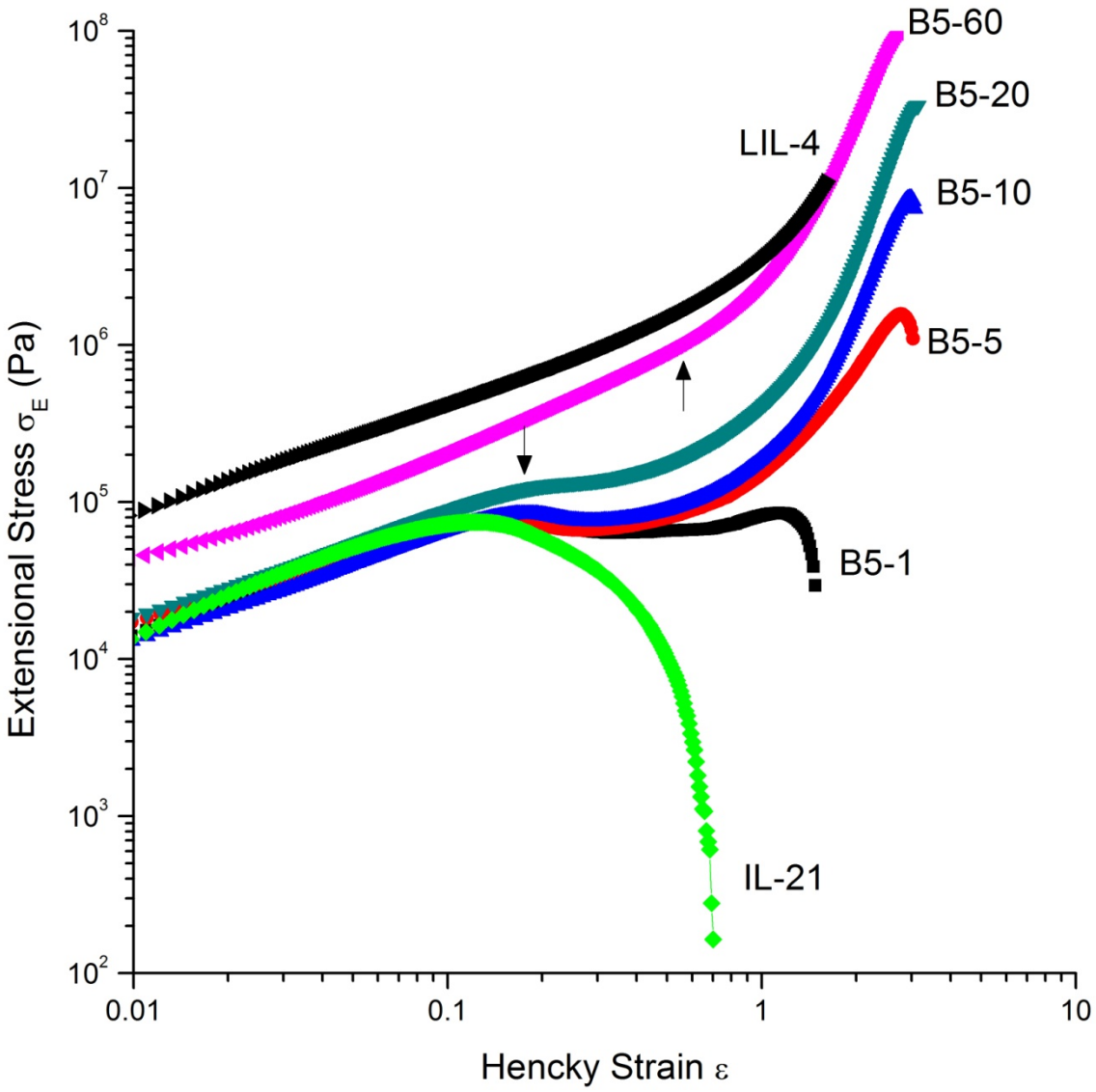

Figure 6.20 Extensional stress σ_E of selected blends from B5series by applying true (Hencky) strain ε of 1 s^{-1} rate at 37 ^oC. Sample names are denoted near failure points and colors are used for clear representation. The variation in σ_E for $\varepsilon < 0.05$ are attributed to an experimental artifact.

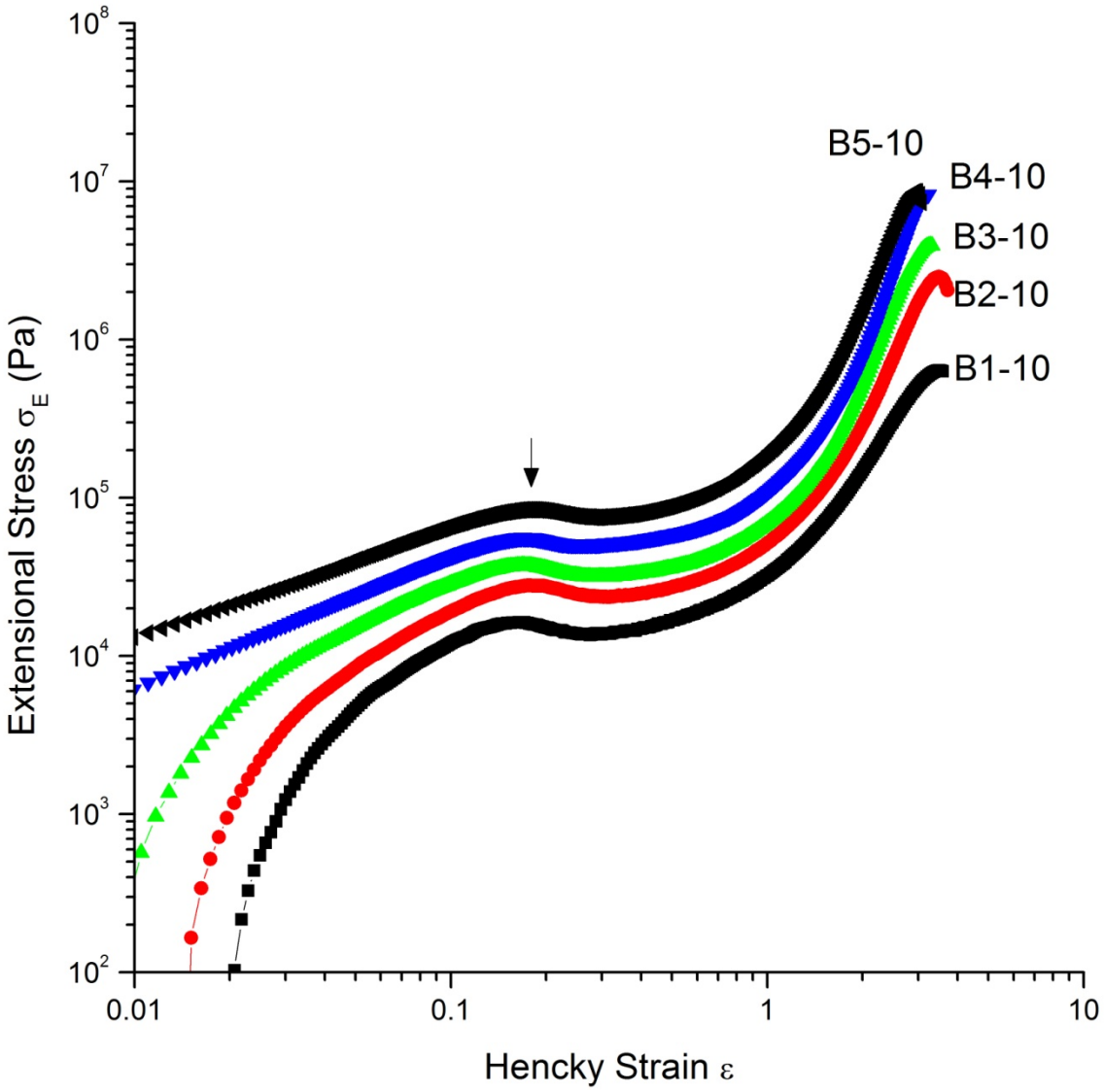

Figure 6.21 Extensional stress σ_E and true strain ε by varying IL-20/IL-21 composition at 10 wt. % of LIL-4. Extensional stress shift by the diblock copolymer composition is evident.

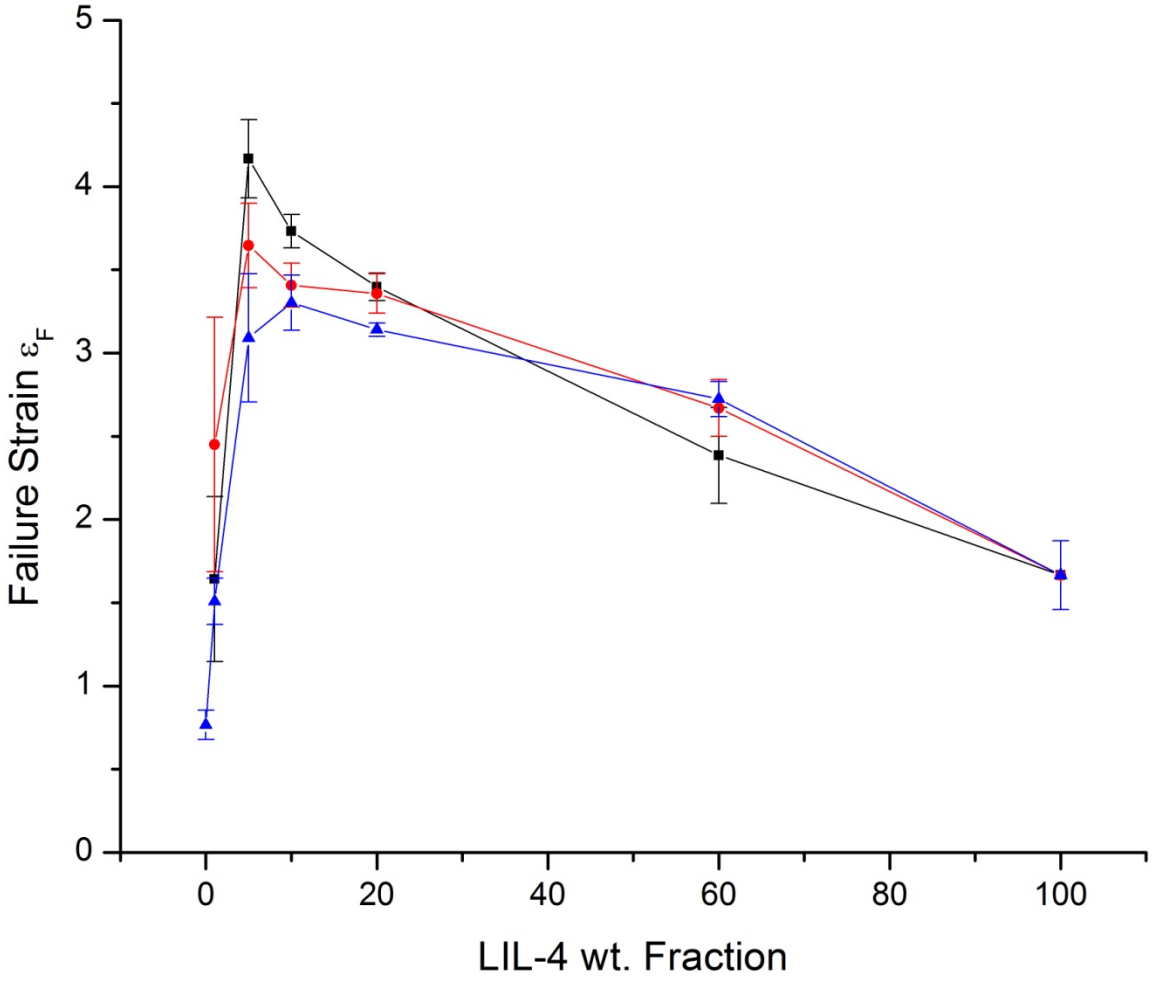

Figure 6.22 Failure strains ε_F versus LIL-4 wt. fraction of B1(■), B3(●), and B5(▲) series.

Colors are used for clear representation.

approximately an order of magnitude and showed the highest failure stress ($\sigma_{E,F} \approx 2\times10^7$ Pa) among the B1 samples, but a smaller failure strain, $\varepsilon_F = 2.4$, than those of other samples; This material strain hardens beginning at $\varepsilon \approx 0.60$ (marked by the up arrow in Figure 6.18). Finally, pure LIL-4 showed the highest linear σ_E, but failed at a smaller strain ($\varepsilon_F = 1.7$) and stress ($\sigma_{E,F} \approx 1\times10^7$ Pa) than B1-60.

The other series of blends (B3 and B5) produced qualitatively similar extensional properties as shown in Figure 6.19 and 6.20. In each system, non-linear behavior begins at $\varepsilon \cong 0.15$ (marked by down arrows in Figure 6.19 and 6.20) for mixtures containing up to 20 % LIL-4 with the maximum ε_F occurring with just 5 % triblock copolymer.

Figure 6.21 compares the extensional stress as a function of the Hencky strain at a constant 10 wt. % LIL-4 loading and variable amount of IL-20 relative to IL-21. Varying the diblock composition leads to significant quantitative changes in σ_E at $\varepsilon > 0.15$, and qualitative differences when $\varepsilon < 0.1$. Above a strain of 0.15, the stress-strain curves shift up vertically with increasing amounts of IL-21. Thus, the extensional stresses and strains can be tuned by adjusting the overall amount of each diblock and the triblock copolymers.

6.4 Discussion

The mechanical properties of block copolymers are directly related to the underlying microstructures, which depend on the molecular architecture, and composition.[104, 232] In this work, the phase behavior and mechanical properties of blends

prepared from moderate molecular weight LIL-4 triblock and low molecular weight IL-20/IL-21 diblock copolymers were characterized

Based on the phase behavior study of IL diblock copolymers described in chapter 5, the χN value for IL-20 and IL-21 are both close to about 30. The observed BCC morphology for IL-20 (f_L = 0.22) at 85 ^oC (Figure 6.2a) is consistent with the IL diblock copolymer phase diagram shown in Figure 5.5, but IL-21 (f_L = 0.41) at 80 and 200 ^oC displayed a HEX morphology, which is different than the (lamellar) phase at the corresponding f_L in the phase diagram. Because the IL phase diagram in Figure 5.5 was constructed using the IL diblock copolymers with approximately half the molecular weight to that of IL-21, this discrepancy may be a reflection of the relatively high χN and the conformational asymmetry of the PI and PLA blocks.[198] The $T_{g,PLA}$'s of IL-20 and IL-21 diblock copolymers are significantly lower than the value of high molecular weight poly(DL-lactide), $T_{g,PLA} \approx 60$ ^oC, clearly reflecting the effect of the low PLA block molecular weights.

Despite the well ordered BCC morphology documented for IL-20 at 85 ^oC, the SAXS pattern obtained from the solvent casted specimen showed only a broad primary peak at q = 0.049 $Å^{-1}$ and broad secondary peak near $q \cong 0.08$ $Å^{-1}$. This SAXS pattern is consistent with liquid-like packing (LLP) of spheres.[2, 191, 193, 195, 249, 250] This result suggests that the solvent casting procedure used to prepare the blends leads IL-20 to a

state of microphase separation, but was not effective in promoting long-range into a BCC morphology.

The linear viscoelastic moduli (G' and G") of the pure block copolymers are weakly dependent on the molecular weight and molecular architecture, i.e., AB or ABA block sequence, as shown in Figure 6.4, but the extensional rheology is hugely dependent on the architecture of the block copolymers as presented in Figure 6.23. The extensional measurement with the pure diblock copolymer IL-21 (Figure 6.23) showed a linear response up to the linear strain limit $\varepsilon \approx 0.15$, and started to deviate thereafter and failed at $\varepsilon_F \approx 0.7$ following a drastic decrease in the extensional stress (strain softening), down to $\varepsilon_{E,F} \approx O(3\times10^2)$ Pa prior to rupture. In contrast, the thermoplastic elastomer LIL-4 showed strain hardening behavior after the linear strain regime as other typical ABA block copolymers, and then failed at $\varepsilon_F \approx 1.7$ and $\sigma_{E,F} \approx 1\times10^7$ Pa (Figure 6.23).[225, 232]

All the solvent cast blend specimens except B1-5 showed multiple broad SAXS peaks consistent with a lack of long-range ordered structures. The two characteristic peak positions marked by * and arrows in Figures 6.6, 6.7 and 6.8 suggest some degree of phase separation into LIL-4 and diblock copolymer macrophases, which contain microphase separated structures. This interpretation is also evidenced by the two qualitatively different domains observed in the TEM micrographs obtained from B5-60, B5-20, and B3-60 (Figure 6.10, 6.11, and 6.12). The regions with large domain spacing correspond to the peak positions labeled "*" in the blend SAXS patterns ($q \approx 0.01$ Å^{-1} and

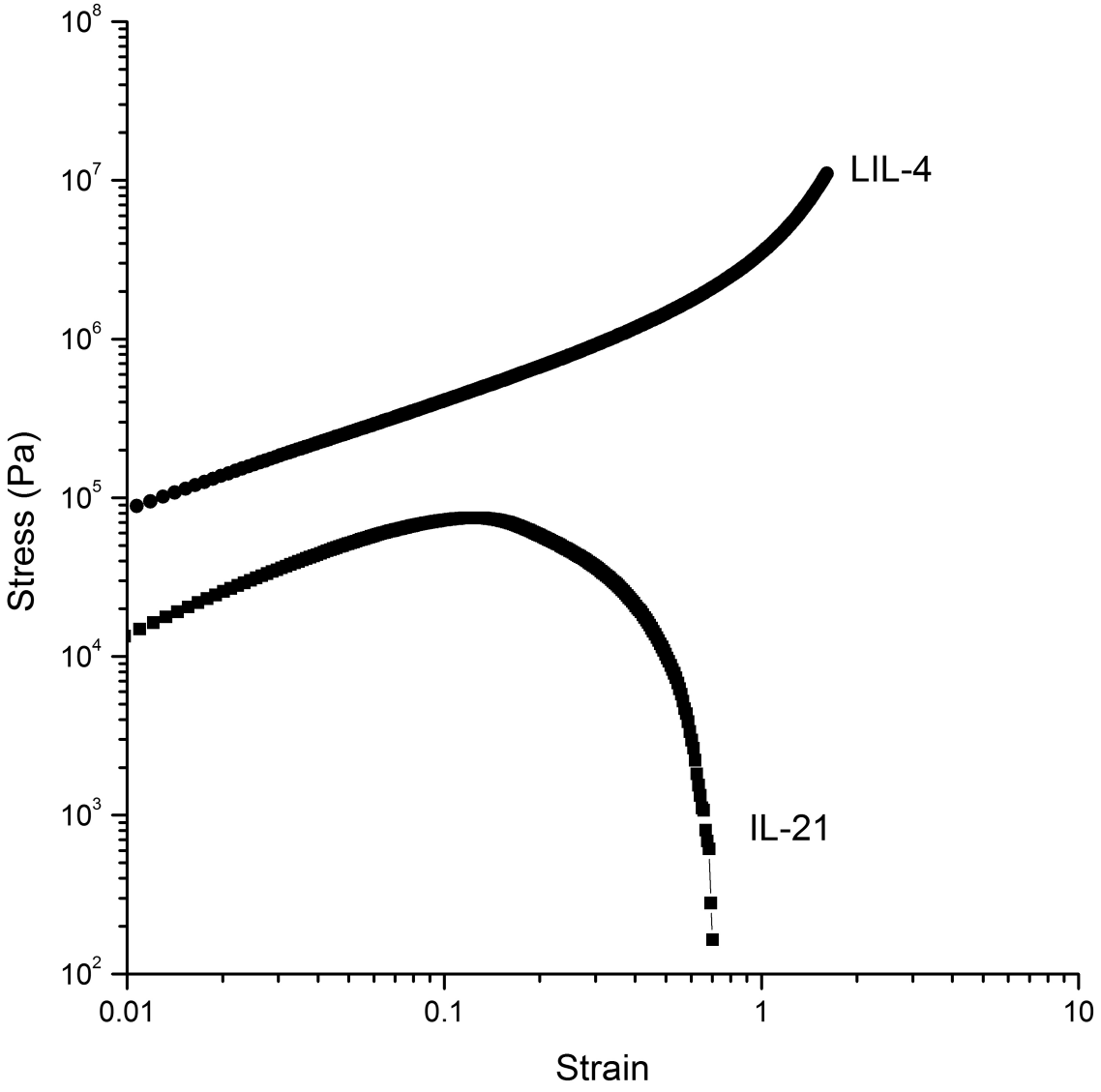

Figure 6.23 Extensional stress σ_E and true (Hencky) strain ε obtained from IL-21 AB type diblock copolymer and LIL-4 ABA type triblock copolymer.

$D \approx 60$ nm) and the relative sizes of these LIL-4 rich regions represent less than 10 % of the area of the micrographs, which is qualitatively consistent with the relative sizes of the peaks labeled "*" versus those identified with arrows. These two regions are believed to be LIL-4 rich (labeled "*", large domain spacing) and diblock copolymer rich (labeled arrows, smaller domain spacing) regions based on the relative molecular size and characteristics of the TEM micrographs (nearly pure PLA domains are much brighter than the stained PI domains).

Figure 6.24 illustrates the phase behavior deduced for the IL-21 rich region of blend B5-20 based on the SAXS and TEM data as a representative case. As observed in the TEM micrographs, the observed area of the LIL-4 rich domains (less than 5 %) is smaller than the overall amount of LIL-4 (20 wt. %) in the blend. This indicates that most of the triblock copolymer is mixed with the IL-21 diblock and is present in the IL-21 rich domains. This conjecture is supported by the intermediate domain spacing of B5-20 ($d_1 \approx d_2 \cong 20$ nm, see Figure 6.24), which lies between the domain spacing of IL-21 ($D_1 \approx 17$ nm) and LIL-4 ($D_2 \approx 39$ nm) as shown in Figure 6.9. The domain spacing of the diblock copolymer rich regions in the other blends also increases with the LIL-4 content (Figure 6.9), and the TEM micrographs obtained from B5-60 and B3-50 displayed relatively small areas of LIL-4 rich regions (less than 10 %), dictating that most of the LIL-4 is blended with diblock copolymers. Therefore, the mechanical properties of these blends described below mostly reflects the diblock rich regions.

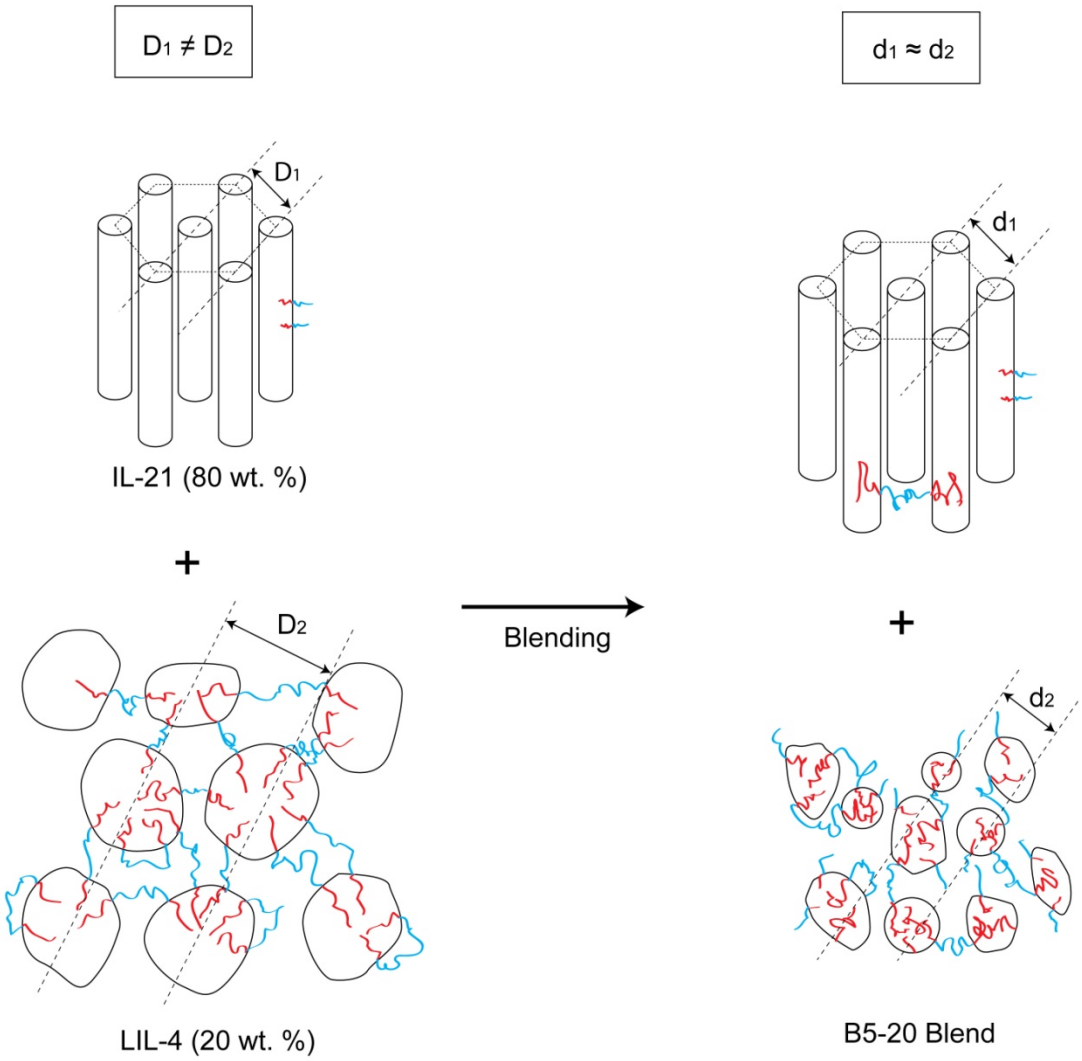

Figure 6.24 Schematic drawing of the phase behavior observed in blend B5-20.

The overall linear viscoelastic moduli (G' and G") of the blends (Figure 6.13 to 6.16) clearly show that these properties are restricted to the limited range determined by the lower limits set by IL-20 and IL-21 and the upper limits set by LIL-4. G' and G" of these blends are relatively insensitive to the blend compositions. As summarized in Figure 6.17, the elastic modulus G' for IL-20/IL-21 compositions at low LIL-4 content is dependent on the net w_{PLA}, reflected by the filler effects from the harder PLA domains (Table 6.2 and Figure 6.17).[232, 251] However, the origin of the parabolic dependence of G' with LIL-4 weight fraction at nearly symmetric compositions is not clear. One possible explanation is that a part of the chain configuration of the PI chains of LIL-4 in the diblock rich domains is confined by the domain spacings of the swollen diblock copolymers (i.e., smaller than the preferred domain spacing of LIL-4), and this might force the middle PI chains to adopt compressed PI chain configurations, which reduces the elastic modulus.

The linear ($\varepsilon \leq 0.15$) extensional stress σ_E of the blends with low content of LIL-4 (< 20 wt. %) has an obvious dependence on the IL-20/IL-21 composition as shown in Figures 6.18 to 6.21. This is consistent with the dependence of the linear elastic modulus G' on the IL-20/IL-21 composition, $\sigma_E \sim G'$. In contrast, the non-linear extensional stress ($\varepsilon \geq 0.15$) is dramatically dependent on the weight fraction of LIL-4 in the blend. Beyond the linear limit ($\varepsilon \geq 0.15$), the non-linear extensional stress σ_E measured with the blends containing low amount of LIL-4 (< 20 wt. %) initially decrease, followed by and strain

hardening, then failure at much larger strains than the failure strain (ε_F) of the pure diblock copolymer (Figure 6.20). However, the degree of the initial drop in stress diminishes with increasing LIL-4 content and finally vanishes at the higher triblock contents (B1-60, B3-60, and B5-60). Surprisingly, the blends with the high LIL-4 content display much improved mechanical properties near the point of failure relative to the pure LIL-4. The failure strains of these blends ($\varepsilon_F \approx 2.5$) are almost 50 % greater than that for pure LIL-4, $\varepsilon_F \approx 1.7$, and the extensional stresses at failure are approximately an order of magnitude higher than for LIL-4, $\sigma_{E,F} \approx 1\times10^7$ Pa. This is quite remarkable. We have demonstrated that the mechanical properties at the point of failure for an ABA triblock copolymer are improved by mixing with mechanically poor diblock copolymers.

In ideal linear deformation, elastomers accumulate all the applied stress (energy), and the associated strain is fully recovered when the stress is released.[1] However, in the non-linear regime, elastomers often connect part of an applied stress into permanent deformation, and this permanent set may not be recovered to the initial shape. Generally, such permanent material is manifested as strain softening (IL-21 in Figure 6.20) or strain hardening (LIL-4) behaviors.[252] We interpret the initial drop in the extensional stress at the beginning of the non-linear regime ($\varepsilon \geq 0.15$), and the subsequent abrupt increase, as evidence of both strain softening and strain hardening. This overall extensional behavior of the LIL-4/IL-20/IL-21 blends indicates that the diblock copolymers exert both strain softening and hardening effects on the triblock copolymer, even at rather low

concentration of LIL-4 (see Figures 6.18 to 6.21). However, detailed structural dynamics and mechanisms responsible for these results during the extensional deformation are not yet clear.

Finally, the non-linear behavior shown at small strain ($\varepsilon \approx 0.05$) in Figures 6.18 and 6.21 warrants a comment. This initial non-linearity appears to be related to an artifact in the measurement of the extensional stress. The $T_{g,PLA}$'s of the blends with high content of IL-20 are lower than the temperature (37 ^{o}C) for the extensional measurements. Because the extensional strain-stress measurements were conducted after a 3 minute annealing period, horizontally loaded samples with low $T_{g,PLA}$'s were stretched down by gravity on the EVF tool, and these gravitationally extended lengths are reflected in the initial measurements. This artifact, which is particularly apparent in Figure 6.21, is not considered any further.

We summarize two important observations from this preliminary work. First, the linear and non-linear behaviors of diblock/triblock blends can be decoupled by blending thermoplastic elastomer and (small molecular weight) diblock copolymers. The linear mechanical properties primarily dependent on the diblock copolymer compositions (IL-20/IL-21) but non-linear properties are mainly controlled by the thermoplastic elastomer (LIL-4). This observation suggests that there are numerous opportunities in the design and control of the mechanical properties of block copolymers especially for soft, but highly stretchable materials. Second, diblock copolymers can be used to improve the non-

linear mechanical properties of pure thermoplastic elastomers. As shown with the blend samples with 60 wt. % of LIL-4 (Figure 6.18 to 6.20), the failure strains and stresses are much improved over the pure LIL-4. This is definitely another design tool to achieve targeted mechanical properties of block copolymers near the point of failure.

Chapter 7
Path-Dependent Microstructures of Block Copolymer Non-ionic Surfactant in Oil and Water*

7.1 Introduction

Surfactants are essential compounds in biological systems to numerous chemical processes for manufacturing various industrial and daily products.[41, 253] In the past century, traditional low molecular weight surfactants (~ 500 g/mol) have been studied extensively, the thermodynamic and dynamic features of these compounds have been documented, yet the rich phase behaviors are still being explored.[49, 51, 75]

Along with traditional surfactant research, the advance of modern synthetic techniques enabled synthesis of various polymeric amphiphiles and heralded a new field

---

* Part of this work was published in 'Sangwoo Lee, Manickam Adhimoolam Arunagirinathan, and Frank S. Bates, *Langmuir*, 2010, 26, 1707'

of surfactant research.[59, 64, 254] Polymeric surfactants have two distinctive strengths relative to the traditional low molecular weight surfactants: freedom in the selection of blocks and facile control of block sizes. Along with these characteristics, the most distinctive thermodynamic characteristic of polymeric surfactants is a very low critical micelle concentrations (CMCs) that plummets with molecular weight.[46, 47, 255-265] This virtually eliminates the free chains, and thus prevents chain exchange between micelles. Thus, a polymeric surfactant system is generally non-communicative between micelles and trapped in a non-ergodic state.[48, 62, 257] As a consequence, the kinetic aspects of polymeric surfactants are extremely important and leading to highly non-equilibrium morphologies.[266]

In the research of emulsification of two incompatible materials, one of the most notable phenomena is the bicontinuous microemulsions.[57, 267] Extensive studies on this topic with the conventional nonionic surfactants revealed that a nonionic surfactant with higher molecular weight improves the efficiency of surfactants, dictating the required amount of surfactant to homogenize equal volumes of oil and water.[49, 51] However, large molecular weights also cause significant kinetic barriers to reaching thermodynamic equilibrium due to the low CMCs. For this reason, there are only a handful of studies on polymeric microemulsions and the overall understanding of these system is still very limited.[77, 78, 268-270]

In the past decade, the pioneering works by the Strey group showed non-ionic polymeric surfactants can be used as an additive to boost the surfactant efficiency of traditional non-ionic surfactants.[80-82] However, as Jakob *et al.* pointed out, attaining an equilibrium state in emulsification with pure polymeric surfactant is virtually impossible. We have confirmed this observation with our 2 year long evaluation of hundreds samples.[80] Our result revealed a pronounced path-dependency to block copolymer non-ionic surfactantcy, i.e. polymeric surfactants develop long-lasting metastable microstructures by evolving along different pathways depending on the initial states and processing methods.

This chapter addresses several topics related to the behavior of the polymeric non-ionic surfactant 1,2-poly(butadiene-*b*-ethylene oxide) (PB-PEO) diblock copolymer in oil, water, and both oil and water. Small angle X-ray scattering (SAXS) and cryogenic scanning electron microscopy (cryo-SEM) were employed to characterize the phase behavior and morphology of numerous conditions of phase ingredients as a function of order of mixing and annealing time.

7.2 Experimental

Material. PB-PEO diblock copolymer OB-29 was synthesized by anionic polymerization and the detailed synthesis and characterization techniques are described elsewhere.[60] OB-29 has a number-averaged molecular weight (M_n) of 33.1 kg/mol, a

weight fraction of PEO (w_{PEO}) of 0.72, and a polydispersity index (PDI) of 1.08. A mixture of HPLC grade water (Fisher) and 99.8 % deuterium oxide (Cambridge Isotopes) was used as PEO block selective solvent and double-distilled 1,5-cyclooctadiene (COD, > 99 %, Sigma) as PB block selective solvent. At the initial design stage of this experiment, neutron scattering experiments were planned using mixture of normal and heavy water, but were not conducted. For the remainder of this chapter, aqueous mixtures will be referred to as containing "water" without regards to the isotopic makeup. PEO homopolymer (M_n = 5 kg/mol) was purchased from Sigma and used as received in a solubility test in COD.

Mixtures. Undiluted OB-29 was prepared by freeze-drying process in benzene. Bulk OB-29 was dissolved in benzene, frozen in a freezer at ~ -20 ^{o}C, and the solution was dried under dynamic vacuum at room temperature. The solidified OB-29 solution remained frozen during the drying process due to the heat of sublimation (vaporization) of benzene. Two different procedures were employed to prepare equivolume oil-water samples. Water-first samples, named OB-29/W, were prepared by addition of the required amount of water to a pre-determined amount of freeze-dried OB-29 block copolymer in a glass vial. These solutions were vigorously vortexed for several hours and heated by hot air (> 45 ^{o}C) several times during the vortexing, followed by quiescent annealing at room temperature for over 1 week. Oil-first samples, referred to as OB-29/C, were prepared in the same manner as used for the preparation of the OB-29/W samples,

except that COD was used instead of water. Several high concentration samples, not easily homogenized by single vortexing, were centrifuged and vortexed repeatedly until apparently homogeneous binary mixtures were obtained. Ternary samples, termed OB-29/W/C or OB-29/C/W depending on the sequences of added solvents, were prepared by addition of the other solvent: the OB-29/W/C were prepared by adding COD to OB-29/W samples and OB-29/C/W were prepared *vice versa*, vacuum sealed, and vortexed for 3 hours with heating by hot air (> 45 ^{o}C). The vortexed samples were annealed at 45 ^{o}C for 3 days, and slowly cooled and stored quiescently at room temperature for at least 1 month.

DSC Differential scanning calorimetry (DSC) experiments were conducted with undiluted OB-29 and selected solution samples. In a hermetic aluminum DSC pan (TA instruments), 5 ~ 10 mg of samples were placed, mounted in a Q1000 TA Instruments calorimeter, heated to 80 ^{o}C at a rate of 10 ^{o}C/min, cooled to -100 ^{o}C, and then heated again at a rate of 10 ^{o}C/min to 80 ^{o}C. Reported DSC thermograms are acquired from the final heating step.

X-ray Scattering. Undiluted OB-29, binary and ternary solutions were characterized using synchrotron small angle X-ray scattering (SAXS) experiments performed at the DND-CAT (beamline 5I-D) at the Advanced Photon Source (APS) located at Argonne National Laboratory (Argonne, IL). The reported SAXS data was collected during two sessions using a Mar CCD area detector and a sample to detector distance of 6.53 m or 6.12 m and X-ray wavelength (λ) of 0.729 Å. Solution samples

were held in quartz capillaries at room temperature during the SAXS measurements. Two-dimensional data were azimuthally averaged to one-dimensional form of intensity (arbitrary units) versus the magnitude of the scattering wavevector [$q=4\pi\lambda^{-1}\sin(\theta/2)$]. Wide angle X-ray scattering (WAXS) measurements also were conducted at the APS with an area detector, a sample to detector distance of 0.134 m, and a wavelength (λ) of 0.729 Å.

SAXS Modeling The one-dimensional SAXS data of binary and ternary solution samples were modeled using IGOR Pro software version 6 (WaveMetrics). The scattering length densities of PB, PEO, COD, and water were determined by the electron density of each component at room temperature (PB and COD have nearly identical scattering length density). The form factor modeling was conducted using the following procedure. A proper particle form factor (hard sphere, cylinder, vesicle, or sheet) was selected based on microscopy results or the degree of agreement with experimental data. The key parameters among a host of structural parameters (core radius, core polydispersity, intensity factor) were first adjusted by hand, and then the other parameters were adjusted by machine fitting.

TEM Projected images of OB-29 were taken using transmission electron microscopy (TEM). Thin slices of OB-29 (~ 70 nm) were prepared using Reichert UltraCut S Ultramicrotome (Leica) at -80 ^{o}C and stained by OsO_4 vapor for 10 minutes at room temperature. The micrographs of OB-29 were acquired at room temperature using a

FEI Tecnai G^2 F30 field emission gun TEM operating at 300 kV equipped with a Gatan 4k × 4k pixels Ultrascan CCD camera.

Cryo-SEM. The microstructures of OB-29 in a solvent(s) were characterized by cryogenic scanning electron microscopy (cryo-SEM) using a Hitachi S-900 field emission gun scanning electron microscope operated at an accelerating voltage of 3 keV. Portions of the binary and ternary mixtures, removed from specific locations in the sample tubes, were transferred with a glass capillary to brass freezer hats (200 μm deep), which were then sandwiched together and frozen with streams of liquid nitrogen (~ 2100 bar) in ~ 9 ms. This procedure vitrifies water (and COD in case of ternary samples) and prevents the formation of significant amounts of solvent crystals which can alter or destroy surfactant microstructures. The frozen samples in the brass hats were fractured in liquid nitrogen, and the fractured surface as etched down to a prescribed depth at a pressure of approximately 10^{-4} Pa, leaving behind only block copolymer. Etching rates were controlled by the specimen temperature, which must be carefully regulated. The sublimation rate of vitrified water is known to occur at approximately 0.2, 2, and 20 nm/s at -110, -100, and -90 ^{o}C, respectively. In the case of COD, the sublimation rate could not be estimated because thermodynamic data is not available so it was determined roughly by observing etched depth of COD at the same etching conditions of vitrified ice. The determined sublimation rate of COD is approximately 30 % of the rate of ice at a given temperature. The etched samples were coated with platinum (~ 10 nm thick) at -130 ^{o}C,

and observed at -172 ^{o}C. Some of the cryo-SEM micrographs reported here were taken by Dr. Manickam Adhimoolam Arunagirinathan.

7.3 Result and Analysis

DSC thermal analysis of undiluted OB-29 showed that the PB domains have a glass transition temperature T_g = -7.0 ^{o}C and the PEO domains have a melting temperature, T_m = 63.4 ^{o}C with 72 % crystallinity (Figure 7.1a). The morphology of the bulk OB-29 was characterized by SAXS and TEM. SAXS results from bulk OB-29 at 140 ^{o}C showed a clear pattern of a lamellar morphology, q/q^* = 1:2:3:4:5:6:7 (q^* = 0.018 Å^{-1}) with the domain spacing $D = 2\pi/q^*$ = 34.8 nm (Figure 7.2a). However, the SAXS pattern at room temperature displayed less defined characteristics (Figure 7.2b) with the strongest peak position q^* = 0.015 Å^{-1}, and TEM micrograph revealed that the PEO domains (brighter domains in Figure 7.3) appeared layered though disconnected PEO domains with alternating features were evident (from right top to left bottom).

Strikingly, SAXS patterns of undiluted freeze-dried OB-29 (from benzene, up to 26.6 wt. %) were very different to the patterns of undiluted bulk OB-29. Freeze-dried OB-29 generated SAXS patterns with two or three broad peaks with $q^* \cong 0.046$ Å^{-1} regardless of the initial concentration of OB-29 in benzene (Figure 7.2c to g.). The ratio of peak positions was q/q^* = 1:2:3, possibly indicating a lamellar morphology with a

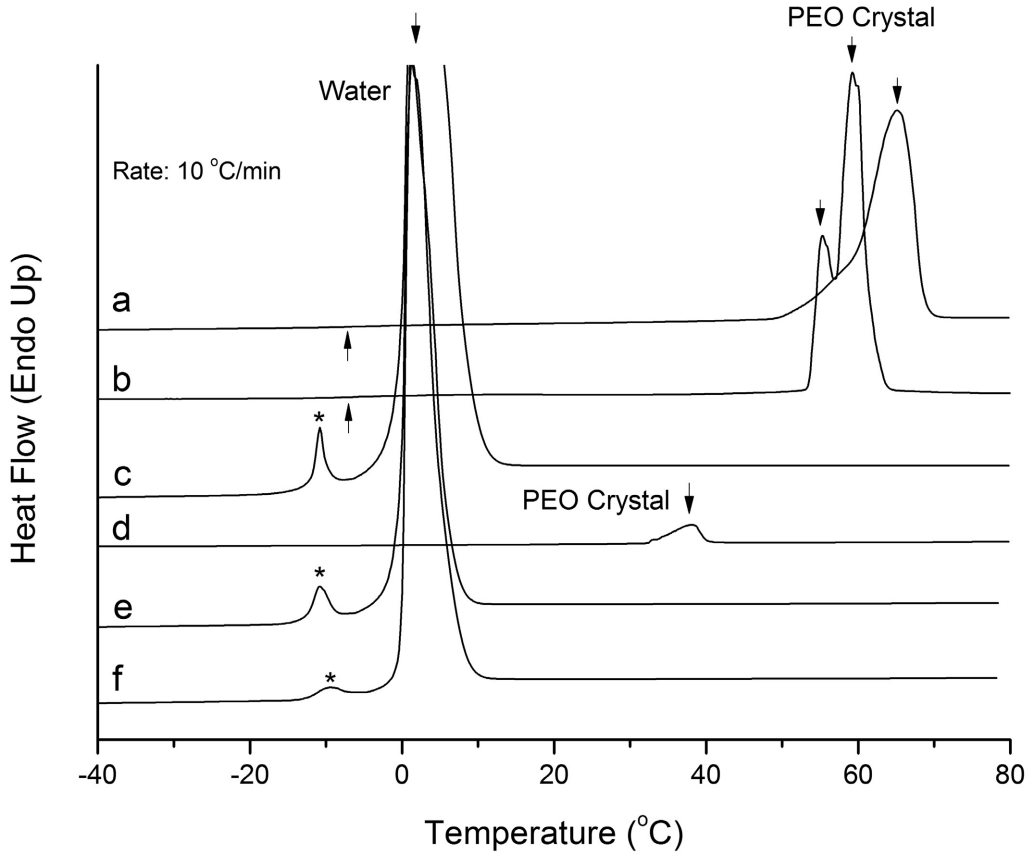

Figure 7.1 DSC thermograms of (a) undiluted OB-29, (b) freeze-dried OB-29 (4.4 wt. % in benzene), (c) OB-29/W-3, (d) OB-29/C-3, (e) OB-29/W/C-3, and (f) OB-29/C/W-3. The signature of the glass transition temperature of PB block $T_{g,B}$ = -7.0 °C is marked by an up arrow. Other crystal peaks are marked by down arrows. Melting of eutectic PEO crystals in water is denoted by a star (*).[271, 272] The degree crystallinity of PEO in bulk and freeze dried OB-29 were similar (72 and 65 % respectively) and greater than for OB-29/C-3 (33 %). DSC thermograms of other samples clearly show that no PEO crystals exists in the presence of water.

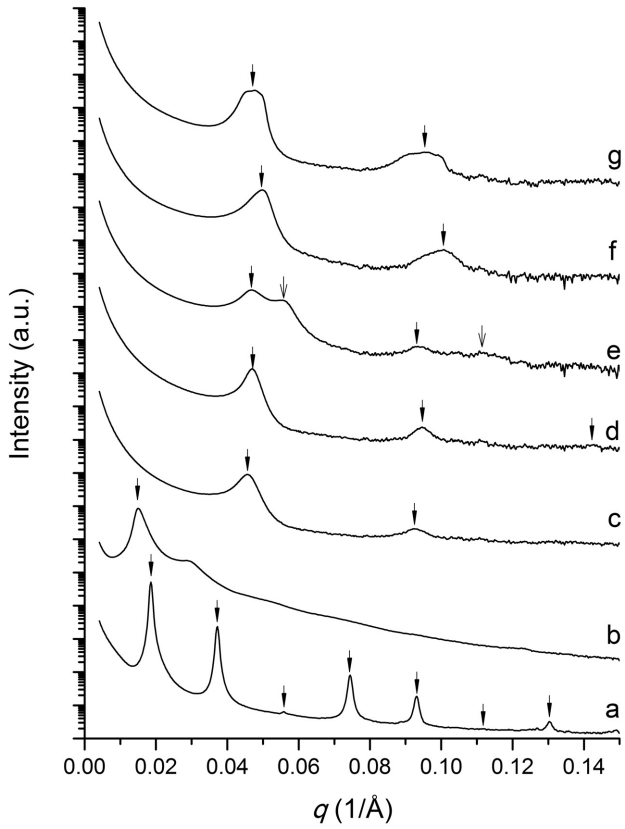

Figure 7.2 Synchrotron SAXS patterns of undiluted and freeze-dried OB-29. The SAXS pattern of undiluted OB-29 at 140 ^{o}C showed relative peak positions (q/q^* = 1:2:3:4:5:6:7 where q^* = 0.0186 Å^{-1}), consistent with the reflection conditions of a lamellar morphology (a). Undiluted OB-29 at 25 ^{o}C showed the SAXS pattern with only two distinctive peaks (q^* = 0.0150 Å^{-1}). The SAXS patterns of freeze-dried OB-29 in benzene showed nearly consistent peak positions (q/q^* = 1:2 or 1:2:3 where $q^* \cong$ 0.046 Å^{-1}) up to 26.6 wt. % in benzene, indicating possibly lamellar morphology (c: 2.6 wt. %, d: 4.4 wt. %, e: 9.3 wt. %, f: 16.3 wt. %, g: 26.6 wt. %). Satellite peaks (marked by line arrows in e) with different domain spacing were also observed.

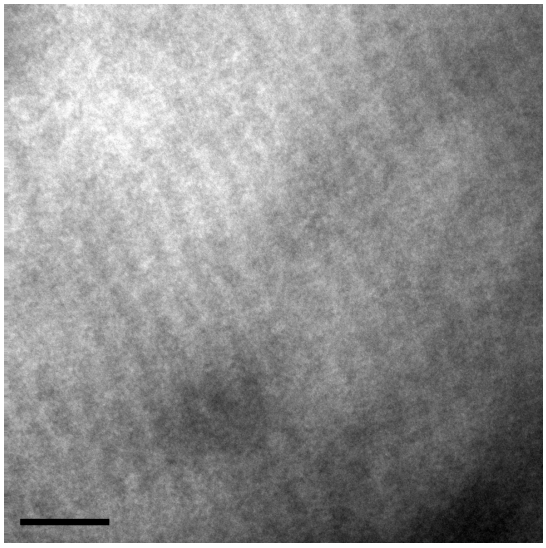

Figure 7.3 TEM micrograph acquired from a thin section of undiluted OB-29. The scale bar represents 100 nm. Although layered structures can be identified (from bottom left to the top right), PEO domains (white) appear undulating and ill-defined.

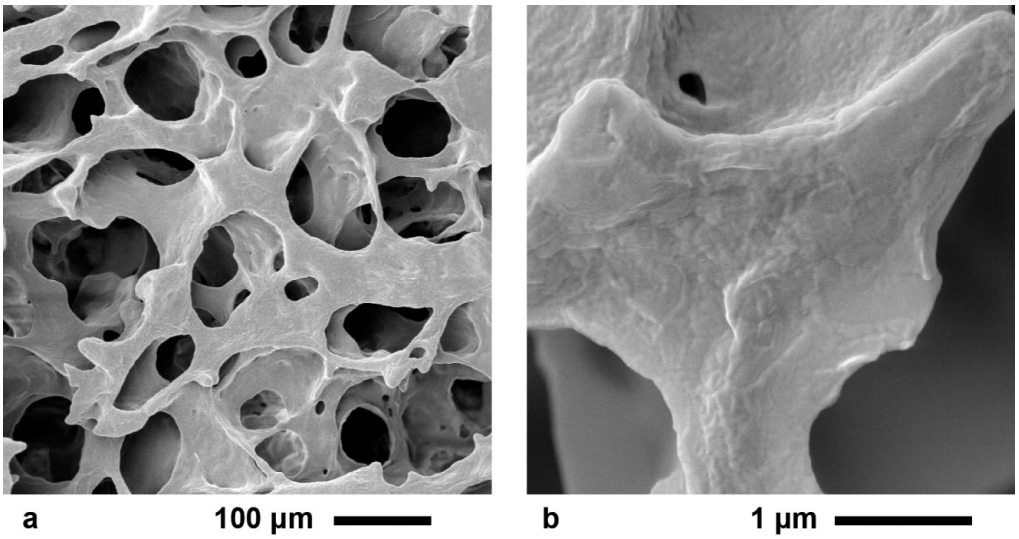

Figure 7.4 Cryo-SEM micrographs of freeze-dried OB-29 from benzene (4.4 wt. %).

domain spacing of roughly 14 nm, roughly 3 times smaller than for undiluted OB-29 at room temperature. However, cryo-SEM microscopy revealed that freeze-dried OB-29 has a porous structure (Figure 7.4) with sizes of around 50 - 200 μm, much larger than can be measured with the SAXS experiments. We return to these results in the discussion section.

The solubility of PB and PEO in COD was tested before block copolymer solution mixtures were prepared. A PEO (M_n = 5 kg/mol) solution in COD (5 wt. %) displayed a clear transparent state above 53 ^{o}C, but became slightly grayish and somewhat translucent at a lower temperature and formed an insoluble mat that sedimented after being annealed quiescently over a period of a few days to 1 week. These observations indicate the PEO solution in COD becomes a 2 phase state below 53 ^{o}C, PEO and COD rich phases. The compatibility of PB homopolymer was found to be completely miscible in COD at room temperature.

The binary solutions described below were prepared from freeze-dried OB-29 and sample compositions are listed in Table 7.1.

OB-29/W Binary Mixtures OB-29/W samples displayed bluish and somewhat translucent liquid states at low concentrations (< 7.1 wt. %, OB-29/W-4) and transparent gel-like states at high concentration (>9.1 wt. %, OB-29/W-5) as shown in the upper panel of Figure 7.5a. Thermal analysis of a representative sample, OB-29/W-3 showed no sign of PEO crystallinity (Figure 7.1c).

Table 7.1 List of OB-29 binary and ternary samples. OB-29/W and OB-29/C denotes the binary samples of OB-29 in water and COD, respectively. The order of added solvents to ternary samples are specified by the order of /W and /C. Selected binary samples were employed to prepare ternary samples (OB-29/W/C or OB-29/C/W).

Binary Sample (water)	**OB-29 wt. % in water**	**Ternary Sample (water-first)**	**OB-29 wt. % in COD and water**	**Binary Sample (COD)**	**OB-29 wt. % in COD**	**Ternary Sample (COD-first)**	**OB-29 wt. % in COD and water**
OB-29/W-1	1.8	OB-29/W/C-1	1	OB-29/C-1	2.1	OB-29/C/W-1	1
OB-29/W-3	5.5	OB-29/W/C-3	3	OB-29/C-2	5.0		
OB-29/W-4	7.2	OB-29/W/C-4	4	OB-29/C-3	6.3	OB-29/C/W-3	3
OB-29/W-5	8.9	OB-29/W/C-5	5	OB-29/C-4	8.2		
OB-29/W-6	10.7			OB-29/C-6	12.2		
OB-29/W-7	12.4			OB-29/C-7	14.0		
OB-29/W-9	15.8			OB-29/C-8	15.9		
OB-29/W-10	17.2	OB-29/W/C-10	10	OB-29/C-10	19.0	OB-29/C/W-10	10
OB-29/W-11	31.7			OB-29/C-11	35.0		
OB-29/W-12	55.0			OB-29/C-12	59.1		
OB-29/W-13	71.6			OB-29/C-13	71.6		
				OB-29/C-14	88.4		

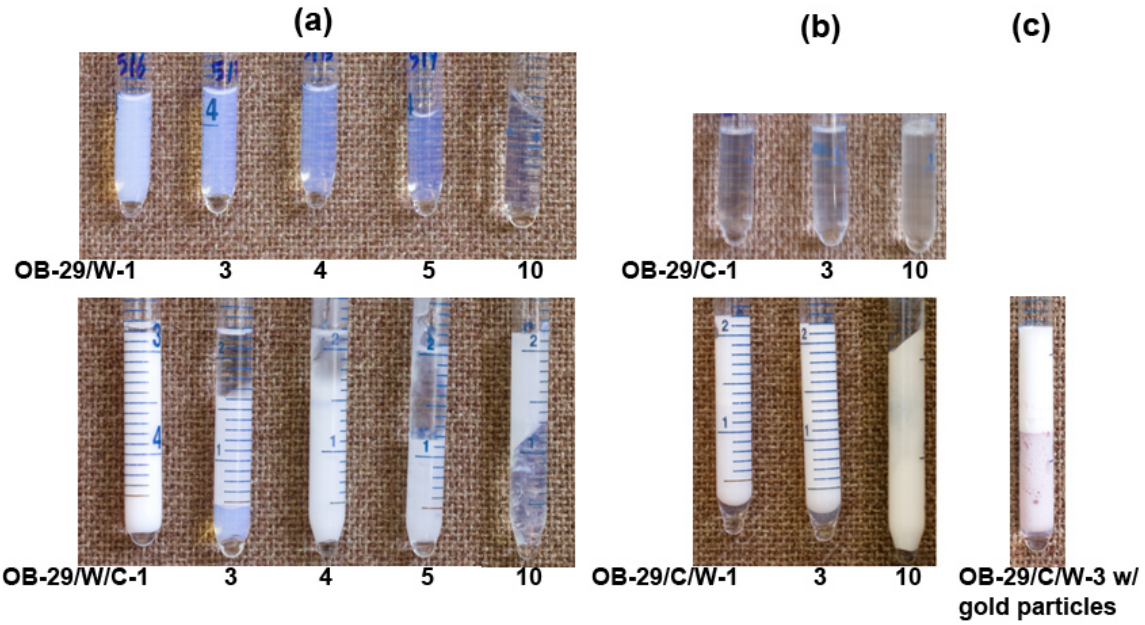

Figure 7.5 Bulk appearance of selected binary and ternary samples. (a) OB-29/W and OB-29/W/C series. The OB-29/W series show bluish and somewhat translucent appearance at low concentration and the opalescence gradually decreases and become a gel-like state at 17.2 wt. % (OB-29/W-10). By addition of COD, the ternary OB-29/W/C samples formed three layers at lower concentrations (< 7.2 wt. % in water, OB-29/W-4) and two layers at higher concentration (> 8.9 wt. %, OB-29/W-5). (b) OB-29/C and OB-29/C/W series. OB-29/C series becomes more translucent as the block copolymer concentration increases. By addition of water, OB-29/C/W-1 and 3 generated three layers. OB-29/C/W-10 appeared inhomogeneous and vigorous shaking this sample revealed a milky lower with low viscosity and gel-like upper layers. (c) Addition of hydrophilic 5 nm gold particles to OB-29/C/W-3 revealed a hidden lower layer in the milky top part.

SAXS patterns obtained from OB-29/W samples containing up to 7 wt. % diblock copolymer (OB-29/W-1, 3, and 4) (Figure 7.6) were analyzed using a spherical micelle form factor with calculated core radii $R_c \cong 21$ nm with $\Delta R/R = 0.07$. However, SAXS patterns of OB-29/W samples of intermediate concentrations (OB-29/W-4 to 11) could not be analyzed by either of spherical, cylinderical, or sheet form factors. Highly concentrated samples containing 55 wt. % OB-29 (OB-29/W-12 and 13) show SAXS patterns with Bragg's reflections consistent with hexagonally packed structures ($q/q^* = \sqrt{1}: \sqrt{3}: \sqrt{4}: \sqrt{7}: \sqrt{9}$).

Complementary real-space morphology information was obtained using cryo-SEM from four representative OB-29/W samples: OB-29/W-3, 5, 10, and 12. Figure 7.7a shows the cryo-SEM micrographs obtained from OB-29/W-3, showing spherical micelles, consistent with the form factor analysis of the OB-29/W-3 SAXS pattern (Figure 7.6). These spherical features were also dominant in OB-29/W-5 (8.9 wt. %), but not discrete. The spherical microstructures are embedded in thin sheet-like structures as shown in Figure 7.7b and c. As shown, the thickness of these sheet structures are apparently smaller than the diameter of spherical features (arrow in Figure 7.7c). OB-29/W-10 (17.2 wt. %) presented a randomly interconnected network morphology, but closer examination revealed hemi-spherical surface features of this network structure (Figure 7.7d and e). The last representative sample, OB-29/W-12 (55 wt. %) showed short cylinders (Figure

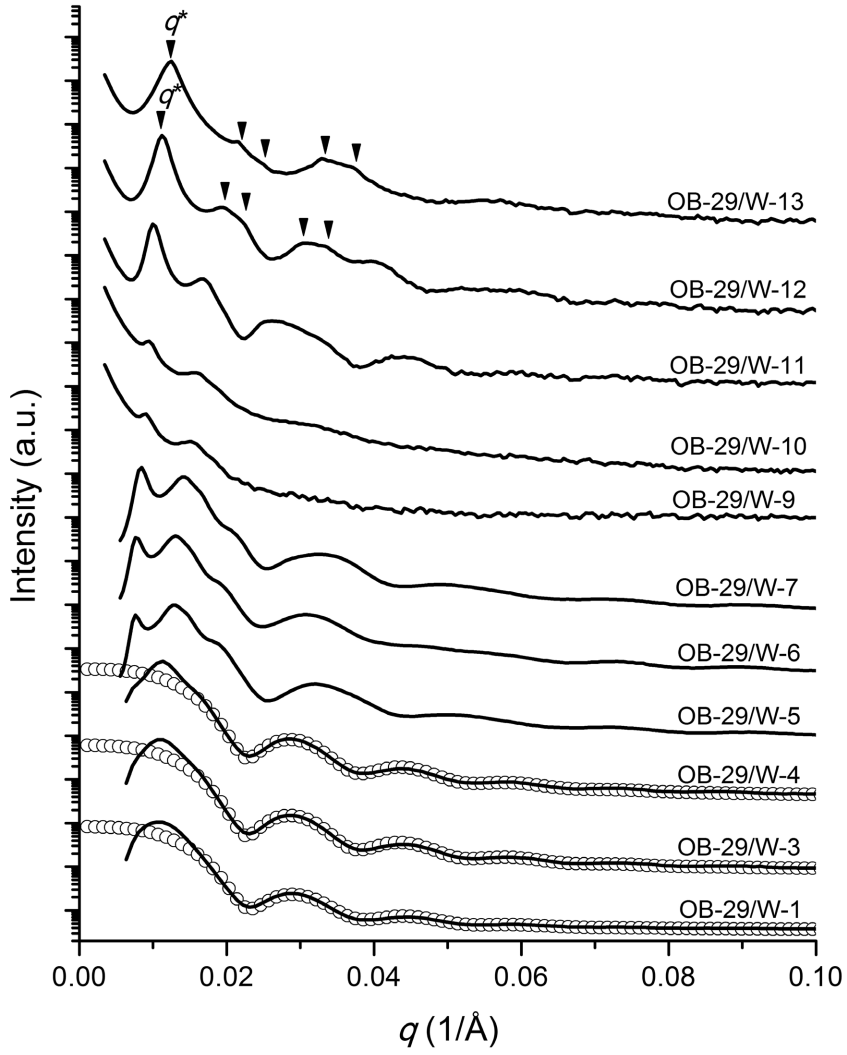

Figure 7.6 Synchrotron SAXS patterns obtained from OB-29/W samples (—) and calculated sphere form factor scattering fit to the OB-29/W-2, 3, and 4 SAXS patterns (○). The calculated radii R of spheres of OB-29/W-2, 3, and 4 were 20.9, 20.5, and 20.7 nm, respectively with the core polydispersity $\Delta R/R = 0.07$. The solid inverse triangles (▼) on OB-29/W/-12 and 13 patterns indicate the Bragg reflections for hexagonally packed structures ($q/q^* = \sqrt{1}:\sqrt{3}:\sqrt{4}:\sqrt{7}:\sqrt{9}$).

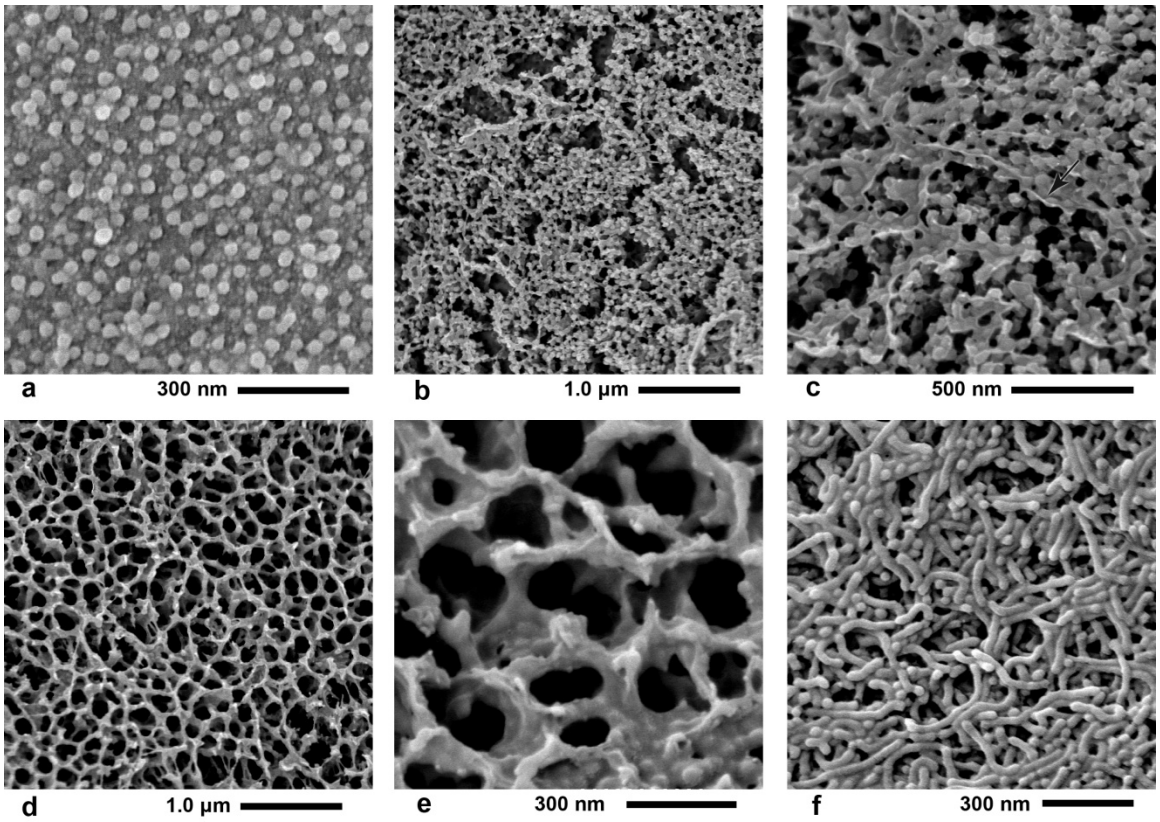

Figure 7.7 Representative cryo-SEM micrographs obtained from OB-29/W samples. (a) Spherical micelles of OB-29/W-3 (5.5 wt. %). Low magnification micrograph (b) and high magnification micrograph (c) of OB-29/W-5 (8.9 wt. %) reveal that spheres are interconnected by sheet structures (arrow). Low magnification micrograph (d) of OB-29/W-10 (17.2 wt. %) shows interconnected network structure with embedded spheres at the junctions (e). (f) Cylinderical micelles of OB-29/W-12 (55.0 wt. %)

7.7f), and these structures are believed the hexagonally packed in a solution state as evidenced by the SAXS pattern shown in Figure 7.6.

OB-29/C Binary Mixtures The visible appearances of the OB-29/C binary samples were grayish and translucent at room temperature similar to the two phase state of the 5 wt. % PEO homopolymer solution in COD, and the degree of translucence was proportional to the concentration of OB-29 (Figure 7.5b upper panel). These solutions could be easily clarified by heating above 45 ^{o}C, and these appearances were reversible by heating and cooling. In a quiescent state, OB-29/C-1, 2, and 3 formed a solvated PB-PEO mat because of the high-density crystalline PEO domain, but could be easily homogenized by gentle stirring. Thermal analysis of a representative sample, OB-29/C-3, showed an exothermic peak at 38 ^{o}C (Figure 7.1d), indicating PEO crystals, confirmed by the WAXS pattern in Figure 7.8.

The microstructures of the OB-29/C samples were characterized using synchrotron SAXS experiments (Figure 7.9). Low concentration samples (OB-29/C-1 to 10, up to ~ 20 wt. %) displayed a similar pattern, smoothly decaying intensity with several bumpy features followed by an upturn around 0.10 Å^{-1}. For clear representation, the expanded SAXS pattern of OB-29/C-3 is shown in Figure 7.10. Because these SAXS patterns could not be easily characterized, real-space morphology information on OB-29/C-2 and 3 was sought using cryo-SEM microscopy. These samples showed disordered sheet-like structures (Figure 7.11a), but high-magnification micrographs showed a

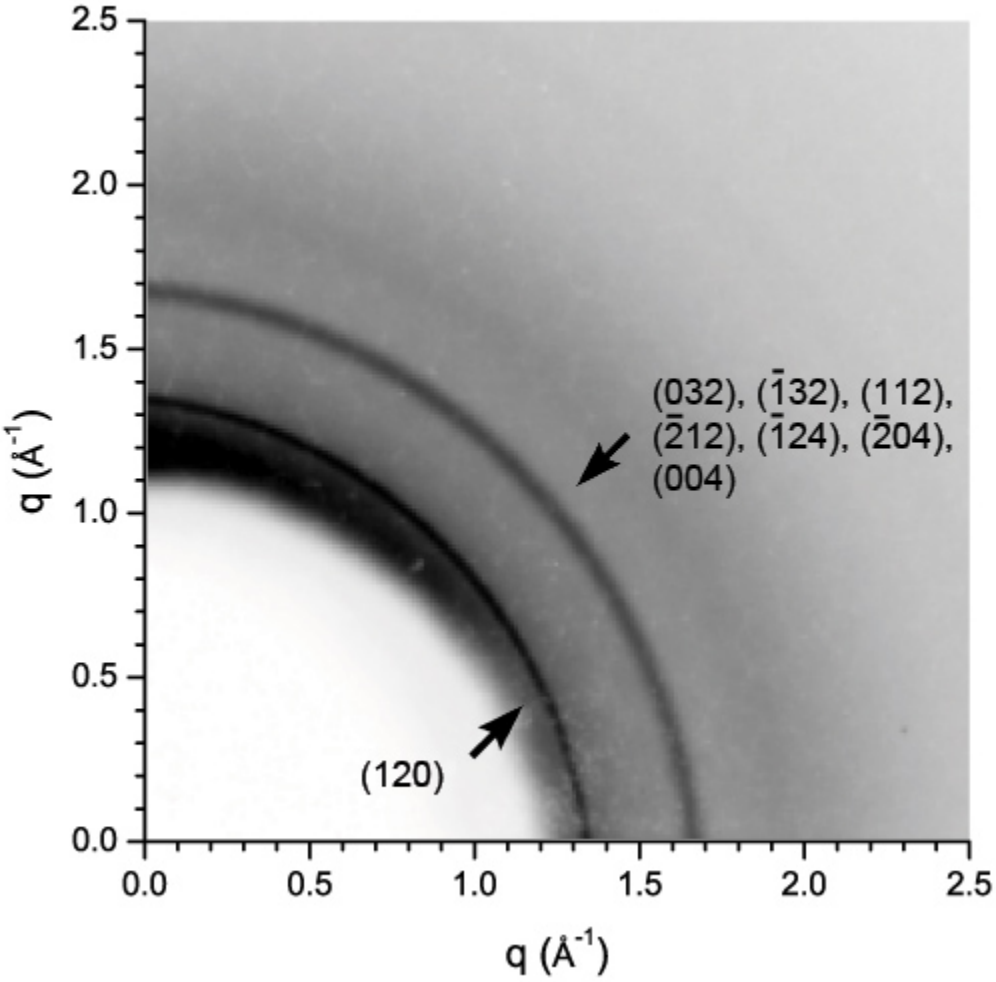

Figure 7.8 Two-dimensional WAXS powder pattern from OB-29/C-3. Bragg reflections are assigned to the first two peaks on the basis of the indexing reported in the literature.[273]

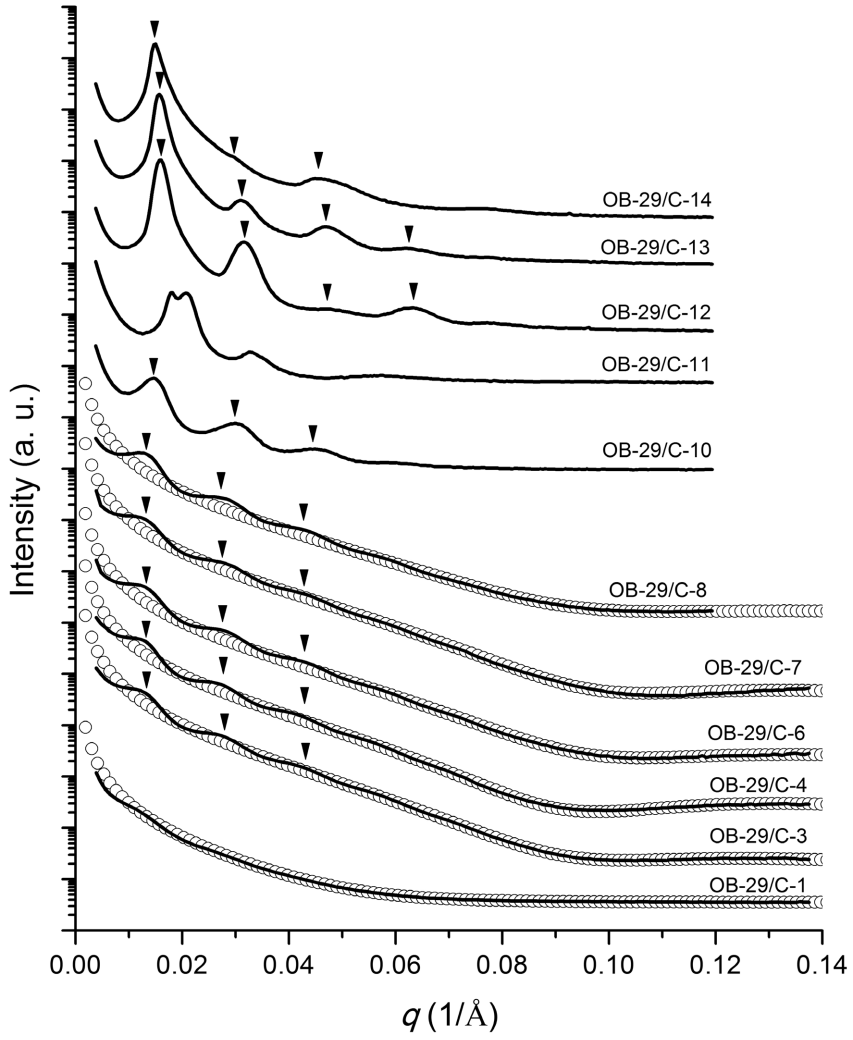

Figure 7.9 Synchrotron SAXS patterns obtained from OB-29/C samples (—) and calculated sheet form factor scattering fir to the experimental scattering patterns (○). The calculated sheet thickness L of OB-29/C-1 to 8 was 6.7 nm ± 0.5 nm with the sheet thickness polydispersity $\Delta L/L = 0.17 \pm 0.08$. The solid inverse triangles (▼) on SAXS patterns mark the Bragg reflections consistent with a lamellar morphology ($q/q^* = 1{:}2{:}3$ for OB-29/C-1 to 10 and $q/q^* = 1{:}2{:}3{:}4$ for OB-29/C-12 to 14).

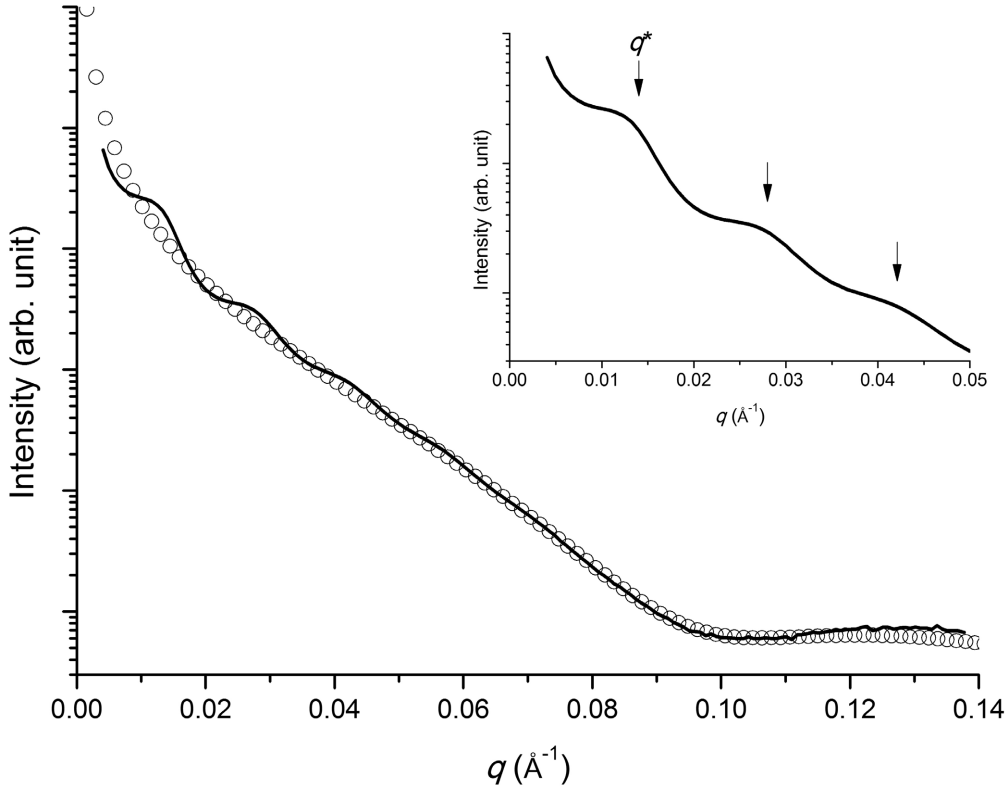

Figure 7.10 Synchrotron SAXS pattern obtained from OB-29/C-3 (solid line, —) and sheet form factor calculation (○). Inset shows the Bragg reflections of lamellar morphology (q/q^* = 1:2:3).

layered morphology (Figure 7.11b), suggesting lamellar phase with alternating swollen PB domains and semi-crystalline PEO domains. In the interpretation of cryo-SEM micrographs, caution should be exercised. The layered morphology might be a result of agglomeration of microstructures during the sublimation of solvent in the preparation of cryo-SEM specimens. However, the bumpy features on the SAXS patterns of OB-29/C-1 to 10 were interpreted as the lamellar reflections ($q/q^* = 1:2:3$ where $q^* \cong 0.015$ Å^{-1} and the domain spacing $D = 2\pi/q^* \cong 42$ nm), indicating the lamellar morphology in Figure 7.11b more likely represents the microstructures in a solution state. Interestingly, the peak positions were nearly invariable regardless of OB-29 concentration up to ~ 16 wt. % (OB-29/C-10). Based on this microstructure geometry, the SAXS patterns of OB-29/C-1 to 8 were analyzed using a flat bilayer form factor model for $q \geq 0.05$ Å^{-1} and the extracted average PEO domain thickness was $L = 6.6$ nm ± 0.5 nm with the sheet thickness polydispersity $\Delta L/L = 0.17 \pm 0.08$.[111]

In contrast to the low concentration samples, the SAXS pattern of OB-29/C-11 (35 wt. %) was qualitatively different. Although a few Bragg reflections were observed, a definitive morphology could not be determined. Cryo-SEM characterization of this sample revealed rather lengthy microstructures, qualitatively different to the lamellar morphology (Figure 7.10c). At high magnification, this morphology looks rather flat, a ribbon-like morphology (Figure 7.10d), c.f. Figure 7.7f.

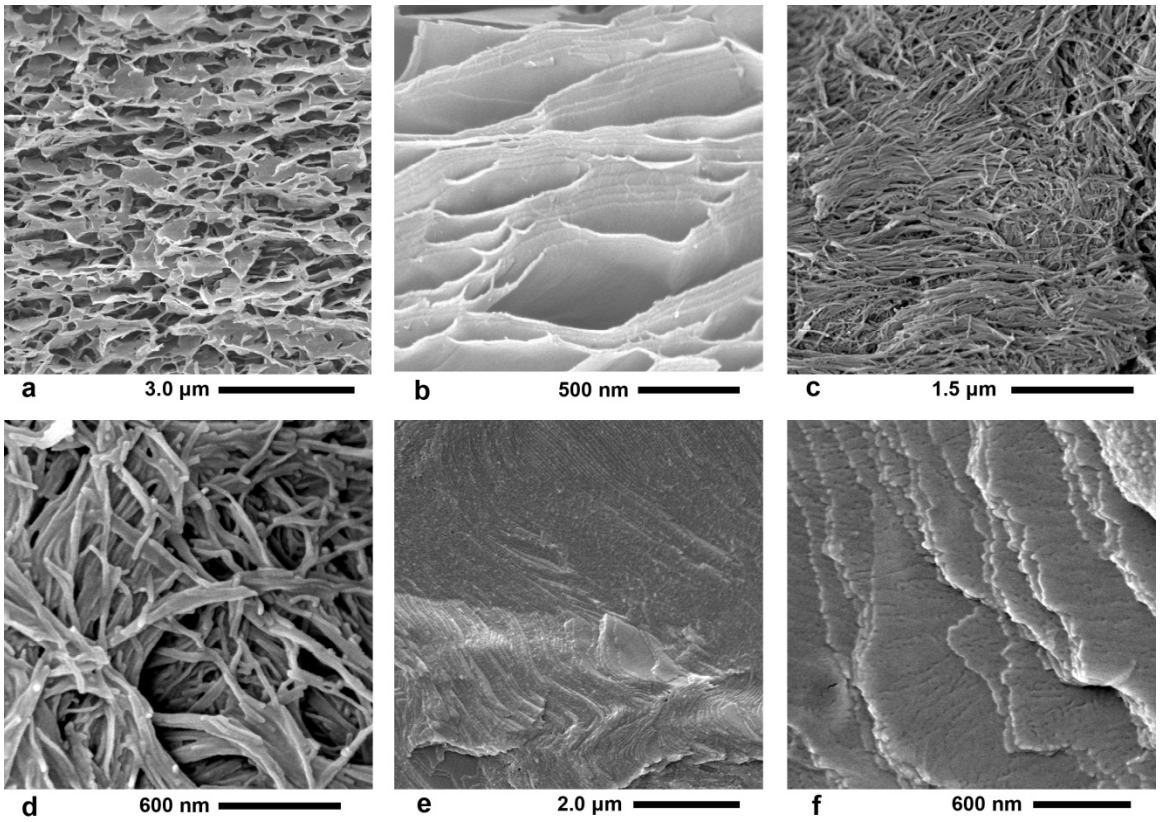

Figure 7.11 Representative cryo-SEM micrographs obtained from OB-29/C samples. (a) OB-29/C-3 (6.3 wt. %) displayed disordered sheet structures and (b) high magnification micrograph obtained from OB-29/C-2 (5.0 wt. %) revealed lamellar structures. Distinctive to other OB-29/C samples, the microstructure of OB-29/C-11 (35 wt. %) was loosely arranged ribbon-like structures aggregated along an axial direction (c and d), c.f. Figure 7.7f. A more concentrated sample, OB-29/C-12 (59 wt. %), displayed terraced lamellar structures (e and f)

The SAXS patterns of OB-29/C-12 to 14 displayed Bragg reflections consistent with a lamellar morphology and this was confirmed with cryo-SEM micrographs (Figure 7.10e and f). The domain spacings of these samples increased as the concentration of OB-29 increases: D = 39.5 nm for 59.1 wt. % (OB-29/C-12), 40.1 nm for 71.6 wt. % (OB-29/C-13), and 42.3 nm for 88.4 wt. % (OB-29/C-13).

OB-29/W/C Ternary Mixtures OB-29/W/C samples formed three layers at lower concentrations (< 7.2 wt. % in water, OB-29/W-1, 3, and 4) and two layers at higher concentration (> 8.9 wt. %, OB-29/W-5 and 10) as shown in the lower panel of Figure 7.5a. Sample forming three layers were in a liquid state, but when two layers formed, the bottom layer was in a gel-like state. The middle layer of OB-29/W/C-3 sample was thermally analyzed by DSC and showed no sign of crystallinity (Figure 7.1e).

The microstructures of the OB-29/W/C samples were characterized using the SAXS and cryo-SEM techniques. Top layers of OB-29/W/C-1, 3, and 4 produced featureless and relatively low intensity profiles, suggesting absence of block copolymer in the oil layer (Figure 7.12a, b and c). The SAXS patterns of the middle and lower layers of OB-29/W/C-1, 3 or 4 were nearly identical, but the lower layers showed roughly 3 to 5 times more intense SAXS pattern than the patterns of the middle layers. These middle and lower layer profiles were analyzed using a sphere form factor model and the calculated core radii were $R_c = 31 \pm 2$ nm with $\Delta R_c/R_c = 0.08 \pm 0.02$, indicating the PB core of spherical micelles of OB-29/W-1, 3, and 4 expanded by 50 % in radius by

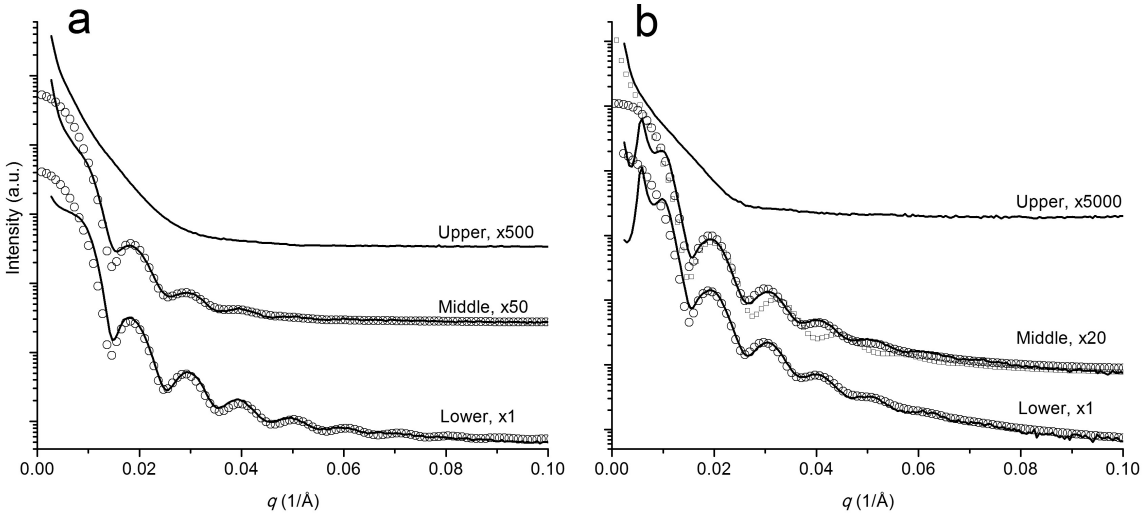

Figure 7.12 Synchrotron SAXS patterns of OB-29/W/C ternary mixtures. Panels c to d are shown in the next page for clear representation. Experimental data (solid line, —) and sphere form factor fitting results (○) are presented. (a) OB-29/W/C-1. (b) OB-29/W/C-3. White square represent a fitting result with a cylinder form factor model. See Figure A.4 in Appendix A for an enlarged representation (c) OB-29/W/C-4. (d) Expanded SAXS patterns of OB-29/W/C-4. Inverse triangles mark the Bragg reflections consistent with a face-centered cubic (FCC) symmetry [q/q^* = √3: √4: √8: √11:(√12: √16: √19: √20: √24:) √27: (√32:) √35 where q^* = 0.0059 Å^{-1}]. (e) OB-29/W/C-5. (f) OB-29/W/C-10.

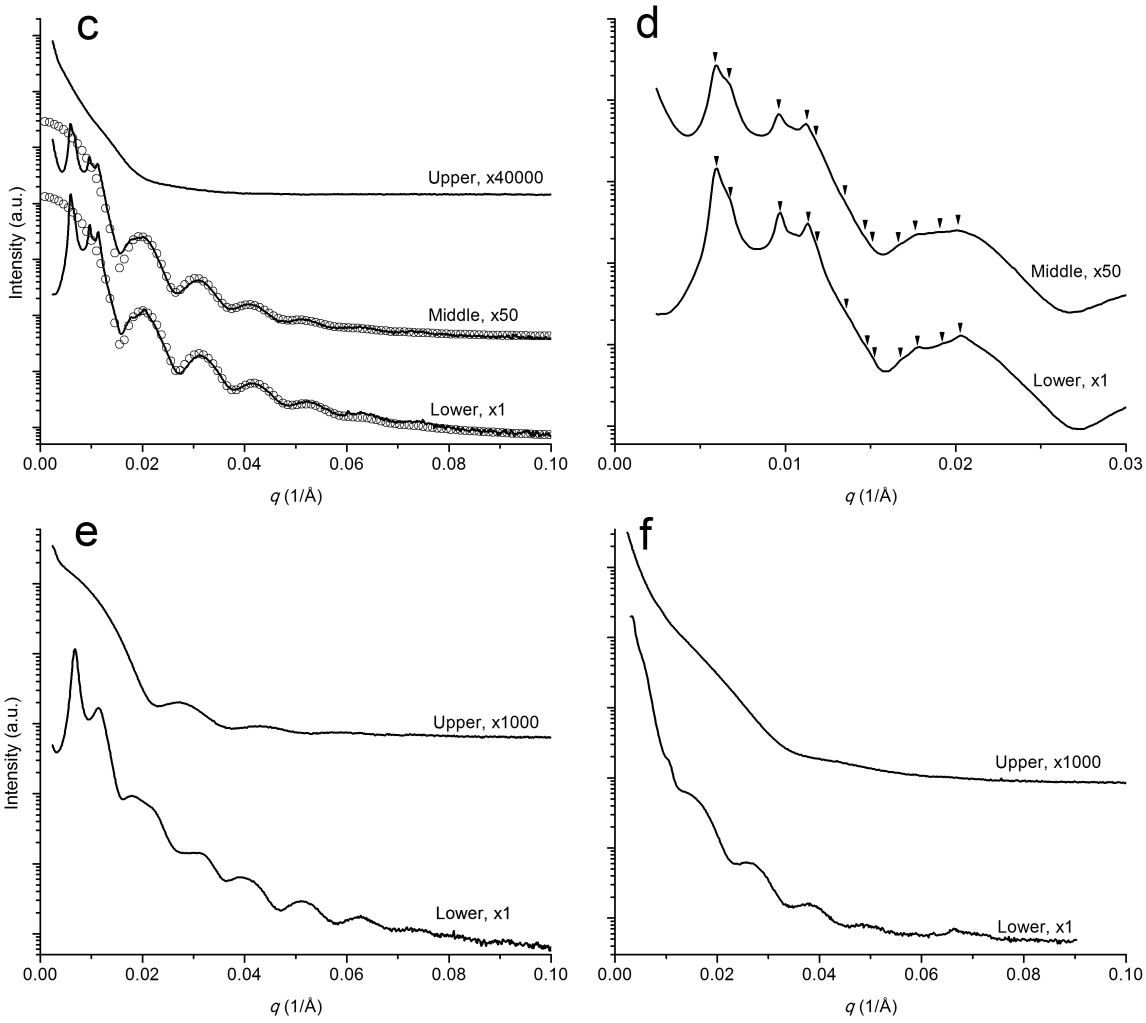

(Continued from the previous page)

imbibing COD.[109] However, cryo-SEM characterization of OB-29/W/C-1 and 3 revealed quite different microstructures to the spherical geometry. The fractured surface of OB-29/W/C-1 middle layer appeared to be a mixture of droplets at low magnification (Figure 7.13a), and two different types of droplets were found: solid droplets surrounded by sponge-like network microstructures with undulating connector features (Figure 7.13b and d) and droplets of the microstructures and solid surrounding (Figure 7.13c). These sponge-like microstructures were also observed in OB-29/W/C-3 (Figure 7.14a and b), but a network with struts of more cylinderical geometry were found together in other fractured areas (Figure 7.14c and d). Based on this observation, the SAXS pattern of OB-29/W/C-3 middle layer was also analyzed using a model of cylinder form (R_c = 26 nm, $\Delta R_c/R_c$ = 0.07, See Figure 7.12b and 7.24), but a noticeable deviation at the high q domain could not be avoided compared to the result with a sphere model.[109]

The middle and lower layer SAXS patterns of OB-29/W/C-4 were also characterized using a sphere form factor; more than 4 Bragg reflections were clearly identified in each case. Relative peak positions of the reflections were q/q^* = √3: √4: √8: √11:(√12: √16: √19: √20: √24:) √27: (√32:) √35 where q^* = 0.0059 Å^{-1}, consistent with the face-centered cubic (FCC) symmetry (Figure 7.12d). Using the core radius from the sphere form factor analysis (R_c = 29 nm) and the unit cell parameter of FCC (a = 123 nm), the volume fraction of swollen PB core was 22 %. Cryo-SEM characterization also found

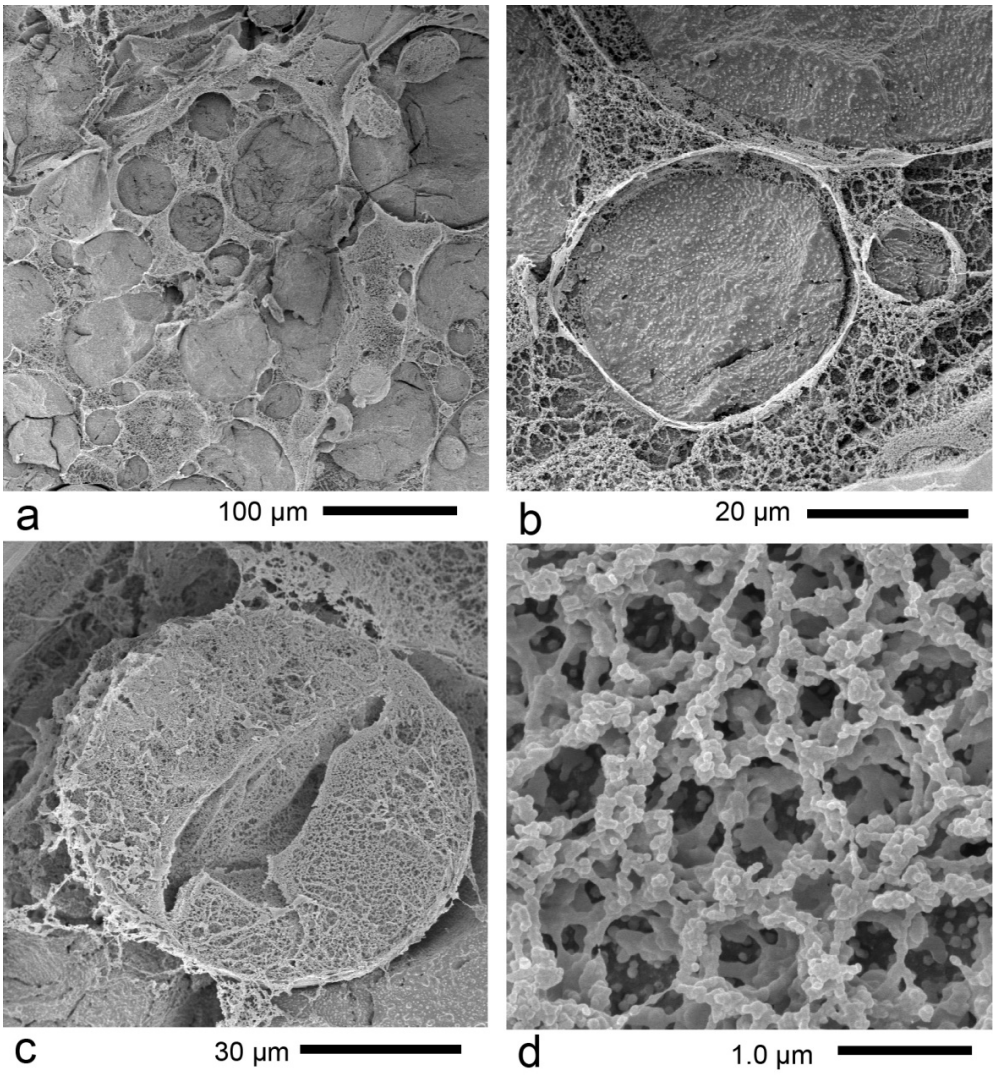

Figure 7.13 Representative cryo-SEM micrographs obtained from OB-29/W/C-1, middle layer. Low magnification micrograph shows (a) a few tens of micrometer scale droplets, and (b) droplets of solid filling surrounded by sponge-like microstructures and (c) droplets with inverse domains (b). Panel (d) presents magnified micrograph of the sponge-like microstructure.

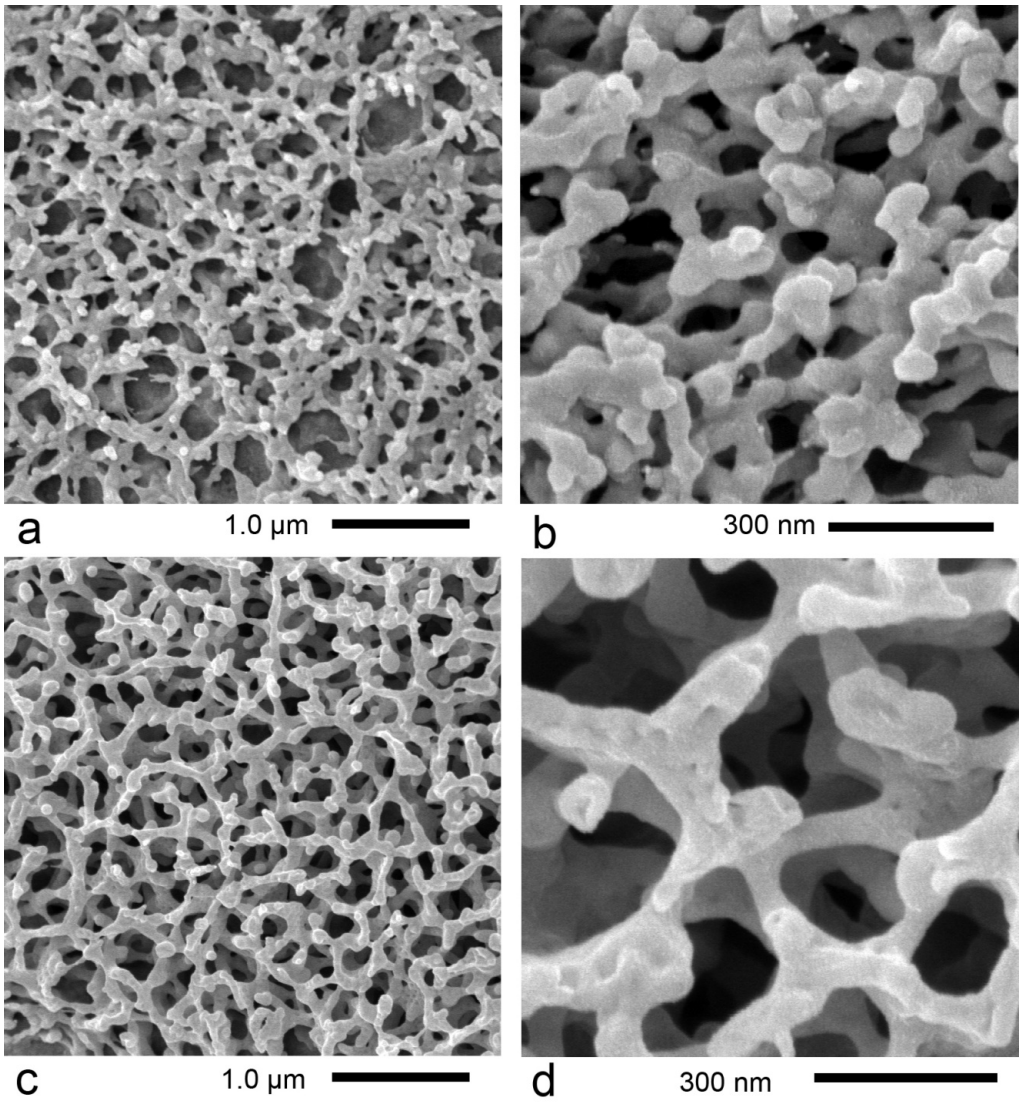

Figure 7.14 Representative cryo-SEM micrographs obtained from OB-29/W/C-3 middle layer. The sponge-like microstructure with spherical surface features observed in OB-29/W/C-1 also was found in this specimen (a and b). In the other domains, network structures with cylinderical struts and irregular junctions were observed (c and d)

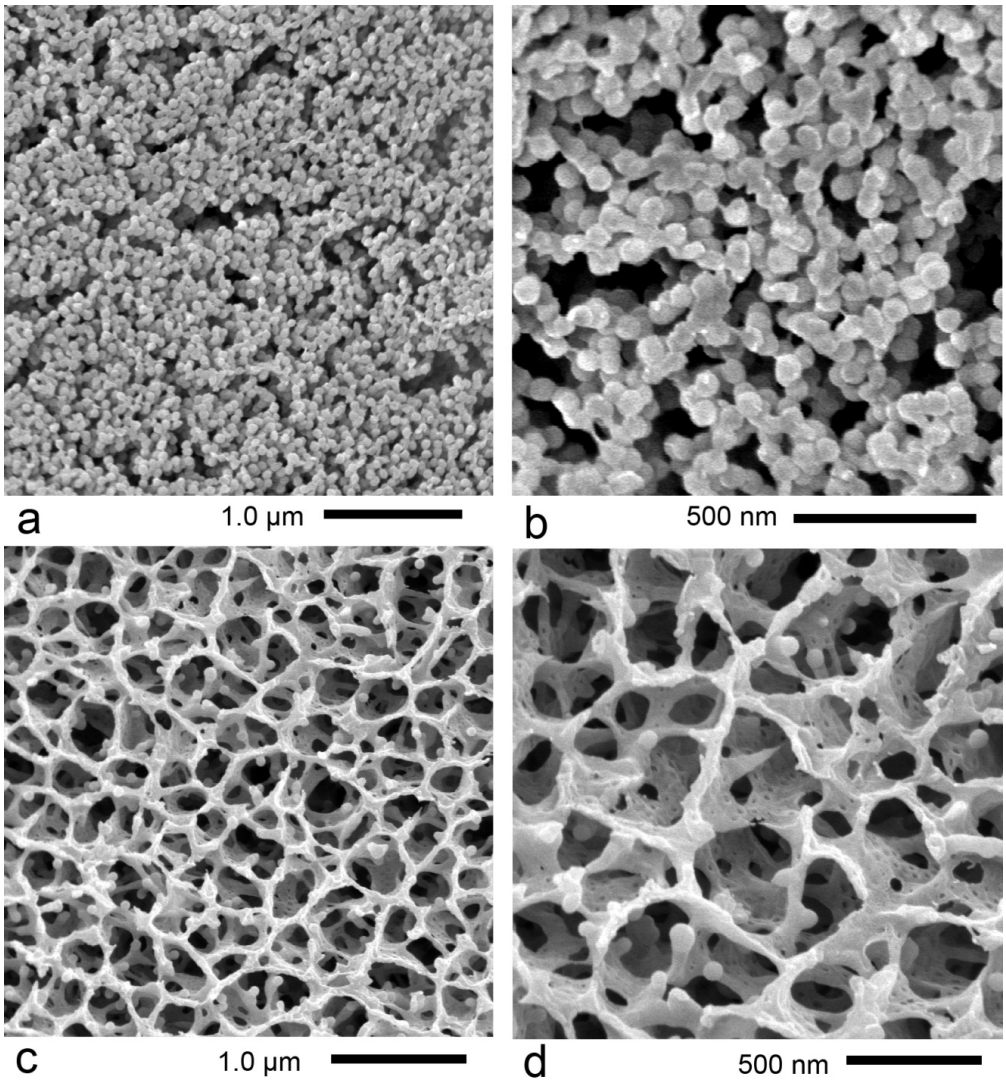

Figure 7.15 Representative cryo-SEM micrographs obtained from OB-29/W/C-4, middle layer. Sizeable sphere domains (a and b) and network microstructures with large sheet shaped junctions (c and d) were found.

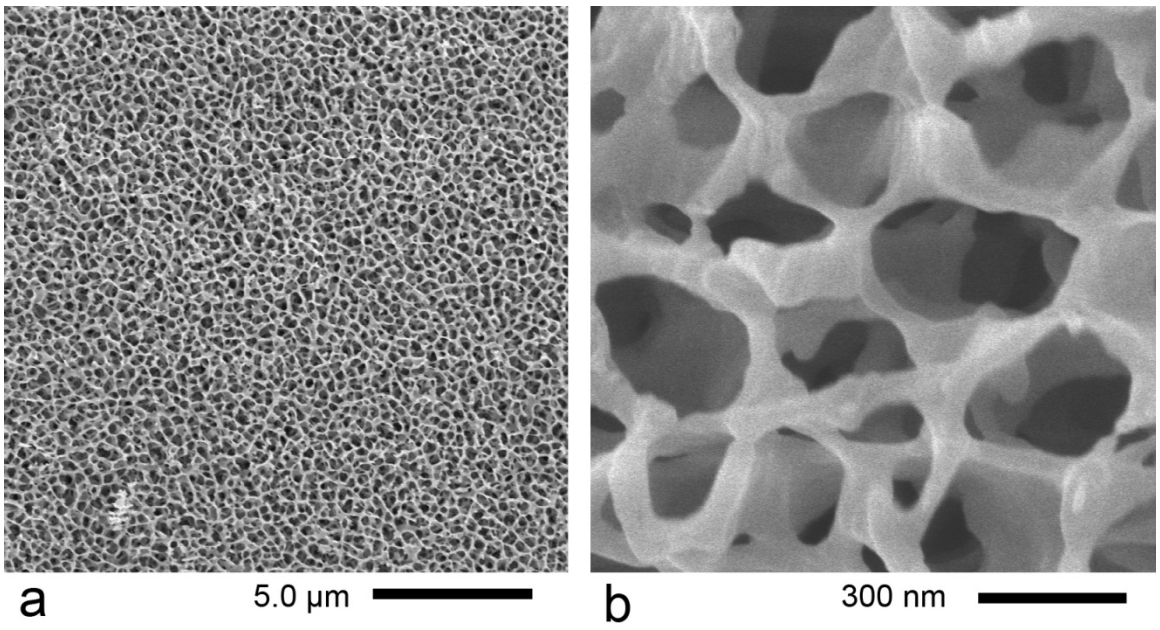

Figure 7.16 Representative cryo-SEM micrographs obtained from OB-29/W/C-5. Network structures are observed.

sizeable domains of dense spheres, but not regularly arranged, possibly disturbed FCC morphology due to removal of solvents (Figure 7.15a and b). However, a network with relatively larger flat junctions to the network morphologies found in OB-29/W/C-3was also observed in other characterized areas (Figure 7.15c and d).

Because we couldn't analyze the SAXS patterns of OB-29/W/C-5 and 10, the meaningful information on the morphologies of these samples were obtained from only the cryo-SEM technique. The micrographs recorded from the lower layer of OB-29/W/C-5 show only a network morphology with relatively consistent topological features (Figure 7.16). The most concentrated sample, OB-29/W/C-10 produced several distinctive

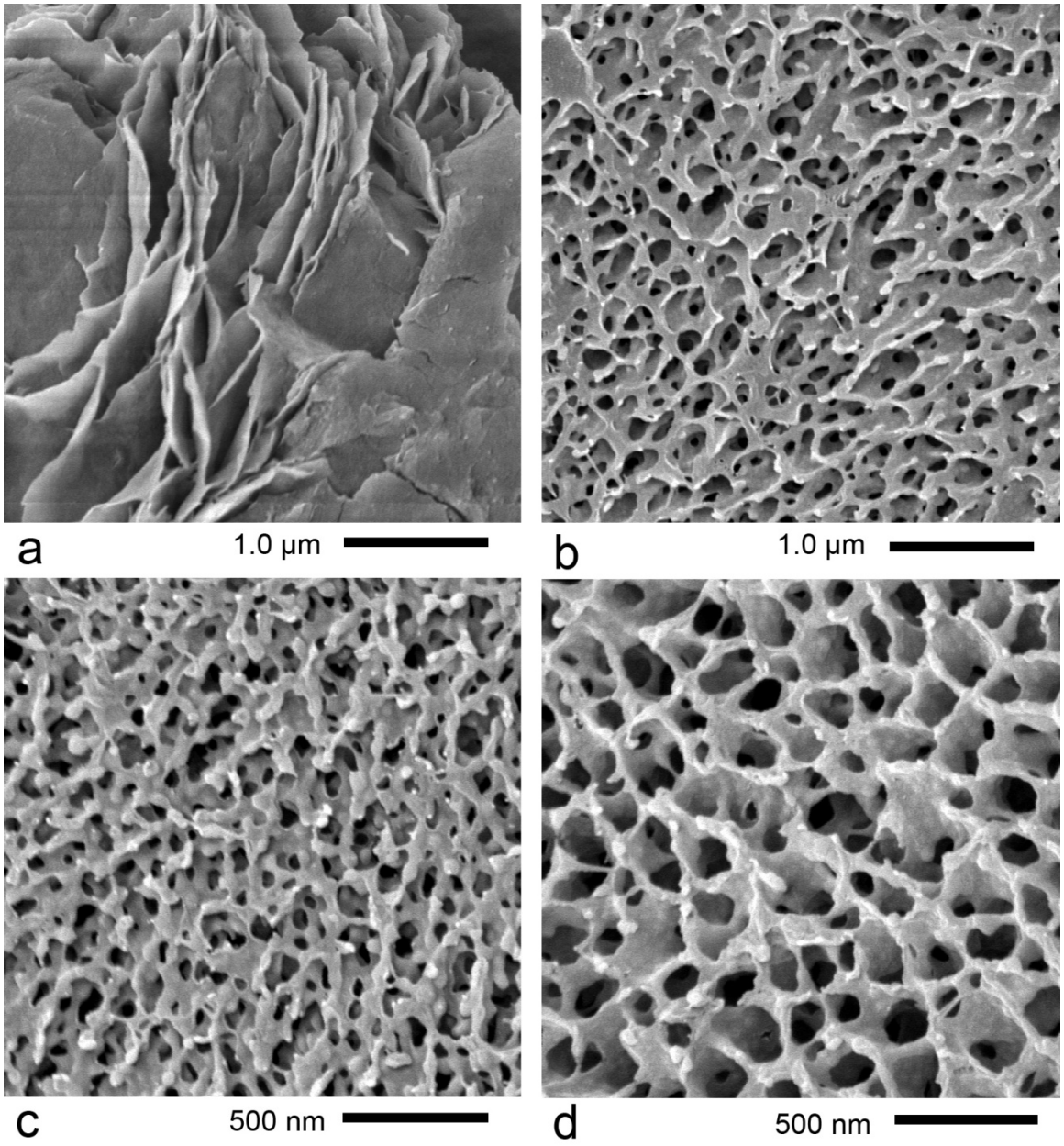

Figure 7.17 Representative cryo-SEM micrographs obtained from OB-29/W/C-10. Sheets (a), sheets with dense perforations (b), interconnected sheets with spherical surface undulations (c), and a network with large sheet structures (d) were observed.

microstructures: sheet (Figure 7.17a), sheets with dense perforations (Figure 7.17b), interconnected sheets with spherical surface undulations (Figure 7.17c), and network with large sheet structures (Figure 7.17d).

OB-29/C/W Ternary Mixtures OB-29/C/W-1 and 3 produced milky top layers, filling most of the sample volume, and the bottom layers were transparent and slightly bluish as shown in the lower panel of Figure 7.5b. However, addition of hydrophilic 5 nm gold particles to OB-29/C/W-3 reveled two layers in the top milky layer (Figure 7.5c), indicating the OB-29/C/W-3 produced three layers. Although all listed ternary samples could be effectively mixed by the described mixing procedure in the experimental section, OB-29/C/W-10 could not be homogenized and showed an inhomogeneous milky gel-like state with relatively clear bluish grains (Figure 7.5b). Vigorous hand shaking revealed another milky fluid layer at bottom, indicating OB-29/C/W-10 formed two layers: an inhomogeneous top layer and a lower fluidic milky layer. A representative sample, the middle layer of OB-29/C/W-3 was analyzed by DSC and showed no sign of PEO crystallinity (Figure 7.1f).

Synchrotron SAXS data from the lower layer of OB-29/C/W-1 and 3 produced featureless patterns, again suggesting negligible amounts of block copolymers in these layers (Figure 7.18). Similar to the middle and lower layer SAXS patterns from the OB-29/W/C solutions, SAXS patterns from the upper layers of OB-29/C/W-1 and 3 were nearly identical, but the upper layer displayed more intense SAXS patterns than those of

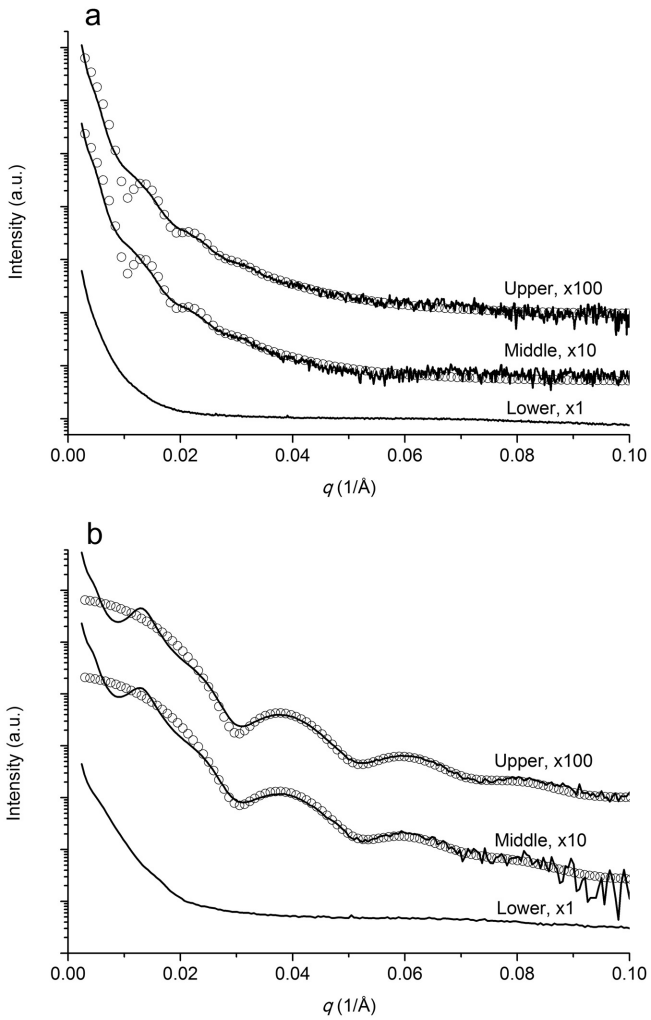

Figure 7.18 Synchrotron SAXS data from OB-29/C/W-1 and 3. Experimental data (solid line, —) and form factor modeling results (○) are presented. (a) Upper and middle layers of OB-29/C/W-1 SAXS patterns were modeled using a sphere form factor (R_c = 37 nm and $\Delta R_c/R_c$ = 0.10 for both layers) and (b) the form factor results for OB-29/C/W-3 upper and middle layers were calculated using vesicle form factor (core thickness d = 14.7 nm and $\Delta d/d$ = 0.15).

middle layers (approximately 3 to 4 times). The upper and middle layer SAXS data from OB-29/C/W-1 (Figure 7.18a) were analyzed using a spherical form factor model, which produced the best agreement with the experimental data, and resulted in a core radius R_c = 37 nm and $\Delta R_c / R_c = 0.10$. However, cryo-SEM micrographs of OB-29/C/W-1 displayed a randomly interconnected microstructure with undulating connectors, similar to the morphology recorded from OB-29/W/C-1 using cryo-SEM (Figure 7.19). Along with these microstructures, relatively large spherical particles in the range of 100 - 200 nm in diameter were observed at a high magnification as marked by arrows in Figure 7.19b.

For OB-29/W/C-3, the SAXS patterns are analyzed in the discussion section because it requires detailed reasoning, and we focus only on the recorded cryo-SEM micrographs in this section. Figure 7.20a displays a representative portion of OB-29/C/W-3 at a low magnification, showing a large droplet containing other smaller droplets. We identified two types of structures in this sample, located in domains labeled b and d in Figure 7.20a. Micrographs from the domain b (Figure 7.20b) reveled spherical structures strung together like grapes on a vine or interconnected into a loose network. Closer examination of this structure at high magnification clearly showed hollow or vesicular geometrical characteristics (Figure 7.20c, arrows), suggesting the morphology found in the domain b is tubular connectors. This morphology was found in roughly 30 % of the recorded micrographs. The other prevalent (~ 70 %) domains, marked d in Figure

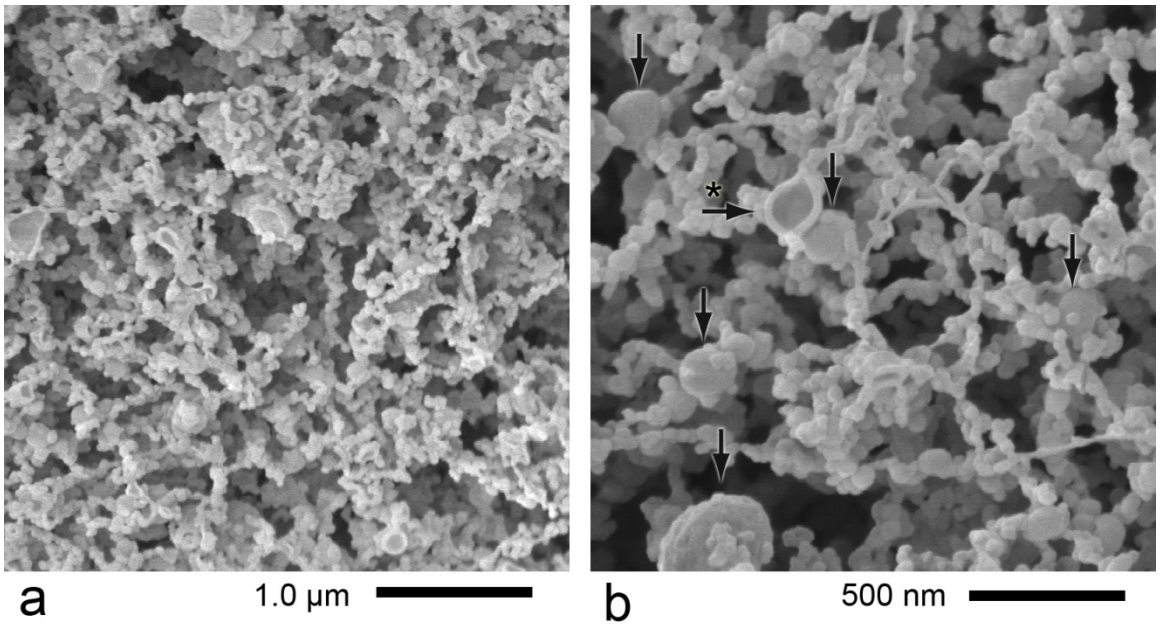

Figure 7.19 Representative cryo-SEM micrographs obtained from the middle layer of OB-29/C/W-1. Randomly interconnected microstructures with undulating surface features were found. Closer examination reveals another type of microstructures at a length scale of 100 - 200 nm (down arrows in the panel b). The microstructure marked by an arrow labeled * is possibly an open structure exposed by cryofracturing.

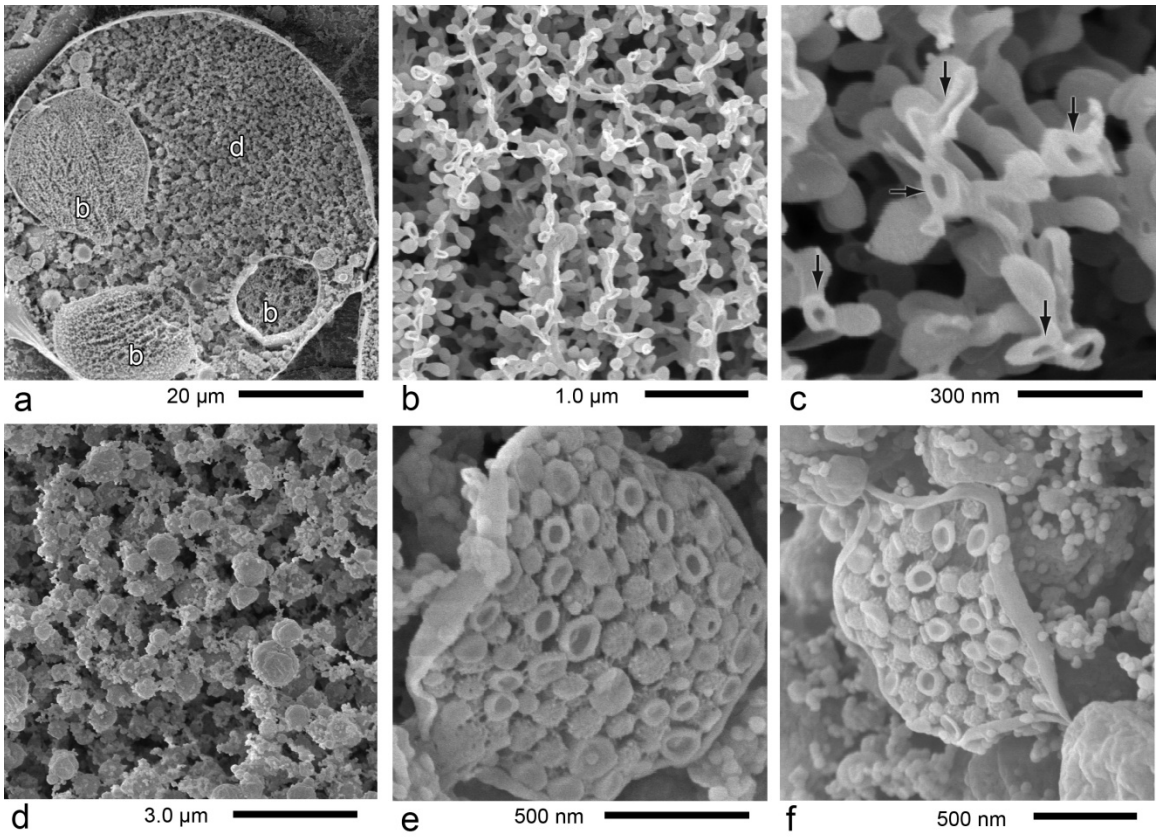

Figure 7.20 Representative cryo-SEM micrographs obtained from OB-29/C/W-3. (a) Low-magnification image showing phase-separated regions b and d. Panels b and c are intermediate and high-magnification images obtained from the region b identified in panel a. The high-magnification image (c) from the region b reveals connected hollow structural elements (arrows). Spherical pods shown in panel d contain dense arrays of bilayer-based vesicles as revealed in higher-magnification pictures (e and f). Access to the interior of the pods occurs during cryo-fracturing.

7.20a are shown in Figure 7.20d to f. Major structure in this domain was spherical objects of roughly 1 μm diameter (Figure 7.20d). Fortunately, we could find several cleaved spherical objects, referred to as "pods" generated by cryofracturing. In these pods, relatively monodisperse spherical particles ranging in size from 100 - 140 nm in diameter were densely packed (Figure 7.20e and f). OB-29/C/W-10 was characterized using only cryo-SEM microscopy. At low magnification, the microstructure of OB-29/C/W-10 appeared as a perforated sheet morphology (Figure 7.21a), but closer examination showed this structure consisted of two different spherical objects (Figure 7.21b and c): interconnected spherical structures ranging from 30 to 50 nm in diameter and spherical particles with sizes of approximately 100 to 300 nm in diameter (b and c).

7.4 Discussion

We examined the morphologies of the non-ionic polymeric surfactant OB-29 from the undiluted state to binary solutions and to the ternary solutions in oil and water by following two different dissolution pathways: dissolution of OB-29 in water first then oil, and in oil first then water.

Undiluted OB-29 In the bulk state, the undiluted diblock copolymer OB-29 produced a well defined lamellar morphology at 140 ^{o}C as evidenced by the SAXS pattern (Figure 7.2a). However, this lamellar morphology became disrupted at room temperature (Figure 7.2b and 7.3) possibly by the formation of large PEO crystals, w_c =

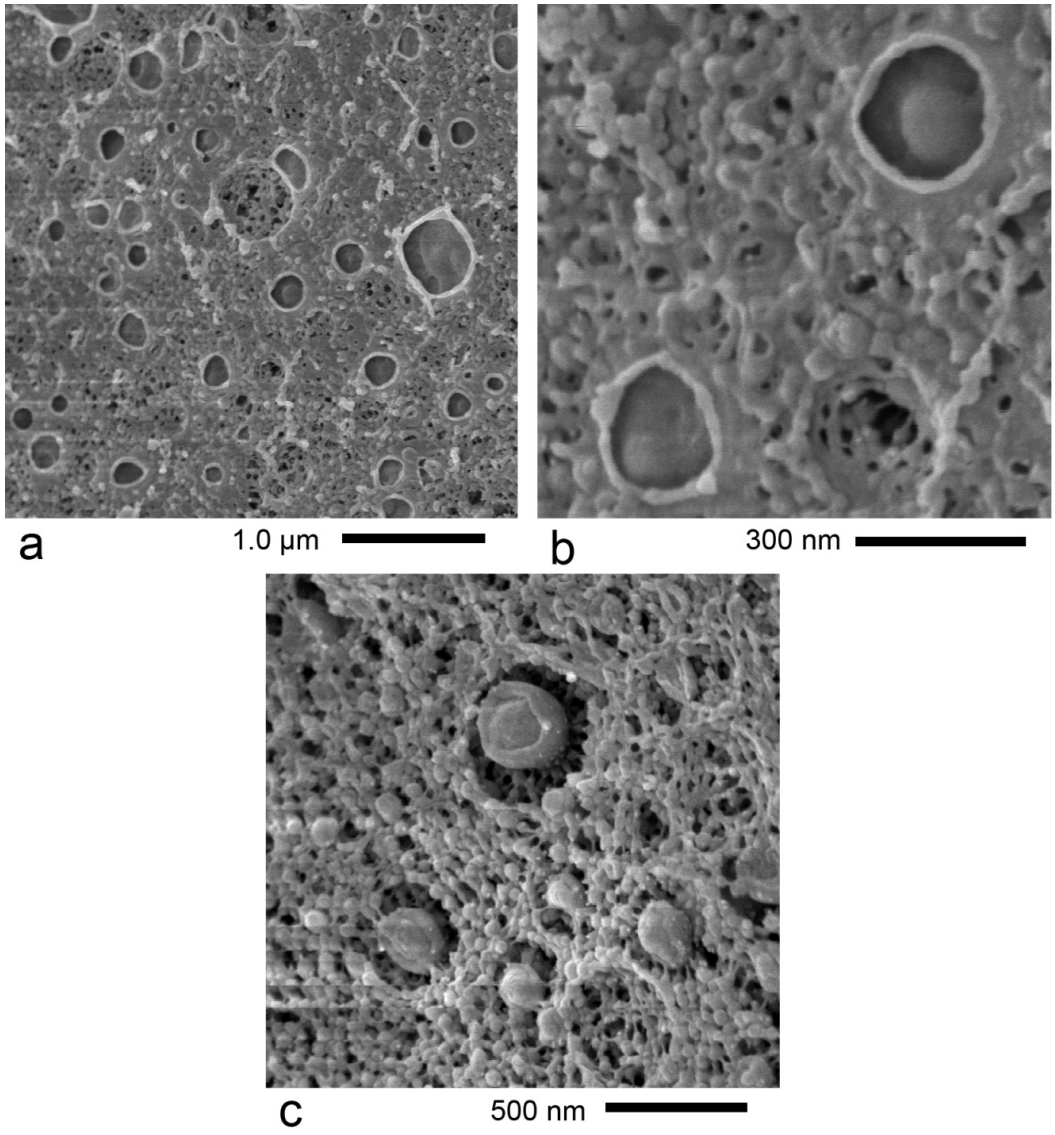

Figure 7.21 Representative cryo-SEM micrographs obtained from OB-29/C/W-10. The low-magnification image (a) appears to be a perforated sheet morphology. High magnification micrographs contain two-dimensional undulating microstructures with around 35 nm diameter spherical objects along with layers, approximately 150 nm in diameter features (b and c).

72 % (Figure 7.1a).[274] Unexpectedly, the morphology of OB-29 varied more significantly after the freeze-drying process from benzene. The domain spacing of the freeze dried morphology $D \cong 14$ nm (up to 26.6 wt. % of OB-29 in benzene) is approximately 3 times smaller than the characteristic domain spacing of OB-29 at room temperature $D = 2\pi/0.015$ Å^{-1} = 41.8 nm. The microphase separation of block copolymer melt is driven by the chemical incompatibility quantified by χN, which is the product of the Flory-Huggins interaction parameter χ and the degree of polymerization N.[2] However, semi-crystalline block copolymers are driven by another qualitatively different microphase separation mechanism, referred to as crystallization-induced microphase separation. The final morphology of a semi-crystalline block copolymer at a temperature lower than the melting point T_m is significantly influenced by the crystallization of semi-crystalline block with incorporation of the microphase separation induced by χN.[229, 275, 276] The lamellar morphology of OB-29 is rather distinctive relative to previously reported morphologies of semi-crystalline block copolymers. The domain spacing is much smaller than the domain spacing in bulk (crystallization often induces a greater domain spacing). It is not clear whether this result is solely directed by the crystallization of PEO block or a combined effect with the freezing and drying process. However, the crystallization of PEO seems at least to have resulted in this unusual morphology in conjunction with the directive role of polymer crystals in microphase separation. Regardless of the mechanism,

both the DSC (Figure 7.1) and SAXS (Figure 7.2) results are consistent with the formation of smaller PEO crystals induced by freeze drying.

OB-29/W Binary Mixtures An experimental phase portrait of OB-29/W is drawn in Figure 7.22. In the dilute limit, OB-29/W solutions (OB-29/W-1 to 4) formed spherical micelles, consistent with the phase behavior of OB block copolymers prepared by direct dissolution in water.[62, 71] The other morphology occurring at high concentration of OB-29, the hexagonally packed cylinders in roughly 20 to 75 wt. % of OB-29 also agrees with the previous result. However, the embedded sphere in thin sheets (OB-29/W-5) and the network with spherical topology (OB-29/W-10) are new in the phase domain where

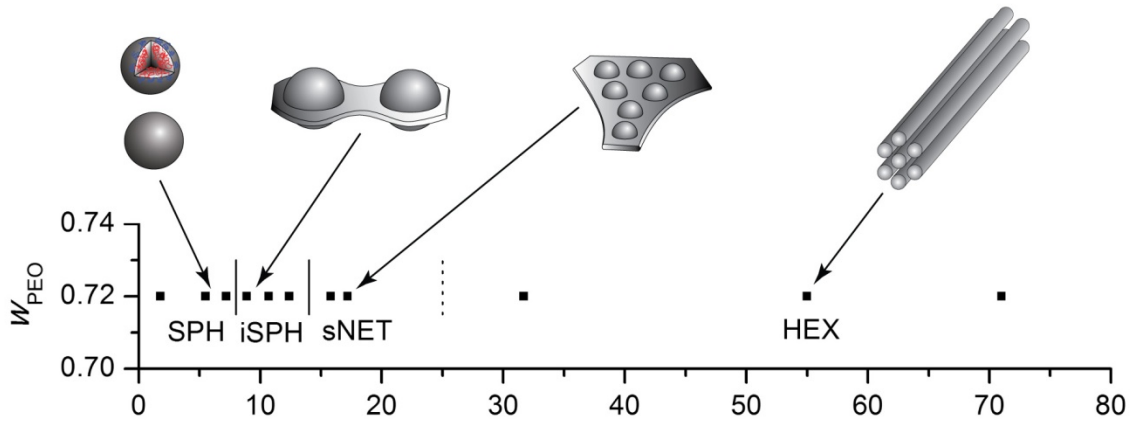

Figure 7.22 Experimental phase portrait of OB-29 in water using freeze-dried OB-29 block copolymer. The following notations are used. SPH: spherical micelles; iSPH: embedded spheres in sheets; sNET: network with spherical topology; and HEX: hexagonally packed cylinders.

these structures were found; in the proximity of the phase domain of the embedded spheres, the face-centered cubic (FCC) morphology was reported.[83] The network phase in the OB system was observed in the phase domain where the OB block copolymer weight fraction ranges from 25 to 55 % and w_{PEO} 30 to 45 % (see Figure 5 in the report by Jain and Bates).[83]

A possible explanation of the origin of these new morphologies begins with the unusual lamellar morphology induced by freeze-drying. The embedded spheres of OB-29/W-5 is very similar to the spherical micelles of OB-29/W-3 (as well as the geometrical feature, the size of these spherical structures of OB-29/W-3 and 5 are comparable as shown in Figure 7.7a and c). Although a quantitatively reliable sheet thickness cannot be determined from the cryo-SEM micrographs, the apparent sheet thickness is considerably smaller than the radii of the spheres (approximately 20 - 35 nm). This is quite remarkable because the domain spacing of bulk OB-29 is roughly 35 nm (see Figure 7.2). Thus, assuming the thin sheets originated from the freeze-dried lamellar morphology is the most plausible interpretation based on the length scale of the microstructure. The embedded spheres in thin sheets of OB-29/W-5 was possibly produced from the locally increased interfacial curvature of the lamellar morphology by PEO chains swollen with water, but this structure development process appear to be frozen at this state due to practically negligible CMC of OB-29 (the effect of dehydration of PEO chains in cryo-SEM characterization was not considered in this crude comparison of sheet thickness

because significant local difference of degree of hydration of PEO chains is not likely).[47] This reasoning also seems related to the spherical topology of the network structures obtained from OB-29/W-10 as well.

OB-29/C Binary Mixtures The OB-29/C series produced only two categories of microstructures: lamellar with $D \cong 42$ nm and ribbon morphologies. At relatively low concentrations of OB-29 (OB-29/C-1 to 10), this binary solution showed the crystallization-induced macrophase separation as evidenced by the formation of OB-29 with swollen PB and COD macrophases and a nearly consistent domain spacing (42 nm) over all concentrations. For the ribbon-like morphology obtained from OB-29/C-11, the formation of cylinderical micelles prior to crystallization of the PEO core must have occurred because polymer crystals generally grow in two dimensions. Ryan and co-workers reported that an asymmetric semi-crystalline block copolymer tends to form a lamellar morphology even when the undiluted block copolymer forms a hexagonally packed cylinder morphology in the melt.[274] However, this morphological transition cannot readily happen for all cylinderical micelles due to the limited diffusivity of cylinderical micelles. Thus, a portion of the cylinderical micelles remains as a ribbon-like morphology after the semi-crystalline core formed and other micelles aggregate into the flat sheet structures by expanding on the sides as observed in Figure 7.11d. Obviously, this hypothesis should be confirmed by time-resolved experiments.

OB-29 Ternary Mixtures The featureless and low intensity SAXS patterns obtained from the second solvent layer (Figure 7.12 and 7.18) indicates that this phase contains almost no OB-29 block copolymer. The other scattering patterns from the water (OB-29/W/C) or COD (OB-29/C/W) and middle layers are nearly identical except for the overall intensity (the scattering intensity from the water or COD layer is several times stronger). These observations apply to the middle layers of OB-29/W/C-1, 3, and 4 and OB-29/C/W-1 and 3 and indicate long-lasting metastable mixtures of the layer that initially contains OB-29 block copolymers and almost pure the other solvent layer. This interpretation is also supported by the μm scale droplets of two kinds observed from OB-29/W/C-1: pure oil droplets surrounded by water with OB-29 (Figure 7.13b) and water droplets with OB-29 in an oil surrounding (Figure 7.13c).

OB-29/W/C Ternary Mixtures At first glance, the micrographs obtained from OB-29/W/C-1(Figure 7.14d) and some parts of OB-29/W/C-3 (Figure 7.14a and b) contain a network morphology with undulating connectors. However, we believe this micrographs may not represent the true unperturbed morphology because the solvent etching process could lead to aggregation of dried spherical micelles. Therefore, further speculation on this microstructure is not presented.

However, the other images of the network structure of OB-29/W/C-3 (Figure 7. 14c and d) are regarded as evidence of a real morphology because the neat cylinderical struts connecting junctions are not likely to be created by the etching process. This

network structure was possibly induced by the fusion of spherical micelles in OB-29/W-3. Addition of COD and vigorous mixing allowed COD to diffuse through the aqueous medium, resulted in swelling of the PB cores, and subsequently the spherical micelles with swollen PB cores fused into a network. This process lowers the (PB-COD)/(PEO-Water) interface curvature (the effective fraction of PEO lowers from 72 to ~ 44 % based on the spherical assumption).[71, 74] This proposed mechanism is drawn schematically in the upper panel of Figure 7.23.

Although the cryo-SEM micrographs obtained from the OB-29/W/C middle layer revealed a network structure with cylinderical struts (Figure 7.14c and d), the result of form factor fitting with a sphere model for the SAXS pattern from this layer agrees better than the result with a cylinder model in the high q domain (Figure 7.12b and 7.24). Possibly, this indicates that non-negligible amount of swollen spheres exist in the layer and/or the undulating feature of the microstructure shown in Figure 7.14a and b is reflected in this SAXS pattern.

Addition of COD to more concentrated OB-29/W solutions produced rather confusing results. OB-29/W/C-4 generated two kinds of microstructures, spheres with FCC symmetry and a network morphology as shown in Figure 7.12d and 7.15. However, OB-29/W/C-5 only generated a network with a consistent and uniform topology and the FCC structure was not observed even though this sample has only a 1 % higher concentration of OB-29 than OB-29/W/C-4. The concentrated sample OB-29/W/C-10

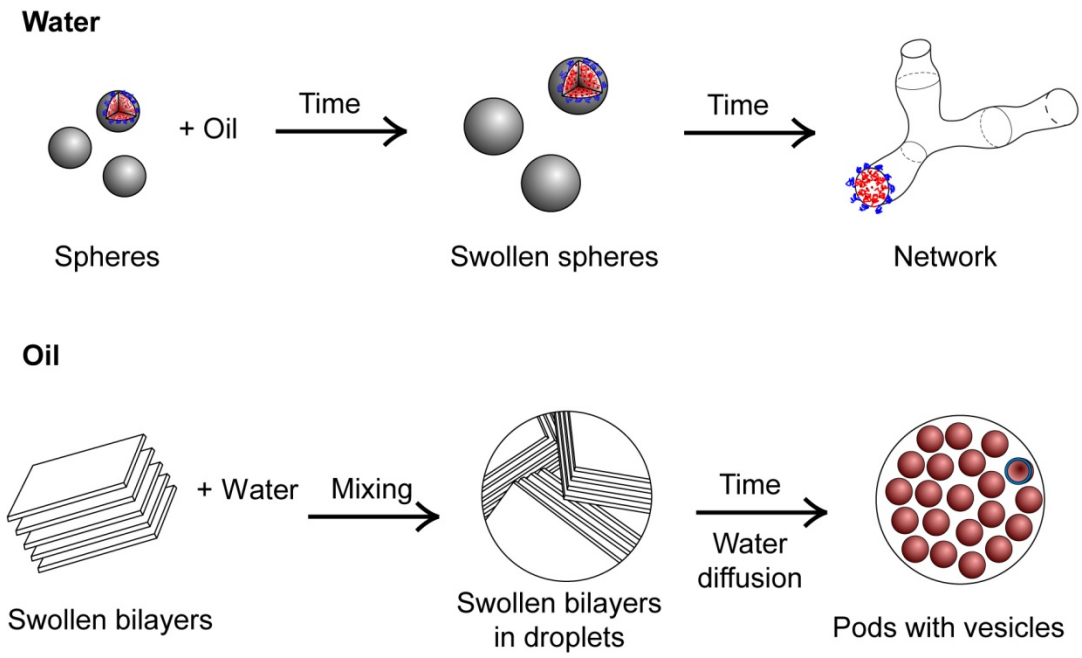

Figure 7.23 Schematic drawing of the proposed processing pathways responsible for the development of two different nonequilibrium morphologies in ternary mixtures. In the top sequence, addition of COD to OB-29/W leads to swelling of the hydrophobic cores followed by micelle fusion. In the bottom sequence, COD-swollen PEO bilayers, trapped within phase-separated droplets, swell with water and then transform into a uniform set of vesicles.

produced a mixture of microstructures as shown in Figure 7.17. These results indicate the microstructures in OB-29/W/C solutions are extremely sensitive to the initial concentration of block copolymer surfactant, even at levels lower than 10 wt. %.

OB-29/C/W Ternary Mixtures The ternary solutions prepared by changing the order of addition of solvents, OB-29/C/W, generated various morphologies as well. The dilute ternary sample, OB-29/C/W-1 produced a network-like morphology with undulating connectors, similar to the one found in OB-29/W/C-1 (Figure 7.18) . The SAXS data from this sample was characterized using a sphere form factor and the calculated sphere radius (R_c = 37 nm) was comparable to the size of a node of undulating connectors found in the cryo-SEM micrographs. However, it is not clear whether this network-like morphology actually reflects the true structure of OB-29 in this solution; as with the interpretation of the OB-29/W/C-1 micrographs (Figure 7.13), we cannot rule out artifacts due to the etching process.

However, this network was not the only microstructures observed in this sample. Spherical particles ranging from 100 to 200 nm in diameter were occasionally observed at high magnification (arrows in Figure 7.19b). Because of the somewhat low occurrence of these large particles compared to the network-like structures, we could not conclude the geometry of these particles solely from the SAXS and cryo-SEM characterization data.

The SAXS data from the upper and middle layers of OB-29/C/W-3 displayed rather well-defined patterns (Figure 7.18b), which could be analyzed using the sphere form factor; The resulting sphere core radius, $R_c \cong 14.5$ nm, is estimated from the first form factor peak occurring at $q \cong 0.04$ Å^{-1} (based on $qR_c \cong 5.8$).[277] The cryo-SEM characterization of OB-29/C/W-3 revealed that the most prevalent microstructure is micron size pods, which are too large to influence the SAXS patterns. As presented in Figure 7.20e and f, these pods contain densely packed spherical particles ranging in size from 100 to 140 nm, also much larger than can be resolved by the SAXS patterns if the sphere form factor is still assumed. Because of this discrepancy, we concluded that the particles are vesicles and analyzed the SAXS patterns from OB-29/C/W-3 using a bilayer vesicle form factor model that contains a $d = 14.7$ nm thick with $\Delta d/d = 0.15$, water swollen PEO core (containing 50 - 60 % water based on the $d = 6.6$ nm core thickness of OB-29/C-3) with a corona of PB swollen with COD.[113] For further verification of this reasoning, a crude estimation of the vesicle wall thickness on the basis of various cryo-SEM images like Figure 7.20e and f was made. The average apparent vesicle thickness was 28 ± 4 nm. However, two significantly uncertain factors should be considered in this measurement: (1) thickness of platinum coating and (2) effects of drying swollen microstructures by water and COD. Subtraction of 8 - 12 nm as a rough estimation of the thickness of the platinum coating from the measured vesicle wall thickness leaves 16 - 20

nm for the bare fractured and etched layers, comparable to the thickness of PEO core d = 14.7 nm based on the SAXS data.

Because of the morphological similarity to the vesicles in OB-29/C/W-3, the large spherical particles in OB-29/C/W-1 are also believed to be vesicles, and this conclusion is supported by the hollow internal structure of these particles (arrow labeled * in Figure 7.19b).

Although the morphologies of OB-29/C/W-1 and 3 were somewhat characterizable, the microstructure of OB-29/C/W-10 could not be deduced beyond a few qualitative characteristics. Embossed sheets and spherical particles in sizes of roughly two domain scales. Although we could not retrieve meaningful characterization data from these micrographs, this drastic change of morphology again emphasizes the subtle nature of self-assembly of polymeric surfactant in two incompatible solvents.

Dynamics of Block Copolymer Surfactants In the past three decades, monodisperse polymeric microstructures have been successfully prepared in good or marginal solvents despite the kinetic associated with polymeric surfactants. The OB-29/W and OB-29/C binary solutions also produced well-defined monodisperse microstructures. However, introduction of a second solvent that is immiscible with the first, as in the OB-29/W/C and OB-29/C/W ternary solutions, results in remarkable morphological complexity that clearly shows evidence of highly nonequilibrium yet metastable morphologies. These nonequilibrium states cannot be attributed to

immobilization of the chains due to glassy or semicrystalline microdomains. The solutions were prepared well above the glass transition temperature of the PB blocks (T_g = -10 ^oC) and the PEO chains are all hydrated. However, the OB-29 polymers are strongly localized at the oil-water interface due to the extreme immiscibility of each block in the opposite solvent medium, which reduces the CMC to a negligible level, thereby eliminating block copolymer exchange. Hence, once water and oil interface and the associated morphology are formed, block copolymers become irreversibly portioned leading to kinetically trapped microstructures.

As observed with OB-29/W/C-1, 3, and 4, addition of COD to OB-29/W binary solutions followed by vigorous mixing created a dispersion of oil droplets in OB/W and vice versa. Diffusion of COD (~ 10^{-5} cm^2/s) through the water medium resulted in swollen PB cores, similar to the transport of hydrocarbon monomer through an aqueous phase in an emulsion polymerization.[59, 278] After the mixing process has been ceased, water and free oil layers separated into lower and upper layers by density, leaving the milky middle layer, a mixture of water holding core-swollen OB-29 spheres and trapped polymer free oil droplets. The other OB-29/W/C-5 and 10 ternary solutions formed two layers. These samples generated 3 dimensional network structures, a solid-like state, which cannot easily deform to accommodate oil droplets. Thus, the three and two layer behaviors appear to result from differences in the solution viscosity, not gross variations in the thermodynamic properties of these solutions.

OB-29/C/W-3 generated relatively monodisperse vesicles with PEO cores and PB/COD on the inside and outside, enclosed by ~ 1 μm diameter pods. This is a rare occurrence because polymer vesicles (polymersomes) are usually generated in a wide range of sizes due to the negligible variation in free energy as a function of vesicle size.[42] Thus, we believe these monodisperse vesicles reflect a kinetic process rather than a thermodynamic effect. As a relevant example, Rank and co-workers have shown that cylinderical micelles can be converted to monodisperse vesicles by manipulating the temperature in the vicinity of the cylinder-vesicle transition.[73] They prepared relatively large vesicles (~ 300 nm in diameter) in an aqueous buffer solution at room temperature using poly(2-vinylpyridine-*b*-ethylene oxide) (P2VP-PEO) diblock copolymer surfactant. Through the deformation of micelle interface curvature, these vesicles thermotropically changed into worm-like micelles after cooled down to 4 ^{o}C and returned to a vesicle morphology at 25 ^{o}C but with monodisperse and much smaller diameter (~ 80 nm) characteristics. Although we cannot firmly establish whether thermodynamic or dynamic effects control the generation of these monodisperse vesicles, a plausible hypothesis can be advanced. Vigorous mixing of OB-29/C/W-3 following the addition of water leads to the generation of oil rich OB-29/C-3 droplets. Diffusion of water into these droplets leads to hydration of the lamellar PEO cores. The hydrated PEO cores drive the bilayers to curve and form vesicles. This uptake of water might even push the swollen bilayers to the point of mechanical instability, resulting in the spontaneous transformation to vesicles

(lower panel of Figure 7.23). This hypothesis may explain why the vesicles are monodisperse, i.e., instability-driven morphological transitions often create narrowly distributed structures.[279, 280] However, this approach does not explain other morphologies of OB-29/C/W-3 shown in Figure 7.20b and c. Possibly, these additional morphologies were produced by local inhomogeneities (e.g., water concentration), which result from the crudely controlled initial mixing procedure. Nevertheless, the bilayer features in OB/C/W-3 are consistently found regardless of other morphological variations.

Summary We draw two general conclusions from this work. First, the non-ionic polymeric surfactant OB-29, and presumably other amphiphilic block copolymers produce phase behavior and morphological transformations when combined with strongly immiscible solvents that are governed by non-equilibrium processes. Nevertheless, the resulting morphologies can be regular and metastable for long time periods. Second, these indefinitely metastable morphologies offer a new opportunity for processing oil, water, and polymeric surfactants to produce well-controlled microstructures.[69, 281] As shown with the OB-29/W/C and OB-29/C/W mixtures, these ternary compounds produced relatively monodisperse microstructures in certain range of composition despite of the poor control of mixing and the non-equilibrium nature originated from the high molecular weight.[72, 83]

Bibliography

1. Hiemenz, P. C.; Lodge, T. P., *Polymer Chemistry*. 2nd ed.; CRC Press: Boca Raton, 2007.
2. Leibler, L., *Macromolecules* **1980,** 13, 1602.
3. Khandpur, A. K.; Förster, S.; Bates, F. S.; Hamley, I. W.; Ryan, A. J.; Bras, W.; Almdal, K.; Mortensen, K., *Macromolecules* **1995,** 28, 8796.
4. Fredrickson, G. H.; Helfand, E., *J. Chem. Phys.* **1987,** 87, 697.
5. Bates, F. S.; Rosedale, J. H.; Fredrickson, G. H.; Glinka, C. J., *Phys. Rev. Lett.* **1988,** 61, 2229.
6. Rosedale, J. H.; Bates, F. S.; Almdal, K.; Mortensen, K.; Wignall, G. D., *Macromolecules* **1995,** 28, 1429.
7. Stühn, B., *J. Poly. Sci. B: Poly. Phys. Ed.* **1992,** 30, 1013.
8. Kasten, H.; Stühn, B., *Macromolecules* **1995,** 28, 4777.
9. Voronov, V. P.; Buleiko, V. M.; Podneks, V. E.; Hamley, I. W.; Fairclough, J. P. A.; Ryan, A. J.; Mai, S. M.; Liao, B. X.; Booth, C., *Macromolecules* **1997,** 30, 6674.
10. Maurer, W. W.; Bates, F. S.; Lodge, T. P.; Almdal, K.; Mortensen, K.; Fredrickson, G. H., *J. Chem. Phys.* **1998,** 108, 2989.
11. Fredrickson, G. H.; Bates, F. S., *Annu. Rev. Mater. Sci.* **1996,** 26, 501.

12. Landau, L. D.; Lifshitz, E. M., *Statistical Physics Part 1*. 3rd ed.; Pergamon Press: New York, 1980.

13. Alexander, S.; McTague, J., *Phys. Rev. Lett.* **1978,** 41, 702.

14. Thomas, E. L.; Anderson, D. M.; Henkee, C. S.; Hoffman, D., *Nature* **1988,** 334, 598.

15. Hasegawa, H.; Tanaka, H.; Yamasaki, K.; Hashimoto, T., *Macromolecules* **1987,** 20, 1651.

16. Hajduk, D. A.; Harper, P. E.; Gruner, S. M.; Honeker, C. C.; Kim, G.; Thomas, E. L.; Fetters, L. J., *Macromolecules* **1994,** 27, 4063.

17. Matsen, M. W.; Bates, F. S., *Macromolecules* **1996,** 29, 7641.

18. Matsen, M. W.; Bates, F. S., *J. Chem. Phys.* **1997,** 106, 2436.

19. Cochran, E. W.; Garcia-Cervera, C. J.; Fredrickson, G. H., *Macromolecules* **2006,** 39, 2449.

20. Takenaka, M.; Wakada, T.; Akasaka, S.; Nishitsuji, S.; Saijo, K.; Shimizu, H.; Kim, M. I.; Hasegawa, H., *Macromolecules* **2007,** 40, 4399.

21. Kim, M. I.; Wakada, T.; Akasaka, S.; Nishitsuji, S.; Saijo, K.; Hasegawa, H.; Ito, K.; Takenaka, M., *Macromolecules* **2008,** 41, 7667.

22. Tyler, C. A.; Qin, J.; Bates, F. S.; Morse, D. C., *Macromolecules* **2007,** 40, 4654.

23. Abetz, V.; Simon, P., Phase Behaviour and Morphologies of Block Copolymers. In 2005; pp 125-212.

24. Matsen, M. W.; Thompson, R. B., *J. Chem. Phys.* **1999,** 111, 7139.

25. Mayes, A. M.; de la Cruz, M. O., *J. Chem. Phys.* **1989,** 91, 7228.

26. Mayes, A. M.; de la Cruz, M. O., *J. Chem. Phys.* **1991,** 95, 4670.

27. Watanabe, H., *Macromolecules* **1995,** 28, 5006.

28. Watanabe, H.; Sato, T.; Osaki, K.; Yao, M.-L.; Yamagishi, A., *Macromolecules* **1997,** 30, 5877.

29. Takano, A.; Kamaya, I.; Takahashi, Y.; Matsushita, Y., *Macromolecules* **2005,** 38, 9718.

30. Nakazawa, H.; Ohta, T., *Macromolecules* **1993,** 26, 5503.

31. Zheng, W.; Wang, Z.-G., *Macromolecules* **1995,** 28, 7215.

32. Mogi, Y.; Mori, K.; Matsushita, Y.; Noda, I., *Macromolecules* **1992,** 25, 5412.

33. Phan, S.; Fredrickson, G. H., *Macromolecules* **1998,** 31, 59.

34. Epps, T. H.; Cochran, E. W.; Bailey, T. S.; Waletzko, R. S.; Hardy, C. M.; Bates, F. S., *Macromolecules* **2004,** 37, 8325.

35. Chatterjee, J.; Jain, S.; Bates, F. S., *Macromolecules* **2007,** 40, 2882.

36. Cochran, E. W.; Bates, F. S., *Phys. Rev. Lett.* **2004,** 93, 087802.

37. Matsen, M. W., *J. Chem. Phys.* **1998,** 108, 785.

38. Meuler, A. J.; Hillmyer, M. A.; Bates, F. S., *Macromolecules* **2009,** 42, 7221.

39. Meuler, A. J.; Ellison, C. J.; Qin, J.; Evans, C. M.; Hillmyer, M. A.; Bates, F. S., *J. Chem. Phys.* **2009,** 130, 234903.

40. Bluemle, M. J.; Zhang, J.; Lodge, T. P.; Bates, F. S., *Macromolecules* **2010,** 43, 4449.

41. Laughlin, R. G., *The Aqueous Phase Behavior of Surfactants*. Academic: San Diego, CA, 1994.

42. Safran, S. A., *Stastistical Thermodynamics of Surfaces, interfaces, and Membrances*. Westview Press: Boulder, CO, 2003.

43. Huibers, P. D. T.; Lobanov, V. S.; Katritzky, A. R.; Shah, D. O.; Karelson, M., *Langmuir* **1996,** 12, 1462.

44. Saeki, S.; Kuwahara, N.; Nakata, M.; Kaneko, M., *Polymer* **1976,** 17, 685.

45. Aniansson, E. A. G.; Wall, S. N., *J. Phys. Chem.* **1974,** 78, 1024.

46. Aniansson, E. A. G.; Wall, S. N.; Almgren, M.; Hoffmann, H.; Kielmann, I.; Ulbricht, W.; Zana, R.; Lang, J.; Tondre, C., *J. Phys. Chem.* **1976,** 80, 905.

47. Leibler, L.; Orland, H.; Wheeler, J. C., *J. Chem. Phys.* **1983,** 79, 3550.

48. Choi, S.-H.; Lodge, T. P.; Bates, F. S., *Phys. Rev. Lett.* **2010,** 104, 047802.

49. Kahlweit, M.; Strey, R., *Angew. Chem., Int. Ed.* **1985,** 24, 654.

50. Kahlweit, M.; Strey, R.; Haase, D.; Kunieda, H.; Schmeling, T.; Faulhaber, B.; Borkovec, M.; Eicke, H. F.; Busse, G.; Eggers, F.; Funck, T.; Richmann, H.; Magid, L.; Söderman, O.; Stilbs, P.; Winkler, J.; Dittrich, A.; Jahn, W., *J. Colloid Interface Sci.* **1987,** 118.

51. Kahlweit, M.; Strey, R.; Busse, G., *Phys. Rev. E* **1993,** 47, 4197.

52. Wang, Y.; Holmes, M. C.; Leaver, M. S.; Fogden, A., *Langmuir* **2006,** 22, 10951.

53. Hiemenz, P. C.; Rajagopalan, R., *Principles of Colloid and Surface Chemistry*. 3rd ed.; Marcel Dekker: New York, 1997.

54. Vinson, P. K. Ph. D. Thesis, University of Minnesota, 1990.

55. Bellare, J. R. Ph.D. Thesis, University of Minnesota, 1988.

56. Scriven, L. E., *Nature* **1976,** 263, 123.

57. Morse, D. C., *Phys. Rev. E* **1994,** 50, R2423.

58. Golubović, L., *Phys. Rev. E* **1994,** 50, R2419.

59. Odian, G., *Principles of Polymerization*. 4th ed.; Wiley: New York, 2004.

60. Hillmyer, M. A.; Bates, F. S., *Macromolecules* **1996,** 29, 6994.

61. Khougaz, K.; Gao, Z.; Eisenberg, A., *Macromolecules* **1994,** 27, 6341.

62. Jain, S.; Bates, F. S., *Macromolecules* **2004,** 37, 1511.

63. Li, Z.; Hillmyer, M. A.; Lodge, T. P., *Nano Lett.* **2006,** 6, 1245.

64. Zhang, L.; Eisenberg, A., *Science* **1995,** 268, 1728.

65. Alexandridis, P., *Macromolecules* **1998,** 31, 6935.

66. Svensson, B.; Alexandridis, P.; Olsson, U., *J. Phys. Chem. B* **1998,** 102, 7541.

67. Förster, S.; Berton, B.; Hentze, H. P.; Krämer, E.; Antonietti, M.; Lindner, P., *Macromolecules* **2001,** 34, 4610.

68. Pochan, D. J.; Chen, Z.; Cui, H.; Hales, K.; Qi, K.; Wooley, K. L., *Science* **2004,** 306, 94.

69. Cui, H.; Chen, Z.; Zhong, S.; Wooley, K. L.; Pochan, D. J., *Science* **2007,** 317, 647.

70. Won, Y.-Y.; Davis, H. T.; Bates, F. S., *Science* **1999,** 283, 960.

71. Jain, S.; Bates, F. S., *Science* **2003,** 300, 460.

72. Li, Z.; Kesselman, E.; Talmon, Y.; Hillmyer, M. A.; Lodge, T. P., *Science* **2004,** 306, 98.

73. Rank, A.; Hauschild, S.; Förster, S.; Schubert, R., *Langmuir* **2009,** 25, 1337.

74. Won, Y.-Y.; Brannan, A. K.; Davis, H. T.; Bates, F. S., *J. Phys. Chem. B* **2002,** 106, 3354.

75. Bernheim-Groswasser, A.; Tlusty, T.; Safran, S. A.; Talmon, Y., *Langmuir* **1999,** 15, 5448.

76. Tlusty, T.; Safran, S. A.; Strey, R., *Phys. Rev. Lett.* **2000,** 84, 1244.

77. Riess, G.; Nervo, J.; Rogez, D., *Polym. Eng. Sci.* **1977,** 17, 634.

78. Omarjee, P.; Hoerner, P.; Riess, G.; Cabuil, V.; Mondain-Monval, O., *Eur. Phys. J. E* **2001,** 4, 45.

79. Riess, G., *Prog. Polym. Sci.* **2003,** 28, 1107.

80. Jakobs, B.; Sottmann, T.; Strey, R.; Allgaier, J.; Richter, D., *Langmuir* **1999,** 15, 6707.

81. Endo, H.; Allgaier, J.; Gompper, G.; Jakobs, B.; Monkenbusch, M.; Richter, D.; Sottmann, T.; Strey, R., *Phys. Rev. Lett.* **2000,** 85, 102.

82. Gompper, G.; Richter, D.; Strey, R., *J. Phys.: Condens. Matter* **2001,** 13, 9055.

83. Jain, S.; Dyrdahl, M. H. E.; Gong, X.; Scriven, L. E.; Bates, F. S., *Macromolecules* **2008,** 41, 3305.

84. Quirk, R. P., *Anionic polymerization principles and practical applications*. Marcel Dekker: New York, 1996.

85. Hoye, T. R.; Eklov, B. M.; Ryba, T. D.; Voloshin, M.; Yao, L. J., *Org. Lett.* **2004,** 6, 953.

86. Hill, S. T.; Mokotoff, M., *J. Org. Chem.* **1984,** 49, 1441.

87. Meuler, A. J.; Mahanthappa, M. K.; Hillmyer, M. A.; Bates, F. S., *Macromolecules* **2007,** 40, 760.

88. Rempp, P.; Merril, E. W., *Polymer Synthesis*. 2nd ed.; Huethig & Wepf: Basel, 1991.

89. Dufour, M.; Guyot, A., *Colloid Polym. Sci.* **2003,** 281, 97.

90. Yu, X.; Shi, T.; Zhang, G.; An, L., *Polymer* **2006,** 47, 1538.

91. Pangborn, A. B.; Giardello, M. A.; Grubbs, R. H.; Rosen, R. K.; Timmers, F. J., *Organometallics* **1996,** 15, 1518.

92. Frick, E. M.; Hillmyer, M. A., *Macromol. Rapid Commun.* **2000,** 21, 1317.

93. Lynd, N. A.; Hillmyer, M. A., *Macromolecules* **2005,** 38, 8803.

94. Skoog, D. A.; Holler, F. J.; Nieman, T. A., *Principles of Instrumental Analysis*. 5th ed.; Thomson Brooks/Cole Belmont, CA, 1997.

95. Wunderlich, B., *Thermal Analysis*. Academic Press: San Diego, 1990.

96. Brandrup, J.; Immergut, E. H., *Polymer Handbook*. 3rd ed.; Wiley: New York, 1989.

97. Han, C. D.; Kim, J. K., *Polymer* **1993,** 34, 2533.

98. Rosedale, J. H.; Bates, F. S., *Macromolecules* **1990,** 23, 2329.

99. Scott C. Schmidt; Marc A. Hillmyer, *J. Polym. Sci., Part B: Polym. Phys.* **2002,** 40, 2364.

100. Kawasaki, K.; Onuki, A., *Phys. Rev. A* **1990,** 42, 3664.

101. Koppi, K. A.; Tirrell, M.; Bates, F. S.; Almdal, K.; Colby, R. H., *J. Phys. II France* **1992,** 2, 1941.

102. Fredrickson, G. H., *J. Rheol.* **1994,** 38, 1045.

103. Ryu, C. Y.; Lee, M. S.; Hajduk, D. A.; Lodge, T. P., *J. Poly. Sci. B: Poly. Phys. Ed.* **1997,** 35, 2811.

104. Kossuth, M. B.; Morse, D. C.; Bates, F. S., *J. Rheol.* **1999,** 43, 167.

105. Tyler, C. A.; Morse, D. C., *Macromolecules* **2003,** 36, 3764.

106. Roe, R.-J., *Methods of X-ray and Neutron Scattering in Polymer Science*. Oxford University Press: New York, 2000.

107. Hahn, T., *International Tables of Crystallography, Volume A: Space Group Symmetry*. Springer: Dordrecht, Netherlands, 2005.

108. Bailey, T. S. Ph.D. Thesis, University of Minnesota, Minneapolis, 2001.

109. Won, Y.-Y.; Davis, H. T.; Bates, F. S.; Agamalian, M.; Wignall, G. D., *J. Phys. Chem. B* **2000,** 104, 7134.

110. Pedersen, J., *J. Appl. Crystallogr.* **2000,** 33, 637.

111. Burge, R. F.; Draper, J. C., *Acta Cryst.* **1967,** 22, 6.

112. Fournet, G., *Bull. soc. franc. min´eral. et crist.* **1951,** 74, 37.

113. Bang, J.; Jain, S.; Li, Z.; Lodge, T. P.; Pedersen, J. S.; Kesselman, E.; Talmon, Y., *Macromolecules* **2006,** 39, 1199.

114. Schatten, H.; Payley, J., *Biological Low-Voltage Scanning Electron Microscopy*. Springer: New York, 2008.

115. Ma, Y. Ph.D. Thesis, University of Minnesota, Minneapolis, MN, 2002.

116. Daivs, H. T., *Statistical Mechanics of Phases, Interfaces and Thin Films*. Wiley-VCH: New York, 1996.

117. Bates, F. S.; Fredrickson, G. H., *Phys.Today* **1999,** 52, 32.

118. Gervais, M.; Gallot, B., *Makromol. Chem.* **1973,** 171, 157.

119. Hashimoto, T.; Nagatoshi, K.; Todo, A.; Hasegawa, H.; Kawai, H., *Macromolecules* **1974,** 7, 364.

120. Epps, T. H.; Cochran, E. W.; Hardy, C. M.; Bailey, T. S.; Waletzko, R. S.; Bates, F. S., *Macromolecules* **2004,** 37, 7085.

121. Matsen, M. W.; Schick, M., *Macromolecules* **1994,** 27, 6761.

122. Tselikas, Y.; Hadjichristidis, N.; Lescanec, R. L.; Honeker, C. C.; Wohlgemuth, M.; Thomas, E. L., *Macromolecules* **1996,** 29, 3390.

123. Finnefrock, A. C.; Ulrich, R.; Toombes, G. E. S.; Gruner, S. M.; Wiesner, U., *J. Am. Chem. Soc.* **2003,** 125, 13084.

124. Lynd, N. A.; Hillmyer, M. A., *Macromolecules* **2007,** 40, 8050.

125. Matsen, M. W., *Phys. Rev. Lett.* **2007,** 99, 148304.

126. Ho, R.-M.; Chiang, Y.-W.; Tsai, C.-C.; Lin, C.-C.; Ko, B.-T.; Huang, B.-H., *Journal of the American Chemical Society* **2004,** 126.

127. Hadziioannou, G.; Skoulios, A., *Macromolecules* **1982,** 15, 267.

128. Hashimoto, T., *Macromolecules* **1982,** 15, 1548.

129. Tanaka, H.; Hasegawa, H.; Hashimoto, T., *Macromolecules* **1991,** 24, 240.

130. Schmidt, S. C.; Hillmyer, M. A., *Macromolecules* **1999,** 32, 4794.

131. Fetters, L. J.; Lohse, D. J.; Richter, D.; Witten, T. A.; Zirkel, A., *Macromolecules* **1994,** 27, 4639.

132. Grijpma, D. W.; Penning, J. P.; Pennings, A. J., *Coll. Polym. Sci.* **1994,** 272, 1068.

133. Frank, F. C.; Kasper, J. S., *Acta Cryst.* **1959,** 12, 483.

134. Ungar, G.; Zeng, X., *Soft Matter* **2005,** 1, 95.

135. Frenkel, D.; Ladd, A. J. C., *J. Chem. Phys.* **1984,** 81, 3188.

136. Woodcock, L. V., *Nature* **1997,** 385, 141.

137. Bolhuis, P. G.; Frenkel, D.; Mau, S.-C.; Huse, D. A., *Nature* **1997,** 388, 235.

138. Mau, S.-C.; Huse, D. A., *Phys. Rev. E* **1999,** 59, 4396.

139. Frank, F. C.; Kasper, J. S., *Acta. Cryst.* **1958,** 11, 184.

140. Watson, R. E.; Weinert, M., Transition-metals and their alloys. In *Solid State Physics*, Ehrenreich, H.; Spaepen, F., Eds. Academic Press: San Diego, 2001; Vol. 56, p 2.

141. Graef, M. D.; McHenry, M. E., *Structure of Materials: An Introduction to Crystallography, Diffraction, and Symmetry*. Cambridge Univ.: Cambridge, 2007.

142. Dickins, G. J.; Douglas, A. M. B.; Taylor, W. H., *Acta Cryst.* **1956,** 9, 297.

143. Buta, F.; Sumption, M. D.; Collings, E. W., *IEEE Trans. Appl. Super.* **2003,** 13, 3462.

144. Elmer, J.; Palmer, T.; Specht, E., *Metall. Mater. Trans. A* **2007,** 38, 464.

145. Bergman, G.; Shoemaker, D. P., *Acta Cryst.* **1954,** 7, 857.

146. Bindi, L.; Steinhardt, P. J.; Yao, N.; Lu, P. J., *Science* **2009,** 324, 1306.

147. C.Lawson, A.; E.Olsen, C.; Jr., J. W. R.; H.Mueller, M.; H.Lander, G., *Acta Cryst.* **1988,** B44, 89.

148. Arakcheeva, A.; Chapuis, G.; Birkedal, H.; Pattisona, P.; Grinevitchb, V., *Acta. Cryst.* **2003,** B59, 324.

149. Ungar, G.; Liu, Y.; Zeng, X.; Percec, V.; Cho, W.-D., *Science* **2003,** 299, 1208.

150. Percec, V.; Imam, M. R.; Peterca, M.; Wilson, D. A.; Graf, R.; Spiess, H. W.; Balagurusamy, V. S. K.; Heiney, P. A., *J. Am. Chem. Soc.* **2009,** 131, 7662.

151. Rosen, B. M.; Wilson, D. A.; Wilson, C. J.; Peterca, M.; Won, B. C.; Huang, C.; Lipski, L. R.; Zeng, X.; Ungar, G.; Heiney, P. A.; Percec, V., *J. Am. Chem. Soc.* **2009,** 131, 17500.

152. Zeng, X.; Ungar, G.; Liu, Y.; Percec, V.; Dulcey, A. E.; Hobbs, J. K., *Nature* **2004,** 428, 157.

153. Steurer, W.; Deloudi, S., *Crystallography of Quasicrystals*. Springer-Verlag: Berlin, 2009.

154. Dzugutov, M., *Phys. Rev. Lett.* **1993,** 70, 2924.

155. Roth, J., *Phys. Rev. Lett.* **1997,** 79, 4042.

156. Dzugutov, M., *Phys. Rev. Lett.* **1997,** 79, 4043.

157. Keys, A. S.; Glotzer, S. C., *Phys. Rev. Lett.* **2007,** 99, 235503.

158. Bates, F. S.; Cohen, R. E.; Berney, C. V., *Macromolecules* **1982,** 15, 589.

159. Shechtman, D.; Blech, I.; Gratias, D.; Cahn, J. W., *Phys. Rev. Lett.* **1984,** 53, 1951.

160. Ishimasa, T.; Nissen, H. U.; Fukano, Y., *Phys. Rev. Lett.* **1985,** 55, 511.

161. Chen, H.; Li, D. X.; Kuo, K. H., *Phys. Rev. Lett.* **1988,** 60, 1645.

162. Conrad, M.; Krumeich, F.; Harbrecht, B., *Angew. Chem. Int. Ed.* **1998,** 37, 1383.

163. Hayashida, K.; Dotera, T.; Takano, A.; Matsushita, Y., *Phys. Rev. Lett.* **2007,** 98, 195502.

164. Lifshitz, R.; Diamant, H., *Philos. Mag.* **2007,** 87, 3021.

165. Dzugutov, M., *Phys. Rev. A* **1992,** 46, R2984.

166. Wang, Z.-G., Morphology, fluctuation, metastability, and kinetics in ordered block copolymers. In *Advances in Chemical Engineering*, Academic Press: 2001; Vol. 28, p 439.

167. Fredrickson, G. H.; Binder, K., *J. Chem. Phys.* **1989,** 91, 7265.

168. Joannopoulos, J. D.; Johnson, S. G.; Winn, J. N.; Meade, R. D., *Photonic Crystals: Molding the Flow of Light*. 2nd ed.; Princeton Univ. Press: Princeton, 2008.

169. Walter, S.; Daniel, S.-W., *J. Phys. D* **2007,** 40, R229.

170. Gruner, S. M., *J. Phys. Chem.* **1989,** 93, 7562.

171. Clark, N. A.; Hurd, A. J.; Ackerson, B. J., *Nature* **1979,** 281, 57.

172. Pusey, P. N.; van Megen, W., *Nature* **1986,** 320, 340.

173. Larson, R. G.; Winey, K. I.; Patel, S. S.; Watanabe, H.; Bruinsma, R., *Rheol. Acta* **1993,** 32, 245.

174. Chung, C. I.; Gale, J. C., *J. Poly. Sci. B: Poly. Phys. Ed.* **1976,** 14, 1149.

175. Almdal, K.; Bates, F. S.; Mortensen, K., *J. Chem. Phys.* **1992,** 96, 9122.

176. Schulz, M. F.; Khandpur, A. K.; Bates, F. S.; Almdal, K.; Mortensen, K.; Hajduk, D. A.; Gruner, S. M., *Macromolecules* **1996,** 29, 2857.

177. Zhao, J.; Majumdar, B.; Schulz, M. F.; Bates, F. S.; Almdal, K.; Mortensen, K.; Hajduk, D. A.; Gruner, S. M., *Macromolecules* **1996,** 29, 1204.

178. Winey, K. I.; Gobran, D. A.; Xu, Z.; Fetters, L. J.; Thomas, E. L., *Macromolecules* **1994,** 27, 2392.

179. Groot, R. D.; Madden, T. J., *J. Chem.. Phys.* **1998,** 108, 8713.

180. Groot, R. D.; Madden, T. J.; Tildesley, D. J., *J. Chem. Phys.* **1999,** 110, 9739.

181. Harkless, C. R.; Singh, M. A.; Nagler, S. E.; Stephenson, G. B.; Jordan-Sweet, J. L., *Phys. Rev. Lett.* **1990,** 64, 2285.

182. Singh, M. A.; Harkless, C. R.; Nagler, S. E.; Shannon, R. F.; Ghosh, S. S., *Phys. Rev. B* **1993,** 47, 8425.

183. Floudas, G.; Pakula, T.; Velis, G.; Sioula, S.; Hadjichristidis, N., *J. Chem. Phys.* **1998,** 108, 6498.

184. Floudas, G.; Vlassopoulos, D.; Pitsikalis, M.; Hadjichristidis, N.; Stamm, M., *J. Chem. Phys.* **1996,** 104.

185. Balsara, N. P.; Garetz, B. A.; Newstein, M. C.; Bauer, B. J.; Prosa, T. J., *Macromolecules* **1998,** 31, 7668.

186. Matsen, M. W., *Phys. Rev. Lett.* **1998,** 80, 4470.

187. Liu, Z.; Shaw, M.; Hsiao, B. S., *Macromolecules* **2004,** 37, 9880.

188. Yamaguchi, D.; Hashimoto, T.; Vaidya, N. Y.; Han, C. D., *Macromolecules* **1999,** 32, 7696.

189. Han, C. D.; Vaidya, N. Y.; Kim, D.; Shin, G.; Yamaguchi, D.; Hashimoto, T., *Macromolecules* **2000,** 33, 3767.

190. Callister, W. D. J.; Rethwisch, D. G., *Fundamentals of Materials Science and Engineering*. 3rd ed.; John Wiley & Sons: Hoboken, NJ, 2008.

191. Schwab, M.; Stühn, B., *Phys. Rev. Lett.* **1996,** 76, 924.

192. Schwab, M.; Stühn, B., *Colloid Polym. Sci.* **1997,** 275, 341.

193. Wang, X.; Dormidontova, E. E.; Lodge, T. P., *Macromolecules* **2002,** 35, 9687.

194. Wang, J.; Wang, Z.-G.; Yang, Y., *Macromolecules* **2005,** 38, 1979.

195. Kinning, D. J.; Thomas, E. L., *Macromolecules* **1984,** 17, 1712.

196. Buitenhuis, J.; Forster, S., *J. Chem. Phys.* **1997,** 107, 262.

197. Shikata, T.; Pearson, D. S., *J. Rheol.* **1994,** 38, 601.

198. M. W. Matsen; F. S. Bates, *J. Poly. Sci. B: Poly. Phys. Ed.* **1997,** 35, 945.

199. Sarasua, J.-R.; Prud'homme, R. E.; Wisniewski, M.; Le Borgne, A.; Spassky, N., *Macromolecules* **1998,** 31, 3895.

200. Scott C. Schmidt; Marc A. Hillmyer, *J. Polym. Sci., Part B: Polym. Phys.* **2001,** 39, 300.

201. Williams, C. K.; Hillmyer, M. A., *Poly. Rev.* **2008,** 48, 1.

202. Zalusky, A. S.; Olayo-Valles, R.; Wolf, J. H.; Hillmyer, M. A., *J. Am. Chem. Soc.* **2002,** 124, 12761.

203. Pitet, L. M.; Hillmyer, M. A., *Macromolecules* **2009,** 42, 3674.

204. Cochran, E. W.; Bates, F. S., *Macromolecules* **2002,** 35, 7368.

205. Barton, A. F. M., *CRC Handbook of Polymer-Liquid Interaction Parameters and Solubility Parameters*. CRC Press: Boston, MA, 1990.

206. Kim, J. K.; Lee, H. H.; Gu, Q.-J.; Chang, T.; Jeong, Y. H., *Macromolecules* **1998,** 31, 4045.

207. Floudas, G.; Hadjichristidis, N.; Stamm, M.; Likhtman, A. E.; Semenov, A. N., *J. Chem. Phys.* **1997,** 106, 3318.

208. Hillmyer, M. A.; Bates, F. S., *Macromol. Symp.* **1997,** 117, 121.

209. Matsen, M. W.; Bates, F. S., *Macromolecules* **1996,** 29, 1091.

210. Anderson, K. S.; Hillmyer, M. A., *Macromolecules* **2004,** 37, 1857.

211. Mark, J. E., *Physical Properties of Polymer Handbook*. 2nd ed.; Springer: London, 2007.

212. Mai, S.-M.; Fairclough, J. P. A.; Terrill, N. J.; Turner, S. C.; Hamley, I. W.; Matsen, M. W.; Ryan, A. J.; Booth, C., *Macromolecules* **1998,** 31, 8110.

213. Floudas, G.; Vazaiou, B.; Schipper, F.; Ulrich, R.; Wiesner, U.; Iatrou, H.; Hadjichristidis, N., *Macromolecules* **2001,** 34, 2947.

214. de Gennes, P. G., *The Physics of Liquid Crystals*. Oxford Univ. Press: London, 1974.

215. Lennon, E. M.; Katsov, K.; Fredrickson, G. H., *Phys. Rev. Lett.* **2008,** 101, 138302.

216. Holden, G.; Legge, N. R.; Quirk, P. R.; Schroeder, H. E., *Thermoplastic Elastomers*. 2nd ed.; Hanser Publishers: New York, 1996.

217. Gehlsen, M. D.; Almdal, K.; Bates, F. S., *Macromolecules* **1992,** 25, 939.

218. Adams, J. L.; Graessley, W. W.; Register, R. A., *Macromolecules* **1994,** 27, 6026.

219. Spontak, R. J.; Smith, S. D., *J. Poly. Sci. B: Poly. Phys. Ed.* **2001,** 39, 947.

220. Wu, L.; Cochran, E. W.; Lodge, T. P.; Bates, F. S., *Macromolecules* **2004,** 37, 3360.

221. Alfonzo, C. G.; Fleury, G.; Chaffin, K. A.; Bates, F. S., *Macromolecules* **2010,** 43, 5295.

222. Matsushita, Y.; Takasu, T.; Yagi, K.; Tomioka, K.; Noda, I., *Polymer* **1994,** 35, 2862.

223. Michler, G. H.; Adhikari, R.; Lebek, W.; Goerlitz, S.; Weidisch, R.; Knoll, K., *J. Appl. Polym. Sci.* **2002,** 85, 683.

224. Bailey, T. S.; Pham, H. D.; Bates, F. S., *Macromolecules* **2001,** 34, 6994.

225. Meuler, A. J.; Fleury, G.; Hillmyer, M. A.; Bates, F. S., *Macromolecules* **2008,** 41, 5809.

226. Hermel, T. J.; Hahn, S. F.; Chaffin, K. A.; Gerberich, W. W.; Bates, F. S., *Macromolecules* **2003,** 36, 2190.

227. Mori, Y.; Lim, L. S.; Bates, F. S., *Macromolecules* **2003,** 36, 9879.

228. Lim, L. S.; Harada, T.; Hillmyer, M. A.; Bates, F. S., *Macromolecules* **2004,** 37, 5847.

229. Koo, C. M.; Wu, L.; Lim, L. S.; Mahanthappa, M. K.; Hillmyer, M. A.; Bates, F. S., *Macromolecules* **2005,** 38, 6090.

230. Fleury, G.; Bates, F. S., *Macromolecules* **2009,** 42, 3598.

231. Watanabe, H.; Sato, T.; Osaki, K., *Macromolecules* **2000,** 33, 2545.

232. Watanabe, H.; Matsumiya, Y.; Sawada, T.; Iwamoto, T., *Macromolecules* **2007,** 40, 6885.

233. Hashimoto, T.; Tanaka, H.; Hasegawa, H., *Macromolecules* **1990,** 23, 4378.

234. Tanaka, H.; Hashimoto, T., *Macromolecules* **1991,** 24, 5713.

235. Winey, K. I.; Thomas, E. L.; Fetters, L. J., *Macromolecules* **1992,** 25, 2645.

236. Matsen, M. W., *Macromolecules* **1995,** 28, 5765.

237. Koizumi, S.; Hasegawa, H.; Hashimoto, T., *Macromolecules* **1994,** 27, 7893.

238. Hashimoto, T.; Yamasaki, K.; Koizumi, S.; Hasegawa, H., *Macromolecules* **1993,** 26, 2895.

239. Hashimoto, T.; Koizumi, S.; Hasegawa, H., *Macromolecules* **1994,** 27, 1562.

240. Koizumi, S.; Hasegawa, H.; Hashimoto, T., *Macromolecules* **1994,** 27, 4371.

241. Shi, A.-C.; Noolandi, J., *Macromolecules* **1994,** 27, 2936.

242. Matsen, M. W., *J. Chem. Phys.* **1995,** 103, 3268.

243. Lin, E. K.; Gast, A. P.; Shi, A.-C.; Noolandi, J.; Smith, S. D., *Macromolecules* **1996,** 29, 5920.

244. Yamaguchi, D.; Hashimoto, T., *Macromolecules* **2001,** 34, 6495.

245. Court, F.; Hashimoto, T., *Macromolecules* **2001,** 34, 2536.

246. Court, F.; Hashimoto, T., *Macromolecules* **2002,** 35, 2566.

247. Lach, R.; Weidisch, R.; Knoll, K., *J. Poly. Sci. B: Poly. Phys. Ed.* **2005,** 43, 429.

248. Mickiewicz, R. A.; Ntoukas, E.; Avgeropoulos, A.; Thomas, E. L., *Macromolecules* **2008,** 41, 5785.

249. Bates, F. S., *Macromolecules* **1984,** 18, 525.

250. Sakamoto, N.; Hashimoto, T.; Han, C. D.; Kim, D.; Vaidya, N. Y., *Macromolecules* **1997,** 30, 1621.

251. Guth, E., *J. Appl. Phys.* **1945,** 16, 20.

252. Larson, R. G., *The Structure and Rheology of Complex Fluids*. Oxford Univ. Press: New York, 1999.

253. Myers, D., *Surfactant Science and Technology*. 3rd ed.; Wiley: New Jersey, 2006.

254. Shen, H.; Eisenberg, A., *Macromolecules* **2000,** 33, 2561.

255. Dormidontova, E. E., *Macromolecules* **1999,** 32, 7630.

256. Lund, R.; Willner, L.; Richter, D.; Dormidontova, E. E., *Macromolecules* **2006,** 39, 4566.

257. Won, Y.-Y.; Davis, H. T.; Bates, F. S., *Macromolecules* **2003,** 36, 953.

258. Cerritelli, S.; Fontana, A.; Velluto, D.; Adrian, M.; Dubochet, J.; De Maria, P.; Hubbell, J. A., *Macromolecules* **2005,** 38, 7845.

259. Frank, C.; Strey, R.; Schmidt, C.; Stubenrauch, C., *J. Colloid Interface Sci.* **2007,** 312, 76.

260. Foster, T.; Safran, S. A.; Sottmann, T.; Strey, R., *J.Chem.Phys.* **2007,** 127, 204711.

261. Wilhelm, M.; Zhao, C. L.; Wang, Y.; Xu, R.; Winnik, M. A.; Mura, J. L.; Riess, G.; Croucher, M. D., *Macromolecules* **1991,** 24, 1033.

262. Jada, A.; Siffert, B.; Riess, G., *Colloids Surf., A* **1993,** 75, 203.

263. Alexandridis, P.; Lindman, B., *Amphiphilic block copolymers : self-assembly and applications*. Elsevier: Amsterdam, Netherlands, 2000.

264. Wanka, G.; Hoffmann, H.; Ulbricht, W., *Macromolecules* **1994,** 27, 4145.

265. Alexandridis, P.; Athanassiou, V.; Fukuda, S.; Hatton, T. A., *Langmuir* **1994,** 10, 2604.

266. Lee, S.; Arunagirinathan, M. A.; Bates, F. S., *Langmuir* **2010,** 26, 1707.

267. Bates, F. S.; Maurer, W. W.; Lipic, P. M.; Hillmyer, M. A.; Almdal, K.; Mortensen, K.; Fredrickson, G. H.; Lodge, T. P., *Phys. Rev. Lett.* **1997,** 79, 849.

268. Marti, S.; Nervo, J.; Periard, J.; Riess, G., *Colloid Polym. Sci.* **1975,** 253, 220.

269. Hadjiyannakou, S. C.; Vamvakaki, M.; Patrickios, C. S., *Polymer* **2004,** 45, 3681.

270. Kyriacou, M. S.; Hadjiyannakou, S. C.; Vamvakaki, M.; Patrickios, C. S., *Macromolecules* **2004,** 37, 7181.

271. Bogdanov, B.; Mihailov, M., *J. Polym. Sci., Part B: Polym. Phys.* **1985,** 23, 2149.

272. Bogdanov, B.; Mihailov, M.; Popov, A.; Uzov, C., *Acta Polym.* **1986,** 37, 628.

273. Huang, P.; Zhu, L.; Cheng, S. Z. D.; Ge, Q.; Quirk, R. P.; Thomas, E. L.; Lotz, B.; Hsiao, B. S.; Liu, L.; Yeh, F., *Macromolecules* **2001,** 34, 6649.

274. Ryan, A. J.; Hamley, I. W.; Bras, W.; Bates, F. S., *Macromolecules* **1995,** 28, 3860.

275. Nojima, S.; Kato, K.; Yamamoto, S.; Ashida, T., *Macromolecules* **1992,** 25, 2237.

276. Hamley, I. W.; Fairclough, J. P. A.; Bates, F. S.; Ryan, A. J., *Polymer* **1998,** 39, 1429.

277. Guinier, A.; Fournet, G., *Small-angle scattering of X-rays*. Wiley: New York, 1955.

278. Burguiere, C.; Pascual, S.; Bui, C.; Vairon, J.-P.; Charleux, B.; Davis, K. A.; Matyjaszewski, K.; Betremieux, I., *Macromolecules* **2001,** 34, 4439.

279. Tran Cong, Q.; Nagaki, T.; Yano, O.; Soen, T., *Macromolecules* **1991,** 24, 1505.

280. Tai-Shung Chung; Zhen-Liang Xu; Cheng-Hon A. Huan, *J. Polym. Sci., Part B: Polym. Phys.* **1999,** 37, 1575.

281. Wang, X.; Guerin, G.; Wang, H.; Wang, Y.; Manners, I.; Winnik, M. A., *Science* **2007,** 317, 644.

Appendix A

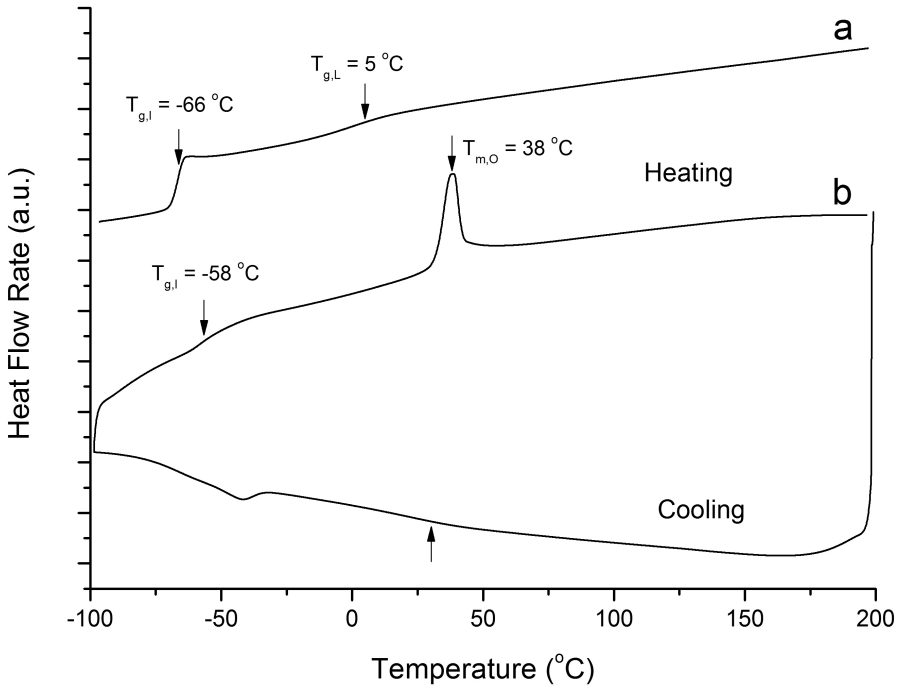

Figure A.1 DSC thermogram of (a) IL-15 and (b) SISO-3. Down-arrows indicate glass transition and melting temperatures. The glass transition temperature of PS (T_g) in SISO-3 is not evident in the heating thermogram. However, the cooling curve shows a signature of vitrification at ~ 30 ^oC (up-arrow), suggesting the T_g of PS exists around 40 ^oC, but buried in the melting peak of PEO (see text).

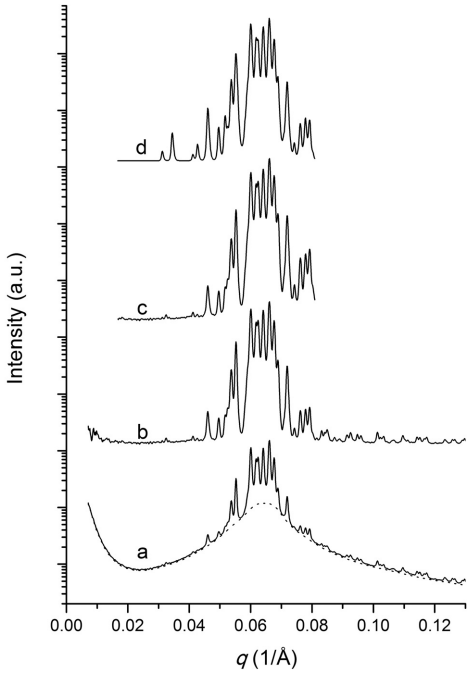

Figure A.2 Scattering pattern modifications of IL-15 SAXS for the JADE software analysis. (a) Experimental SAXS pattern obtained from IL-15 after 26 days aging(solid line) and background intensity modeled after correlation hole (dotted line). (b) Background subtracted IL-15 SAXS pattern. A constant background of 0.3 % of maximum peak intensity was added for neat representation. (c) IL-15 SAXS pattern after the sphere form factor and atomic scattering factor corrections. (d) Rietveld refinement pattern from IL-15 SAXS data after the reverse corrections of sphere form and atomic scattering factors. Only high intensity SAXS pattern (0.017 to 0.08 $Å^{-1}$) was used for the Rietveld refinement. The scattering power of each site was adjusted based on the Wigner-Seitz cell volume (see text).

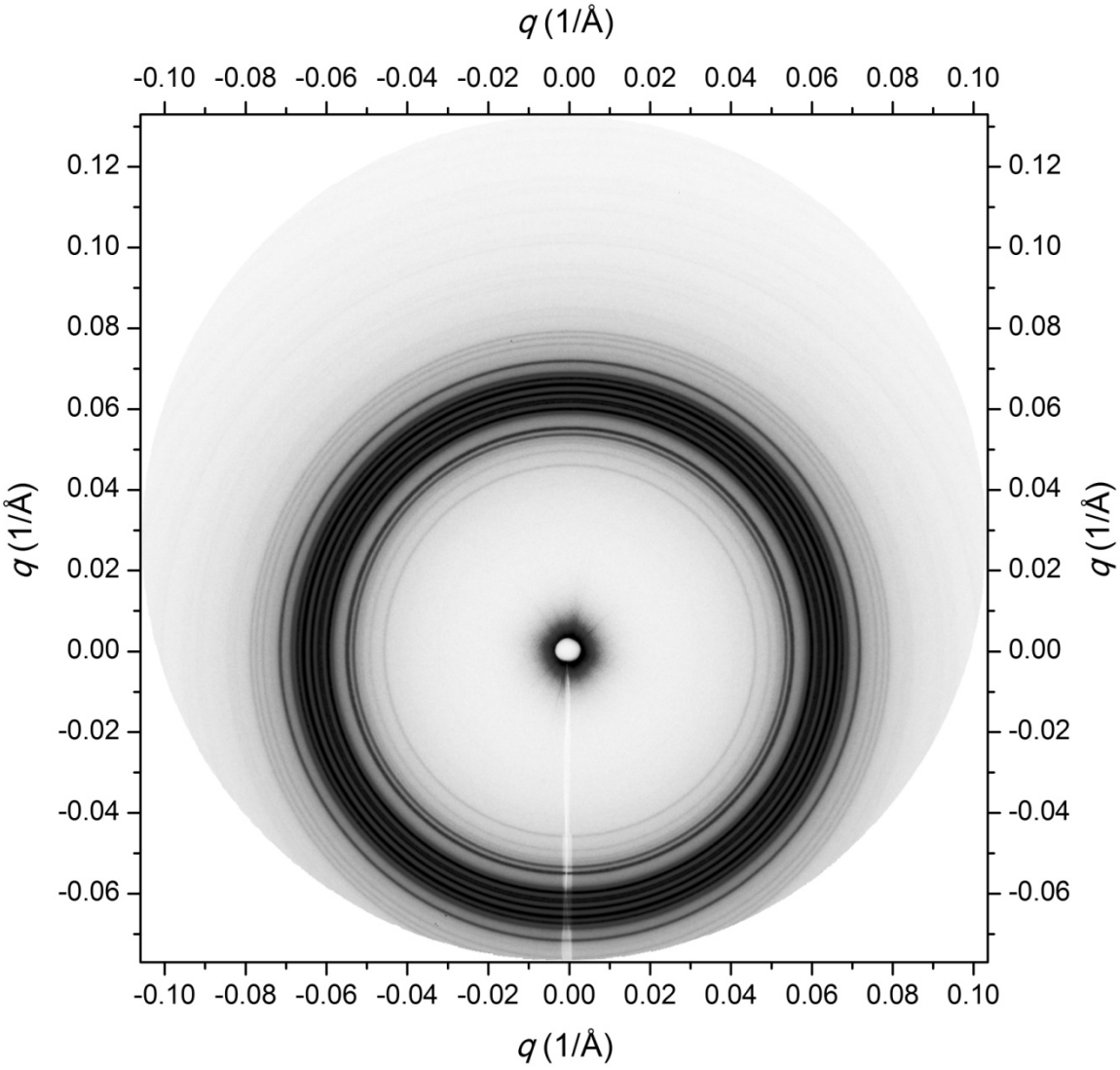

Figure A.3 Two dimensional small angle X-ray scattering power pattern obtained from IL-15 (poly(1,4-isoprene-b-DL-lactide) diblock copolymer) at room temperature acquired at the DND-CAT (beamline 5IDD) at the Advanced Photon Source (APS) located at the Argonne National Laboratory (Argonne, IL), March 2010.

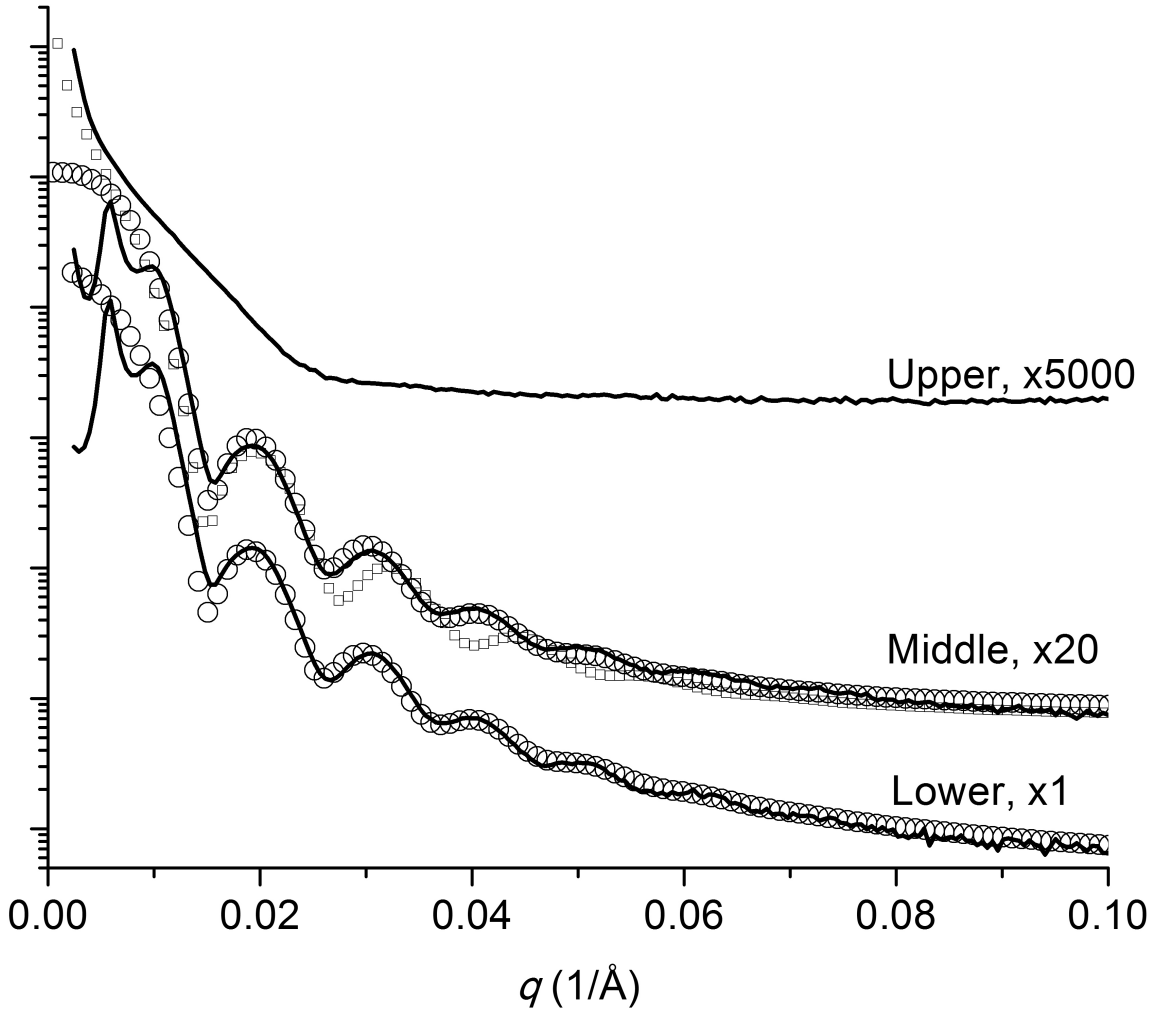

Figure A.4 Synchrotron SAXS patterns of OB-29/W/C-3 ternary mixtures. Experimental data (solid line, —) and sphere form factor fitting results (○) are presented. White square represent a fitting result with a cylinder form factor model.

Appendix B

Mathematica Code (version 7.0, Wolfram) for the Wigner-Seitz Cell representation

```
(* Wyckoff Position 2b, Coordination No. 12 *)
(* Total Sphere No. 2 *)

(* Summary of Variables;

NV: Number of Outer Vertices +1 (by surrounding domains);
V: Vertice Position;
Ro: Outer Vertice radius;
GOV: Graphic Representation of Outer Vertices as spheres;
NVOF: Number of outer faces;
OFace: Outer Face sets with vertices;
GOF: Graphic Representation of outer faces;
GCOVL:Graphic Representation of Center to Vertice Lines;
IV: Vertice Position of Wigner-Seitz Cell;
GWSC: Graphic Representation of Wigner-Seitz Cell (Vertices);
WSCFace: Set of vertices make up one face plane;
GWSCF: Graphic Representation of Wigner-Seitz Cell;

*)

(* Only required input is the sphere positions surrounding the \
center. Coordination Number will be calculated based on the number of \
spheres *)

(* Loading Vertice Values *)
(* V: Positions of Vetices *)



a = 431.6787;
c = 227.7387;
Ro = ((a*a*c)/30/(4 \[Pi])*3)^(1/3);
f = 0.22;(* Volume fraction of core *)
Rc = 41.6 ;(* Radius of core. It can be calculated from lattice \
parameter or set Rc=(Ro^3*f)^(1/3);  *)

ClearAll[V];
V = {{0, 0, 0}, {109.7586, 31.53845, 0}, {31.53845, 109.7586,
    0}, {-109.759, -31.5384, 0}, {-31.5384, -109.759, 0}, {-77.9784,
    77.97844, -58.0984}, {-77.9784, 77.97844,
    58.09842}, {77.97844, -77.9784, -58.0984}, {77.97844, -77.9784,
```

```
    58.09842}, {-45.0198, -45.0198, -113.869}, {-45.0198, -45.0198,
    113.8694}, {45.01977, 45.01977, -113.869}, {45.01977, 45.01977,
    113.8694}};
NV = Dimensions[V][[1]];

Ro = 10;  (* Ro is Sphere radius for visual representation. It is not \
necessary to be exact sphere radius *)
GOV = (* GOV is graphical representation of verticies *)
 Graphics3D[
  Table[{Specularity[White, 1], Red, Sphere[V[[i]], Ro],
    Text[Style[i, FontColor -> Black, FontSize -> 12,(*Background ->
      White, *)FontFamily -> "Helvetica", FontWeight -> Bold],
     V[[i]]]}, {i, 1, NV}], Axes -> False(*,AxesLabel -> {x,y,z}*),
  Boxed -> False];

(* Line representation of center to vertices *)


COVL = Table[{V[[1]], V[[i]]}, {i, 2, NV}];
GCOVL = Graphics3D[{Thickness[0.01], Line[COVL]}, Axes -> False,
   Boxed -> False];
Show[GOV, GCOVL]

(* Outer Face Sets. All outer sets should be written in OFace \
variable without any error becuase those sets will be used for \
Wigner-Seitz Cell Calculation. Face vertices set should be \
constructed by observation of above graphics, Show[GOV, GCOVL]. OFace \
= {Face1, Face2, Face3, Facex,....} and Facex={Three set of Vertices \
Number} which construct a neat triangle in same plane*)

NVOF = (NV -
    3)*2; (* Number of faces = (No. of Outer Vertices - 2) * 10 *)
Clear[OFace];

OFace = {{2, 3, 13}, {2, 13, 9}, {2, 9, 8}, {2, 8, 12}, {2, 12,
    3}, {8, 5, 10}, {12, 8, 10}, {12, 10, 6}, {3, 12, 6}, {3, 6,
    7}, {13, 3, 7}, {13, 7, 11}, {9, 13, 11}, {9, 11, 5}, {8, 9,
    5}, {4, 10, 5}, {4, 5, 11}, {4, 11, 7}, {4, 7, 6}, {4, 6, 10}};


GOF =(* Visual Representation of Outer Faces *)
  Graphics3D[{Opacity[0.1], Yellow,
    GraphicsComplex[V, Polygon[OFace]]}, Axes -> False(*,
   AxesLabel -> {x,y,z}*), Boxed -> False];

Show[GOV, GCOVL, GOF]

(* ------------End of First Block --------------------*)
```

```
(* Calculating Vertices of Winger-Seitz Cell *)
(* Number of vertices of a Wigner-Seitz Cell is same to number of \
faces by outer vertices *)

ClearAll[IV];
S = {x, y, z}; (* defining a variable for calculation *)

IV = Table[
   TS = Solve[{V[[OFace[[i, 1]]]].(S - V[[OFace[[i, 1]]]]/2) == 0,
      V[[OFace[[i, 2]]]].(S - V[[OFace[[i, 2]]]]/2) == 0,
      V[[OFace[[i, 3]]]].(S - V[[OFace[[i, 3]]]]/2) == 0}, {x, y, z}];
   Tx = x /. TS; Ty = y /. TS; Tz = z /. TS;
   {Tx[[1]], Ty[[1]], Tz[[1]]}, {i, 1, NVOF}];

(* Graphic Plot of Wigner-Seitz Cell *)

ri = 10; (* Radius of Wigner-Seitz Cell Verticies *)
GWSC = Graphics3D[
   Table[{Specularity[White, 1], Blue, Sphere[IV[[i]], ri],
     Text[Style[i, FontColor -> Red, FontSize -> 12,(*Background ->
       White,*)FontFamily -> "Helvetica", FontWeight -> Bold],
      IV[[i]] ]}, {i, 1, NVOF}], Axes -> False(*,AxesLabel ->
{x,y,z}*),
    Lighting -> "Neutral", Boxed -> False];
Show[GOV, GCOVL, GWSC]
(* ------------End of Second Block --------------------*)



(* Wigner-Seitz Cell Faces *)
(* From above graphical representation, You should input below cell \
face sequence to follow outer vertice sequence starting No. 2 (1st \
Vetice is the center ) *)

WSCFace = {{1, 2, 3, 4, 5},
   {1, 5, 9, 10, 11},
   {16, 17, 18, 19, 20},
   {15, 14, 17, 16, 6},
   {9, 8, 20, 19, 10},
   {11, 10, 19, 18, 12},
   {4, 3, 15, 6, 7},
   {3, 2, 13, 14, 15},
   {7, 6, 16, 20, 8},
   {13, 12, 18, 17, 14},
   {5, 4, 7, 8, 9},
   {1, 11, 12, 13, 2}};
```

```
GWSCF = Graphics3D[{Opacity[0.1], Yellow,
    EdgeForm[
     Directive[Thickness[0.003], White(*, Dashing[{0.03,0.03}],*)]],
    GraphicsComplex[IV, Polygon[WSCFace]]}, Boxed -> False];
Show[GWSC, GWSCF]

GC = Graphics3D[
   Table[{Sphere[V[i], Rc],
     Text[Style[Core, FontColor -> Black,
       FontSize -> 20,(*Background -> White,*)
       FontFamily -> "Helvetica", FontWeight -> Bold], V[i]]}, {i, 0,
     0}], Axes -> False(*,AxesLabel -> {x,y,z}*), Boxed -> False];
(* Show[GC,GWSCF] *)  (* Represenataion of Wigner-Seitz Cell with \
core *)

(* Assigning coorindation site to each face. OFace data can be used *)
\

(*{Vertice No., First Inner Vertice No., Second Inner Vetice No.} *)
(* VVL[i]={Vertex Number i, First Inner Vertex, Second Inner Vertex} *)

ClearAll[VVL, DIMi];
VVL = {0}; (* VVL should have some finite element for maniplulation. \
First 0 will be removed at the end of this block *)
NLCount = 0;

For[i = 2, i <= NV, i++,
 DIMi = Dimensions[WSCFace[[i - 1]]][[1]];
 For[j = 1, j <= (DIMi - 1), j++,
   NLCount++;
   VVL = Append[
     VVL, {i, WSCFace[[i - 1, j]], WSCFace[[i - 1, j + 1]]}];
   ]
  NLCount++;
 VVL = Append[VVL, {i, WSCFace[[i - 1, DIMi ]], WSCFace[[i - 1, 1]]}];
 ]
VVL = Take[VVL, {2, NLCount + 1}]; (* Remove first 0 *)
(* ------------End of Third Block --------------------*)



(* Calculation Part over Polygon *)
(* This code was written to calculate polygon volume, but it can be \
modified for calculation of any Wigner-Seitz Cell related physical \
properties *)
(* Volume calculation can be done by analytical method or numerical \
method *)

(* SetDirectory["C:\Users\username\Desktop"]; *)
```

```
(* str=OpenWrite["Sigma_1_2b_Volume.txt"]; *)

Clear[x, y, Rc, Ro, TV, TIV1, TIV2, TVIV1, TVIV2, Tx1, Tx2, Ty];

TddNSum = 0;
TddDSum = 0;
VolSum = 0;

(* Calculation Part *)

For[i = 1, i <= NLCount, i++,


  TV = V[[VVL[[i, 1]]]];
  TIV1 = IV[[VVL[[i, 2]]]];
  TIV2 = IV[[VVL[[i, 3]]]];

  VolSum = VolSum + Abs[Det[{TV/2, TIV1, TIV2}]]/6;


  (* Below Part is for numberical integration routin for calculation \
polygon volume that does same work above.
  It is intentenionally left for further modification *)


  (*

  TVIV1=TIV1-TV/2;
  TVIV2=TIV2-TV/2;
  TL=Norm[TV/2];


  (* Print["i=", i, " TL=", Norm[TL], " VIV1=", Norm[TVIV1],
  " VIV2=", Norm[TVIV2]]; *)

  (* Write[str,"i=", i, " TL=", Norm[TL], " VIV1=", Norm[TVIV1],
  " VIV2=", Norm[TVIV2]]; *)


  If[VectorAngle[TVIV1, TVIV2]<= (\[Pi]/2),

  Tx1=Min[Norm[TVIV1],Norm[TVIV2]]*Cos[VectorAngle[TVIV1,TVIV2]];
  Tx2=Max[Norm[TVIV1],Norm[TVIV2]];
  Ty=Min[Norm[TVIV1],Norm[TVIV2]]*Sin[VectorAngle[TVIV1,TVIV2]];

  (* Left Triangle *)
  X0=0;X1=Tx1;Y0=0;Y1=Ty/Tx1 x;
  Vol1=Integrate[Integrate[TL,{y,Y0,Y1}],{x,X0,X1}]/3;
```

```
  (* Right Triangle *)
  X0=Tx1;X1=Tx2;Y0=0;Y1=-(Ty/(Tx2-Tx1))(x-Tx1)+Ty;
  Vol2=Integrate[Integrate[TL,{y,Y0,Y1}],{x,X0,X1}]/3;


  VolSum=VolSum+Vol1+Vol2;
  Print["Act. or  Rgt. i=",i, " ,VolSum=", VolSum];
  (* Write[str, "Act. or  Rgt. i=",i, " ,VolSum=", VolSum]; *)

  ,

  (* Print["Obtuse"];*)  (* False Case, Obtuse Angle *)

  Tx1=Norm[TVIV1]*Cos[VectorAngle[TVIV1,TVIV2]];
  Tx2=Norm[TVIV2];
  Ty1=Norm[TVIV1]*Sin[\[Pi]-VectorAngle[TVIV1,TVIV2]];
  Ty2=Ty1*Tx2/(Tx2-Tx1);

  (* Left Triangle,
  I found it takes too long when y integral has variables at both \
boundary conditions so split below integrations into two parts *)
  X0=Tx1;X1=0;Y0=0;Y1=Ty1/Tx1 (x-Tx1)+Ty1;Y2=-(Ty2/Tx2)x+Ty2;

  Vol1=Integrate[Integrate[TL,{y,Y0,Y1}],{x,X0,X1}]/3;

  (* Right Triangle *)
  X0=0;X1=Tx2;Y0=0;Y1=-Ty2/Tx2 x+Ty2;
  Vol2=Integrate[Integrate[TL,{y,Y0,Y1}],{x,X0,X1}]/3;
  VolSum=VolSum+Vol1+Vol2;
  Print["Act. or  Rgt. i=",i, " ,VolSum=", VolSum];
  (* Write[str, "Act. or  Rgt. i=",i, " ,VolSum=", VolSum]; *)

  ];

  *)
  ];

Print["VolSum=", VolSum];
(* Write[str, "VolSum=", VolSum]; *)
(* Close[str]; *)
```